Control of a Traction/Charging Structure for a Hybrid Electric Vehicle

Saeid Aghaei Hashjin

Université de Lorraine : GREEN
Ecole Doctorale : Informatique Automatique Electrotechnique Electronique Mathématiques
Commission de mention : Electrotechnique Electronique

Thèse

présentée en vue de l'obtention du titre de

Docteur de l'Université de Lorraine

Spécialité : Génie électrique

par **Saeid AGHAEI HASHJIN**

Control of a Traction/Charging Structure for a Hybrid Electric Vehicle

Soutenue publiquement le 06/11/2020 devant de la commission d'examen composée de

Rapporteurs :	Dr. Daniela CHRENKO	UTBM
	Dr. Alexandre DE BERNARDINIS	Université Gustave Eiffel
Examinateurs :	Dr. Karim AIT-ABDERRAHIM	ESME Sudria
	Dr. Ouafae EL GANAOUI-MOURLAN	IFP School
Directeur :	Prof. Babak NAHID-MOBARAKEH	Univ. de Lorraine, GREEN
Co-directeur :	Dr. El-Hadj MILIANI	IFP School
Invités :	Mme. Véronique BONNET	ESME Sudria
	Dr. Alexandre BATTISTON	IFP Energies nouvelle

Groupe de Recherche en Electrotechnique et Electronique de Nancy
Ecole Nationale Supérieure d'Electricité et de Mécanique - TSA 60604 - 54518 Vandœuvre-lès-Nancy

DEDICATION

This work is wholeheartedly dedicated to my beloved parents, who have been my source of inspiration and gave me strength when I thought of giving up, who continually provide their moral, spiritual, emotional, and financial support. My love for you can never be quantified. Thank you.

ACKNOWLEDGMENTS

I would like to thank my Ph.D. supervisor, Prof. Babak NAHID-MOBARAKEH, to give me the opportunity to carry out my PhD studies and for his continuous support, motivation and academic guidance throughout this research. He always responded my questions with patience and his door was always open for me for further discussions. I owe my profound gratitude to him for being a resourceful person with unfailing guidance and valuable suggestions for me to constantly fighting failures and disappointments. I would like to gratefully acknowledge Dr. Karim AIT-ABDERRAHIM and Mme. Véronique BONNET, director of École spéciale de mécanique et d'électricité (ESME) d'Ivry-sur-seine for financing this research project and accepting me in his engineering school warmly. Working for them was one of my greatest experiences. I would like to also thank co-supervisor of this study, Dr. El-hadj MILIANI, whom we had fruitful discussions throughout my period of studies.

I should express my thanks to the members of the jury; Dr. Daniela CHRENKO, Dr. Alexandre DE BERNARDINIS, Dr. Ouafae EL GANAOUI-MOURLAN and Dr. Alexandre BATTISTON for their time and precious comments. I should express my gratitude to Prof. Farid MEIBODY-TABAR, Prof. Serge PIERFEDERICI, Dr, Thiery BOILEAU, Dr. Matthieu URBAIN and Dr. Jean Philippe MARTIN to participate in the supervising committee of my thesis. Their comments and fruitful discussions that we had helped me to increases the quality of my work. I would like also thank Prof. Noureddine TAKORABET, director of the GREEN laboratory, for his help and supports. He made a lot of efforts to make this project available for us.

I would like also to thank all my colleagues in the laboratory of GREEN for their help and support. Dr. Adrien Corne, Dr. Davide Dell'isola, Dr. Shengzhao Pang, Dr. Hamidreza Zandi, Dr. Thibaud Plazenet, Dr. Milad Bahrami, Peyman Haghgooei, Abderrahmane Djaouti, and Maxime Lapique thank you all for helping me. I can remember my first days in this laboratory when Mme. Sylvie Colinet and Latifa Zoua were helping me to advance my administrative staff. Thanks Sylvie and Latifa for helping me in administrative issues while always smiling.

I also owe gratitude to all my Iranian friends who were always with me and supporting me. Zia Alborzi & Mahta Mapar, Soheib Maghsoodi & Mojdeh Lahoori, Payam Mapar & Samira Poorjafari, Esmaeil Moosavi & Mahdieh Amin, Mohsen Babayizadeh & Elaheh Bastani, Parinaz Mapar, Farhad Nikfarjam, and Shirin Enferad you have always believed in me and I appreciate your friendship. Thank you for being my friend.

ABSTRACT

Control of a traction/charging structure for a hybrid electric vehicle

The electrification of the transportation is one of the relevant solutions to reduce greenhouse gas emissions. Indeed, new European standards impose increasingly restrictive limits on CO_2 emissions per km. This is an important industrial issue for automobile manufacturers. Therefore, the industries are moving towards hybrid and electric vehicles in which an electric traction chain is present. This consists of an electrical machine, powered by a static power electronic converter connected to an electrical energy source and storage elements. For more than two decades, different topologies have been studied for electric traction and several solutions have been marketed. These products are increasingly light, reliable and efficient while respecting the constraints of the automobile manufacturers on the costs.

This thesis focuses on improving the reliability of electromechanical energy conversion chains. The objective of the thesis is to continue the development of new actuator control laws ensuring better reliability of the traction chain. With this in mind, reducing the number of sensors in control of the conversion chain will be considered. In fact, there are already current sensors in traction chains. However, these generate significant additional costs because of their frequent failures and the need for replacement. Thus, current sensorless control of the AC drive systems allows the elimination of the sensors of the stator of the machine and therefore to avoid their cost.

In this thesis, the model-free adaptive controller (MFAC) is presented to be used in the control of the conversion chain to reduce the number of sensors. In this regard, MFAC is used in two different approaches. First, it is used for controlling a WRSM system, with and without additional current sensors. Then, it is used for the control of the power converters used in the conversion chain. The experimental results, obtained on a test bench built in the laboratory, are conclusive in transient and steady-state: the unmeasured currents are converged with a satisfying precision for an automotive application and allow performing a current sensorless control of the machine. In addition, a satisfactory performance of MFAC is also obtained for controlling the power converters with only using one voltage sensor.

Keywords: Electric machine, sensorless control, model-free control, electric model, electric vehicle.

RÉSUMÉ

Contrôle D'une Structure De Traction/Recharge Pour Véhicule Electrique Hybride

L'électrification des moyens de transport est considérée comme l'une des solutions pertinentes pour réduire les émissions des gaz à effet de serre. En effet, les nouvelles normes européennes imposent des limites de plus en plus restrictives sur les émissions de CO_2 par km. Ceci est un enjeu industriel important pour les constructeurs d'automobiles. Par conséquent, ces derniers s'orientent vers les véhicules hybrides et électriques dans lesquels une chaine de traction électrique est présente. Celle-ci est constituée d'une machine électrique, alimentée par un convertisseur statique d'électronique de puissance connecté à une source d'énergie électrique et des éléments de stockage. Depuis plus de deux décennies, différentes topologies ont été étudiées pour la traction électrique et plusieurs solutions ont été commercialisées. Ces produits sont de plus en plus légers, fiables et efficaces tout en respectant les contraintes des constructeurs d'automobile sur les coûts.

Cette thèse s'inscrit sur l'amélioration de la fiabilité des chaînes de conversion d'énergie électromécanique. Le travail de thèse a pour objectif de poursuivre le développement de nouvelles lois de commande d'actionneur assurant une meilleure fiabilité de la chaîne de traction. Dans cette optique, réduire le nombre de capteurs de la chaîne de conversion dans la commande sera envisagée. En effet, il existe déjà des capteurs de courant dans les chaînes de traction. Cependant, ceux-ci engendrent des surcoûts importants à cause de leurs défaillances fréquentes et la nécessité de remplacement très couteuse. Ainsi l'étude réalisée de commande de machine synchrone à griffes sans capteur de courant permet la suppression des capteurs du stator de la machine et donc de s'affranchir de leur coût.

Dans cette thèse, le model-free adaptive Controller (MFAC) est présenté pour être utilisé dans le contrôle de la chaîne de conversion pour réduire le nombre de capteurs. À cet égard, MFAC est utilisé dans deux approches différentes. Premièrement, il a été utilisé pour le contrôle d'un système WRSM, avec et sans capteurs de courant supplémentaires. Puis, il a été utilisé pour le contrôle des convertisseurs de puissance utilisés dans la chaîne de conversion. Les résultats expérimentaux, obtenus sur un banc de test réalisé en laboratoire, sont concluants en régime établi : les courants non mesurés sont contrôlés avec une précision satisfaisante pour une application automobile et permettent le contrôle sans capteur de courant de la machine. En plus, une performance satisfaisante du MFAC est également obtenue pour commander les convertisseurs de puissance avec un seul capteur de tension.

Mots clés : Moteur électrique, commande sans capteur, model-free control, modèle électrique, véhicule électrique.

CONTENTS

LIST OF FIGURES

LIST OF TABLES

ABBREVIATIONS

AC	Alternating current
BEV	Battery electric vehicle
BIBO	Bounded-input bounded-output
CFDL	Compact form dynamic linearization
CO_2	Carbon dioxide
DAB	Dual active bridge
DC	Direct current
DDC	Data driven control
DL	Dynamic linearization
DPS	Dual phase shift
DTC	Direct torque control
EKF	Extended Kalman filter
EM	Electric motor
ESS	Energy storage system
EV	Electric vehicle
FCV	Fuel cell vehicle
FEA	Finite element analysis
FFDL	Full form dynamic linearization
GA	Genetic algorithm
GHG	Green house gases
HEV	Hybrid electric vehicle
ICE	Internal combustion engine
IFT	Iterative feedback tuning
IPM	Internal permanent magnet
i-StARS	Integrated stator alternator revisable system
LV	Low voltage
MBC	Model based control
MFAC	Model free adaptive control
MIMO	Multi input multi output
MISO	Multi input single output
PFDL	Partial form dynamic linearization
PG	Pseudo gradient
PI	Proportional integral
PID	Proportional integral derivative
PJM	Pseudo jacobian matrix
PM	Permanent magnet
PPD	Pseudo partial derivative
PPJM	Pseudo partitioned jacobian matrix
PWM	Pulse width modulation
RFOC	Rotor field-oriented control
SISO	Single input single output
SPS	Single phase shift

UC	Ultra capacitor
UDFVC	Unified direct flux vector control
UPS	Uninterruptable Power Supplies
VRFT	Virtual reference feedback tuning
WRSM	Wired rotor synchronous machine
ZVS	Zero voltage switching

INTRODUDTION

The increasing amount of greenhouse gases (GHG) are considered as a major challenge for climate change and global warming. Transportation sector contributes to a 24% of global CO_2 emissions which are considered as the main composition of GHGs. The growing concerns about climate change and energy security have accelerated a global transition to a more sustainable transport system. Electric cars, representing an innovative technology with the potential to reduce greenhouse gas emissions and support the mitigation of climate change, have gained substantial interests in recent years.

So far, different configurations and options of the EVs have been proposed in the industry. EVs can run solely on electric propulsion or they can have an internal combustion engine (ICE) working alongside it. Having only batteries as energy source constitutes the basic kind of EV, but there are kinds that can employ other energy source modes. These can be called hybrid EVs (HEVs). Vehicles using two or more types of energy source, storage or converters can be called as an HEV as long as at least one of those provide electrical energy. There is another kind of EVs that use chemical reactions to produce electricity. The hydrogen is the fuel that carries out this reaction, so they are called fuel cell vehicles (FCV).

At the dawn of the second automotive century it is apparent that the nature of the automotive industry has become very competitive. In this situation, the automotive companies need to stay competitive by proposing new strategies to reach to a good performance with minimum cost. To do so, developing mild hybrid solutions have been Valeo's first choice. The mild hybrid solution has some advantages compared to the Start-Stop solution which is the most frequently used hybridization type on vehicles. In Start-Stop type, the electric actuator activates only for the restarting of the fuel engine, while in mild-hybrid solution the electric actuator can be activated each time the vehicle needs a power boost. Finally, the technical solution proposed by firm Valeo has been resulted in developing the "i-StARS" (integrated Starter Alternator Reversible System). The topology used for i-StARS machine is a doubly-fed claw pole wired rotor synchronous machine (WRSM). In order to optimize this kind of machine for mild hybrid application, a first study has been realized in the GREEN laboratory to enhance the finite elements modeling of a claw pole WRSM within Dr. Devornique's thesis work.

The second solution for Valeo, to stay competitive in automotive industry, was the cost optimization on the electronic part of the powertrain. To do so, Valeo proposed a study to remove the phase current sensors for the control of the i-StARS machine. Indeed, on a doubly-fed machine, at least 4 current sensors are required to control the electric powertrain. As it will be detailed in chapter three, the system operates under low voltage (12 V) and the currents in the stator are high (up to 150 A) and the current sensors capable of measuring such large currents are rather expensive. Thus, the benefits of removing those sensors on the manufacturing costs are clear. The proposed study was in collaboration with GREEN laboratory which resulted in PhD thesis study of Dr. Adrien CORNE. According to Dr. Corne's thesis work, a state observer is used to estimate the stator currents using the available measures, then the estimated currents are injected in a closed-loop controller. According to this configuration, a reliable current sensorless control method was achieved for mentioned WRSM system.

Despite all the advantages of the observation-based current sensorless control method, it has also some critical limitations. Since this method uses a state model of the system to estimate the unmeasured variables its effectiveness is highly dependent on the correctness of this model. However, reaching a very precise model is usually impossible or at least time-consuming. In addition, the performance of this control method is very sensitive to the parameters. The transient response is another challenge related to this method that contains a considerable amount of error.

According to the abovementioned statements, the aim of this thesis work is to continue the development of new actuator control laws that will improve the reliability of the AC drive train used in automotive area. In this context, the control of the AC machine and the power electronic interface will be considered. The objective is to design a controller to guarantee the stability of the system in both transient and steady-state condition. The designed controller is subjected to work with minimum number of sensors and fix the limitations related to the already developed sensorless controllers. To do so, the data-driven control (DDC) theory, as a good alternative for existing methods, is considered to be used in control of AC drive systems thanks to its intrinsic features. In this regard, the model-free adaptive control (MFAC), as a candidate of the data-driven control (DDC), is considered to be used in thesis work to overcome the previously mentioned limitations.

This thesis work consists of four chapters. In chapter 1, a brief background of the EVs is presented. This mainly includes a brief overview of the battery EVs, HEVs and FCVs. In this chapter, the control approaches and fundamentals of a standard electric drive system are also reviewed. The last section of this chapter is allocated to present the context and contribution of this study.

In chapter 2, the basic fundamentals, different categories and applications of data-driven control (DDC) methods are presented. The main focus of this chapter will be on presentation of the model-free adaptive control (MFAC). In this regard, the theory, application, stability analysis and controller design approach of MFAC are provided for any nonlinear system with single-input single-output (SISO), multi-input single-output (MISO) and multi-input multi-output (MIMO) structure. Some examples are also provided to simplify the understanding the application of the MFAC. The main purpose of this chapter is to provide the basic knowledge about the DDC theories that is used in this thesis work.

The third chapter is divided into three main sections. The first section of this chapter is dedicated to the modeling of the studied i-StARS system, including a claw-pole WRSM, an inverter, an input filter and a 12V battery. The modeling presented in this section includes a modeling based on finite elements analysis (FEA) and a modeling based on the electric approach for the studied WRSM. In second section of this chapter, the MFAC is developed for current control of the studied WRSM system. In this configuration the stator phase currents are measured and controlled directly. The aim behind this work is to show that the MFAC is totally independent from system model and parameter variations. In third section of this chapter, the MFAC is used for current sensorless control of the studied WRSM system. In this case, neither any measurements nor any observations are considered for stator phase currents and all the control tasks are considered to be done with only measuring the mechanical rotor speed. The effectiveness of the MFAC in control of the WRSM system, with and without using current sensors, is tested in simulation and experimental works and compared with

another existing current controller, such as PI, and current sensorless control algorithm, such as observation-based controller.

In chapter 4, control of the power converters, used in electric drive systems, are provided. Since the electric drive systems include several power converters, the control of two different converters (a DC/DC boost converter and a three-phase dual-active bridge (DAB) converter) are studied in this chapter, respectively. Similar to the chapter 3, the goal is to design a robust and reliable controller with minimum number of sensors for mentioned converters. In this case, the output voltage of the converters is considered as the only measured variable to design a robust controller using MFAC. The effectiveness of the MFAC in control of the power converters is tested in simulation and experimental works and compared with another existing control algorithm.

Chapter-1 BACKGROUND OF HYBRID ELECTRIC VEHICLES

Contents

Introduction

The automotive industry has been growing over the years and continues to grow today. Influenced by both government regulations and consumer demand, auto manufacturers have continued to pursue technologies to improve efficiency and fuel economy [1]. However, the highly developed automotive industry and the large number of automobiles in use around the world have caused and are still causing serious problems for society and human life. Deterioration in air quality, global warming, and a decrease in petroleum resources are becoming the major threats to human beings [2]. By increasing the global environmental concern, the importance of reducing green house gases (GHG) emissions became more apparent. In this regard, the European Union have made an agreement to increase the taxes of the emissions of GHG for the industries inside european countries. Approval of this agreement have widely influenced the automotive industries. Since most of the vehicles running today are still powered by internal combustion engines (ICE), the transportation industry is responsible for an estimated 25% to 30% of the global greenhouse effect gas emission according to the International Energy Agency in its Global EV Outlook [3], [4]. Consequently, the new European standards impose increasingly restrictive limits on CO_2 emissions per km. This is an important industrial issue for automakers.

More and more stringent emissions and fuel consumption regulations are stimulating an interest in the development of safe, clean, and high-efficiency transportation. In this regard, electrification of transport is considered as one of the relevant solutions to reduce emissions of greenhouse gases. It has been well recognized that electric, hybrid electric, and fuel cell-powered drive train technologies are the most promising solutions to the problem of land transportation in the future [2]. Indeed, the automotive industry is moving towards hybrid and electric vehicles in which an electric traction chain is present. This consists of an electric machine, powered by a static converter of power electronics connected to a source of electrical energy and storage elements. For more than two decades, different topologies have been studied for electric traction and several solutions have been marketed. These products are increasingly light, reliable and efficient while respecting the constraints of the automakers on the costs.

According to the abovementioned statements, this thesis study is founded based on the latest trend in the automotive industry which is the electrification of the vehicles. The aim of this thesis work is to continue the development of new actuator control laws that will improve the reliability of the AC drive train used in automotive area. In this context, the control of the AC machine and the power electronic interface will be considered. The objective is to design a controller to guarantee the stability of the system in both transient and steady-state condition. The goal is to develop a controller to work with minimum number of sensors. Indeed, there are already several sensors in a standard traction chain. However, these generate significant additional costs because of their frequent failures and the need for a very expensive replacement of manpower.

This chapter will first discuss the importance and advantages of the electric, hybrid and fuel cell vehicles. Classification of the existing hybrid electric vehicles will also be reviewed briefly. Fundamentals of a standard electric drive system will be given in second part. The details about the context and goal of this study will be given in last section of this chapter.

1.1. Electric, Hybrid and Fuel Cell Vehicles

Vehicles equipped with conventional internal combustion engines (ICE) have been in existence for over 100 years. With the increase of the world population, the demand for vehicles for personal transportation has increased dramatically in the past decade. This trend of increase will only intensify with the catching up of developing countries, such as China, India, and Mexico. The demand for oil has increased significantly [5].

Another problem associated with the ever-increasing use of personal vehicles is the emissions. The greenhouse effect, also known as global warming, is a serious issue that we have to face. There have been increased tensions in part of the world due to the energy crisis. Government agencies and organizations have developed more stringent standards for the fuel consumption and emissions. Nevertheless, with the ICE technology being matured over the past 100 years, although it will continue to improve with the aid of automotive electronic technology, it will mainly rely on alternative evolution approaches to significantly improve the fuel economy and reduce emissions[1], [2], [5], [6].

In recent decades, the research and development activities related to transportation have emphasized the development of high efficiency, clean, and safe transportation. Electric vehicles (EVs), hybrid electric vehicles (HEVs), and fuel cell vehicles (FCVs) have been typically proposed to replace conventional vehicles in the near future [1], [2], [5]. In this category, the electric vehicles (full electric vehicles) uses only electric energy for propulsion, hybrid electric vehicles (HEV) uses both fossil fuel and electric energy for propulsion and fuel cell electric vehicles (FCV) use hydrogen fuel cells to generate energy for propulsion. Table 1.1 shows a comparison of the major characteristics of EVs, HEVs and FCVs.

This section reviews the different aspects of EVs, HEVs, and FCVs. It also gives a brief review of the development of electric vehicles, hybrid electric vehicles, and fuel cell technology.

Table 1.1 Characteristics of BEVs, HEVs, and FCVs [5]

Types of EVs	Battery EVs	Hybrid EVs	Fuell cell EVs
Propulsion	• Electric motor drives	• Electric motor drives • Internal combustion engines	• Electric motor drives
Energy system	• Battery • Ultracapacitor	• Battery • Ultracapacitor • ICE generating unit	• Fuel cells • Need battery/ultracapacitor to enhance power density for starting
Energy source & infrastructure	• Electric grid charging facilities	• Gasoline stations • Electric grid charging facilities (for Plug In Hybrid)	• Hydrogen • Hydrogen production and transportation infrastructure
Characteristics	• Zero emission • High energy efficiency • Independent on crude oils • Relatively short range • High initial cost • Commercially available	• Very low emission • Higher fuel economy as compared with ICE vehicles • Long driving range • Dependence on crude oil (for non Plug In Hybrid) • Higher cost as compared with ICE vehicles • The increase in fuel economy and reduce in emission depending on the power level of motor and battery as well as driving cycle • Commercially available	• Zero emission or ultra low emission • High energy efficiency • Independent on crude oil (if not using gasoline to produce hydrogen • Satisfied driving range • High cost
Major issues	• Battery and battery management • Charging facilities • Cost	• Multiple energy sources control, optimization and management • Battery sizing and management	• Fuel cell cost, cycle life and reliability • Hydrogen infrastructure

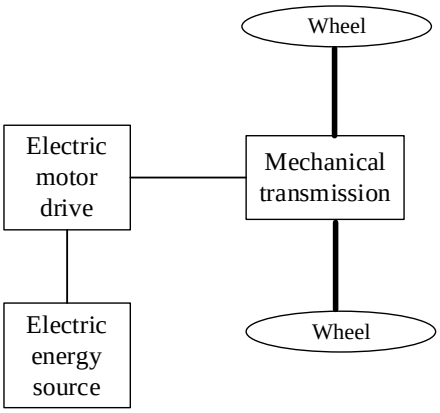

Figure 1.1 Primary electric vehicle powertrain [2].

1.1.1. Electric Vehicles

An electric vehicle (EV), uses one or more electric motors or traction motors for propulsion. Three main types of electric vehicles exist, those that are directly powered from an external power station, those that are powered by stored electricity originally from an external power source, and those that are powered by an on-board electrical generator, such as an engine (a hybrid electric vehicle), or a hydrogen fuel cell. Electric vehicles include electric cars, electric trains, electric lorries, electric airplanes, electric boats, electric motorcycles and scooters and electric spacecraft [7].

Battery-powered electric vehicles were one of the solutions proposed to tackle the energy crisis and global warming. However, the high initial cost, short driving range, long charging (refueling) time, and reduced passenger and cargo space have proved the limitation of battery-powered EVs.

Previously, the EV was mainly converted from the existing ICEV by replacing the internal combustion engine and fuel tank with an electric motor drive and battery pack while retaining all the other components, as shown in Figure 1.1. Drawbacks such as its heavy weight, lower flexibility, and performance degradation have caused the use of this type of EV to fade out. In its place, the modern EV is built based on original body and frame designs. This satisfies the structure requirements unique to EVs and makes use of the greater flexibility of electric propulsion.

A modern electric drive train is conceptually illustrated in Figure 1.2. The drive train consists of three major subsystems: electric motor propulsion, energy source, and auxiliary. The electric propulsion subsystem is comprised of a vehicle controller, power electronic converter, electric motor, mechanical transmission, and driving wheels. The energy source subsystem involves the energy source, the energy management unit, and the energy refueling unit. The auxiliary subsystem consists of the power steering unit, the hotel climate control unit, and the auxiliary supply unit. Based on the control inputs from the accelerator and brake pedals, the vehicle controller provides proper control signals to the electronic power converter, which functions to regulate the power flow between the electric motor and energy source. The backward power flow is due to the

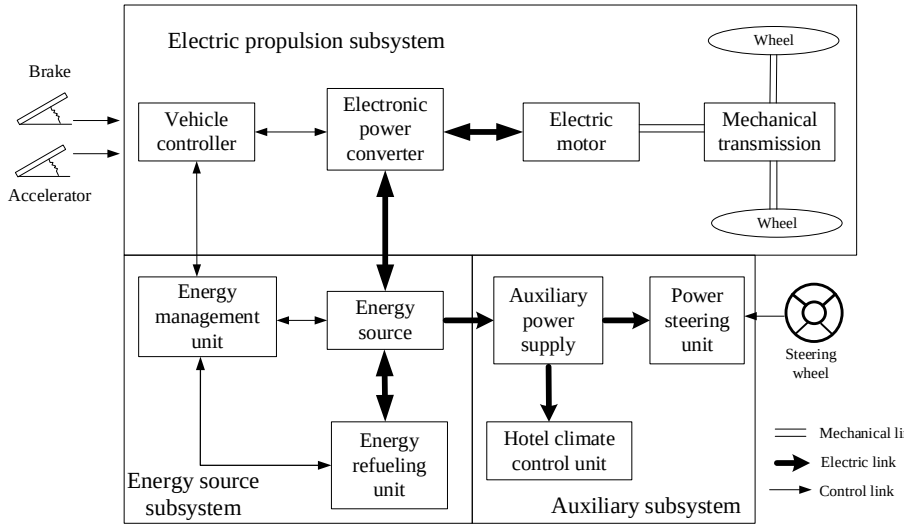

Figure 1.2 Conceptual illustration of general EV configuration [2].

regenerative braking of the EV and this regenerated energy can be restored to the energy source, provided the energy source is receptive. Most EV batteries as well as ultracapacitors and flywheels readily possess the ability to accept regenerated energy. The energy management unit cooperates with the vehicle controller to control the regenerative braking and its energy recovery. It also works with the energy refueling unit to control the refueling unit, and to monitor the usability of the energy source. The auxiliary power supply provides the

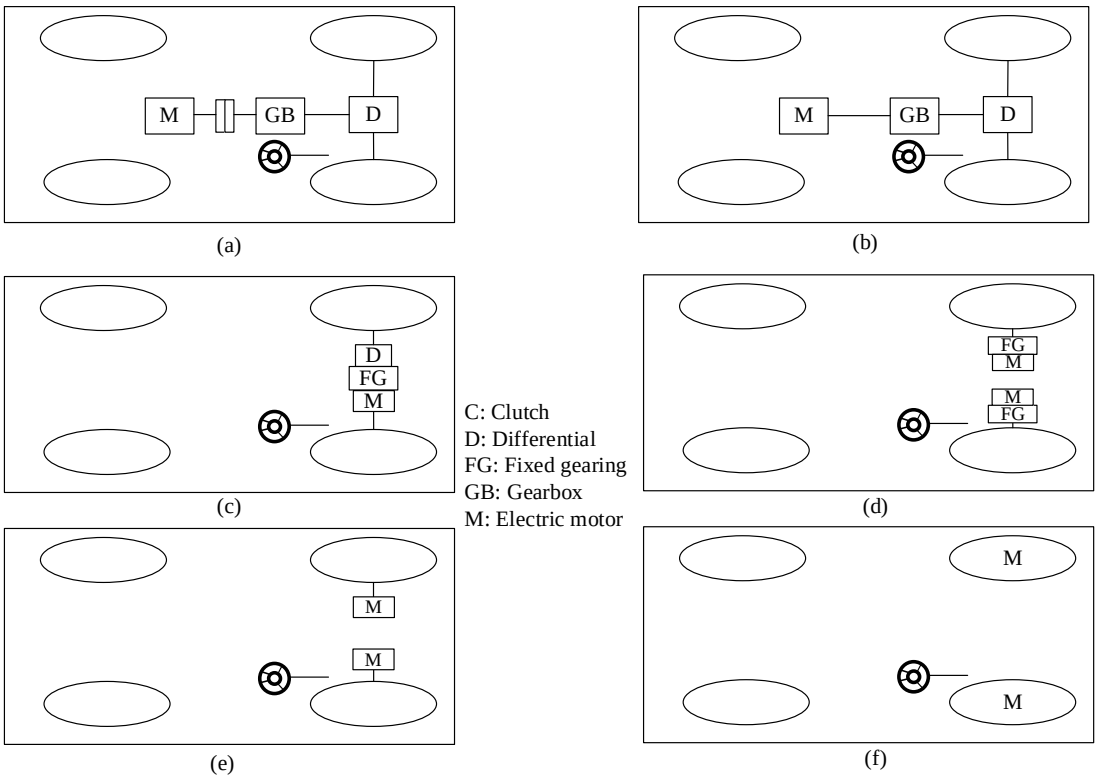

Figure 1.4 Possible EV configurations [2].

necessary power at different voltage levels for all the EV auxiliaries, especially the hotel climate control and power steering units.

There are a variety of possible EV configurations due to the variations in electric propulsion characteristics and energy sources, as shown in Figure 1.3.

a) Figure 1.3 (a) shows the configuration of the first alternative, in which an electric propulsion replaces the IC engine of a conventional vehicle drive train. It consists of an electric motor, a clutch, a gearbox, and a differential. The clutch and gearbox may be replaced by automatic transmission. The clutch is used to connect or disconnect the power of the electric motor from the driven wheels. The gearbox provides a set of gear ratios to modify the speed-power (torque) profile to match the load requirement. The differential is a mechanical device (usually a set of planetary gears), which enables the wheels of both sides to be driven at different speeds when the vehicle runs along a curved path.
b) With an electric motor that has constant power in a long speed range, a fixed gearing can replace the multispeed gearbox and reduce the need for a clutch. This configuration not only reduces the size and weight of the mechanical transmission, but also simplifies the drive train control because gear shifting is not needed.
c) Similar to the drive train in (b), the electric motor, the fixed gearing, and the differential can be further integrated into a single assembly while both axles point at both driving wheels. The whole drive train is further simplified and compacted.
d) In Figure 1.3 (d), the mechanical differential is replaced by using two traction motors. Each of them drives one side wheel and operates at a different speed when the vehicle is running along a curved path.
e) In order to further simplify the drive train, the traction motor can be placed inside a wheel. This arrangement is the so-called in wheel drive. A thin planetary gear set may be used to reduce the motor speed and enhance the motor torque. The thin planetary gear set offers the advantage of a high-speed reduction ratio as well as an inline arrangement of the input and output shaft.
f) By fully abandoning any mechanical gearing between the electric motor and the driving wheel, the out-rotor of a low-speed electric motor in the in-wheel drive can be directly connected to the driving wheel. The speed control of the electric motor is equivalent to the control of the wheel speed and hence the vehicle speed. However, this arrangement requires the electric motor to have a higher torque to start and accelerate the vehicle.

1.1.1.1. Advantages of EVs over traditional vehicles

The most obvious advantage of any electric car over combustion engine car is its zero tail pipe emissions, which is an unquestionable fact. However, the electric energy used for the propelling of the engine still needs to be produced somewhere to supply its consumption. Thus, the EVs only shift the air pollution up on its production stream towards the electricity plants, which in most of the cases still use fossil fuels for their production. As an impact of this is then anyway the positive fact, that the air polluting process now moves to

the nonurban areas and the agglomerations profit from locally lower emissions and the and pollutants harmful to the health, which go hand in hand (i.e. CO, NOx, THC, NMHC) [8]. The emissions produced by the power plants are far easier to manage in a unified form at the plants, producing the energy with much higher carbon dioxide efficiency, than in the case of huge amounts of single cars in the daily traffic. Another fact is the reduction of noise caused by the traffic, since the EV's motor running is significantly quieter, thanks to the missing exhaust [8].

Another major advantage of any type of fully electrically powered vehicle is a significantly lower consumption cost. Moreover, the price and consumption of kWh of EVs represent a significant difference of the consumption of any gasoline or diesel car.

Moving on, the electric engine entirely misses the transmission with the clutch and consists of just very few moving particles, unlike the combustion engine. Therefore, there is no need for change of any type of oil, coolant, water or start sparks of the engine. This fact has a consumer-friendly aspect of less wear out of the engine components, going hand in hand with lower maintenance costs, dedicated to the service of the vehicle [9]. The electric cars are usually enhanced with the system of regenerative engine braking, when the foot is removed from the gas pedal. This process eventually prolongs the lifetime of the braking pads and simultaneously recharges the batteries while braking.

The average efficiency of today's combustion engines, namely the way how effectively it operates with the consumed fuels, is between 25% and 35%. The electric engines, on the other hand, have more than triple the amount of efficiency, at least 90% [10].

The next positive impact of the missing transmission and the overall nature of the electric unit is its instant torque, offering maximum power from the standstill, whereas a combustion engine can only achieve this at high speed [10]. The power delivery is extremely smooth and achievable at any moment of the drive, making it a security element in case of possible fast response needed in traffic situations, such as overtaking.

Finally yet importantly, the buy of any new EV is in many countries subsidized by the government, stimulating the public interest to purchase the EVs over the conventional automobiles in order to reduce the country's dependency on foreign oil. This is usually the case for the fully electric BEVs, but subsidizing hybrid cars might be considered as well in many destinations.

1.1.1.2. Challenges for EVs

A. Range and batteries

The major barrier for buying any EV is the range of a single charge of the car, which is much lower than for any fully tanked conventional automobile. The vast majority of the EV market nowadays, are only able to travel from 80 to 160 km on a single charge (with the Tesla, however, up to 500km, but becoming very pricy) [10][11]. This could be considered sufficient as a daily range for most of the population, however, it is still incomparable with the range of any combustion engine vehicle. Those normally achieve 500km on a single tank, without being limited by the charging station network and being able to refill their tank at any gas station. For any regularly long-distance travelling driver, the limited range might present a problem.

Continuing the talk about the range of EVs, it markedly decreases while driving on the highway at speeds higher than 130km/h, at which the car needs more power. However, cruising up to the speed of 110km/h, the EVs usually still manage well without any significant range drops [10][11].

B. Charging

When somebody owns an electric car, his/her basic need is to have the possibility to charge it conveniently, in order to calm down his/her worries. In case of shorter distances around the town, for journeys to the work place, grocery stores or schools, the usual car range is most of the time sufficient for one day.

A majority of the EV owners (95%) usually charge their cars' batteries during the night, when they are not using the car [10][11]. Anyway, not all the members of the population have the luxury of parking in a garage, where they can simply plug in their vehicle. Many people park their cars in the street and they would have to be lucky to have any public charging point in their living area [12].

The next problem occurs for trips that are longer than the one charge range of the vehicle. In this case, the customers are forced to rely on the charging points' network. Although the number of charging stations is increasing, it is still incomparable with the convenience of the gas stations and their geographical density. The charging time is another issue, which might be solved with the so-called rapid chargers, adding to the vehicle's range within less than an hour. However, their occurrence is rather rare today [12].

C. Purchase price

Finally, there is the question of the purchase price of any electric car, which is generally speaking much higher than any other conventional market product from given class and quality segment. The main reason for electric cars being so expensive is mainly their battery price, where we face nowadays the price of 350 USD per 1 kWh of its capacity [13]. Speaking of the purchase price of any EV, let us observe it through the example of fully battery electric Chevrolet Bolt, where the battery capacity is 60 kWh and its selling price is around

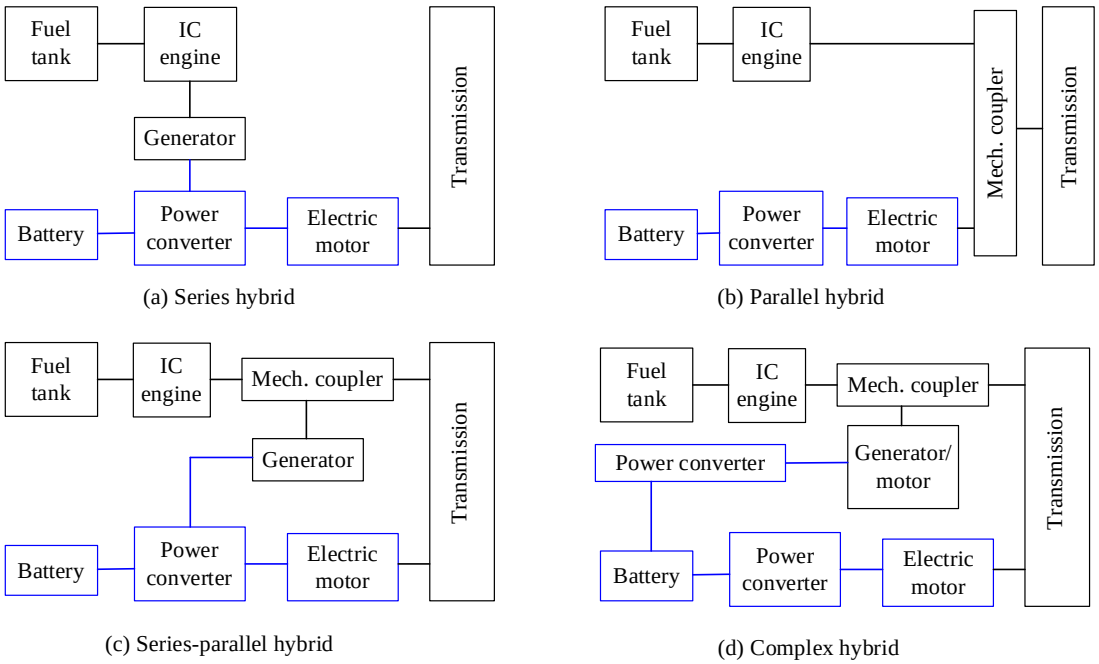

(a) Series hybrid

(b) Parallel hybrid

(c) Series-parallel hybrid

(d) Complex hybrid

Figure 1.6 Classification of hybrid electric vehicles [2].

37.495 USD in the US. Given the above-mentioned price of 1 kWh, we face a battery price of 21.000 USD, which is more than half of the final selling price [14]. This fact makes it difficult for the automakers to satisfy their profit margin, while trying to offer an affordable car and that is why the electric cars are more expensive than competing conventional vehicles.

1.1.2. Hybrid electric vehicles

The HEV was developed to overcome the disadvantages of both internal combustion engine (ICE) vehicles and the pure battery-powered electric vehicle. The HEV uses the onboard ICE to convert energy from the onboard gasoline or diesel to mechanical energy, which is used to drive the onboard electric motor, in the case of a series HEV, or to drive the wheels together with an electric motor, in the case of parallel or complex HEV.

The purpose of hybrid electric vehicles is to achieve a better fuel economy and better car efficiency. The electric motor minimizes idling and improves the vehicle's ability to stop and go, which is particularly useful in the city traffic. Moreover, the electric motor assists or fully donates the vehicle's acceleration and the low-speed driving [10]. Another major advantage of the HEVs over the BEVs is, due to the addition of the combustion engine, the much higher range of the vehicle, when the batteries of the electric engine run out of power.

In hybrid vehicles, two or more sources of power/energy are combined to obtain the required power to propel the vehicle. HEVs combine the advantages of the electric motor drive and an internal combustion engine to propel the vehicle [15]. The architecture of a hybrid vehicle is loosely defined as the connection between the components that define the energy flow routes and control ports. Traditionally, HEVs were classified into two basic types: series and parallel. Recently, series– parallel and complex HEVs have been developed to improve the power performance and fuel economy [2][15]. All different topologies of the HEVs are shown in Figure 1.4 . The next few sections will review the topologies related to series hybrid vehicle, parallel hybrid vehicle, series-parallel hybrid vehicles, and complex hybrid vehicles. Thus, the various strategies to combine the ICE and traction motor in a hybrid arrangement will be highlighted.

A. Series HEV

In case of series hybrid system (Figure 1.4.a) the mechanical output is first converted into electricity using a generator. The converted electricity either charges the battery or can bypass the battery to propel the wheels via the motor and mechanical transmission. Conceptually, it is an ICE assisted Electric Vehicle (EV). There are six possible different operation modes in a series HEV [2][5]:

1) battery alone mode: engine is off, vehicle is powered by the battery only;
2) engine alone mode: power from ICE/G;
3) combined mode: both ICE/G set and battery provides power to the traction motor;
4) power split mode: ICE/G power split to drive the vehicle and charge the battery;
5) stationary charging mode;
6) regenerative braking mode.

The advantages of series hybrid drivetrains are:

- mechanical decoupling between the ICE and driven wheels allows the IC engine operating at its very narrow optimal region.
- nearly ideal torque-speed characteristics of electric motor make multi gear transmission unnecessary.

However, a series hybrid drivetrain has the following disadvantages:

- the energy is converted twice (mechanical to electrical and then to mechanical) and this reduces the overall efficiency.
- Two electric machines are needed and a big traction motor is required because it is the only torque source of the driven wheels.

The series hybrid drivetrain is used in heavy commercial vehicles, military vehicles and buses. The reason is that large vehicles have enough space for the bulky engine/generator system.

B. Parallel HEV

The parallel HEV (Figure 1.4.b) allows both ICE and electric motor (EM) to deliver power to drive the wheels. Since both the ICE and EM are coupled to the drive shaft of the wheels via two clutches, the propulsion power may be supplied by ICE alone, by EM only or by both ICE and EM. The EM can be used as a generator to charge the battery by regenerative braking or absorbing power from the ICE when its output is greater than that required to drive the wheels. The following are the possible different operation modes of parallel hybrid [5][2][15]:

1) motor alone mode: engine is off, vehicle is powered by the motor only;
2) engine alone mode: vehicle is propelled by the engine only;
3) combined mode: both ICE and motor provides power to the drive the vehicle;
4) power split mode: ICE power is split to drive the vehicle and charge the battery (motor becomes generator);
5) stationary charging mode;
6) regenerative braking mode (include hybrid braking mode).

The advantages of the parallel hybrid drivetrain are:

- both engine and electric motor directly supply torques to the driven wheels and no energy form conversion occurs, hence energy loss is less.
- compactness due to no need of the generator and smaller traction motor.

The drawbacks of parallel hybrid drivetrains are:

- mechanical coupling between the engines and the driven wheels, thus the engine operating points cannot be fixed in a narrow speed region.
- The mechanical configuration and the control strategy are complex compared to series hybrid drivetrain.

Due to its compact characteristics, small vehicles use parallel configuration. Most passenger cars employ this configuration.

C. Series-Parallel HEV

The series-parallel HEV is a combination of the series and parallel hybrids. There is an additional mechanical link between the generator and the electric motor, compared to the series con- figuration, and an additional generator compared to the parallel hybrid, as shown in Figure 1.4.c With this design, it is possible to combine the advantages of both the series and parallel HEV configurations. It must be highlighted here that the series-parallel HEV is also relatively more complicated and expensive. There are many possible combinations of the ICE and traction motor. Two major classifications can be identified as electric-in- tensive and engine-intensive. The electric-intensive series-parallel HEV configuration indicates that the electric motor is more active than the ICE for propulsion, whereas, in the engine-in- tensive case, the ICE is more active. A common operative characteristic for both types of series-parallel HEV systems is that the electric motor is used alone at start with ICE turned off [2][5][16].

D. Complex HEV

The complex hybrid system (Figure 1.4.d) involves a complex configuration which cannot be classified into the above three kinds. The complex hybrid is similar to the series-parallel hybrid since the generator and electric motor is both electric machines. However, the key difference is due to the bidirectional power flow of the electric motor in complex hybrid and the unidirectional power flow of the generator in the series-parallel hybrid. The major disadvantage of complex hybrid is higher complexity.

In addition to the classification above, HEVs can be also classified into the following categories according to the level of hybridization and electric power [5].

a. Micro hybrid

The typical electric motor power for a sedan micro hybrid is about 2.5 kW at 12 V. It is essentially the integration of starter and alternator in the conventional ICE vehicle. The main function of the electric motor is for start and stop, hence the energy saving gained mainly is due to using the motor for start and stop. In city driving where there are frequent starts and stops, the energy saving may reach about 5% to 10%. The cost of a micro hybrid is only few percent higher than that of conventional vehicle, since the motor is small and the structure is simple. In the market, there is the C3 Citroen micro hybrid using the Valeo motor system.

b. Mild hybrid

The typical electric motor power for a sedan mild hybrid is about 10–20 kW at 100– 200 V. In this case, the motor is designed in a flat shape and is directly coupled with the engine. The high ratio of diameter to length of the motor enables the motor to have high inertia such that the original flywheel of the engine can be removed. The motor can join the propulsion as in parallel hybrid architecture. In city driving, typically it can save energy 20%–30%, but the cost will also increase 20%–30%. Available models are the Honda Civic and Honda Insight that belong to the mild hybrid category.

c. Full hybrid

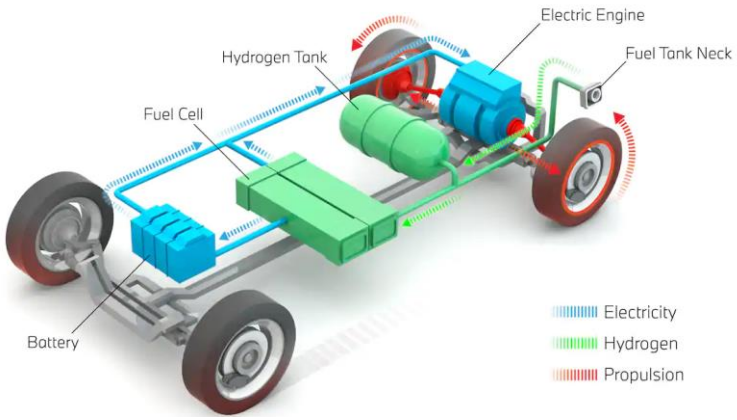

Figure 1.8 Propulsion system for a fuel-cell vehicle.

The typical electric motor power for a full sedan hybrid is about 50 kW at 200–300 V. Normally, there is a motor, generator, and engine, adopting series–parallel or a complex hybrid architecture. With the aid of power split devices such as a planetary gear, the power flow among engine, motor, generator, and battery is flexible in order to achieve optimum drive performance at maximum energy efficiency and minimum emission. The propulsion can be executed by motor only (for start and stop), engine only (for cruising whenever the engine at optimum operation region), or a combination of motor and engine (for sudden acceleration or normal driving when the required propulsion power is less than the engine optimum power range, thus the engine will drive the generator to charge the battery, and hence the engine will deliver more power than the required propulsion power such as that to reach optimum operation region). Typically, a full hybrid in city driving can save energy about 30%– 50%, while the cost increases about 30%–40%. The full hybrid vehicles can be further subdivided into Synergy Hybrid and Power Hybrid. Synergy Hybrid compromises the drive performance, energy efficiency, and emission reduction. In this subcategory, the engine is downsized as compared with conventional vehicle, such as in the Toyota Prius. Power Hybrid is aiming to have better driving performance, thus the engine is not downsized, and with the conjunction of the motor, the vehicle will have better drive performance as compared with a conventional vehicle, such as in the Toyota Highlander.

1.1.3. Fuel cell vehicles

A typical fuel cell-based propulsion system is shown in Figure 1.5 Fuel cell electric vehicles (FCVs) are powered by hydrogen. FCVs use a propulsion system similar to that of electric vehicles, where energy stored as hydrogen is converted to electricity by the fuel cell. Unlike conventional internal combustion engine vehicles, they produce no harmful tailpipe emissions. FCVs are fueled with pure hydrogen gas stored in a tank on the vehicle. Similar to conventional internal combustion engine vehicles, they can fuel in less than 5 minutes and have a driving range over 300 miles. FCVs are equipped with other advanced technologies to increase efficiency, such as regenerative braking systems, which capture the energy lost during braking and store it in a battery. Major automobile manufacturers are offering a limited but growing number of production FCVs to the public in certain markets, in sync with what the developing infrastructure can support. Fuel cell

vehicles can be considered as series-type hybrid vehicles. The onboard fuel cell produces electricity, which is either used to provide power to the propulsion motor or stored in the on board battery for future use.

1.2. Fundamentals of Electric Drives

1.2.1. The Electric drive structure

The essential parts of an electric drive, as shown in Figure 1.6, are: electrical machine, power converter and control system.

A. Electrical machine

Electric machine converts the energy supplied by the battery into mechanical energy to be used in many automotive parts such as traction motors, hybrid-coolant water pumps, alternators, starters, engine-cooling fans, electric power steering, sun roofs and air-conditioning compressors. It is the motor with the controller that determines the characteristics of the propulsion system and the ratings of the power devices in the power converter. The main requirements for propulsion motor are ruggedness, high torque to inertia ratio, high torque density, wide speed range, low noise, little or no maintenance, small size, ease of control, and low cost.

Several types of electric machine technologies have been investigated for automotive propulsion. Induction, permanent magnet (PM) and switched reluctance machines are the three main categories of electric machines that are suitable for EV, HEV and FCVs.

Induction machines are used for EV, HEV and FCV powertrain due their simplicity, robustness, and wide speed range. Besides, induction machines do not have back emf to deal with at high speeds. Field-oriented control makes an induction machine behave just like the way a dc machine behaves. The efficiency is generally lower than a PM machine due to the inherent rotor loss. For the same reason, the size of an induction machine is generally bigger than a PM machine with the same power and speed rating.

Permanent magnet (PM) and wound rotor (WR) synchronous machines possess unique characteristics such as high efficiency, high torque, and high power density. However, PM motors inherently have a short constant power range due to its rather limited field weakening capability, resulting from the presence of the PM field, which can only be weakened through production of a stator field component, which opposes the rotor magnetic field. Besides, the back emf can be an issue at high speed: the inverter must be able to withstand the maximum

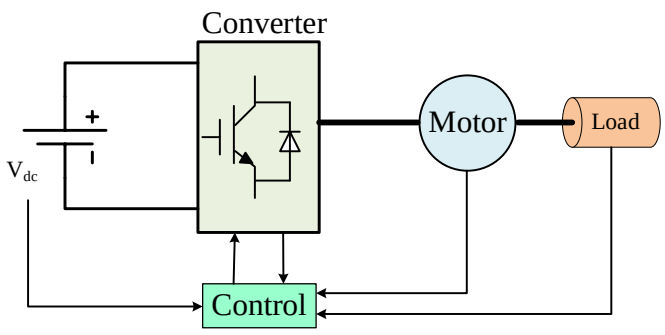

Figure 1.10 Electric drive structure [18].

back emf generated by the stator winding. In the case of a stator winding short circuit fault, the system can run into problems due to the existence of a rotor PM field.

Switched reluctance motor (SRM) is gaining interest as a candidate of electric propulsion for EVs, HEVs, and FCVs because of its simple and rugged construction, simple control, ability of extremely high-speed operation, and hazard-free operation. These prominent advantages are more attractive for traction application than other kinds of machines. However, since SRM is not yet widely produced as a standard motor, its cost may be higher than the induction motor.

Among all passenger EVs and HEVs, a very small number of models use an induction motor, including the electric cars made by Tesla. General Motors also has an induction motor design for the Chevy Spark. The Hyundai Sonata uses a surface-mount permanent-magnet (PM) machine. Almost all of the other major car companies use an interior permanent-magnet (IPM) machine for EVs and HEVs [5], [6], [17], [18].

B. Power converters

Power electronics is an enabling technology for the development of electric and hybrid vehicle propulsion systems. The power converter supplies the machine with desired three-phase voltage vectors determined by the control system. A number of converter configurations and command techniques exist which are chosen based on various system constraints and requirements. Some typical types are: voltage/current fed two-level three-phase bridge inverters, multi-level bridge inverters, cycloconverters, and matrix converters. The most widely used configuration is the voltage-fed two- level bridge converter and its control techniques are: square wave or six-step, pulse width modulation (PWM) and its variants. The power electronic system should be efficient to improve the range of the electric vehicles and fuel economy in hybrid vehicles. The selection of power semiconductor devices, converters/inverters, control and switching strategies, the pack- aging of the individual units, and the system integration are very crucial to the development of efficient and high-

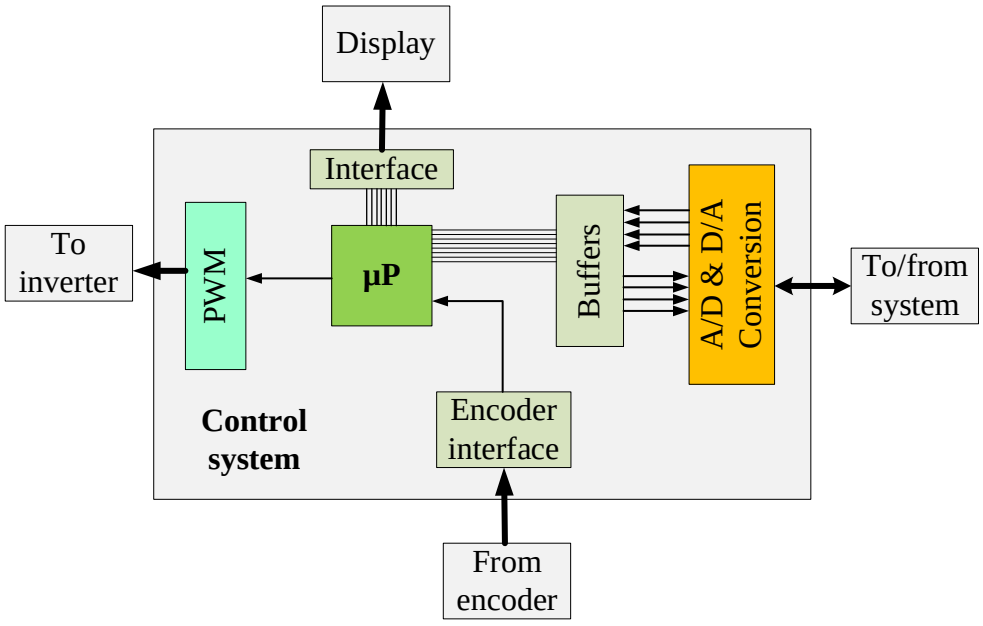

Figure 1.12 Control system for electric drive.

performance vehicles. In addition to power devices and controllers, there are several other components such as capacitors, inductors, bus bars, thermal systems, etc., that form a major portion of a power electronic unit [5], [6], [17], [18].

C. Control system

The main function of the control system block is to ensure that the command is executed and demand is met within certain set limits. This block hosts all the hardware and software related to control algorithms, system start-up information, data acquisition routines, signal processing, system protection checks, and command generation code. The core of the control system is a powerful microcontroller/microprocessor that executes all the routines, acquires external system variables, synchronizes the software and hardware operations, and outputs variables for visualization. Figure 1.7 shows important blocks of the control system. Apart from the signals shown in Figure 1.7, some auxiliary inputs and outputs such as hardware protection statuses, auxiliary supply alarms, temperature sensing signals and drive status commands are usually included [18][2].

1.2.2. Vector control for Electric drive system

The drive's control system (of Figure 1.7) receives the command from the user or supervisory control logic in a process. This command is processed based on the programmed algorithm to carry out the commanded operation. Usually, the command is in terms of position/displacement, speed or torque demand.

Depending on whether a position, a speed, current or a torque control is needed, appropriate feedback is needed to carry out the commanded task. The mechanical position sensors are usually employed in electric drives' applications to obtain the necessary feedback for position and speed drives. In case of torque drives, however, the torque sensors are rarely used due to cost constraints; therefore the shaft torque is estimated from other measured quantities for control feedback.

Comparing the demand against the feedback, the control issues appropriate commands to the inverter to meet the demand. Since the motive element in an electric drive is an electric motor, the plant of the basic control system is the motor itself. The overall drive operation is fundamentally dependent on how efficiently the control of the electric motor works. Various motor control strategies are in use in industry that continuously evolve to respond to increasingly challenging performance and efficiency requirements.

Regardless of whether a position, speed, current or torque reference signal is to be tracked by the control, the electric motor always works as a generator of mechanical torque. For this reason, the control block of Figure 1.7 must ensure that necessary torque is produced to carry out the desired control action. The electromagnetic torque of any electrical machine is a vector product of magnetic flux and current as given by (1.1) where k is a constant depending on machine data and λ and i are flux and current vectors, respectively.

$$T_e = k(\bar{\lambda} \times \bar{\imath}) \tag{1.1}$$

The motor control has to make sure that the angle between current and flux vectors is maintained such that the torque obtained is at its maximum. Maintaining an optimum angle necessitates that one of these vectors is taken as a reference and the other's direction is varied to obtain the desired angle. From this basic requirement

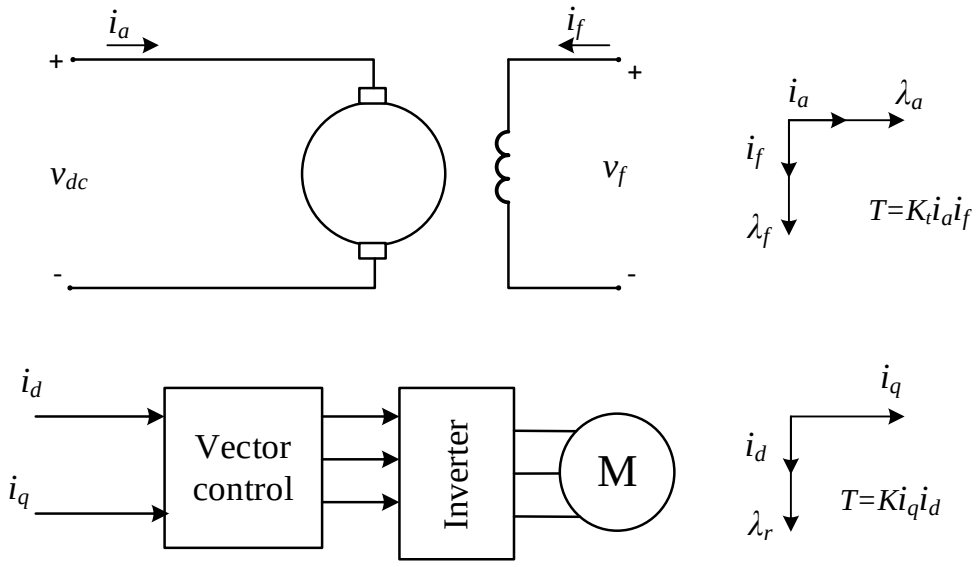

Figure 1.14 Analogy between (separately excited) dc machine and vector controlled ac machine [192].

for maximizing electromagnetic torque comes the concept of vector control. The vector control has now become the most widely used control strategy. It originated as the field oriented control (FOC) of ac machines. It was first discovered by Blaschke [19] for induction machines.

Vector control finds its basis in the theory of dc machines. The dc machines had been widely used in industry in the past for their ability to give high performance torque control with fast response, reduced harmonics, low audible noise and minimal torque ripple. The secret of this performance was the ability to control machine flux and torque independently of each other. The reason for this is that in dc machines, the field circuit is always independent of the armature (torque producing) circuit, especially when separately excited dc machines are considered Figure 1.8. However, in the ac machines, the flux and torque producing current components are hard to separate when the machine is supplied directly from the mains. The development of solid state power converters did away with this limitation and permitted independent control of the two current components. Closed-loop current control allows application of a certain current space phasor

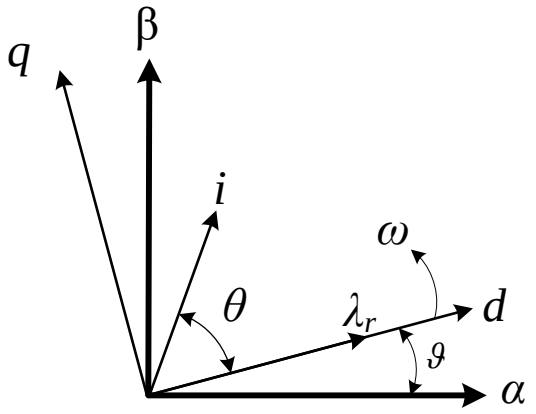

Figure 1.16 Rotor field oriented *d*-axis.

in a given direction with respect to machine flux. Figure 1.8 defines the analogy between dc machine and vector controlled ac machine torque production phenomenon.

The vector control requires the application of a current vector in a direction fixed in space with respect to the flux vector. This is achieved only when the direction of the flux vector is known. In this situation, the *'dq'* rotating reference frame comes in handy in that once the two vectors (current and flux) are referenced to the *dq*-frame, their exact position with respect to each other is always ensured provided the dq-frame is accurately identified. As shown in Figure 1.9, the flux and current vectors, after being referenced to *dq*-frame are at a certain angle (θ) and this angle remains fixed in steady state conditions when the torque demand is constant. The determination of this angle is possible when the flux vector's angle with respect to the stationary axis (α) is known. The power converter discussed earlier in this chapter allows application of voltage vectors in space at any angle by commanding appropriately its power switches, what is more important is that the angle of these vectors can be changed almost instantaneously thanks to the fast switching capability of power switches. This is helpful in coping with fast torque transients. For a high dynamic response, the current vector is controlled instead of the flux vector since the current control loop can be designed with high bandwidth whereas the flux loop usually involves inherent delays, such as the rotor time constant in case of an ac induction machine.

The rotor field oriented control (RFOC), direct torque control (DTC) and unified direct flux vector control (UDFVC) are the main category of the vector control which are reviewed briefly as follows.

1.2.2.1. Rotor field oriented control

When the d-axis of the rotating dq reference frame of Figure 1.9 is tied to the rotor flux vector of the machine, the new vector diagram of Figure 1.10 can be drawn. The control of the machine under this new vector diagram becomes the rotor field oriented control. This convention simplifies the control and allows decoupled control of flux and torque by appropriately controlling the respective current components. Depending on the type of ac machine used, the rotor field can either be that produced by the permanent magnets (in PM machines) or through the induced currents in the rotor circuit due to transformer action of stator alternating currents (in ac induction machine).

The block diagram of Figure 1.11 shows the rotor field is oriented control of a generic speed controlled ac machine. The proportional-integral (PI) speed controller outputs torque command based on the speed error

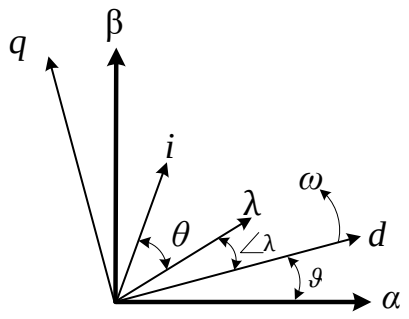

Figure 1.18 Current and flux vectors in *dq*-frame.

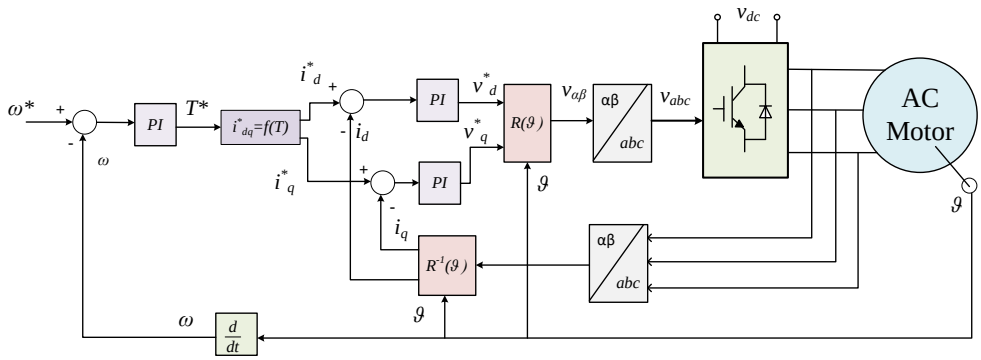

Figure 1.20 Rotor field oriented vector control block diagram.

between reference and feedback inputs. The demanded torque signal is translated to *d*- and *q*-axis current demands which are then fed to two separate PI current controllers as shown. The function correlating *dq* currents with torque depend on the parameters of the particular machine in use.

The PI current controllers give appropriate d- and q-axis voltages to ensure that the desired current vector is maintained in space with respect to the rotor flux vector to generate the demanded torque. The position of rotor flux vector is obtained from the rotor position feedback obtained through a shaft mounted position sensor or by using a position estimation algorithm (sensorless applications). This position information is highly important for a completely decoupled flux and torque control, especially for ac induction machines. In case the rotor flux vector position contains errors, the relation between demanded torque and realized torque is no longer linear. More details about the RFOC method are given in [18], [20]–[23].

1.2.2.2. Direct torque control

Commanding the inverter switches directly based on the required torque demand is what is known as direct torque control. It is also called direct flux and torque control, however, since only the mechanical torque is what matters the most in electromechanical conversion, the name is usually shortened to direct torque control only.

Direct torque control (DTC) is one method used in variable-frequency drives to control the torque (and thus finally the speed) of three-phase AC electric motors. This involves calculating an estimate of the motor's magnetic flux and torque based on the measured voltage and current of the motor. Stator flux linkage is estimated by integrating the stator voltages. Torque is estimated as a cross product of estimated stator flux linkage vector and measured motor current vector. The estimated flux magnitude and torque are then compared with their reference values. If either the estimated flux or torque deviates too far from the reference tolerance, the transistors of the variable frequency drive are turned off and on in such a way that the flux and torque errors will return in their tolerant bands as fast as possible. Thus direct torque control is one form of the hysteresis or bang-bang control. Figure 1.12 shows a general diagram of the DTC method. More details about the operation, design and advantages of the DTC method are given in [18][24]–[28].

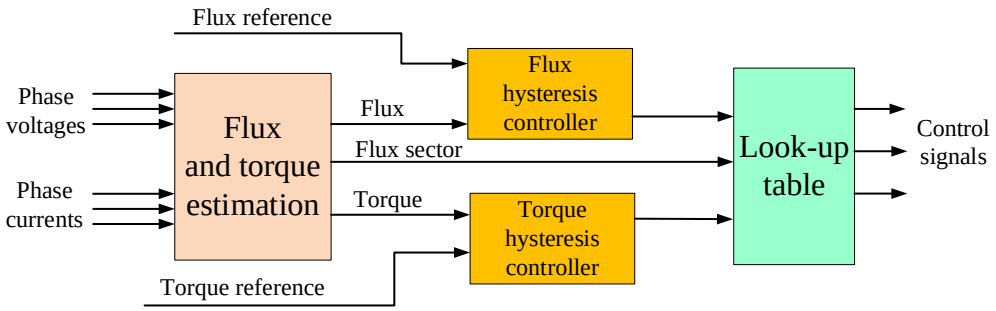

Figure 1.22 Direct torque and flux control scheme.

Effectiveness of the DTC method is highly dependent on the accurate estimation of the motor's magnetic flux and torque. To reach an accurate estimation of the magnetic flux and torque of the controlled machine, in one hand, having a very precise and complex model of the motor is inevitable. On the other hand, several sensors are required to measure the voltages and currents of the controlled motor. In addition, a higher sampling rate (up to 40 kHz as compared with 6–15 kHz for the FOC) is needed which may lead to higher switching loss in the inverter.

1.2.2.3. Unified direct flux vector control

While the field oriented current control strategy gives less torque ripple but also has inferior dynamic response especially for flux regulation, the direct torque control has better dynamic performance but it comes with more torque ripple that causes noise and mechanical wear. The Unified Direct Flux Vector Control (UDFVC) is a hybrid of these two and combines the advantages of both. Although the direct control of inverter switches (as in DTC) does not take place, the higher dynamics in flux control are achieved anyway. The torque control is through current control loop similar to the ones shown in Figure 1.11.

The UDFVC operates in stator flux-oriented frame in which the d-axis of the reference frame is tied to the stator flux magnitude instead of rotor flux (cf. Figure 1.10). In the stator flux frame, the generic voltage equation of an AC machine can be written as in (1.2). When resolved into *dq* components while assuming that all the stator flux remains along the *d*-axis, the *d*-axis equation simplifies to (1.3).

$$v_s = R_s i_s + \frac{d\lambda_s}{dt} \tag{1.2}$$

$$v_d = R_s i_d + \frac{d\lambda_s}{dt} \tag{1.3}$$

It can be observed in (1.3) that the stator flux can be controlled by acting on the *d*-axis voltage directly without passing through any current controllers, thus the name 'direct flux control'. In UDFVC scheme, the stator flux is controlled through a high bandwidth PI controller using (1.3). The PI controller takes in the command in terms of flux magnitude and outputs *d*-axis voltage command to establish commanded stator flux magnitude.

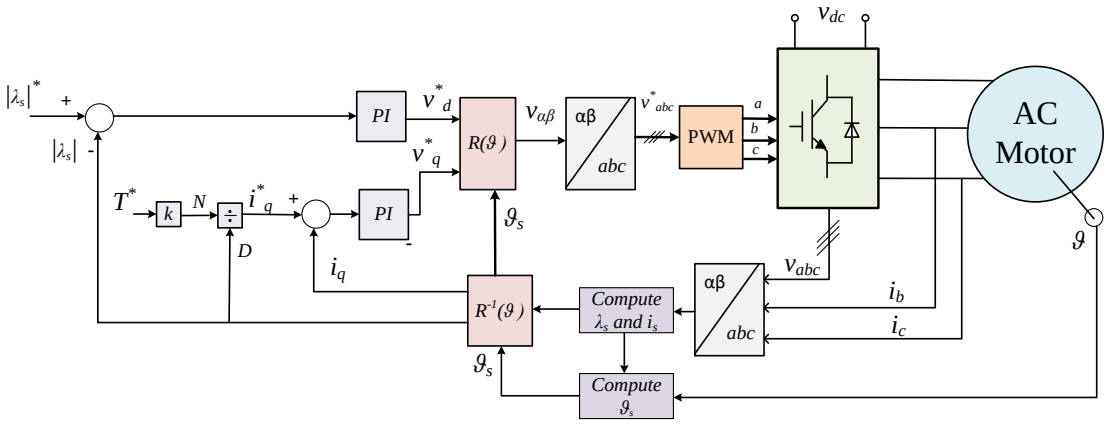

Figure 1.24 Unified direct flux vector control scheme.

With the stator flux established by the flux controller as above, the mechanical torque produced by the machine can be controlled by maintaining an appropriate current vector with respect to the flux vector. The position and magnitude of current vector with respect to flux vector depends on the magnitude of the *q*-axis current component. Thus a PI current controller is all that is needed in the *q*-axis to control the torque produced as can be deduced from (1.1). Figure 1.13 shows a generic UDFVC scheme for all ac machines. It can be seen that the flux and torque are both controlled through PI regulators. More details about function and design of the UDFVC method are given in [29]–[31].

1.2.3. Measured variables in a standard drive

Accurate measurement of essential physical variables of the drive is important for proper operation and control. In a standard drive supplying a three-phase machine through a power converter, at least two of the three phase currents must be measured to properly implement the control techniques discussed in section 1.2.2. The third phase current is usually not measured and it is computed from the other two exploiting the zero-sum definition of isolated neutral systems. In the laboratory environment, however, all three currents are measured for allowing operation for machines with star point connection. Moreover, the dc-link voltage is also required for all three control strategies. Specifically, the dc-link voltage is necessary for generating pulse width modulated commands for the inverter switches in case the control of Figure 1.11 and Figure 1.13 is implemented. For the direct torque control, the dc-link voltage is used to reconstruct the stator voltage vector for flux estimation and sextant identification as well as for torque estimation. Apart from these three variables, the rotor position is almost always measured for better control accuracy. Other quantities such the shaft torque and stator winding temperature are sometimes measured for better supervisory control and for safety reasons.

The measurement of current occurs either through current transformers or through high precision Hall Effect current sensors. The latter are usually preferred due to low cost and weight. The accuracy of commercially available Hall Effect current sensors ranges from 0.002% to 1%. Similarly, the accuracy of the voltage sensing devices used for dc-link voltage measurement goes from 0.2% to 1.2%.

Of the other measurement signals commonly used is the rotor position information. For closed loop speed control and for position servo drives, the rotor position is so important that its direct measurement is preferred over its estimation (sensorless drives). The position sensing devices are usually of two types: (i) optical encoders, (ii) resolvers, and (iii) tachogenerators.

1.3. Context of the Study

At the dawn of the second automotive century it is apparent that the nature of the automotive industry has become very competitive. In this situation, the automotive companies need to stay competitive by proposing new strategies to reach to a good performance with minimum cost. In this regard, the firm Valeo started to propose hybrid solutions in 2004 with Stop-Start systems and extended their hybrid solution product range to mild-hybrid in 2010. In this case, Valeo has developed a mild-hybrid system to be supplied by a 12V-battery, called the i-StARS. This system is composed of an AC motor, a doubly fed Wound Rotor Synchronous Machine (WRSM), supplied by two 3-leg inverters and connected to the 12V battery when mounted on a vehicle. A full and detailed description of this system, constituting the electric powertrain, is made in chapter 3.

As stated in section 1.2.3, several sensors are used in a standard drive to provide an effective control for the system. On the other hand, increase of the number of sensors cause to increase of the manufacturing and maintenance cost also. With this thought in mind, Valeo has also made efforts to reduce the manufacturing cost by reducing the number of sensors used in powertrain. In this regard, Valeo proposed a study to remove the phase current sensors for the control of the i-StARS machine. Indeed, on a doubly-fed machine, at least 4 current sensors are required to control the electric powertrain. As it will be detailed in chapter three, the system operates under low voltage (12 V) and the currents in the stator are high (up to 150 A) and the current sensors capable of measuring such large currents are rather expensive. Thus, the benefits of removing those sensors on the manufacturing costs are clear. The proposed study was in collaboration with GREEN laboratory which resulted in PhD thesis study of Dr. Adrien CORNE [32]. This mentioned work will be continued in this current

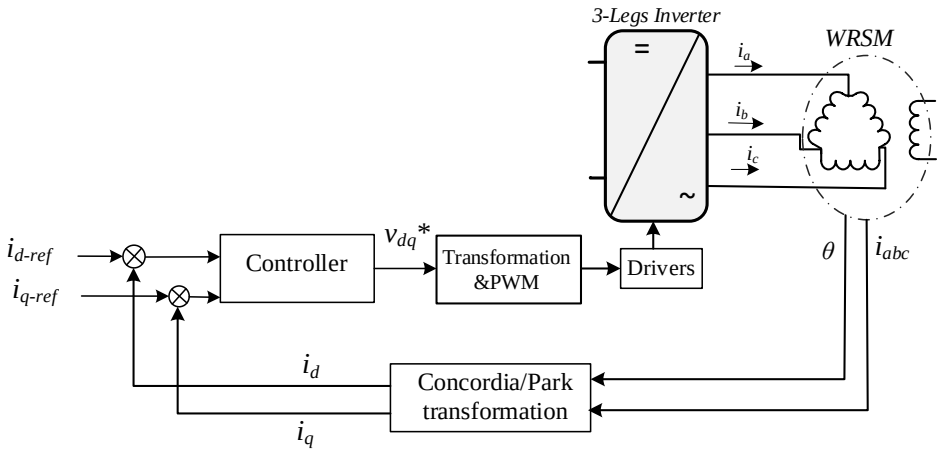

Figure 1.26 Block diagram of the vector control of an AC WRSM [32].

thesis study to reach to a robust controller for AC drive systems with the maximum reduction in number of the sensors. In this case the main goal is to remove the phase current sensors in stator side of the i-StARS machine.

In this section, a brief overview of the studied work in Dr. Corne thesis will be given. Then, the general context of the study developed in this thesis will be detailed by giving the limitations and challenges related to the work which is done in Dr Corne thesis.

1.3.1. Existing observation-based current sensorless control for WRSM

Usually controllers are based on the feedback of the different sensors on the system. For a regular current or torque control of an AC machine, as shown in Figure 1.14, the phase current sensors are needed because the information that they carry constitute the feedback. In this case, since the current feedback is available, the controller block can be filled with any current-loop based controller, such as classic PID, sliding-mode controller [33][34] and Flatness Based Controller (FBC).

Torque and current controllers are widely used for hybrid automotive applications. Indeed the electric powertrain is designed to supply a specific torque to the main powertrain. In addition, controlling the currents in the stator is important for the reliability and the safety of the system: it avoids the peak currents to become to high and potentially to become destructive for the system and accelerate the wear of the components.

In Dr Corne thesis work, the aim was to reach to a current control in order to impose the mechanical torque and avoid current overshoots, but without any measurements of the phase currents. In this case, there is no measurements on phase currents, it is impossible to use abovementioned controllers which require the current feedback. To overcome this difficulty, Dr Corne has proposed to estimate the phase currents with a nonlinear state observer. Indeed, according to this approach, the existing current-loop based control scheme is used with the only difference that the nonlinear observer is added in the loop to achieve the phase currents that are then used in existing control loop. It is remarkable that the observability of the system is the important condition

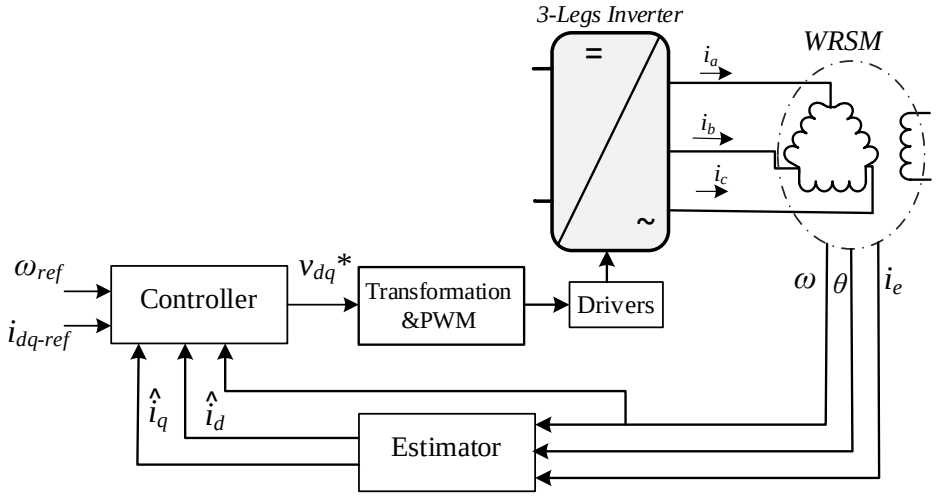

Figure 1.28 Block diagram of the observation-based current sensorless control of an AC WRSM [32].

that should be guaranteed in order to be able to use this strategy. This current sensorless control algorithm, with the use of an observer, is given in Figure 1.15.

The observer block, shown in Figure 1.15, can stand for different kinds of nonlinear observer. In this regard, Dr. Corne has proposed a state observer based on Lyapunove candidate function convergence. In addition, he used another existing state observer as Extended Kalman Filter (EKF) to compare with the proposed observer.

The EKF is a well-known nonlinear tool that is widely used in industrial applications. Looking at the operation principle of the EKF, it includes two main steps, as shown in Figure 1.16:

- First a prediction part, that calculates the next step observed variables based on the state-model of the system.
- The second step includes an update that calculates a prediction on the error made on the system output.

The performance of the EKF is highly dependent on the initial estimation condition, indeed, if the initial estimate of the state is wrong, or if the process is modeled incorrectly, the filter may quickly diverge, owing to its linearization. Another problem with the extended Kalman filter is that the estimated covariance matrix tends to underestimate the true covariance matrix and therefore risks becoming inconsistent in the statistical sense without the addition of stabilising noise. In addition, effectiveness of the EKF is also highly dependent of the correctness of the model and parameters used in the studied system. Furthermore, the EKF intrinsically is a complex observer method due to the excessive use of numerical calculations during the estimation procedure which can increase the complexity and extend the response time of the controller.

Facing those challenges related to the EKF, another Lyapunov-based observer is used in PhD thesis work of Dr Corne. According to the theory and performance of the Lyapunov-based observer, provided in Dr Corne thesis [32], this observer has a faster response and more reliable performance under different operating conditions.

Despite all the differences and advantages of the Lyapunov-based observer compared to the EKF, this method is inherently an observer and uses a state model of the system to estimate the unmeasured variables and its effectiveness is highly dependent on the correctness of this model. However, reaching a very precise

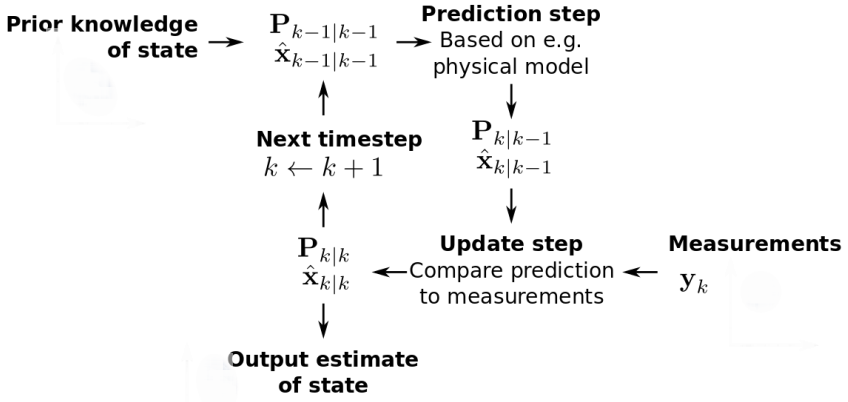

Figure 1.30 Basic concept of Kalman filter.

model is usually impossible or at least time-consuming. In addition, precise information about the system parameters is another required factor for proper operation of this observer. In this regard, since the exact value of the system components are often not available or can be changed due to the temperature or aging phenomena, a full characterization of the studied drive system for different operating point is necessary to guarantee a more correct estimation for unmeasured variables. Another challenge according to this observation-based control method is related to the transient error. Normally, the observation function starts using a prior knowledge of the measured and unmeasured states. Since the precise knowledge is not available, observer starts with an approximate knowledge which may lead to a considerable transient error. Furthermore, the effectiveness of the observer is directly related to the amount of available measured variables. Indeed, more measured data will help to have a more correct estimation of the unmeasured variables. In overall, the faced challenges related to the observation-based sensorless control can be listed as follows.

1) Need for a precise knowledge of the state model and parameters of the studied system.
2) Considerable transient error.
3) Sensitivity against the parameter variation.
4) Using the observer increase the complexity of the controller.
5) Require more measured variables to have a correct estimation of unmeasured ones.

1.3.2. Contribution

Facing those limitations of abovementioned observation-based sensorless control method led us to find a solution to fix them. In this regard, the data-driven control (DDC) theory was considered as one of the best alternatives thanks to its intrinsic features. The DDC is a control scheme that the controller is designed solely using the online/offline (I/O) data measured from the controlled system and without using any information about the mathematical model of the controlled system [35]. According to this feature, the need for a precise knowledge of the state model and parameters of the studied system can be fixed by using DDC methods. Hence, several existing DDC techniques was investigated in order to find the best DDC candidate. The proportional integral differential (PID) algorithm, model-free sliding mode control, virtual reference feedback tuning (VRFT) method, iterative feedback tuning (IFT), model-free adaptive control (MFAC) was included. The model-free adaptive control (MFAC) in particular, as a candidate of the data-driven control (DDC), was selected as an appropriate alternatives due to its intrinsic independence from the model of the studied system and its capability to be developed for any nonlinear system with single-input single-output (SISO), multi-input single-output (MISO) and multi-input multi-output (MIMO) structure. A full and detailed description of the different kinds of the DDC algorithms, particularly MFAC algorithm, is provided in chapter 2.

In this thesis, the focus is on the MFAC as a solution to fix the previously mentioned limitations of the model-based and observation-based control approaches. In this regard, the MFAC is used in two different approaches to control the WRSM system. First, it has been used for current control of a WRSM drive system, according to diagram shown in Figure 1.14. In this configuration the stator phase currents are measured and

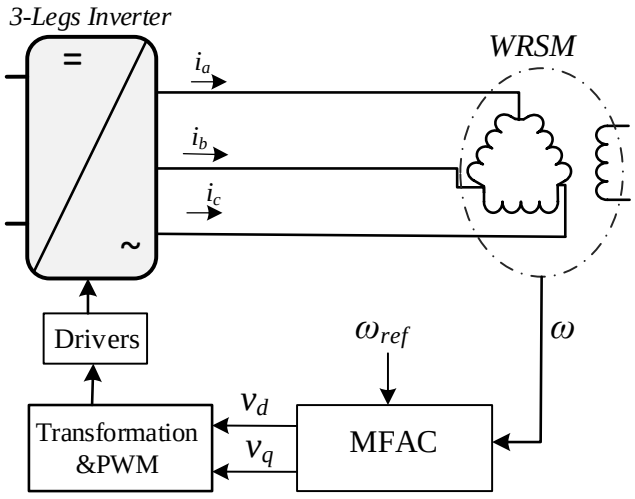

Figure 1.32 Current sensorless control scheme using MFAC.

controlled directly. The aim behind this work is to show that the MFAC is totally independent from system model and parameter variations.

As it mentioned earlier, the main goal of this thesis work is to design a reliable current sensorless controller for AC drive system. For this, the second control approach was allocated to the current sensorless control for AC drive systems, using MFAC. In this control algorithm, as shown in Figure 1.17, neither any measurements nor any observations are considered for stator phase currents and all the control tasks are considered to be done with only measuring the mechanical rotor speed. The proposed strategy, using MFAC to remove the phase current sensors, is appealing and seems to be a solution presenting numerous advantages as follows.

1) Since controller is model-free, there is no sensitivity against system model or parameters.
2) All the control task will be done with only using one rotor speed sensor, while the observation-based method requires more sensors.
3) Since there is no additional observer, the complexity of the control system can be considerably reduced.

A full and detailed description of the control of an AC drive, with and without current sensors, particularly using MFAC algorithm, is provided in chapter 3.

Finally, since the electric drive systems include several power converters, the control of two different converters (a DC/DC boost converter and a three-phase dual-active bridge (DAB) converter) are also studied individually in this thesis work. In this case, the MFAC is developed for mentioned converters to design a robust and reliable controller with minimum number of sensors. This work is detailed in chapter 4.

Conclusion

The first chapter of this thesis is allocated to introduce the context. The control of an electric drive system, specifically focused on sensorless control, is incorporated in this study. The state of the art of the electric, hybrid, and fuel cell vehicles are reviewed comprehensively. The topologies, advantages and challenges for each category are also discussed.

Since the main objective of this study is about control of the electric drive systems, the fundamentals of a standard electric drive system are investigated. In this regard, the electric machines, power converters and control system are considered as the main components. Several types of electric machine technologies are being used for automotive propulsion. Induction, permanent magnet (PM), wound rotor (WR) and switched reluctance machines are the main categories which are investigated in this chapter. The theory, application and different types of the vector control are explained in detail in order to obtain a general vision about the control algorithm which is considered to be used in this study.

The automotive field being extremely competitive, the manufacturing costs always need to be optimized. For this reason, it could be interesting for Valeo to remove the current sensors of the stator of its i-StARS claw-pole machine to avoid their costs. Some current sensorless control strategies exist but in a particular configuration, when the stator phase currents are estimated using a nonlinear state observer. Related to this control method, a brief overview of the observation-based current sensorless control of the WRSM machine, already realized in Dr. Corne's work, has been presented. According to Dr. Corne's work, a precise state model of the system and several measurements are needed for an effective performance of the observation-based current sensorless control method. In this situation, the control system is very sensitive against model and parameters error. Furthermore, using an observer for unmeasured variables increase the complexity of the control system.

To overcome to the drawbacks related to the exist control methods, the model-free adaptive control (MFAC) in particular, and the data-driven control (DDC) in general, is proposed as appropriate alternatives due to their intrinsic independence from the model of the studied system. In this paper, the focus is on the MFAC as a solution to fix the previously mentioned limitations of the model-based and observation-based current sensorless control approaches.

Chapter-2 MODEL FREE ADAPTIVE CONTROL THEORY

Contents

Introduction

With proposing the state-space models by Kalman in 1960 [36], [37], the modern control methods were started to develop for industrial applications. All these modern control theories were proposed by relying the fact that the mathematical model or the precise model of controlled plant is accurately available, for this, these methods are also called as Model Based Control (MBC) methods. In this last decades, many effective MBC methods are developed for industrial applications. The zero-pole method, optimal control and linear quadratic regular (LQR) design are some common control system design for linear systems. For the non-linear systems also the majority of control methods includes Lyapunov-based schemes such as sliding mode, passivity-based control method, backstepping control, feedback linearization, adaptive control theory, estimation theory, optimal control theory and so on. Looking to the typical structure of MBC, presented in Figure 2.1, the mathematical model of studied system plays a key role in this control design method. Relying on this fact, the control performance, safety, and reliability of MBC methods are highly dependent on correctness of the system model used in control design procedure. However, on the other hand the uncertainties, parameter variation and unmodelled dynamics are unavoidable phenomena in industrial applications and are always exist. Since these factors are not considered in mathematical model, they may affect the control system and lead to inappropriate performance[38]. By this way, it can be concluded that the MBC methods derive from system model and finish up in the system model.

By development of technology, many industrial applications have been significantly changed and became to a more complex system. Accordingly, modelling the dynamic and process of these application using the mathematical models becomes very difficult or at least time consuming. In this case, using the MBC methods for these kinds of applications will be impossible. Conversely, the almost of industrial applications generate and save large number of process data which contains all the necessary information related to the operation of system. In this case, it is of high importance to use these generated data, obtained online/offline, directly for designing the controller or other purposes. By this way, the foundation of Data-Driven-Control (DDC) theory is very important in control of industrial applications.

The DDC is a control method that uses only the online/offline (I/O) data obtained from the controlled system, to design the controller without the extra need of information about the mathematical model or

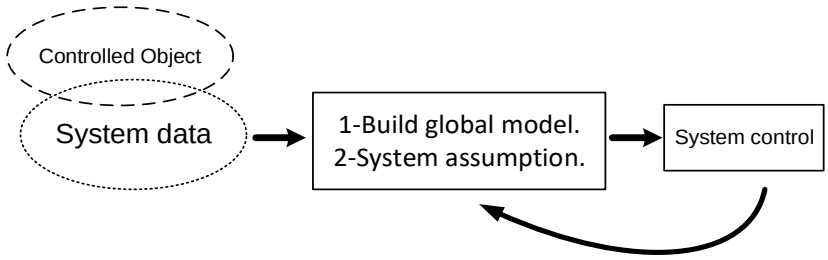

Figure 2.1 Architecture of model base control method.

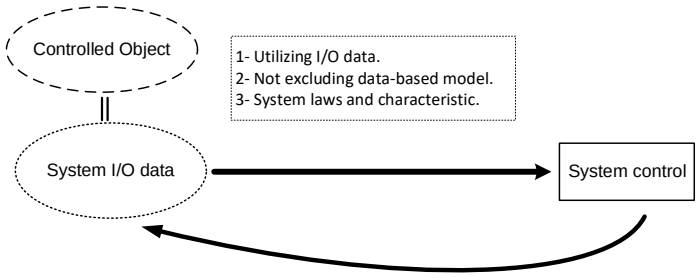

Figure 2.2. Architecture of DDC method.

parameters of the studied system[35]. Contrarily with MBC methods, the DDC methods does not require any knowledge of dynamic model or parameters of the studied plant and deal with only the I/O data obtained from controlled system. Thus, this method can be applicable for all nonlinear systems with complex or unknown structure. The architecture of DDC method, given in Figure 2.2, shows that the section related to system model is eliminated in this case and the control system consists of two major sections which are the controlled plant and controller.

So far, several types of DDC methods have been already developed in the literature. These methods can be classified into different branches considering the type of data usage and the controller structure. According to the type of data usage the main classes of DDC can be categorized as the: offline data-based DDC, online data-based DDC and online/offline data-based DDC. The DDC methods can be also categorized into two different classes according to the type of controller structure as: DDC with a known controller structure and DDC with an unknown controller structure. Regarding these considerations, the different classes of DDC methods will be shortly discussed in following sections.

- ***DDC Methods According to Data Usage***

Offline data based DDC: These methods contain the Iterative Feedback Tuning (IFT), Proportional Integral Derivative (PID) control, Virtual Reference Feedback Tuning (VRFT), correlation-based Tuning (CBT) and so on.

Iterative Feedback Tuning: this method was firstly developed by H. Hjalmarsson in 1994 [39]. In this method the parameters of feedback controller are iteratively optimized utilizing an offline gradient assessment of a control performance reference corresponding to control input. The gradient is estimated during each iteration by utilizing limited series of data collected from the closed-loop system under normal operating condition, and from an experiment whose reference signal is a defined signal. Some examples of development of IFT for nonlinear systems are given in[40]–[43]. Some industrial examples are also given in [44]–[46].

PID Control: this method is considered as the primal DDC control scheme. This method is one of the well known DDC control methods and is already applied successfully on many industrial and practical applications. Since this method is one of the most popular and practical methods, the techniques for this scheme are still under development.

Virtual Reference Feedback Tuning: was firstly proposed in 2000 by O. Gurdabassi and S. M. Savaresi [47]. This method is a direct data-driven scheme for optimizing the controller parameters with a prespecified controller structure for a linear time-invariant (LTI) system. Using a virtual reference signal, the VRFT

transforms the controller design issue into a controller parameter identification issue. In [48]–[54] several examples are given in which that the VRFT is developed for different nonlinear systems are.

Online/Offline Data Based DDC: these series contain Iterative Learning Control (ILC) and Lazy Learning (LL), etc.

Iterative Learning Control: this control method has a simple controller structure which is suitable method for the system that operates a same function over a limited interval. ILC is such a DDC technique that requires little previous information of system and by increasing the iteration number to infinity, it can guarantee the learning error convergence. The ILC is broadly developed for practical applications as presented in [55], [56].

Lazy Learning: the LL method is a supervised machine learning algorithm in which its purpose is finding the connection between the system input and output by using the obtained input/output data. In this method the prior system data is used to create a local linear dynamic model for the nonlinear system, then a local controller is designed at each step time.

Online Data Based DDC: This class of DDC methods contains the Simultaneous Perturbation Stochastic Approximation (SPSA) based DDC, Unfalsified Control (UC) and Model Free Adaptive Control (MFAC), etc.

SPSA-based DDC Method: this method was originally proposed in 1992 by J. C. Spall [57]. In this method, instead of using the mathematical model, the closed-loop measured data is only used for tuning the controller parameters. This method supposes that the nonlinear dynamic of the studied system is not available in which the controller performs as a function estimator with a fixed structure and tunable parameters. This control scheme has been developed in industrial control [58] and traffic control [59].

Unfalsified Control: In this method also all the control process is done by using the I/O data measured instead of using the mathematical model of the controlled system. UC repeatedly falsifies the inappropriate control parameter series in order to reach to the appropriate parameter to satisfy the performance specifications.

Model Free Adaptive Control: The MFAC method was firstly suggested by Hou in 1994 for a class of general unknown non-affine discrete-time nonlinear system [60]–[63]. In this scheme, rather than utilizing the non-linear state-space model of system, the MFAC builds and uses a dynamic linearization (DL) data model of the studied system at every operating point of the closed-loop system to design the controller. The mentioned dynamic linearization data model is created by pseudo partial derivative (PPD) or pseudo gradient (PG) approaches for single input single output (SISO) systems and pseudo-Jacobina matrix (PJM) approach for multi-input multi-output (MIMO) systems. The time varying PPD, PG or PJM should be also estimated at every operating point only by utilizing the collected I/O data from controlled plant. Several dynamic linearization methods are used in MFAC, where the main three categories include the compact-form dynamic linearization (CFDL) data model, partial-form dynamic linearization (PFDL) data model and full-form dynamic linearization (FFDL) data model. Compared with other adaptive control methods, the MFAC technique has some advantages which make it a superior approach for many control applications. First, the MFAC is totally DDC scheme in which it uses only the I/O data measured from controlled system and does not require any extra knowledge about model of studied plant. Second, compare with the neural network-based adaptive nonlinear control methods, the MFAC does not need any exterior testing signal. This feature may lead to a low-cost controller. Third, development of MFAC is easy for any complex system and brings less

computational burden while has considerable robustness. Forth, it is adaptable simply for any single-input single-output (SISO), multi-input-multi-output (MIMO) and multi-input single-output (MISO) systems.

Different structures of MFAC method has been developed successfully in various industrial applications in recent years. A CFDL-based MFAC scheme is developed for active stabilization of a dc microgrid in [64], in [65] a data-driven control has been developed for interlinked microgrids by using MFAC. This controller is also developed for launch vehicle [54], chemical process [66], and for a MIMO power system [67]. Experimental validation of MFAC and virtual reference feedback tuning for a MIMO system is introduced in [68]. The control of a permanent magnet synchronous machine (PMSM) drive system have been done using MFAC in [69].

- ***DDC Methods According to Controller Structure Design***

In this step, the DDC control methods are categorized according to the type of structure of controller. According to this pattern, the DDC techniques can be divided to the DDC methods with known controller structure and DDC methods with unknown controller structure.

DDC methods with known controller structure: This class contains the PID, IFT, VRFT, UC, SPSA-based control, etc.

In this type of DDC approaches, like all DDC methods, the controller design is performed with utilizing the I/O data measured from the controlled plant. But, in this class of DDC, the structure of controller is supposed to be known and the controller parameters are unknown. The controller design is allocated to obtain the proper controller parameters by using some optimization-based algorithms.

DDC methods with unknown controller structure: In this type of DDC approaches, the controller design is carried out only using the I/O data measured from controlled plant based on an unknown controller structure. This kind of control methods have symmetric framework which brings a symmetric stability analysis. The ILC and MFAC are two main candidates for this class of DDC approaches.

According to the abovementioned consideration of DDC approaches, the Model-Free Adaptive Control (MFAC), due to its superior advantages, is selected to perform the control task of this study. To do so, the theory of MFAC is detailed in this chapter for better understanding its application. It is notable that the theory of MFAC is already exist in the literature and we just propose this controller to be applied for different applications of this thesis. Since the MFAC uses a dynamic linearization data model of studied system to design the controller, the control-design-oriented dynamic linearization techniques are firstly discussed in first section for a class of SISO and MIMO discrete-time nonlinear systems, respectively. Then, the MFAC related to each dynamic linearization technique, the stability analysis and controller design for both SISO and MIMO systems are presented in second section. To better understanding the application of MFAC, this controller is developed for some discrete-time nonlinear systems and the provided examples and simulation results are given in each related section.

2.1. Dynamic Linearization Approaches

In this section, the dynamic linearization (DL) techniques which are used in controller design of MFAC are detailed for the class of SISO and MIMO discrete-time nonlinear systems. This DL approaches are mainly classified into three types as: compact form dynamic linearization (CFDL) data model, partial form dynamic linearization (PFDL) data model and full form dynamic linearization (FFDL) data model [60]–[63],[70]–[72].

2.1.1. SISO Discrete-Time Nonlinear System

2.1.1.1. Compact Form Dynamic Linearization

Regard a type of SISO discrete time nonlinear system as:

$$y(k+1) = f\left(y(k), \dots, y(k-n_y), u(k), \dots, u(k-n_u)\right) \tag{2.1}$$

where $y(k) \in R$ and $u(k) \in R$ are the system output and control inputs at the time instant k, respectively. The $f(\dots): R^{n_u+n_y+2} \to R$ is an unknown nonlinear function and the n_u and n_y are two unknown integers.

To expand the CFDL approach for system (2.1), the following two assumptions should be considered for this mentioned SISO system.

Assumption 2.1: The partial derivative of $f(\dots)$ is continuous corresponding to the $(n_y+2)th$ variable, for all k.

Assumption 2.2: The SISO system (2.1) is generalized *Lipschitz* which means that

$$|y(k_1+1) - y(k_2+1)| \le b|u(k_1) - u(k_2)|,$$

for $\forall k_1 \neq k_2$, $k_1, k_2 \ge 0$, $u(k_1) \neq u(k_2)$ and $b > 0$.

In *Assumption 2.2*, the $y(k_i+1)$ stands as a function where $y(k_i+1) = f\left(y(k_i), \dots, y(k_i - n_y), u(k_i), \dots, u(k_i - n_u)\right)$, $i = 1,2$.

These indicated Assumptions are common conditions in non-linear system domain. Assumption 2.1 is a routine condition and majority of non-linear systems satisfy that. Assumption 2.2 means that the changes of system output are totally bounded by changes of all system variables including control input. Furthermore, this condition clarifies that if the changes of system variables and control inputs are finite, the changes of system output cannot be infinite.

Satisfying the abovementioned Assumptions by the system (2.1), if $|\Delta u(k)| \neq 0$, then there exists a time-varying scalar parameter $\varphi_c(k) \in R$, named *pseudo-partial derivative* (PPD), where the nonlinear system (2.1) can be transformed into the coming CFDL data model:

$$\Delta y(k+1) = \varphi_c(k)\Delta u(k) \tag{2.2}$$

where $\Delta y(k+1) = y(k+1) - y(k)$, $\Delta u(k) = u(k) - u(k-1)$ and $\varphi_c(k)$ is bounded for all k.

Proof 1,

According to the equations (2.1) and (2.2) we reach to,

$$\Delta y(k+1) = f\left(y(k), \dots, y(k-n_y), u(k), \dots, u(k-n_u)\right) - f\left(y(k), \dots, y(k-n_u), u(k-1), \dots, u(k-n_u)\right) + f\left(y(k), \dots, y(k-n_y), u(k-1), u(k-1), \dots, u(k-n_u)\right) - f\left(y(k-1), \dots, y(k-n_y-1), u(k-1), \dots, u(k-n_u-1)\right) \quad (2.3)$$

where

$$y(k) = f\left(y(k), \dots, y(k-n_y), u(k-1), u(k-1), \dots, u(k-n_u)\right) - f\left(y(k-1), \dots, y(k-n_y-1), u(k-1), \dots, u(k-n_u-1)\right).$$

Thanks to the Assumption 2.1, and Cauchy's mean value theorem [73], the (2.3) can be edited as:

$$\Delta y(k+1) = \frac{\partial f^*}{\partial u(k)} \Delta u(k) + y(k) \quad (2.4)$$

where $\frac{\partial f^*}{\partial u(k)}$ is the partial derivative of $f(\dots)$ corresponding to the $(n_y + 2)$th variable at a fixed point between

$$\left[y(k), \dots, y(k-n_y), u(k-1), \dots, u(k-n_u)\right]^T$$

and

$$\left[y(k), \dots, y(k-n_y), u(k), u(k-1) \dots, u(k-n_u)\right]^T.$$

Regard the coming equation, with a variable $\eta(k)$, for any fixed time k:

$$y(k) = \eta(k) \Delta u(k) \quad (2.5)$$

As $|\Delta u(k)| \neq 0$, there should exist a specific solution $\eta^*(k)$ for equation (2.5).

Let $\varphi_c(k) = \eta^*(k) + \frac{\partial f^*}{\partial u(k)}$, then equation (2.4) can be rewritten as $\Delta y(k+1) = \varphi_c(k) \Delta u(k)$, which is the principle of the mentioned theorem. The boundness of the $\varphi_c(k)$ is directly covered by the Assumption 2.2.

Remark 2.1

Clearly, the PPD is a time-varying parameter which is only depends on the input and output signals. According to the abovementioned proof, it can be concluded that all the possible complicated behavior specifics, such as nonlinearity, time-varying structure and parameters, of the main system are squeezed into the single time-varying scalar parameter $\varphi_c(k)$. Consequently, the mathematical description of dynamics of PPD $\varphi_c(k)$ may be difficult. On the other hand, estimation of the numerical behavior of the $\varphi_c(k)$ may be easy. Specifically, while the time-varying structure and parameter delay are expressed in the first-principle model, which are difficult to handle in the structure of the model-based control design approach, the numerical variation of the $\varphi_c(k)$ manner may not be sensitive to those time-varying elements.

The PPD is only a mathematical approach. Using some precise analysis based on the abovementioned proof, the existence of the $\varphi_c(k)$ can be theoretically approved, but generally, it is not possible to analytically formulate the $\varphi_c(k)$. It is concluded cooperatively by the mean value of the partial derivative at some point within an interval and a nonlinear remaining term. Relying on the fact that, the mean value in Cauchy's mean value theorem cannot be exactly evaluated in an analytical form even for a known nonlinear system, the $\varphi_c(k)$ cannot evaluated analytically.

Remark 2.2

The presented dynamic linearization data model is only dependent on the I/O data measured from the closed-loop controlled system. During the dynamic linearization algorithm, neither structure information nor any knowledge of parameters of the dynamic model of the studied system is included. Since it is a data-driven approach, the developed dynamic linearization method is suitable to controller design for most of the practical applications, regardless that the system parameters and model structure are time-varying or not.

The presented dynamic linearization data model in (2.2) is a precise, correspondent, I/O data-based model at every sampling time and is only a control-design-oriented linearization model, which cannot be used for other objectives such as monitoring and so on.

Remark 2.3

For a linear system, whose model and states are known, the easiest approach for checking the controllability of the $x(k+1) = Ax(k) + Bu(k)$ is to examine the rank of the matrix $[B\ AB\ \dots\ A^{n-1}\ B]$, so called controllability matrix. While all the states in the past and in the future can be totally defined by the coefficient matrices, the controllability of the system can be guaranteed with the non-singularity of the controllability matrix. In the data-driven method, whose model is unknown, the only exist information is the I/O data measured from controlled system in which the measured data in the future is not exist at current time. Consequently, it is not simple to talk about the controllability of the main nonlinear system or about controllability of its corresponding dynamic linearization data model. To tackle this problem, it is useful to consider the theory of "output controllability" as follows. Supposing that the system output is driven to a possible defined setting point in a limited period with a series of control input, then it can be said that the system is output controllable at a definite I/O data point at present time instant k.

2.1.1.2. Partial Form Dynamic Linearization

As seen in previous section, the CFDL approach transforms the general discrete-time nonlinear system into a linear time-varying data model, which has only one scalar parameter $\varphi_c(k)$. In this case, all the possible complicated behavior of the general nonlinear system is compacted into a single time-varying parameter $\varphi_c(k)$. By this way, the estimation of the behavior of $\varphi_c(k)$ can be difficult.

Furthermore, the CFDL basically works simply with the time-varying dynamic relation between the changes of system output at the next sampling time and the variation of the control input at the current sampling time. But, in a general nonlinear system, the changes of the system output at next sampling time can be linked to the variation of previous control inputs as well as variation of control input at the current sampling time. Relying on this consideration, the partial form dynamic linearization (PFDL) approach is presented to consider the previous variation of control input in changes of system output. PFDL makes a relation between the changes of system output at the next sampling time due to the changes of control input during current and previous times within a fixed-length period. In this approach, since the memory of control input changes are considered, the obtained linear time-varying data model has multiple parameters, instead of one scalar parameter in the CFDL, which may lead to better estimation of all possible complicated behavior of the original system.

Defining the $U_L(k) \in R^L$ as a vector including all the control input signals within period $[k-L+1, k]$,

$$U_L(k) = [u(k), \dots, u(k-L+1)]^T \tag{2.6}$$

with $U_L(k) = 0_L$ for $k \leq 0$. The L is an integer named as the control input linearization length constant (LLC), and 0_L is the zero vector of dimension L.

Similar to the CFDL section, to expand the PFDL approach for system (2.1), the following two assumptions should be considered for this mentioned SISO system.

Assumption 2.3: The partial derivative of $f(\dots)$ is continuous corresponding to the variables from $(n_y + 2)th$ to the $(n_y + L + 1)$th, that is $u(k), \dots, u(k-L+1)$.

Assumption 2.4: The system (1.1) is generalized *Lipschitz* as follows,

$$|y(k_1+1) - y(k_2+1)| \leq b \, \|U_L(k_1) - U_L(k_2)\|,$$

For $U_L(k_1) \neq U_L(k_2)$ and $k_1 \neq k_2$, $k_1, k_2 \geq 0$, where $y(k_i+1) = f\left(y(k_i), \dots, y(k_i - n_y), u(k_i), \dots, u(k_i - n_u)\right)$, $i = 1, 2$, and b is a positive constant.

Satisfying the abovementioned Assumptions by the system (2.1), for any fixed L, if $\|\Delta U_L(k)\| \neq 0$, then there exists a time-varying vector $\varphi_{p,L}(k) \in R$, named *pseudo-gradient* (PG), where the nonlinear system (2.1) can be transformed into the coming PFDL data model:

$$\Delta y(k+1) = \varphi_{p,L}^T(k) \Delta U_L(k) \tag{2.7}$$

where $\varphi_{p,L}(k) = [\varphi_1(k), \dots, \varphi_L(k)]^T$ is a bounded vector for any k.

Proof

According to the equations (2.1) and (2.7) we reach to,

$$\begin{aligned}\Delta y(k+1) = {} & f\left(y(k), \dots, y(k-n_y), u(k), u(k-1), \dots, u(k-n_u)\right) \\ & - f\left(y(k), \dots, y(k-n_u), u(k-1), u(k-1), \dots, u(k-n_u)\right) \\ & + f\left(y(k), \dots, y(k-n_y), u(k-1), u(k-1), \dots, u(k-n_u)\right) \\ & - f\left(y(k-1), \dots, y(k-n_y-1), u(k-1), u(k-2), \dots, u(k-n_u-1)\right)\end{aligned} \tag{2.8}$$

Thanks to the Assumption 2.3, and Cauchy's mean value theorem, the (2.8) can be edited as:

$$\begin{aligned}\Delta y(k+1) = {} & \frac{\partial f^*}{\partial u(k)} \Delta u(k) + f\left(y(k), \dots, y(k-n_y), u(k-1), u(k-1), \dots, u(k-n_u)\right) \\ & - f\left(y(k-1), \dots, y(k-n_y-1), u(k-1), u(k-2), \dots, u(k-n_u-1)\right)\end{aligned} \tag{2.9}$$

where $\frac{\partial f^*}{\partial u(k)}$ is the partial derivative of $f(\dots)$ corresponding to the $(n_y + 2)$th variable at a fixed point between

$$\left[y(k), \dots, y(k-n_y), u(k-1), u(k-1), \dots, u(k-n_u)\right]^T$$

and

$$\left[y(k), \dots, y(k-n_y), u(k), u(k-1) \dots, u(k-n_u)\right]^T.$$

From (2.1) we have,

$$y(k) = f\left(y(k-1), \dots, y(k-n_y-1), u(k-1), \dots, u(k-n_u-1)\right) \tag{2.10}$$

Substituting (2.10) into (2.9),

$$\begin{aligned}\Psi_1\left(y(k-1),\dots,y\left(k-n_y-1\right),u(k-1),u(k-2),\dots,u(k-n_u-1)\right)\\ \triangleq\ f\Big(f\left(y(k-1),\dots,y\left(k-n_y-1\right),u(k-1),\dots,u(k-n_u-1)\right),\\ y(k-1),\dots,y\left(k-n_y\right),u(k-1),u(k-1),\dots,u(k-n_u)\Big)\\ -f\left(y(k-1),\dots,y\left(k-n_y-1\right),u(k-1),\dots,u(k-n_u-1)\right)\end{aligned} \tag{2.11}$$

Equation (2.9) can be edited as,

$$\begin{aligned}\Delta y(k+1)=\frac{\partial f^*}{\partial u(k)}\Delta u(k)+\Psi_1\left(y(k-1),\dots,y\left(k-n_y-1\right),u(k-1),u(k-2),\dots,u(k-n_u-1)\right)\\ -\Psi_1\left(y(k-1),\dots,y\left(k-n_y-1\right),u(k-2),u(k-2),\dots,u(k-n_u-1)\right)\\ +\Psi_1\left(y(k-1),\dots,y\left(k-n_y-1\right),u(k-2),u(k-2),\dots,u(k-n_u-1)\right)\\ =\frac{\partial f^*}{\partial u(k)}\Delta u(k)+\frac{\partial \Psi_1^*}{\partial u(k-1)}\Delta u(k-1)\\ +\Psi_2\left(y(k-2),\dots,y\left(k-n_y-2\right),u(k-2),u(k-3),\dots,u(k-n_u-2)\right)\end{aligned} \tag{2.12}$$

where $\frac{\partial \Psi_1^*}{\partial u(k-1)}$ is the partial derivative of $\Psi_1(\dots)$ corresponding to the (n_y+2)th variable at a fixed point between

$$\left[y(k-1),\dots,y\left(k-n_y-1\right),u(k-2),u(k-2),\dots,u(k-n_u-1)\right]^T$$

and

$$\left[y(k-1),\dots,y\left(k-n_y-1\right),u(k-1),u(k-2)\dots,u(k-n_u-1)\right]^T$$

and

$$\Psi_2\left(y(k-2),\dots,y\left(k-n_y-2\right),u(k-2),u(k-3),\dots,u(k-n_u-2)\right)\ \triangleq\ \Psi_1\Big(f\left(y(k-2),\dots,y\left(k-n_y-2\right),u(k-2),u(k-3),\dots,u(k-n_u-2)\right),y(k-2),\dots,y\left(k-n_y-1\right),u(k-2),u(k-2),\dots,u(k-n_u-1)\Big)$$

Similarly, from (2.12) with a fixed L, we have

$$\begin{aligned}\Delta y(k+1)=\frac{\partial f^*}{\partial u(k)}\Delta u(k)+\frac{\partial \Psi_1^*}{\partial u(k-1)}\Delta u(k-1)+\cdots+\frac{\partial \Psi_{L-1}^*}{\partial u(k-L+1)}\Delta u(k-L+1)\\ +\Psi_L\left(y(k-L),\dots,y\left(k-n_y-L\right),u(k-L),\dots,u(k-n_u-L)\right)\end{aligned} \tag{2.13}$$

where

$$\Psi_i\left(y(k-i),\dots,y\left(k-n_y-i\right),u(k-i),u(k-i-1),\dots,u(k-n_u-i)\right)$$
$$\triangleq \Psi_{i-1}\left(f\left(y(k-i),\dots,y\left(k-n_y-i\right),u(k-i),u(k-i-1),\dots,u(k-n_u-i)\right),y(k\right.$$
$$\left.-i),\dots,y\left(k-n_y-i+1\right),u(k-i),u(k-i),\dots,u(k-n_u-i+1)\right)$$

for $1=2,\dots,L$.

For each fixed k, regard the coming equation with a variable $\eta(k)$

$$\Psi_L\left(y(k-L),\dots,y\left(k-n_y-L\right),u(k-L),\dots,u(k-n_u-L)\right)=\eta^T(k)[\Delta u(k)\ \dots\ \Delta u(k-L+1)]^T$$
$$=\eta^T(k)\Delta U_L(k) \tag{2.14}$$

As $\|\Delta U_L(k)\|\neq 0$, there at least exist one solution $\eta^*(k)$ for equation (1.14). Let

$$\varphi_{p,L}(k)=\eta^*(k)+\left[\frac{\partial f^*}{\partial u(k)},\frac{\partial \Psi_1^*}{\partial u(k-1)},\dots,\frac{\partial \Psi_{L-1}^*}{\partial u(k-L+1)}\right]^T$$

Equation (2.13) can be edited as the PFDL data model (2.9).

Finally, considering the PFDL data model (2.9) and Assumption 1.4, we reach to the

$$|\Delta y(k+1)|=\left|\varphi_{p,L}^T(k)\Delta U_L(k)\right|\leq b\|\Delta U_L(k)\|$$

For any k and $\|\Delta U_L(k)\|\neq 0$. According to abovementioned equation, if any component of $\varphi_{p,L}(k)$ is unbounded, it would break the inequality, therefore the boundness of $\varphi_{p,L}(k)$ is guaranteed for any k.

2.1.1.3. Full Form Dynamic Linearization

As seen in previous section, the PFDL approach purely works with the dynamic linearization data model which is related to the system output variation at the next time instant and variation of the control inputs within a fixed-length period at the current time. On the other hand, the variation of the system output at the next time instant can be also relevant to the variation of system outputs at previous and current time. Regarding this consideration, the full form dynamic linearization (FFDL) method is proposed to consider all the effects on the variation of the system output at next time instant generated by both of the control inputs and system outputs variation within an input-related and output-related fixed length period at the current time. Compared to the CFDL and PFDL methods, which has only a scalar parameter (PPD) and a vector (PG) during the dynamic linearization, using the FFDL method, the possible complicated behavior of the main system can be better evaluated due to the presenting more parameters in dynamic linearization transformation.

Defining the $H_{L_y,L_u}(k)\in R^{L_y+L_u}$ as a vector including all the control input signals inside an input related period $[k-L_u+1,k]$, and all system output signals inside a output-related period $\left[k-L_y+1,k\right]$,

$$H_{L_y,L_u}(k)=\left[y(k),\dots,y\left(k-L_y+1\right),u(k),\dots,u(k-L_u+1)\right]^T \tag{2.15}$$

with $H_{L_y,L_u}(k)=0_{L_y,L_u}$ for $k\leq 0$. The L_u and L_y are integers named as the control input linearization length constant (LLC) and controlled output linearization length constant (LLC), in which $0\leq L_u\leq n_u, 0\leq L_y\leq n_y$, and $0_{L_y,L_u}$ is the zero vector.

Similar to the CFDL and PFDL approaches, to expand the FFDL approach for system (2.1), the following two assumptions should be considered for this mentioned SISO system.

Assumption 2.5: The partial derivative of $f(\dots)$ is continuous corresponding to all variables.

Assumption 2.6: The system (1.1) is generalized *Lipschitz* as follows,

$$|y(k_1+1)-y(k_2+1)| \le b \left\| H_{L_y,L_u}(k_1)-H_{L_y,L_u}(k_2)\right\|,$$

for $H_{L_y,L_u}(k_1) \ne H_{L_y,L_u}(k_2)$ and $k_1 \ne k_2$, $k_1,k_2 \ge 0$, where $y(k_i+1)=f\left(y(k_i),\dots,y\left(k_i-n_y\right),u(k_i),\dots,u(k_i-n_u)\right)$, $i=1,2$, and b is a positive constant.

Satisfying the abovementioned Assumptions by the system (2.1), for any fixed L_u and L_y, if $\left\|\Delta H_{L_y,L_u}(k)\right\| \ne 0$, then there exists a time-varying vector $\varphi_{p,L_u,L_y}(k) \in R^{L_u+L_y}$, named *pseudo-gradient* (PG), where the nonlinear system (2.1) can be transformed into the coming PFDL data model:

$$\Delta y(k+1)=\varphi^T_{p,L_u,L_y}(k)\Delta H_{L_y,L_u}(k) \tag{2.16}$$

where $\varphi_{p,L_u,L_y}(k)=\left[\varphi_1(k),\dots,\varphi_{L_y}(k),\varphi_{L_y+1}(k),\dots,\varphi_{L_y+L_u}(k)\right]^T$ is a bounded vector for any k, and $\Delta H_{L_y,L_u}(k)=H_{L_y,L_u}(k)-H_{L_y,L_u}(k-1)$.

Proof

According to the equations (2.1),

$$\begin{aligned}\Delta y(k+1) &= f\left(y(k),\dots,y\left(k-n_y\right),u(k),\dots,u(k-n_u)\right)-f\left(y(k-1),\dots,y\left(k-n_y-1\right),u(k-1),\dots,u(k-n_u-1)\right)\\ &= f\left(y(k),\dots,y\left(k-L_y+1\right),y\left(k-L_y\right),\dots,y\left(k-n_y\right),u(k),u(k-L_u+1),u(k-L_u),\dots,u(k-n_u)\right)\\ &- f\left(y(k-1),\dots,y\left(k-L_y\right),y\left(k-L_y\right)\dots,y\left(k-n_y\right),u(k-1),\dots u(k-L_u),u(k-L_u),\dots,u(k-n_u)\right)\\ &+ f\left(y(k-1),\dots,y\left(k-L_y\right),y\left(k-L_y\right)\dots,y\left(k-n_y\right),u(k-1),\dots u(k-L_u),u(k-L_u),\dots,u(k-n_u)\right)\\ &- f\left(y(k-1),\dots,y\left(k-L_y\right),y\left(k-L_y-1\right),\dots,y\left(k-n_y-1\right),u(k-1),\dots u(k-L_u),u(k-L_u\right.\\ &\left.-1),\dots,u(k-n_u-1)\right)\end{aligned} \tag{2.17}$$

Denote,

$\Psi(k) \triangleq f\left(y(k-1),y(k-2),\dots,y\left(k-L_y\right),y\left(k-L_y\right),\dots,y\left(k-n_y\right),u(k-1),u(k-2),\dots,u(k-L_u),u(k-L_u),\dots,u(k-n_u)\right)-f\left(y(k-1),y(k-2),\dots,y\left(k-L_y\right),y\left(k-L_y-1\right),\dots,y\left(k-n_y-1\right),u(k-1),u(k-2),\dots,u(k-L_u),u(k-L_u-1),\dots,u(k-n_u-1)\right)$.

Thanks to the Assumption 2.5, and Cauchy's mean value theorem, the (2.17) can be edited as:

$$\Delta y(k+1)=\frac{\partial f^*}{\partial y(k)}\Delta y(k)+\dots+\frac{\partial f^*}{\partial y(k-L_y)}\Delta y\left(k-L_y+1\right)+\frac{\partial f^*}{\partial u(k)}\Delta u(k)+\dots+\frac{\partial f^*}{\partial u(k-L_u)}\Delta u(k-L_u+1)+\Psi(k) \tag{2.18}$$

where $\frac{\partial f^*}{\partial y(k-i)}$, $0 \le i \le L_y-1$ and $\frac{\partial f^*}{\partial u(k-j)}$, $0 \le j \le L_u-1$ are the partial derivative of $f(\dots)$ corresponding to the $\left(n_y+2+j\right)$th variable at a fixed point between

$[y(k), y(k-1), \dots, y(k-L_y+1), y(k-L_y) \dots, y(k-n_y), u(k), u(k-1), \dots, u(k-L_u+1), u(k-L_u), \dots, u(k-n_u)]^T$

and

$[y(k-1), y(k-2), \dots, y(k-L_y), y(k-L_y) \dots, y(k-n_y), u(k-1), u(k-2), \dots, u(k-L_u), u(k-L_u), \dots, u(k-n_u)]^T$.

For each fixed k, regard the coming equation with a variable $\eta(k)$

$$\Psi(k) = \eta^T(k)\left[\Delta y(k) \dots \Delta y(k-L_y+1), \Delta u(k) \dots \Delta u(k-L_u+1)\right]^T = \eta^T(k)\Delta H_{L_y,L_u}(k) \tag{2.19}$$

As $\left\|\Delta H_{L_y,L_u}(k)\right\| \neq 0$, there at least exist one solution $\eta^*(k)$ for equation (2.19). Let

$$\varphi_{p,L_y,L_u}(k) = \eta^*(k) + \left[\frac{\partial f^*}{\partial y(k)}, \dots, \frac{\partial f^*}{\partial y(k-L_y)}, \frac{\partial f^*}{\partial u(k)}, \dots, \frac{\partial f^*}{\partial u(k-L_u)}\right]^T.$$

Equation (2.19) can be edited as the FFDL data model (1.16).

Finally, considering the PFDL data model (2.9) and Assumption 2.4, we reach to the

$$|\Delta y(k+1)| = \left|\varphi^T_{p,L_y,L_u}(k)\Delta H_{L_y,L_u}(k)\right| \leq b \left\|\Delta H_{L_y,L_u}(k)\right\|$$

For any k and $\left\|\Delta H_{L_y,L_u}(k)\right\| \neq 0$. According to abovementioned equation, if any component of $\varphi_{p,L_y,L_u}(k)$ is unbounded, it would break the inequality, therefore the boundness of $\varphi_{p,L_y,L_u}(k)$ is guaranteed for any k.

Remark 2.4

The full-form dynamic linearization (FFDL) technique includes the PFDL and CFDL techniques. Technically, choosing the input-related and output-related pseudo orders as $L_y = 0, L_u = L > 1$, and $L_y = 0, L_u = 1$, the FFDL method will become the PFDL and CFDL respectively. Thus, the FFDL approach may be considered as the most general DL methods. Particularly, the FFDL with large LLC orders brings a more precise data model but may bring some issues related to the complexity of the dynamics of the PG. Normally, for better assessment of the behavior of the main system, it would be better to chose higher LLC order for complicated systems and lower LLC orders for simple systems.

2.1.2. MIMO Discrete-Time Nonlinear Systems

In this part, the previously mentioned dynamic linearization methods are expanded for a MIMO discrete-time nonlinear system as:

$$y(k+1) = f\left(y(k), \dots, y(k-n_y), u(k), \dots, u(k-n_u)\right) \tag{2.20}$$

where $y(k) = [y_1(k) \;\; y_2(k) \;\dots\; y_m(k)]^T \epsilon R^m$ and $u(k) = [u_1(k) \;\; u_2(k) \;\dots\; u_m(k)]^T \epsilon R^m$ are the system output and control input vectors respectively. m is the number of control inputs and system outputs. The n_y and n_u are two unknown positive integers. The $f(\dots) = [f_1(\dots), \dots, f_m(\dots)]^T \epsilon \prod_{n_y+n_u+2} R^m \to R^m$ is a vector-valued unknown nonlinear function.

2.1.2.1. Compact Form Dynamic Linearization

Similar to the CFDL described for SISO system, in order to develop the CFDL data model for MIMO discrete-time nonlinear system (2.20), the following assumptions are considered for this system.

Assumption 2.7: The partial derivatives of $f_i(\dots)$, $i = 1, \dots, m$, is continuous corresponding to all $u(k)$.

Assumption 2.8: The MIMO system (2.20) satisfies the following generalized *Lipschitz* condition:

$$\|y(k_1 + 1) - y(k_2 + 1)\| \leq b \, \|u(k_1) - u(k_2)\|,$$

for $\forall k_1 \neq k_2$, $k_1 \geq 0$ & $k_2 \geq 0$, $u(k_1) \neq u(k_2)$ and $b > 0$.

where $y(k_i + 1) = f\left(y(k_i), \dots, y\left(k_i - n_y\right), u(k_i), \dots, u(k_i - n_u)\right)$, $i = 1,2$.

Satisfying the mentioned Assumptions by system (2.20), if $\|\Delta \mathrm{u}(k)\| \neq 0$, then there exist a time-varying matrix $\varphi_c(k) \in R^{m \times m}$, called *pseudo Jacobian matrix* (PJM), in which that system (2.20) can be transformed into the CFDL data model as follows.

$$\Delta y(k + 1) = \varphi_c(k) \Delta \, u(k) \tag{2.21}$$

where $\varphi_c(k)$ is bounded for any time k.

The proof is in the same manner with the *proof 1* which is presented in section CFDL for SISO systems.

Remark 2.5

In the case of multi-input single-output (MISO) system, that is, $y(k) \epsilon R$ and $u(k) = [u_1(k) \;\; u_2(k) \;\; \dots \;\; u_m(k)]^T \in R^m$, the system (2.20) becomes as

$$y(k + 1) = f\left(y(k), \dots, y\left(k - n_y\right), u(k), \dots, u(k - n_u)\right) \tag{2.22}$$

Where the $f(\dots) \in \prod_{n_y+1} R \to \prod_{n_u+1} R^m$ is a vector-valued unknown nonlinear function. By this way, the Assumptions 2.7 and 2.8 should be rewritten as:

Assumption 2.7′: The partial derivatives of $f(\dots)$, is continuous corresponding to each entry of the $(n_y + 2)$th variable $u(k)$.

Assumption 2.8′: The MISO system (2.22) satisfies the following generalized *Lipschitz* condition:

$$|y(k_1 + 1) - y(k_2 + 1)| \leq b \, \|u(k_1) - u(k_2)\|,$$

for $\forall k_1 \neq k_2$, $k_1 \geq 0$ & $k_2 \geq 0$, $u(k_1) \neq u(k_2)$ and $b > 0$. Where $y(k_i + 1) = f\left(y(k_i), \dots, y\left(k_i - n_y\right), u(k_i), \dots, u(k_i - n_u)\right)$, $i = 1,2$.

Satisfying the Assumptions *2*.7′ and *1*.8′ by system (2.22), if $\|\Delta \mathrm{u}(k)\| \neq 0$, then there exist a time-varying matrix $\varphi_c(k) \in R^m$, called *pseudo gradient* (PG), in which that system (2.22) can be transformed into the CFDL data model as follows.

$$\Delta y(k + 1) = \varphi_c^T(k) \Delta \, u(k) \tag{2.23}$$

where $\varphi_c(k)$ is bounded for any time k.

2.1.2.2. Partial Form dynamic Linearization

Defining the $U_L(k) \in R^{m \times L}$ as a vector including all control input vectors within a period $[k - L + 1, k]$ as:

$$U_L(k) = [u^T(k), \dots, u^T(k - L + 1)]^T \tag{2.24}$$

where $L > 0$ is the control input LLC, and $U_L(k) = 0_{mL}$ for $k \leq 0$.

In order to expand the PFDL approach for system (1.20), similar to previous sections, the following two assumptions are considered for this system.

Assumption 2.9: The partial derivatives of $f_i(\dots)$, $i = 1, \dots, m$, is continuous corresponding to all entries of the variable from the $(n_y + 2)$th to the $(n_y + L + 1)$th, namely, $u(k), \dots, u(k - L + 1)$.

Assumption 2.10: The MIMO system (1.20) satisfies the following generalized *Lipschitz* condition:

$$\|y(k_1 + 1) - y(k_2 + 1)\| \leq b \, \|U_L(k_1) - U_L(k_2)\|,$$

for $\forall k_1 \neq k_2$, $k_1 \geq 0 \,\&\, k_2 \geq 0$, $U_L(k_1) \neq U_L(k_2)$ and $b > 0$. Where $y(k_i + 1) = f\left(y(k_i), \dots, y\big(k_i - n_y\big), u(k_i), \dots, u(k_i - n_u)\right)$, $i = 1{,}2$.

Satisfying the mentioned Assumptions by system (2.20), for any fixed L, if $\|\Delta U_L(k)\| \neq 0$, then there exist a time-varying matrix $\varphi_{p,L}(k) \in R^{m \times mL}$, called *pseudo partial Jacobian matrix* (PPJM), in which that system (2.20) can be transformed into the PFDL data model as follows.

$$\Delta y(k + 1) = \varphi_{p,L}(k) \Delta U_L(k) \tag{2.25}$$

where $\varphi_{p,L}(k) = [\varphi_1(k), \dots, \varphi_L(k)]$ is bounded for any time k, and the $\varphi_i(k) \in R^{m \times m}$, $i = 1, \dots, L$.

Since the dynamic linearization presented here is an extension of the method in section 2.1.1.2 to the MIMO system, all the given remarks are valid for this section too.

Remark 2.6

In the case of multi-input single-output (MISO) system, the PFDL method can be extended for this system by considering the following assumptions.

Assumption 2.9′: The partial derivatives of $f(\dots)$, is continuous corresponding to each entry of the variable from $(n_y + 2)$th to the $(n_y + L + 1)$th, namely, $u(k), \dots, u(k - L + 1)$.

Assumption 2.10′: The MISO system (2.22) satisfies the following generalized *Lipschitz* condition:

$$|y(k_1 + 1) - y(k_2 + 1)| \leq b \, \|U_L(k_1) - U_L(k_2)\|,$$

for $\forall k_1 \neq k_2$, $k_1 \geq 0 \,\&\, k_2 \geq 0$, $U_L(k_1) \neq U_L(k_2)$ and $b > 0$. Where $y(k_i + 1) = f\left(y(k_i), \dots, y\big(k_i - n_y\big), u(k_i), \dots, u(k_i - n_u)\right)$, $i = 1{,}2$.

Satisfying the Assumptions $2.9'$ and $2.10'$ by system (2.22), for any fixed L, if $\|\Delta U_L(k)\| \neq 0$, then there exist a time-varying matrix $\varphi_{p,L}(k) \in R^{mL}$, called *pseudo partial gradient* (PPG), in which that system (2.22) can be transformed into the PFDL data model as follows.

$$\Delta y(k + 1) = \varphi_{p,L}^T(k) \Delta U_L(k) \tag{2.23}$$

Where $\varphi_{p,L}(k) = [\varphi_1^T(k), \dots, \varphi_L^T(k)]^T$ is bounded for any time k, and $\varphi_i(k) \in R^m$, $i = 1, \dots, L$.

2.1.2.3. Full Form dynamic Linearization

Along with considerations mentioned in section 2.1.1.3, the FFDL data model is developed for MIMO system (2.20). to do so, the following two assumptions are specified for MIMO system (1.20).

Assumption 2.11: The partial derivatives of $f_i(\dots)$, $i = 1, \dots, m$, is continuous corresponding to all $u(k)$.

Assumption 2.12: The MIMO system (2.20) satisfies the following generalized *Lipschitz* condition:

$$\|y(k_1+1)-y(k_2+1)\| \le b \left\|\boldsymbol{H}_{L_y,L_u}(k_1)-\boldsymbol{H}_{L_y,L_u}(k_2)\right\|,$$

for $\forall k_1 \ne k_2$, $k_1 \ge 0$ & $k_2 \ge 0$, $H_{L_y,L_u}(k_1) \ne H_{L_y,L_u}(k_2)$ and $b > 0$.

where $\boldsymbol{H}_{L_y,L_u}(k) = \left[y^T(k),\dots,y^T\left(k-L_y+1\right),u^T(k),\dots,u^T(k-L_u+1)\right]^T \in R^{mL_y+mL_u}$ is a vector containing all the control input and system output signals within an input-related $[k-L_u+1,k]$ and output-related $\left[k-L_y+1,k\right]$ fixed-length period, where the $0 \le L_u \le n_u$ and $0 \le L_y \le n_y$ are the control output and control input LLC, respectively.

Satisfying the mentioned Assumptions by system (2.20), for any fixed L_y and L_u if $\left\|\Delta H_{L_y,L_u}(k)\right\| \ne 0$, then there exist a time-varying matrix $\varphi_{f,L_y,L_u}(k) \in R^{mL_y+mL_u}$, called *pseudo partitioned Jacobian matrix* (PPJM), in which that system (2.20) can be transformed into the FFDL data model as follows.

$$\Delta y(k+1) = \varphi_{f,L_y,L_u}(k)\Delta\, H_{L_y,L_u}(k) \tag{2.24}$$

where $\varphi_{f,L_y,L_u}(k) = \left[\varphi_1(k),\dots,\varphi_{L_y}(k),\varphi_{L_y+1}(k),\dots,\varphi_{L_y+L_u}(k)\right]^T$ is bounded as $\left\|\varphi_{f,L_y,L_u}(k)\right\| \le b$ for all k and $\varphi_i(k) \in R^{m\times m}$, $i = 1,\dots,L_y+L_u$.

The equation (2.24) is a virtual correspondent dynamic linearization data model of system (2.20) that should reproduce all the possible behavior of main system (2.20). The $\varphi_{L_y+1}(k)$ of PPJM matrix, $\varphi_{f,L_y,L_u}(k)$, is also supposed to be a diagonally dominant matrix as (2.25) and the sign of its elements should stay unchanged.

$$\left|\varphi_{ij(L_y+1)}\right| \le b_1,\ b_2 \le \left|\varphi_{ii(L_y+1)}\right| \le ab_2,\ i = 1,\dots,m, j = 1,\dots,m, i \ne j \tag{2.25}$$

Where $a > 1$, $b_2 > 0$ and b_1 is an integer satisfying $b_2 > b_1(2a+1)(m-1)$.

Remark 2.7

In the case of multi-input single-output (MISO) system, the FFDL method can be extended for this system by following considerations.

Denote the $\breve{\boldsymbol{H}}_{L_y,L_u}(k) = \left[y^T(k),\dots,y^T\left(k-L_y+1\right),u^T(k),\dots,u^T(k-L_u+1)\right]^T \in R^{L_y+mL_u}$ is a new vector containing all the control input and system output signals within an input-related $[k-L_u+1,k]$ and output-related $\left[k-L_y+1,k\right]$ fixed-length period. The Assumptions 11 and 12 are rewritten as follows for MISO system.

Assumption* $\mathbf{2.11'}$*: The partial derivatives of $f(\dots)$, is continuous corresponding to all $u(k)$.

Assumption* $\mathbf{2.12'}$*: The MISO system (2.22) satisfies the following generalized *Lipschitz* condition:

$$|y(k_1+1)-y(k_2+1)| \le b \left\|\breve{\boldsymbol{H}}_{L_y,L_u}(k_1)-\breve{\boldsymbol{H}}_{L_y,L_u}(k_2)\right\|,$$

For $\forall k_1 \ne k_2$, $k_1 \ge 0$ & $k_2 \ge 0$, $\breve{\boldsymbol{H}}_{L_y,L_u}(k_1) \ne \breve{\boldsymbol{H}}_{L_y,L_u}(k_2)$ and $b > 0$.

Satisfying the mentioned Assumptions by system (2.22), for any fixed L_y and L_u if $\left\|\Delta\breve{\boldsymbol{H}}_{L_y,L_u}(k)\right\| \ne 0$, then there exist a time-varying matrix $\varphi_{f,L_y,L_u}(k) \in R^{L_y+mL_u}$, called *pseudo partitioned Jacobian gradient*, in which that system (2.22) can be transformed into the FFDL data model as follows.

$$\Delta y(k+1) = \varphi_{f,L_u,L_y}^T(k)\Delta\breve{\boldsymbol{H}}_{L_y,L_u}(k) \tag{2.26}$$

where $\varphi_{f,L_y,L_u}(k) = \left[\varphi_1(k), \dots, \varphi_{L_y}(k), \varphi_{L_y+1}^T(k), \dots, \varphi_{L_y+L_u}^T(k)\right]^T$ is bounded for all k and $\varphi_i(k) \in R^m$, $i = 1, \dots, L_y + L_u$.

2.1.3. Summary on Dynamic Linearization Methods

1) No knowledge of dynamic model of system is used during dynamic linearization. The dynamic linearization is only dependent on I/O data measured from controlled plant. So, this method can be applicable for any unknown complex system.
2) The dynamic linearization method brings a precise, corresponding, I/O data based dynamic linearization data model in a step-by-step form to the general system at each instant time. Thus, the unmodelled dynamics, which is an unavoidable problem for the model-based control systems, are not included in this data model.
3) Three different dynamic linearization approaches are presented in this chapter. The explained full-form dynamic linearization (FFDL) is the most general one and includes the PFDL and CFDL techniques. Technically, choosing the input-related and output-related pseudo orders as $L_y = 0, L_u = L > 1$, and $L_y = 0, L_u = 1$, the FFDL method will be changed to PFDL and CFDL respectively.
4) The dynamic linearization data model, presented in this chapter, is control-oriented and it can be used only to controller design. In next section, the mentioned DL approaches will be used in structure of MFAC to design the controller.

2.2. Model Free Adaptive Control

Adaptive control approaches generally suppose that the system structure of controlled plant is known but its parameters are unknown. So far, couple of adaptive controller methods have been developed for nonlinear systems. Feedback linearization based adaptive control [74], [75], adaptive predictive control [76]–[79], backstepping approach [80]–[83], sliding mode adaptive control [84], [85] and the multiple mode method [86], [87] are some of adaptive control methods proposed for nonlinear systems. All these mentioned methods are model-based control strategies and require a precise dynamic model of studied plant to design the controller. In the case of lacking a precise dynamic model or in presence of large uncertainties, the mentioned model-based adaptive controllers will be hard to design. Therefore, it is of great importance to develop the data-driven adaptive control methods to tackle the limitations related to the lack of precise dynamic model or knowledge about the system parameters.

Motivated by abovementioned considerations, the model-free adaptive control (MFAC) as a data-drive control theory is presented and investigated here to apply for the nonlinear systems. The MFAC method was firstly suggested by Hou in 1994 for a class of general unknown non-affine discrete-time nonlinear system [88]. In this scheme, rather than utilizing the non-linear state-space model of system, the MFAC builds and uses a dynamic linearization (DL) data model of the studied system at every operating point to design the controller. As mentioned in previous section, the dynamic linearization data model is created by pseudo partial derivative

(PPD) or pseudo gradient (PG) approaches for single input single output (SISO) systems and pseudo-Jacobina matrix (PJM) approach for multi-input multi-output (MIMO) systems. The time-varying PPD, PG or PJM should be also estimated at every operating point only by utilizing the collected I/O data from controlled plant [35], [89].

In this section, a series of MFAC method and analysis are given for SISO and MIMO nonlinear systems. The different series of MFAC include the CFDL-based, PFDL-based and FFDL-based MFAC which are investigated separately in this section.

2.2.1. MFAC for SISO Discrete-Time Nonlinear Systems

2.2.1.1. CFDL Data Model Based MFAC

Let consider the SISO discrete-time nonlinear system (2.1) here again as,

$$y(k+1) = f\left(y(k), \dots, y(k-n_y), u(k), \dots, u(k-n_u)\right) \tag{2.27}$$

In section 2.1.1.1, it is proved that system (2.27), satisfying Assumption 2.1 and 2.2, can be transformed into the following CFDL data model.

$$\Delta y(k+1) = \varphi_c(k)\Delta u(k) \tag{2.28}$$

This equation is a virtual correspondent dynamic linearization data model of system (2.27) that should include all the possible behavior of main system (2.27). As stated before, this is a control-design-oriented linear time-varying data model with a scalar parameter. The CFDL-based MFAC control scheme will be designed according to this virtual dynamic linearization data model in following section.

2.2.1.1.1. Controller Algorithm

Using the one-step-ahead prediction error cost function to design the controller for discrete-time nonlinear systems may lead to extra control effort and damage the control system. On the other hand, using the weighted one-step-ahead prediction error cost function may also cause to tracking error. Therefore, the coming cost function is used to design the controller scheme.

$$J\big(u(k)\big) = |y^*(k+1) - y(k+1)|^2 + \lambda|u(k) - u(k-1)|^2 \tag{2.29}$$

where $\lambda > 0$, is a weighting factor to limit the changing rate of the control input. $y^*(k+1)$ is the reference trajectory of system output.

Putting the CFDL data model (2.28) into cost function (2.29) and differentiating according to $u(k)$ and setting to zero bring the following control law.

$$u(k) = u(k-1) + \frac{\rho\varphi_c(k)}{\lambda + |\varphi_c(k)|^2}\big(y^*(k+1) - y(k)\big) \tag{2.30}$$

where the $\rho \in (0, 1]$ is the step factor which is added to make the controller algorithm more general.

The λ is used in control algorithm (2.30) as a penalty factor to prevent system from large overshoots and guarantee the smoothness of the control input.

As seen in (2.30), the measured outputs $y(k)$, desired trajectories $y^*(k)$ and time varying PPD scalar parameter, $\varphi_c(k)$, are the essential components for the controller design. As mentioned before, the PPD scalar

parameter, obtained from dynamic linearization, has unknown structure and should be estimate at each operating point. On the other hand, the control algorithm (2.30) is usable only if the PPD scalar parameter is known. Since the exact value of PPD is unknown or hard to evaluate, the estimation of PPD scalar parameter is used here to make the control law (2.30) useable.

2.2.1.1.2. PPD Estimation Algorithm

The cost functions, which are commonly used for estimation of time-varying parameters, are normally to minimize the square of the error between desired system output and real output of system. Using this kind of cost function usually leads to an estimated value which is sensitive against the inaccurate sampling data, which can be due to the sensor error or other factors. To tackle this weakness, the following cost function is used for estimation of PPD scalar parameter.

$$J\big(\varphi_c(k)\big) = |y(k) - y(k-1) - \varphi_c(k)\Delta u(k-1)|^2 + \mu|\varphi_c(k) - \hat{\varphi}_c(k)|^2 \tag{2.31}$$

where $\mu > 0$ is a weigh factor.

Minimizing the cost function (2.31) according to $\varphi_c(k)$ brings the coming PPD estimation law.

$$\hat{\varphi}_c(k) = \hat{\varphi}_c(k-1) + \frac{\eta\Delta u(k-1)}{\mu+\Delta u(k-1)^2}\big(\Delta y(k) - \hat{\varphi}_c(k-1)\Delta u(k-1)\big) \tag{2.32}$$

where the $\eta \in (0, 2]$ is the step factor which is added to make the estimation algorithm more general and the $\hat{\varphi}_c(k)$ stands as the estimated value of $\varphi_c(k)$.

In addition, a reset structure is used for estimation law (2.32) to empower this estimation algorithm with a powerful capability to track the time-varying parameter as below.

$$\hat{\varphi}_c(k) = \hat{\varphi}_c(1),\ if\ |\hat{\varphi}_c(k)| \le \varepsilon\ or\ |\Delta u(k-1)| \le \varepsilon\ \ or\ sign\big(\hat{\varphi}_c(k)\big) \ne sign\big(\hat{\varphi}_c(1)\big) \tag{2.33}$$

where the $\hat{\varphi}_c(1)$ denotes the initial estimated value of $\hat{\varphi}_c(k)$, the sign of parameter is supposed to stay unchanged for all k and ε is a small positive constant.

2.2.1.1.3. Stability Analysis

In order to do the stability analysis, the following assumption is considered for system (2.27).

Assumption 2.13: for each certain bounded output trajectory $y^*(k+1)$, there exists a bounded control input $u^*(k)$, in which the system output running by $u^*(k)$ is equal to $y^*(k+1)$.

Satisfying Assumption 2.13 by system (2.27), then if system (2.27) is controlled by the CFDL-based MFAC approach (2.30)-(2.32), for a regulation problem, where is, $y^*(k+1) = y^* = constant.$, then there exists a fixed $\lambda_{min} > 0$, so that two characteristics keep for any $\lambda > \lambda_{min}$ as:

a. The system output tracking error converges uniformly and $\lim_{k\to\infty}|y^* - y(k+1)| = 0$.

b. The $\{y(k)\}$ and $\{u(k)\}$ are bounded and the closed-loop system is BIBO stable.

Proof

The boundness of the $\hat{\varphi}_c(k)$ is guaranteed since one of the conditions $|\hat{\varphi}_c(k)| \le \varepsilon,\ |\Delta u(k-1)| \le \varepsilon\ \ or\ sign\big(\hat{\varphi}_c(k)\big) \ne sign\big(\hat{\varphi}_c(1)\big)$.

Otherwise, taking the $\tilde{\varphi}_c(k) = \hat{\varphi}_c(k) - \varphi_c(k)$ as the estimation error of $\varphi_c(k)$ and putting in the equation (2.32) brings the

$$\tilde{\varphi}_c(k) = \left(1 - \frac{\eta|\Delta u(k-1)|^2}{\mu+|\Delta u(k-1)|^2}\right)\tilde{\varphi}_c(k-1) + \varphi_c(k-1) - \varphi_c(k) \tag{2.34}$$

By taking the absolute value on both sides of (2.34), we have

$$|\tilde{\varphi}_c(k)| \leq \left|\left(1 - \frac{\eta|\Delta u(k-1)|^2}{\mu+|\Delta u(k-1)|^2}\right)\right| |\tilde{\varphi}_c(k-1)| + |\varphi_c(k-1) - \varphi_c(k)| \tag{2.35}$$

The term $\frac{\eta|\Delta u(k-1)|^2}{\mu+|\Delta u(k-1)|^2}$ is uniformly increasing according to $|\Delta u(k-1)|^2$ and its minimum amount is $\frac{\eta\varepsilon^2}{(\mu+\varepsilon^2)}$. While $\mu > 0$ and $0 < \eta \leq 2$, there should exist a constant d_1 so that

$$0 \leq \left|\left(1 - \frac{\eta|\Delta u(k-1)|^2}{\mu+|\Delta u(k-1)|^2}\right)\right| \leq 1 - \frac{\eta\varepsilon^2}{(\mu+\varepsilon^2)} = d_1 < 1 \tag{1.36}$$

In addition, the $|\varphi_c(k)| \leq b$ feature cause to the $|\varphi_c(k-1) - \varphi_c(k)| \leq 2b$. Therefore, from (2.35) and (2.36) we have

$$|\tilde{\varphi}_c(k)| \leq d_1|\tilde{\varphi}_c(k-1)| + 2b \leq d_1^2|\tilde{\varphi}_c(k-2)| + 2d_1 b + 2b \leq \cdots \leq d_1^{k-1}|\tilde{\varphi}_c(1)| + \frac{2b\left(1-d_1^{k-1}\right)}{1-d_1} \tag{2.37}$$

which shows that $\tilde{\varphi}_c(k)$ is bounded. Then the boundness of $\hat{\varphi}_c(k)$ is also guaranteed as $\varphi_c(k)$ is bounded.

Taking the tracking error as:

$$e(k+1) = y^* - y(k+1) \tag{2.38}$$

Putting the CFDL data model (2.28) into (2.38) and taking absolute value we have

$$|e(k+1)| = |y^* - y(k+1)| = |y^* - y(k) - \varphi_c(k)\Delta u(k)| \leq \left|1 - \frac{\rho\varphi_c(k)\hat{\varphi}_c(k)}{\lambda+|\hat{\varphi}_c(k)|^2}\right| |e(k)| \tag{2.39}$$

From resetting algorithm (2.33) and since the sign of $\varphi_c(k)$ stay unchanged for all k, the $\varphi_c(k)\hat{\varphi}_c(k) \geq 0$ can be concluded.

Taking $\lambda_{min} = \frac{b^2}{4}$, using $\alpha^2 + \beta^2 \geq 2\alpha\beta$ and corresponding to $\hat{\varphi}_c(k) \geq \varepsilon$, relying on the fact that the sign of $\varphi_c(k)$ stay unchanged for all k, there should exist a constant M_1 ($0 < M_1 < 1$) in which that

$$0 < M_1 \leq \frac{\varphi_c(k)\hat{\varphi}_c(k)}{\lambda+|\hat{\varphi}_c(k)|^2} \leq \frac{b\hat{\varphi}_c(k)}{\lambda+|\hat{\varphi}_c(k)|^2} \leq \frac{b\hat{\varphi}_c(k)}{2\sqrt{\lambda}\hat{\varphi}_c(k)} < \frac{b}{2\sqrt{\lambda_{min}}} = 1 \tag{2.40}$$

keeps for $\lambda > \lambda_{min}$, where b is the constant who satisfies $|\varphi_c(k)| < b$.

According to (2.40), $0 < \rho \leq 1$ and $\lambda > \lambda_{min}$, there should exist a positive constant $d_2 < 1$ so that

$$\left|1 - \frac{\rho\varphi_c(k)\hat{\varphi}_c(k)}{\lambda+|\hat{\varphi}_c(k)|^2}\right| = 1 - \frac{\rho\varphi_c(k)\hat{\varphi}_c(k)}{\lambda+|\hat{\varphi}_c(k)|^2} \leq 1 - \rho M_1 = d_2 < 1 \tag{2.41}$$

Collecting the (2.38) and (2.40) brings the conclusion (a) as

$$|e(k+1)| \leq d_2|e(k)| \leq d_2^2|e(k-1)| \leq \cdots \leq d_2^k|e(1)| \tag{2.42}$$

Since the $y^*(k)$ is constant, the convergence of $e(k)$ guarantees that the $y(k)$ is also bounded.

Utilizing $\left(\sqrt{\lambda}\right)^2 + |\hat{\varphi}_c(k)|^2 \geq 2\sqrt{\lambda}\hat{\varphi}_c(k)$ and $\lambda > \lambda_{min}$, the coming inequality can be obtained from (2.30):

$$|\Delta u(k)| = \left|\frac{\rho\hat{\varphi}_c(k)(y^*-y(k))}{\lambda+|\hat{\varphi}_c(k)|^2}\right| = \left|\frac{\rho\hat{\varphi}_c(k)}{\lambda+|\hat{\varphi}_c(k)|^2}\right||e(k)| \le \left|\frac{\rho\hat{\varphi}_c(k)}{2\sqrt{\lambda}\hat{\varphi}_c(k)}\right||e(k)| \le \left|\frac{\rho}{2\sqrt{\lambda_{min}}}\right||e(k)| = M_2|e(k)| \tag{2.43}$$

where $M_2 = \frac{\rho}{2\sqrt{\lambda_{min}}}$ is a bounded constant.

From (2.42) and (2.43), we have

$$\begin{aligned}|\Delta u(k)| &\le |\Delta u(k)-\Delta u(k-1)| + |\Delta u(k-1)| \\ &\le |\Delta u(k)-\Delta u(k-1)| + |\Delta u(k-1)-\Delta u(k-2)| + |\Delta u(k-2)| \\ &\le |\Delta u(k)| + |\Delta u(k-1)| + \cdots + |\Delta u(2)| + |u(1)| \\ &\le M_2\,(|e(k)| + |e(k-1)| + \cdots + |e(2)|) + |u(1)| \\ &\le M_2\,(d_2^{k-1}|e(1)| + d_2^{k-1}|e(1)| + \cdots + d_2|e(1)|) + |u(1)| < M_2\,\frac{d_2}{1-d_2}|e(1)| + |u(1)|\end{aligned} \tag{2.44}$$

Therefore, the conclusion (b) is obtained from (2.44).

By this way, it is concluded that applying the MFAC method to any unknown nonlinear system for regulation issue can promise the error convergence and the stability of the system.

2.2.1.1.4. Simulation Results

In this section, in order to verify the effectiveness of CFDL-based MFAC scheme, a numerical simulation study is carried out for a SISO discrete-time nonlinear system. In this example, the model dynamics is not included in CFDL-based MFAC algorithm, and the controller have only used the I/O data of the controlled plant.

Example 2.1

Consider a SISO discrete-time nonlinear system as follows.

$$y(k+1) = 0.6y(k) - 0.1y(k-1) + 1.8u(k) - 1.8u^2(k) + 0.6u^3(k) - 0.15u(k-1) + 0.15u^2(k-1) - 0.05u^3(k-1)$$

where $y(k)$ and $u(k)$ are the system output and control input, respectively.

The desired output signal $y^*(k+1)$ is given as

$$y^*(k+1) = \begin{cases} 0.5, & 0 \le k < 100 \\ 1.0, & 100 \le k < 200 \\ 2.0, & 200 \le k < 300 \\ 1.5, & 300 \le k < 400 \end{cases}$$

Using the CFDL approach, the abovementioned nonlinear system is transformed into the following data model:

$$y(k+1) = \varphi(k)u(k)$$

The control algorithm, including the estimation of $\varphi(k)$ and controller design, is performed by selecting the proper controller parameters as $\rho = 0.7$, $\mu = 2$ and $\eta = 0.9$, and using the initial values as $u(1) = 0$, $y(1) = 0.25$ and $\hat{\varphi}(1) = 0$. It is noteworthy that selecting the weighting factor λ is one important factor to have a desired response time and overshoot. For this reason, the simulation results, shown in Figure 2.3, are presented for two different weighting factor. From the simulation results, one can find that the CFDL-based MFAC brings

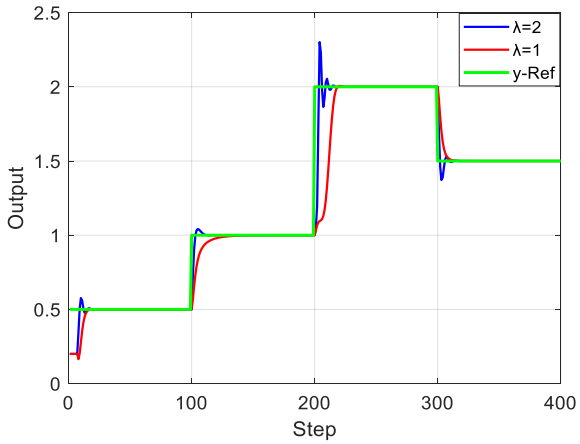

Figure 2.3. Simulation results in Example 2.1 using CFDL-based MFAC.

a satisfactory control performance by selecting $\lambda = 2.5$, and a little faster response with a larger overshoot comes with selecting $\lambda = 1$.

2.2.1.2. PFDL Data Model Based MFAC

It is previously proved in section 2.2.1.1.2, that the nonlinear system (2.27), satisfying the assumptions 2.3 and 2.4, with $\|\Delta U_L(k)\| \neq 0$ for all k, can be transferred to the PFDL data model as:

$$\Delta y(k+1) = \varphi_{p,L}^T(k)\Delta U_L(k) \tag{2.45}$$

where $\varphi_{p,L}(k) = [\varphi_1(k), \dots, \varphi_L(k)]^T$ is a bounded vector for any k, $U_L(k) = [u(k), \dots, u(k-L+1)]^T$ and L is the fixed control input LLC.

2.2.1.2.1. Controller Algorithm

The following cost function is used to design the controller algorithm.

$$J(u(k)) = |y^*(k+1) - y(k+1)|^2 + \lambda|u(k) - u(k-1)|^2 \tag{2.46}$$

where λ is a weight factor.

Putting the PFDL data model (2.45) into cost function (2.46) and minimizing according to the $u(k)$ brings the coming control algorithm.

$$u(k) = u(k-1) + \frac{\rho_1\varphi_1(k)(y^*(k+1)-y(k))}{\lambda+|\varphi_1(k)|^2} - \frac{\varphi_1(k)\sum_{i=2}^{L}\rho_i\varphi_i(k)\Delta u(k-i+1)}{\lambda+|\varphi_1(k)|^2} \tag{2.47}$$

where $\rho_i \in (0,1]$, $i = 1,2,\dots,L$, is the step factor and $\lambda > 0$ is the weight factor.

As seen in (2.47), the measured outputs $y(k)$, desired trajectories $y^*(k)$ and time varying PG vector, $\varphi_{p,L}(k)$, are the essential components for the controller design. As mentioned before, the PG vector, obtained from dynamic linearization, has unknown structure and should be estimate at each operating point. On the other hand, the control algorithm (2.47) is usable only if the PG vector is known. Since the exact value of PG vector is unknown or hard to evaluate and it is a time-varying vector, the estimation of PG vector is used here to make the control law (2.47) useable.

2.2.1.2.2. PG Estimation Algorithm

Similar to the analysis in Section 2.1.1.2, the following cost function is used for estimation of PG vector as follows:

$$J\left(\varphi_{p,L}(k)\right) = \left|y(k) - y(k-1) - \varphi_{p,L}^{T}(k)\Delta U_L(k-1)\right|^2 + \mu\left|\varphi_{p,L}(k) - \hat{\varphi}_{p,L}(k)\right|^2 \quad (2.48)$$

where $\mu > 0$ is the weight factor.

Then, using the Matrix Inversion Lemma [90] and mentioned cost function, the estimation algorithm for PG vector will be derived.

Matrix Inversion Lemma: Let A, B, C and D be real matrices with proper dimensions. If the inversions of matrices A, C and $DA^{-1}B + C^{-1}$ exist, it follows that,

$$[A + BCD]^{-1} = A^{-1} - A^{-1}B[DA^{-1}B + C^{-1}]^{-1}DA^{-1}.$$

Minimizing the cost function (2.48) according to $\varphi_{p,L}(k)$ and using the abovementioned matrix inversion brings

$$\hat{\varphi}_{p,L}(k) = \hat{\varphi}_{p,L}(k-1) + \frac{\eta\Delta U_L(k-1)\left(y(k) - y(k-1) - \hat{\varphi}_{p,L}^{T}(k-1)\Delta U_L(k-1)\right)}{\mu + \|\Delta U_L(k-1)\|^2} \quad (2.49)$$

where the $\eta \in (0, 2]$ is the step factor which is added to make the estimation algorithm more general and the $\hat{\varphi}_{p,L}(k)$ stands as the estimated value of $\varphi_{p,L}(k)$.

In addition, a reset structure is used for estimation law (2.49) to empower this estimation algorithm with a powerful capability to track the time-varying parameter as below.

$$\hat{\varphi}_{p,L}(k) = \hat{\varphi}_{p,L}(1),\ if\ \left\|\hat{\varphi}_{p,L}(k)\right\| \le \varepsilon\ or\ \|\Delta U_L(k-1)\| \le \varepsilon\ \ or\ sign\left(\hat{\varphi}_1(k)\right) \ne sign\left(\hat{\varphi}_1(1)\right) \quad (2.50)$$

where the $\hat{\varphi}_{p,L}(1)$ denotes the initial value of $\hat{\varphi}_{p,L}(k)$, and the sign of first parameter ($\hat{\varphi}_1(k)$) in PG vector $\hat{\varphi}_{p,L}(k)$ is supposed to stay unchanged for all k.

In this control algorithm the estimated PG vector $\hat{\varphi}_{p,L}(k)$ is a L-dimensional vector which is tuned online in the PFDL-based MFAC approach. The L is the control input length linearization constant (LLC) which is an adjustable parameter and should be selected as an integer between 1 and $n_y + n_u$. Since the n_y and n_u are unknown, L can be selected to be 1 for very simple system and bigger value for more complex systems. Due to presenting several step factors $\rho_1, \rho_1, \dots, \rho_L$, in PFDL-based MFAC, this control scheme has more adjustable parameters compared to the CFDL-based MFAC. It is noteworthy that by choosing $L = 1$, the PFDL-based MFAC becomes to the CFDL-based MFAC.

2.2.1.2.3. Stability Analysis

In order to do the stability analysis, the following Lemma [91], should be considered in this section.

Lemma 2.1: Let $A = \begin{bmatrix} a_1 & a_2 & \cdots & a_{L-1} & a_L \\ 1 & 0 & \cdots & 0 & 0 \\ 0 & 1 & \cdots & 0 & 0 \\ \vdots & \vdots & \vdots & \vdots & \vdots \\ 0 & 0 & \cdots & 1 & 0 \end{bmatrix}$,

if $\sum_{i=1}^{L}|a_i| < 1$, then $s(A) < 1$, where $s(.)$ is the spectral radius.

Theorem 2.1

If nonlinear system (2.27) is controlled by PFDL-based MFAC approach (2.47)-(2.50) for a regulation issue $y^*(k+1) = y^* = constant.$, then there exists a fixed $\lambda_{min} > 0$, so that two characteristics keep for any $\lambda > \lambda_{min}$ as:

a. System output tracking error converges asymptotically, then $\lim_{k\to\infty} |y^* - y(k+1)| = 0$.

b. The $\{y(k)\}$ and $\{u(k)\}$ are bounded and the closed-loop system is BIBO stable.

Proof

Similar to the stability analysis in CFDL-based MFAC, this proof has two steps. The first step includes the proof of the boundness of PG estimation and second step includes the proof of the tracking error convergence.

Step 1: The boundness of the $\hat{\varphi}_{p,L}(k)$ is guaranteed since one of the conditions $\left|\hat{\varphi}_{p,L}(k)\right| \le \varepsilon$, $|\Delta U_L(k-1)| \le \varepsilon \ or \ sign\left(\hat{\varphi}_1(k)\right) \ne sign\left(\hat{\varphi}_1(1)\right)$ is contented.

Otherwise, taking the $\tilde{\varphi}_{p,L}(k) = \hat{\varphi}_{p,L}(k) - \varphi_{p,L}(k)$ as the estimation error of $\varphi_{p,L}(k)$ and putting in the equation (2.48) brings the

$$\tilde{\varphi}_{p,L}(k) = \left(I - \frac{\eta \Delta U_L(k-1)\Delta U_L^T(k-1)}{\mu + \|\Delta U_L(k-1)\|^2}\right)\tilde{\varphi}_{p,L}(k-1) + \varphi_{p,L}(k-1) - \varphi_{p,L}(k) \tag{2.51}$$

where I is an identity matrix with related dimension.

In the previous sections it is proven that $\|\varphi_{p,L}(k)\| < b$, which meant to the boundness of $\|\varphi_{p,L}(k)\|$. By taking the norms value on both sides of (2.51), we have

$$\begin{aligned}\|\tilde{\varphi}_{p,L}(k)\| &\le \left\|\left(I - \frac{\eta \Delta U_L(k-1)\Delta U_L^T(k-1)}{\mu + \|\Delta U_L(k-1)\|^2}\right)\tilde{\varphi}_{p,L}(k-1)\right\| + \|\varphi_{p,L}(k-1) - \varphi_{p,L}(k)\| \\ &\le \left\|\left(I - \frac{\eta \Delta U_L(k-1)\Delta U_L^T(k-1)}{\mu + \|\Delta U_L(k-1)\|^2}\right)\tilde{\varphi}_{p,L}(k-1)\right\| + 2b\end{aligned} \tag{2.52}$$

Squaring the first on the right side of (2.52) brings

$$\begin{aligned}&\left\|\left(I - \frac{\eta \Delta U_L(k-1)\Delta U_L^T(k-1)}{\mu + \|\Delta U_L(k-1)\|^2}\right)\tilde{\varphi}_{p,L}(k-1)\right\|^2 \\ &\qquad < \left\|\tilde{\varphi}_{p,L}(k-1)\right\|^2 + \left(-2 + \frac{\eta\|\Delta U_L(k-1)\|^2}{\mu + \|\Delta U_L(k-1)\|^2}\right)\frac{\eta(\tilde{\varphi}_{p,L}^T(k-1)\Delta U_L(k-1))^2}{\mu + \|\Delta U_L(k-1)\|^2}\end{aligned} \tag{2.53}$$

for $0 < \eta \le 2$ and $\mu > 0$, we have

$$-2 + \frac{\eta\|\Delta U_L(k-1)\|^2}{\mu + \|\Delta U_L(k-1)\|^2} < 0 \tag{2.54}$$

Combining the (2.53) and (1.54) leads to

$$\left\|\left(I - \frac{\eta \Delta U_L(k-1)\Delta U_L^T(k-1)}{\mu + \|\Delta U_L(k-1)\|^2}\right)\tilde{\varphi}_{p,L}(k-1)\right\|^2 < \left\|\tilde{\varphi}_{p,L}(k-1)\right\|^2 \tag{2.55}$$

that indicates that there exists a constant $0 < d_1 < 1$, in which that

$$\left\|\left(I - \frac{\eta \Delta U_L(k-1)\Delta U_L^T(k-1)}{\mu + \|\Delta U_L(k-1)\|^2}\right)\tilde{\varphi}_{p,L}(k-1)\right\| \le d_1\left\|\tilde{\varphi}_{p,L}(k-1)\right\|^2 \tag{1.56}$$

Here we just need to prove the existence of d_1 instead of finding its exact value.

Putting (2.56) into (2.52) brings

$$\left\|\tilde{\varphi}_{p,L}(k)\right\| \le d_1\left\|\tilde{\varphi}_{p,L}(k-1)\right\| + 2b \le d_1^2\left\|\tilde{\varphi}_{p,L}(k-2)\right\| + 2d_1 b + 2b \le \cdots \le d_1^{k-1}\left\|\tilde{\varphi}_{p,L}(1)\right\| + \frac{2b\left(1-d_1^{k-1}\right)}{1-d_1} \tag{2.57}$$

which shows that $\tilde{\varphi}_c(k)$ is bounded. Since the boundness of $\hat{\varphi}_{p,L}(k)$ and $\varphi_{p,L}(k)$ is guaranteed in previous sections.

Step 2: While $\hat{\varphi}_{p,L}(k)$ and $\varphi_{p,L}(k)$ are bounded, there should exist constants M_2, M_3, M_4 and $\lambda_{min} > 0$, in which the coming equations hold for $\lambda > \lambda_{min}$.

$$\left|\frac{\hat{\varphi}_1(k)}{\lambda+|\hat{\varphi}_1(k)|^2}\right| \le \left|\frac{\hat{\varphi}_1(k)}{2\sqrt{\lambda}|\hat{\varphi}_1(k)|}\right| < \frac{1}{2\sqrt{\lambda_{min}}} \triangleq M_1 < \frac{0.5}{b} \tag{2.58}$$

$$0 < M_2 \le \left|\frac{\hat{\varphi}_1(k)\hat{\varphi}_i(k)}{\lambda+|\hat{\varphi}_1(k)|^2}\right| \le b\left|\frac{\hat{\varphi}_1(k)}{2\sqrt{\lambda}\,|\hat{\varphi}_1(k)|}\right| < \frac{b}{2\sqrt{\lambda_{min}}} < 0.5 \tag{2.59}$$

$$M_1\left\|\varphi_{p,L}(k)\right\|_v \le M_3 < 0.5 \tag{2.60}$$

$$M_2 + M_3 < 1 \tag{2.61}$$

$$\left(\sum_{i=2}^{L}\left|\frac{\hat{\varphi}_1(k)\hat{\varphi}_i(k)}{\lambda+|\hat{\varphi}_1(k)|^2}\right|\right)^{1/(L-1)} \le M_4 \tag{2.62}$$

Chose max ρ_i, $i = 2, \dots, L$, such that

$$\sum_{i=2}^{L}\rho_i\left|\frac{\hat{\varphi}_1(k)\hat{\varphi}_i(k)}{\lambda+|\hat{\varphi}_1(k)|^2}\right| \le (\max\rho_i)\sum_{i=2}^{L}\rho_i\left|\frac{\hat{\varphi}_1(k)\hat{\varphi}_i(k)}{\lambda+|\hat{\varphi}_1(k)|^2}\right| \le (\max\rho_i)M_4^{L-1} \triangleq M_5 < 1 \tag{2.63}$$

Take the tracking error as

$$e(k) = y^* - y(k) \tag{2.64}$$

Let

$$A(k) = \begin{bmatrix} -\frac{\rho_2\hat{\varphi}_1(k)\hat{\varphi}_2(k)}{\lambda+|\hat{\varphi}_1(k)|^2} & -\frac{\rho_3\hat{\varphi}_1(k)\hat{\varphi}_3(k)}{\lambda+|\hat{\varphi}_1(k)|^2} & \cdots & -\frac{\rho_L\hat{\varphi}_1(k)\hat{\varphi}_L(k)}{\lambda+|\hat{\varphi}_1(k)|^2} & 0 \\ 1 & 0 & \cdots & 0 & 0 \\ 0 & 1 & \cdots & 0 & 0 \\ \vdots & \vdots & \vdots & \vdots & \vdots \\ 0 & 0 & \cdots & 1 & 0 \end{bmatrix}_{L\times L},$$

$$\Delta U_L(k) = [\Delta u(k), \dots, \Delta u(k-L+1)]^T, \qquad C = [1, 0, \dots, 0]^T \in R^L.$$

So, the controller algorithm can be edited as

$$\begin{aligned}\Delta U_L(k) = [\Delta u(k), \dots, \Delta u(k-L+1)]^T &= A(k)[\Delta u(k-1), \dots, \Delta u(k-L)]^T + \frac{\rho_1\hat{\varphi}_1(k)}{\lambda+|\hat{\varphi}_1(k)|^2}Ce(k) \\ &= A(k)\Delta U_L(k-1) + \frac{\rho_1\hat{\varphi}_1(k)}{\lambda+|\hat{\varphi}_1(k)|^2}Ce(k)\end{aligned} \tag{2.65}$$

The characteristic equation of $A(k)$ is

$$z^L + \frac{\rho_2\hat{\varphi}_1(k)\hat{\varphi}_2(k)}{\lambda+|\hat{\varphi}_1(k)|^2}z^{L-1} + \cdots + \frac{\rho_L\hat{\varphi}_1(k)\hat{\varphi}_L(k)}{\lambda+|\hat{\varphi}_1(k)|^2}z = 0 \tag{2.66}$$

From (2.63) we already have $|z| < 1$. Therefore, the following equation comes

$$|z|^{L-1} \le \sum_{i=2}^{L}\rho_i\left|\frac{\hat{\varphi}_1(k)\hat{\varphi}_i(k)}{\lambda+|\hat{\varphi}_1(k)|^2}\right||z|^{L-i} \le \sum_{i=2}^{L}\left|\frac{\hat{\varphi}_1(k)\hat{\varphi}_i(k)}{\lambda+|\hat{\varphi}_1(k)|^2}\right| \le (\max\rho_i)M_4^{L-1} < 1 \tag{2.67}$$

which indicates $|z| \le (\max \rho_i)^{1/(L-1)} M_4 < 1$. In addition, there exists an optional small positive constant ε_1 that

$$\|A(k)\|_v \le s\big(A(k)\big) + \varepsilon_1 \le (\max \rho_i)^{1/(L-1)} M_4 + \varepsilon_1 < 1 \tag{2.68}$$

where $\|A(k)\|_v$ is the consistent matrix norm for $A(k)$.

Take $d_2 = (\max \rho_i)^{1/(L-1)} M_4 + \varepsilon_1$. From description of $\Delta U_L(k)$, $k \le 0$, we have $\|\Delta U_L(k)\|_v = 0$. By taking the norm on both sides of equation (2.65) we have

$$\begin{aligned} \|\Delta U_L(k)\|_v &\le \|A(k)\|_v \, \|\Delta U_L(k-1)\|_v + \rho_1 \left| \frac{\hat{\varphi}_1(k)}{\lambda + |\hat{\varphi}_1(k)|^2} \right| |e(k)| < d_2 \|\Delta U_L(k-1)\|_v + \rho_1 M_1 |e(k)| \ldots \\ &= \rho_1 M_1 \sum_{i=1}^{k} d_2^{k-i} \, |e(i)| \end{aligned} \tag{2.69}$$

Putting the PFDL data model (2.45) and controller algorithm (2.47) into the (2.64) brings

$$\begin{aligned} e(k+1) &= y^* - y(k+1) = y^* - y(k) - \varphi_{p,L}^T(k) \Delta U_L(k) \\ &= e(k) - \varphi_{p,L}^T(k) \left(A(k) \Delta U_L(k-1) + \frac{\rho_1 \hat{\varphi}_1(k)}{\lambda + |\hat{\varphi}_1(k)|^2} C e(k) \right) \\ &= \left(1 - \frac{\rho_1 \hat{\varphi}_1(k) \varphi_1(k)}{\lambda + |\hat{\varphi}_1(k)|^2} \right) e(k) - \varphi_{p,L}^T(k) A(k) \Delta U_L(k-1) \end{aligned} \tag{2.70}$$

From (2.59) one can select $0 < \rho_1 \le 1$ that

$$\left| 1 - \frac{\rho_1 \hat{\varphi}_1(k) \varphi_1(k)}{\lambda + |\hat{\varphi}_1(k)|^2} \right| = \left| 1 - \left| \frac{\rho_1 \hat{\varphi}_1(k) \varphi_1(k)}{\lambda + |\hat{\varphi}_1(k)|^2} \right| \right| \le 1 - \rho_1 M_2 < 1$$

Let $d_3 = 1 - \rho_1 M_2$. Taking norms on both sides of (1.70) brings

$$\begin{aligned} |e(k+1)| &\le \left| \left(1 - \frac{\rho_1 \hat{\varphi}_1(k) \varphi_1(k)}{\lambda + |\hat{\varphi}_1(k)|^2} \right) \right| |e(k)| + \left\| \varphi_{p,L}(k) \right\|_v \|A(k)\|_v \|\Delta U_L(k-1)\|_v \\ &< d_3 |e(k)| + d_2 \left\| \varphi_{p,L}(k) \right\|_v \|\Delta U_L(k-1)\|_v < \cdots \\ &< d_3^k |e(1)| + d_2 \sum_{i=1}^{k-1} d_3^{k-1-i} \left\| \varphi_{p,L}(i+1) \right\|_v \|\Delta U_L(i)\|_v \\ &< d_3^k |e(1)| + d_2 \sum_{i=1}^{k-1} d_3^{k-1-i} \left\| \varphi_{p,L}(i+1) \right\|_v \rho_1 M_1 \sum_{j=1}^{i} d_2^{i-j} \, |e(j)| \end{aligned} \tag{2.71}$$

Let $d_4 = \rho_1 M_3$. Collecting (2.60) and (2.71) brings

$$|e(k+1)| < d_3^k |e(1)| + d_2 d_4 \textstyle\sum_{i=1}^{k-1} d_3^{k-1-i} \sum_{j=1}^{i} d_2^{i-j} \, |e(j)| \tag{2.72}$$

Denote

$$g(k+1) = d_3^k |e(1)| + d_2 d_4 \textstyle\sum_{i=1}^{k-1} d_3^{k-1-i} \sum_{j=1}^{i} d_2^{i-j} \, |e(j)| \tag{2.73}$$

Then the equation (2.72) can be edited as

$$|e(k+1)| < g(k+1), \forall k = 1,2,\dots \tag{1.74}$$

with $g(2) = d_3|e(1)|$.

Clearly, while $g(k+1)$ converges uniformly to zero, the $e(k+1)$ will also converge to zero. By computing $g(k+2)$ we have

$$\begin{aligned} g(k+2) &= d_3^{k+1}|e(1)| + d_2 d_4 \sum_{i=1}^{k} d_3^{k-i} \sum_{j=1}^{i} d_2^{i-j} |e(j)| \\ &= d_3 g(k+1) + d_4 d_2^k |e(1)| + \cdots + d_4 d_2^2 |e(k-1)| + d_2 d_4 |e(k)| \\ &< d_3 g(k+1) + d_4 d_2^k |e(1)| + \cdots + d_4 d_2^2 |e(k-1)| + d_2 d_4 |e(k)| = d_3 g(k+1) + b(k) \end{aligned} \tag{2.75}$$

where $b(k) \triangleq d_4 d_2^k |e(1)| + \cdots + d_4 d_2^2 |e(k-1)| + d_2 d_4 |e(k)|$.

From (2.61), we have $d_3 = 1 - \rho_1 M_2 > \rho_1 (M_2 + M_3) - \rho_1 M_2 = \rho_1 M_3 = d_4$. Therefore, the following equation comes as

$$\begin{aligned} b(k) &< d_4 d_2^k |e(1)| + \cdots + d_4 d_2^2 |e(k-1)| + d_3 d_2 |g(k)| \\ &< d_4 d_2^k |e(1)| + \cdots + d_4 d_2^2 |e(k-1)| \\ &+ d_3 d_2 \left(d_3^{k-1} |e(1)| + d_2 d_4 \sum_{i=1}^{k-2} d_3^{k-2-i} \sum_{j=1}^{i} d_2^{i-j} |e(j)| \right) \\ &= d_2 \left(d_3^k |e(1)| + d_2 d_4 \sum_{i=1}^{k-1} d_3^{k-1-i} \sum_{j=1}^{i} d_2^{i-j} |e(j)| \right) = d_2 g(k+1) \end{aligned} \tag{2.76}$$

Putting (2.76) into (2.75) brings

$$g(k+2) < d_3 g(k+1) + b(k) < (d_3 + d_2) g(k+1) \tag{2.77}$$

Choosing $0 < \rho_i \leq 1, i = 1, \dots, L$, such that $0 < max\{\rho_i\}^{1/(L-1)} M_4 < \rho_1 M_2 < 1$, and

$$0 < 1 - \rho_1 M_2 + max\{\rho_i\}^{1/(L-1)} M_4 < 1 \tag{2.78}$$

Since the ε_1 is an optional small positive constant, we have

$$d_3 + d_2 = 1 - \rho_1 M_2 + \max_{i \in (2,L)} \{\rho_i\}^{1/(L-1)} M_4 + \varepsilon_1 < 1 \tag{2.79}$$

Putting (2.79) into (2.77) brings

$$\lim_{k \to \infty} g(k+2) < \lim_{k \to \infty} (d_3 + d_2) g(k+1) < \cdots < \lim_{k \to \infty} (d_3 + d_2)^k g(2) = 0 \tag{2.80}$$

Therefore, the conclusion (a) can be concluded directly from (2.74) and (2.80).

Thanks to the boundness of y^* and $e(k)$, the $y(k)$ is also bounded. From equations (2.69), (2.74) and (2.80) we have

$$\|U_L(k)\|_v \le \sum_{i=1}^{k} \|\Delta U_L(i)\|_v < \rho_1 M_1 \sum_{i=1}^{k} \sum_{j=1}^{i} d_2^{i-j} |e(j)| < \frac{\rho_1 M_1}{1-d_2} (|e(1)| + \cdots + |e(k)|)$$
$$< \frac{\rho_1 M_1}{1-d_2} \big(e(1) + g(2) + \cdots + g(k)\big) < \frac{\rho_1 M_1}{1-d_2} \left(e(1) + \frac{g(2)}{1-d_2-d_3}\right) \tag{2.81}$$

Therefore, the conclusion (b) is hold.

2.2.1.2.4. Simulation Results

In this section, in order to verify the effectiveness of PFDL-based MFAC scheme, a numerical simulation study is carried out for a SISO discrete-time nonlinear system. In this example, the model dynamics is not included in PFDL-based MFAC algorithm, and the controller have only used the I/O data of the controlled plant.

Example 2.2

Consider a SISO discrete-time nonlinear system as follows.

$$y(k+1) = -0.1y(k) - 0.2y(k-1) - 0.3y(k-2) + 0.1u(k) + 0.02u(k-1) + 0.03u(k-2)$$

where $y(k)$ and $u(k)$ are the system output and control input, respectively. In this system, changes of system output at next sampling time $y(k+1)$, is dependent to previous changes of control input and system output ($y(k-1), y(k-2)$ and $u(k-1), u(k-2)$).

The desired output signal $y^*(k+1)$ is given as

$$y^*(k+1) = 2\sin\left({}^{k}/_{50}\right) + \cos\left({}^{k}/_{20}\right)$$

Choosing the linearization length constant (LLC) as $L = 4$, the abovementioned nonlinear system is transformed into the following PFDL data model:

$$y(k+1) = [\varphi_1(k)\ \varphi_2(k)\ \varphi_3(k)\ \varphi_4(k)] \begin{bmatrix} \Delta u(k) \\ \Delta u(k-1) \\ \Delta u(k-2) \\ \Delta u(k-3) \end{bmatrix}$$

where the previous variation of control input is included in this linearized data model, but the previous variation of system output is not considered.

Then, the control algorithm, including the estimation of $\varphi_i(k)$ and controller design, is performed by selecting the proper controller parameters, as $\rho_1 = 0.6, \rho_1 = 0.55, \rho_3 = \rho_4 = 0.7, \mu = 2, \lambda = 0.002$ and $\eta = 0.6$ and using the initial values as $u(1) = 0, y(1) = 0$ and $\hat{\varphi}_{p,L}(1) = [1.5, 0.2, 0]$. The simulation result is shown in Figure 2.4. From the simulation results, the PFDL-based MFAC brings a satisfactory control performance but there is still a little error between the reference and controlled output. This error may be generated due to ignoring the previous changes of system output in dynamic linearization data model.

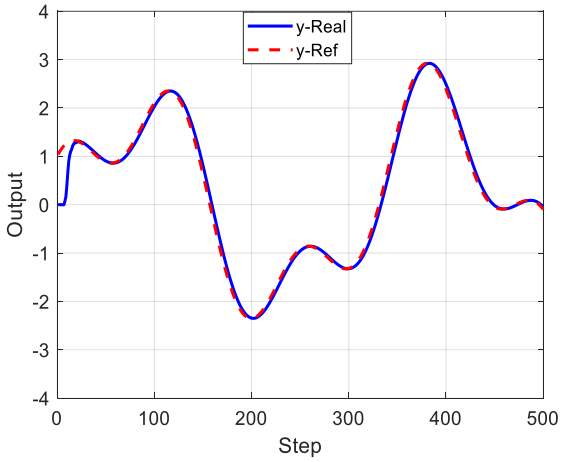

Figure 2.4. Simulation results in Example 2.2 using PFDL-based MFAC.

2.2.1.3. FFDL Data Model Based MFAC

It is previously proved in section 2.1.1.3, the nonlinear system (2.27), satisfying the assumptions 2.5 and 2.6, with $\left\|\Delta H_{L_y,L_u}(k)\right\| \neq 0$ for all k, can be transferred to the FFDL data model as:

$$\Delta y(k+1) = \varphi_{p,L_u,L_y}^{T}(k)\Delta H_{L_y,L_u}(k) \tag{2.82}$$

where $\varphi_{p,L_u,L_y}(k) = [\varphi_1(k), \dots, \varphi_{L_y}(k), \varphi_{L_y+1}(k), \dots, \varphi_{L_y+L_u}(k)]^T$ is a bounded vector for any k, and $\Delta H_{L_y,L_u}(k) = H_{L_y,L_u}(k) - H_{L_y,L_u}(k-1)$.

2.2.1.3.1. Controller Algorithm

In order to design the controller algorithm, a cost function of control input is used as

$$J\big(u(k)\big) = |y^*(k+1) - y(k+1)|^2 + \lambda|u(k) - u(k-1)|^2 \tag{2.83}$$

where $\lambda > 0$ is a weight factor.

Putting the FFDL data model (2.82) into cost function (2.83) and minimizing according to the control input brings the following control scheme:

$$u(k) = u(k-1) + \frac{\rho_{L_y+1}\varphi_{L_y+1}(k)\big(y^*(k+1) - y(k)\big)}{\lambda + \left|\varphi_{f,L_y+1}(k)\right|^2} - \frac{\varphi_{L_y+1}(k)\sum_{i=1}^{L_y}\rho_i\varphi_i(k)\Delta y(k-i+1)}{\lambda + \left|\varphi_{f,L_y+1}(k)\right|^2}$$
$$- \frac{\varphi_{L_y+1}\sum_{i=L_y+2}^{L_y+L_u}\rho_i\varphi_i(k)\Delta u(k+L_y-i+1)}{\lambda + \left|\varphi_{f,L_y+1}(k)\right|^2} \tag{2.84}$$

where $\rho_i \in (0,1], i = 1, \dots, L_y + L_u$ is the step factor.

As seen in (2.84), the measured outputs $y(k)$, desired trajectories $y^*(k)$ and time varying PG vector, $\varphi_{f,L_y,L_u}(k)$, are the essential components for the controller design. As mentioned before, the PG vector, obtained from dynamic linearization, has unknown structure and should be estimate at each operating point. On the other hand, the control algorithm (2.84) is usable only if the PG vector is known. Since the exact value

of PG vector is unknown or hard to evaluate, the estimation of PG vector is used here to make the control law (2.84) useable.

2.2.1.3.2. PG Estimation Algorithm

The following cost function is used to estimation of PG vector as follows:

$$J\left(\varphi_{f,L_y,L_u}(k)\right) = \left|y(k) - y(k-1) - \varphi^T_{f,L_y,L_u}(k)\Delta H_{L_y,L_u}(k-1)\right|^2 + \mu \left\|\varphi_{f,L_y,L_u}(k) - \hat{\varphi}_{f,L_y,L_u}(k-1)\right\|^2 \tag{2.85}$$

where $\mu > 0$ is the weight factor.

Then, minimizing the cost function (2.85) according to the $\varphi_{f,L_y,L_u}(k)$, in optimal condition, and using the matrix inversion lemma bring

$$\hat{\varphi}_{f,L_y,L_u}(k) = \hat{\varphi}_{f,L_y,L_u}(k-1) + \frac{\eta\Delta H_{L_y,L_u}(k-1)\left(y(k) - y(k-1) - \hat{\varphi}^T_{f,L_y,L_u}(k-1)\Delta H_{L_y,L_u}(k-1)\right)}{\mu + \left\|\Delta H_{L_y,L_u}(k-1)\right\|^2} \tag{2.86}$$

where the $\eta \in (0, 2]$ is the step factor which is added to make the estimation algorithm more general and the $\hat{\varphi}_{f,L_y,L_u}(k)$ stands as the estimated value of $\varphi_{f,L_y,L_u}(k)$.

In addition, a reset structure is used for estimation law (2.86) to empower this estimation algorithm with a powerful capability to track the time-varying parameter as below.

$$\begin{aligned}\hat{\varphi}_{f,L_y,L_u}(k) = \hat{\varphi}_{f,L_y,L_u}(1),\\ if\ \left\|\hat{\varphi}_{f,L_y,L_u}(k)\right\| \le \varepsilon\ or\ \left\|\Delta H_{L_y,L_u}(k-1)\right\| \le \varepsilon\ or\ sign\left(\hat{\varphi}_{L_y+1}(k)\right)\\ \neq sign\left(\hat{\varphi}_{L_y+1}(1)\right)\end{aligned} \tag{2.87}$$

where the $\hat{\varphi}_{f,L_y,L_u}(1)$ denotes the initial value of $\hat{\varphi}_{f,L_y,L_u}(k)$, and the sign of $(L_y + 1)$th parameter $(\hat{\varphi}_{L_y+1}(k))$ in PG vector $\hat{\varphi}_{f,L_y,L_u}(k)$ is supposed to stay unchanged for all k.

In this control algorithm the estimated PG vector $\hat{\varphi}_{f,L_y,L_u}(k)$ is an $(L_y + L_u)$-dimensional which is tuned online in the FFDL-based MFAC approach. The L_y, L_u are the system output and control input length linearization constant (LLC), respectively, and are adjustable parameters and should be selected as an integer between 1 and n_y and n_u. Since the n_y and n_u are unknown, LLC can be selected to be 1 for very simple system and bigger value for more complex systems. It is noteworthy that by choosing $L_y = 0$ and $L_u = L$, the FFDL-based MFAC becomes to the PFDL-based MFAC. Similarly, by choosing $L_y = 0$ and $L_u = 1$, the FFDL-based MFAC becomes to the CFDL-based MFAC. Due to presenting several step factors $\rho_1, \rho_1, \dots, \rho_{L_y+L_u}$, in FFDL-based MFAC, this control scheme has more adjustable parameters compared to the CFDL-based and PFDL-based MFAC.

2.2.1.3.3. Simulation Results

In order to verify the effectiveness of FFDL-based MFAC scheme, a numerical simulation study is carried out for a SISO discrete-time nonlinear system. In this example, the model dynamics is not included in FFDL-based MFAC algorithm, and the controller have only used the I/O data of the controlled plant.

Example 2.3

Consider the SISO discrete-time nonlinear system used in example 2.2 here again.

$$y(k+1) = -0.1y(k) - 0.2y(k-1) - 0.3y(k-2) + 0.1u(k) + 0.02u(k-1) + 0.03u(k-2)$$

where $y(k)$ and $u(k)$ are the system output and control input, respectively. Remember that changes of system output at next sampling time, $y(k+1)$, is dependent to previous changes of control input and system output $((k-1),(k-2))$.

The desired output signal $y^*(k+1)$ is given as

$$y^*(k+1) = 2\sin\left({}^{k}/_{50}\right) + \cos\left({}^{k}/_{20}\right)$$

Choosing the input-related and output related linearization length constant (LLC) as $L_u = L_y = 4$, the abovementioned nonlinear system is transformed into the following FFDL data model:

$$y(k+1) = [\varphi_1(k)\ \varphi_2(k)\ \varphi_3(k)\ \varphi_4(k)\ \varphi_5(k)\ \varphi_6(k)\ \varphi_7(k)\ \varphi_8(k)] \begin{bmatrix} \Delta y(k) \\ \Delta y(k-1) \\ \Delta y(k-2) \\ \Delta y(k-3) \\ \Delta u(k) \\ \Delta u(k-1) \\ \Delta u(k-2) \\ \Delta u(k-3) \end{bmatrix}$$

where the previous variation of both control input and system output are included in this linearized data model. The control algorithm, including the estimation of $\varphi_i(k)$ and controller design, is performed by selecting the proper controller parameters, as $\rho_1 = 0.6, \rho_1 = 0.55, \rho_3 = \rho_4 = 0.7, \rho_5 = 0.5, \rho_6 = 0.35, \rho_3 = \rho_4 = 0.75$ $\mu = 2$, $\lambda = 0.002$ and $\eta = 0.6$ and using the initial values as $u(1) = 0$, $y(1) = 0$ and $\hat{\varphi}_{p,L}(1) = [0,0,0,0,1.5,0.2,0,0]$. It is noteworthy that the parameter selection and design procedure is same with example 2.2, the just difference is that the previous changes of system output are included in the dynamic

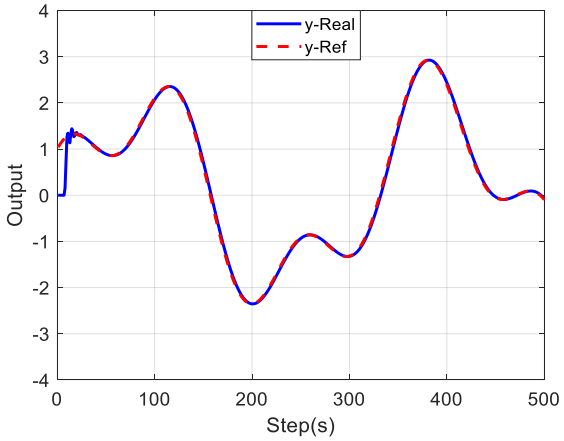

Figure 2.5. Simulation results in Example 2.3 using FFDL-based MFAC.

linearization data model. The simulation results are shown in Figure 2.5. From the simulation results, the FFDL-based MFAC brings a satisfactory control performance and the tracking error is decreased compared to the PFDL-based MFAC performance.

2.2.2. MFAC for MIMO Discrete-Time Nonlinear Systems

2.2.2.1. CFDL Data Model Based MFAC

Consider the presented MIMO discrete-time nonlinear system (2.20) here again

$$y(k+1) = f\left(y(k), \dots, y\left(k-n_y\right), u(k), \dots, u(k-n_u)\right) \tag{2.88}$$

where $y(k) = [y_1(k) \;\; y_2(k) \;\; \dots \;\; y_m(k)]^T \epsilon R^m$ and $u(k) = [u_1(k) \;\; u_2(k) \;\; \dots \;\; u_m(k)]^T \epsilon R^m$ are the system output and control input vectors respectively. m is the number of control inputs and system outputs. The n_y and n_u are two unknown positive integers. The $f(\dots) = [f_1(\dots), \dots, f_m(\dots)]^T \epsilon \prod_{n_y+n_u+2} R^m \to R^m$ is a vector-valued unknown nonlinear function.

In section 2.1.2.1, it is proved that system (2.88), satisfying Assumptions 2.7 and 2.8, can be transformed into the CFDL data model as

$$\Delta y(k+1) = \varphi_c(k) \Delta u(k) \tag{2.89}$$

where

$$\varphi_c(k) = \begin{bmatrix} \varphi_{11}(k) & \varphi_{12}(k) & \varphi_{13}(k) & \cdots & \varphi_{1m}(k) \\ \varphi_{21}(k) & \varphi_{22}(k) & \varphi_{23}(k) & \cdots & \varphi_{2m}(k) \\ \varphi_{31}(k) & \varphi_{32}(k) & \varphi_{33}(k) & \cdots & \varphi_{3m}(k) \\ \vdots & \vdots & \vdots & \vdots & \vdots \\ \varphi_{m1}(k) & \varphi_{m2}(k) & \varphi_{m3}(k) & \cdots & \varphi_{mm}(k) \end{bmatrix}_{m \times m} \in R^{m \times m}$$

is the unknown bounded PJM of system (2.89).

Assumption 2.14: The $\varphi_c(k)$ is a diagonally dominant matrix in which that, $\left|\varphi_{i,j}(k)\right| \leq b_1$, $b_2 \leq \left|\varphi_{i,j}(k)\right| \leq a b_2$, $a \geq 1$, and $b_2 > b_1(2a+1)(m-1), i = 1, \dots, m, j = 1, \dots, m, i \neq j$, and the sign of all the arrays of $\varphi_c(k)$ stay unchanged.

2.2.2.1.1. Controller Algorithm

Following cost function of the control input is used for controller design.

$$J\left(u(k)\right) = \|y^*(k+1) - y(k+1)\|^2 + \lambda \|u(k) - u(k-1)\|^2 \tag{2.90}$$

where the $\lambda > 0$ is a weight factor which is used to limit the changes of control input, and the $y^*(k+1)$ is the reference trajectory of system output.

Putting the CFDL data model (2.89) into cost function (2.90) and differentiating according to $u(k)$ and setting to zero bring the following control law:

$$u(k) = u(k-1) + \frac{\rho \varphi_c^T(k)\left(y^*(k+1) - y(k)\right)}{\lambda + \|\varphi_c(k)\|^2} \tag{2.91}$$

where the $\rho \in (0, 1]$ is the step factor which is added to make the controller algorithm more general.

2.2.2.1.2. PJM Estimation Algorithm

The following cost function of PJM $\varphi_c(k)$ estimation for MIMO systems is used here for estimation of the PJM matrix.

$$J\big(\varphi_c(k)\big) = \|y(k) - y(k-1) - \varphi_c(k)\Delta u(k-1)\|^2 + \mu\|\varphi_c(k) - \hat{\varphi}_c(k)\|^2 \tag{2.92}$$

where the $\mu > 0$ is a weight factor which is used to limit the changes of PJM estimation.

Minimizing cost function (2.92) brings the following estimation algorithm.

$$\hat{\varphi}_c(k) = \hat{\varphi}_c(k-1) + \frac{\eta\big(\Delta y(k) - \hat{\varphi}_c(k-1)\Delta u(k-1)\big)\Delta u^T(k-1)}{\mu + \|\Delta u(k-1)\|^2} \tag{2.93}$$

where the $\eta \in (0, 2]$ is the step factor and

$$\hat{\varphi}_c(k) = \begin{bmatrix} \hat{\varphi}_{11}(k) & \hat{\varphi}_{12}(k) & \hat{\varphi}_{13}(k) & \cdots & \hat{\varphi}_{1m}(k) \\ \hat{\varphi}_{21}(k) & \hat{\varphi}_{22}(k) & \hat{\varphi}_{23}(k) & \cdots & \hat{\varphi}_{2m}(k) \\ \hat{\varphi}_{31}(k) & \hat{\varphi}_{32}(k) & \hat{\varphi}_{33}(k) & \cdots & \hat{\varphi}_{3m}(k) \\ \vdots & \vdots & \vdots & \vdots & \vdots \\ \hat{\varphi}_{m1}(k) & \hat{\varphi}_{m2}(k) & \hat{\varphi}_{m3}(k) & \cdots & \hat{\varphi}_{mm}(k) \end{bmatrix}_{m\times m} \in R^{m\times m}$$

is the estimation of the PJM $\varphi_c(k)$ matrix.

In addition, a reset structure is used for estimation law (2.93) to empower this estimation algorithm with a powerful capability to track the time-varying parameter as below.

$$\hat{\varphi}_{ii}(k) = \hat{\varphi}_{ii}(1),\ if\ |\hat{\varphi}_{ii}(k)| < b_2\ or\ |\hat{\varphi}_{ii}(k)| > ab_2\ \ or\ sign\big(\hat{\varphi}_{ii}(k)\big) \neq sign\big(\hat{\varphi}_{ii}(1)\big), i = 1, \dots, m \tag{2.94}$$

$$\hat{\varphi}_{ij}(k) = \hat{\varphi}_{ij}(1), \qquad if\ \big|\hat{\varphi}_{ij}(k)\big| < b_1\ \ or\ sign\left(\hat{\varphi}_{ij}(k)\right) \neq sign\left(\hat{\varphi}_{ij}(1)\right), i, j = 1, \dots, m, i \neq j \tag{2.95}$$

where the $\hat{\varphi}_{ii}(1)$ denotes the initial value of $\hat{\varphi}_{ij}(k), i = 1, \dots, m, j = 1, \dots, m$, and the sign of parameter is supposed to stay unchanged for all k.

Remark 2.8

In the case of multi-input single-output (MISO) system, where $u(k) \in R^m$ and $y(k) \in R$, using CFDL data model of the general system $\Delta y(k+1) = \varphi_c^T(k)\Delta u(k)$, the CFDL-based MFAC algorithm is obtained as:

$$u(k) = u(k-1) + \frac{\rho\varphi_c^T(k)\big(y^*(k+1) - y(k)\big)}{\lambda + \|\varphi_c(k)\|^2} \tag{2.96}$$

$$\hat{\varphi}_c(k) = \hat{\varphi}_c(k-1) + \frac{\eta\Delta u(k-1)\big(\Delta y(k) - \hat{\varphi}_c^T(k-1)\Delta u(k-1)\big)}{\mu + \|\Delta u(k-1)\|^2} \tag{2.97}$$

$$\hat{\varphi}_i(k) = \hat{\varphi}_i(1), \qquad if\ |\hat{\varphi}_i(k)| < b_2\ \ or\ sign\big(\hat{\varphi}_i(k)\big) \neq sign\big(\hat{\varphi}_i(1)\big), i = 1, \dots, m \tag{2.98}$$

where $\hat{\varphi}_c(k) = [\hat{\varphi}_1(k), \hat{\varphi}_2(k), \dots, \hat{\varphi}_m(k)]^T \in R^m$ is the estimation of PG in CFDL data model.

2.2.2.1.3. Stability Analysis

The stability analysis will be done using the following lemma.

Lemma 2.2 [92]**:** Let $A = (a_{ij}) \in C^{n\times n}$. For each $1 \le i \le n$, the Gerschgorin disk is defined as $D_i = \{z||z - a_{ii}| \le \sum_{j=1,j\ne i}^{n}|a_{ij}|\}, z \in C$, and the Gerschgorin domain is defined as a union of all the Gerschgorin disks $D_A = \cup_{i=1}^{n} D_i$. All eigenvalues of matrix A lie in the Gerschgorin domain D_A.

By satisfying the Assumption 2.14 by system (2.88), if the system (2.88) is controlled by the CFDL-based MFAC approach (2.91)-(2.95) for a regulation problem, $y^*(k+1) = y^* = constant.$, then there exists a fixed $\lambda_{min} > 0$, so that two characteristics keep for any $\lambda > \lambda_{min}$ as:

a. The system output tracking error converges uniformly and $\lim_{k\to\infty}\|y^* - y(k+1)\|_v = 0$.

b. The $\{y(k)\}$ and $\{u(k)\}$ are bounded and the closed-loop system is BIBO stable.

Proof

This proof has two steps. The first step includes the proof of the boundness of PG estimation and second step includes the proof of the tracking error convergence.

Step 1: Let $\hat{\varphi}_c(k) = [\hat{\varphi}_1^T(k), \dots, \hat{\varphi}_m^T(k)]^T$, $\hat{\varphi}_i(k) = [\hat{\varphi}_{i1}(k), \dots, \hat{\varphi}_{im}(k)]$, $i = 1, \dots, m$.

The estimation algorithm (2.93) can be rewritten as

$$\hat{\varphi}_i(k) = \hat{\varphi}_i(k-1) + \frac{\eta\left(\Delta y_i(k) - \hat{\varphi}_i(k-1)\Delta u(k-1)\right)\Delta u^T(k-1)}{\mu + \|\Delta u(k-1)\|^2} \tag{2.99}$$

where $\Delta y_i(k) = \varphi_i(k-1)\Delta u(k-1)$, $i = 1, \dots, m$.

Let $\tilde{\varphi}_i(k) = \hat{\varphi}_i(k) - \varphi_i(k)$. Deducting $\varphi_i(k)$ from both sides of equation (2.99) brings

$$\tilde{\varphi}_i(k) = \tilde{\varphi}_i(k-1) + \varphi_i(k-1) - \varphi_i(k) - \frac{\eta\tilde{\varphi}_i(k-1)\Delta u(k-1)\Delta u^T(k-1)}{\mu + \|\Delta u(k-1)\|^2} \tag{2.100}$$

In addition, it is previously proved that $\|\varphi_c(k)\|$ is bounded as $\|\varphi_c(k)\| \le b$, thus $\|\varphi_i(k-1) - \varphi_i(k)\| \le 2b$. Therefore, taking norm on both sides of (2.100) brings

$$\begin{aligned}\|\tilde{\varphi}_i(k)\| &\le \left\|\tilde{\varphi}_i(k-1)\left(I - \frac{\eta\Delta u(k-1)\Delta u^T(k-1)}{\mu + \|\Delta u(k-1)\|^2}\right)\right\| + \|\varphi_i(k-1) - \varphi_i(k)\| \\ &\le \left\|\tilde{\varphi}_i(k-1)\left(I - \frac{\eta\Delta u(k-1)\Delta u^T(k-1)}{\mu + \|\Delta u(k-1)\|^2}\right)\right\| + 2b\end{aligned} \tag{2.101}$$

Squaring the first part on the right side of (2.101) brings

$$\begin{aligned}&\left\|\tilde{\varphi}_i(k-1)\left(I - \frac{\eta\Delta u(k-1)\Delta u^T(k-1)}{\mu + \|\Delta u(k-1)\|^2}\right)\right\|^2 \\ &\qquad = \|\tilde{\varphi}_i(k-1)\|^2 + \left(-2 + \frac{\eta\|\Delta u(k-1)\|^2}{\mu + \|\Delta u(k-1)\|^2}\right)\frac{\eta\|\tilde{\varphi}_i(k-1)\Delta u(k-1)\|^2}{\mu + \|\Delta u(k-1)\|^2}\end{aligned} \tag{2.102}$$

As $\eta \in (0,2]$ and $\mu > 0$, the following equation comes

$$-2 + \frac{\eta\|\Delta u(k-1)\|^2}{\mu + \|\Delta u(k-1)\|^2} < 0 \tag{2.103}$$

Collecting the (2.102) and (2.103) shows that there exists a constant $0 < d_1 < 1$, such that

$$\left\|\tilde{\varphi}_i(k-1)\left(I - \frac{\eta\Delta u(k-1)\Delta u^T(k-1)}{\mu + \|\Delta u(k-1)\|^2}\right)\right\| \le d_1\|\tilde{\varphi}_i(k-1)\| \tag{2.104}$$

Putting (2.104) into (2.101) brings

$$\|\tilde{\varphi}_i(k)\| \le d_1\|\tilde{\varphi}_i(k-1)\| + 2b \le d_1^2\|\tilde{\varphi}_i(k-2)\| + 2d_1 b + 2b \le \cdots \le d_1^{k-1}\|\tilde{\varphi}_i(1)\| + \frac{2b(1-d_1^{k-1})}{1-d_1} \tag{2.105}$$

Equation (2.105) indicates that $\tilde{\varphi}_i(k)$ is bounded. As $\varphi_i(k)$ is bounded, $\tilde{\varphi}_i(k)$ and $\tilde{\varphi}_c(k)$ are also bounded.

Step 2: describe the tracking error as

$$e(k) = y^* - y(k) \tag{2.106}$$

Putting the CFDL data model (2.89) and the controller algorithm (2.91) into (2.106) leads to

$$e(k+1) = e(k) - \varphi_c(k)\Delta u(k) = \left[I - \frac{\rho\varphi_c(k)\hat{\varphi}_c^T(k)}{\lambda + \|\hat{\varphi}_c(k)\|^2}\right] e(k) \tag{2.107}$$

From lemma 2.2,

$$D_j = \left\{ z \middle| \left| z - \left| 1 - \frac{\rho\sum_{i=1}^m \varphi_{ji}(k)\hat{\varphi}_{ji}(k)}{\lambda + \|\hat{\varphi}_c(k)\|^2} \right| \right| \le \sum_{l=1, l\ne j}^m \left| \frac{\rho\sum_{i=1}^m \varphi_{ji}(k)\hat{\varphi}_{li}(k)}{\lambda + \|\hat{\varphi}_c(k)\|^2} \right| \right\} \tag{2.108}$$

where z is the eigenvalue for the $I - \frac{\rho\varphi_c(k)\hat{\varphi}_c^T(k)}{\lambda + \|\hat{\varphi}_c(k)\|^2}$ matrix and D_j is the Gerschgorin disk with $j = 1, \dots, m$.

By using the triangle inequality, the (2.108) can be transformed into

$$D_j = \left\{ z \middle| |z| \le \left| 1 - \frac{\rho\sum_{i=1}^m \varphi_{ji}(k)\hat{\varphi}_{ji}(k)}{\lambda + \|\hat{\varphi}_c(k)\|^2} \right| + \sum_{l=1, l\ne j}^m \left| \frac{\rho\sum_{i=1}^m \varphi_{ji}(k)\hat{\varphi}_{li}(k)}{\lambda + \|\hat{\varphi}_c(k)\|^2} \right| \right\} \tag{2.109}$$

Considering the resetting condition (2.94)-(2.95) and the Assumption 2.14, the following equations comes as

$$1 - \frac{\rho\sum_{i=1}^m |\varphi_{ji}(k)||\hat{\varphi}_{ji}(k)|}{\lambda + \|\hat{\varphi}_c(k)\|^2} \le 1 - \frac{\rho|\varphi_{jj}(k)||\hat{\varphi}_{jj}(k)|}{\lambda + \|\hat{\varphi}_c(k)\|^2} \le 1 - \frac{\rho b_2^2}{\lambda + \|\hat{\varphi}_c(k)\|^2} \tag{2.110}$$

$$\begin{aligned}
\sum_{l=1, l\ne j}^m \left| \frac{\rho\sum_{i=1}^m \varphi_{ji}(k)\hat{\varphi}_{li}(k)}{\lambda + \|\hat{\varphi}_c(k)\|^2} \right| &\le \rho \sum_{l=1, l\ne j}^m \frac{\sum_{i=1}^m |\varphi_{ji}(k)||\hat{\varphi}_{li}(k)|}{\lambda + \|\hat{\varphi}_c(k)\|^2} \\
&= \rho\frac{\sum_{l=1, l\ne j}^m |\varphi_{jj}(k)||\hat{\varphi}_{lj}(k)|}{\lambda + \|\hat{\varphi}_c(k)\|^2} + \rho \sum_{l=1, l\ne j}^m \frac{\sum_{i=1, i\ne j}^m |\varphi_{ji}(k)||\hat{\varphi}_{li}(k)|}{\lambda + \|\hat{\varphi}_c(k)\|^2} \\
&= \rho\frac{\sum_{l=1, l\ne j}^m |\varphi_{jj}(k)||\hat{\varphi}_{lj}(k)|}{\lambda + \|\hat{\varphi}_c(k)\|^2} + \rho\frac{\sum_{l=1, l\ne j}^m |\varphi_{jl}(k)||\hat{\varphi}_{ll}(k)|}{\lambda + \|\hat{\varphi}_c(k)\|^2} \\
&+ \rho \sum_{l=1, l\ne j}^m \frac{\sum_{i=1, i\ne j}^m |\varphi_{ji}(k)||\hat{\varphi}_{li}(k)|}{\lambda + \|\hat{\varphi}_c(k)\|^2} \le \rho\frac{2ab_1b_2(m-1) + b_1^2(m-1)(m-2)}{\lambda + \|\hat{\varphi}_c(k)\|^2}
\end{aligned} \tag{2.111}$$

And we have from Assumption 2.14 that $b_2 > b_1(2a+1)(m-1)$.

Summing (2.110) and (2.111) brings

$$1-\frac{\rho\sum_{i=1}^{m}\left|\varphi_{ji}(k)\right|\left|\hat{\varphi}_{ji}(k)\right|}{\lambda+\|\hat{\varphi}_c(k)\|^2}+\sum_{b=1,b\neq j}^{m}\left|\frac{\rho\sum_{i=1}^{m}\varphi_{ji}(k)\hat{\varphi}_{bi}(k)}{\lambda+\|\hat{\varphi}_c(k)\|^2}\right|$$

$$\leq 1-\rho\frac{b_2^2-2ab_1b_2(m-1)-b_1^2(m-1)(m-2)}{\lambda+\|\hat{\varphi}_c(k)\|^2}$$

$$=1-\rho\frac{b_2\big(b_2-2ab_1(m-1)\big)-b_1^2(m-1)(m-2)}{\lambda+\|\hat{\varphi}_c(k)\|^2}$$

$$<1-\rho\frac{b_1b_2(m-1)-b_1^2(m-1)(m-2)}{\lambda+\|\hat{\varphi}_c(k)\|^2}<1-\rho\frac{b_1b_2(m-1)-b_1^2(m-1)(m-1)}{\lambda+\|\hat{\varphi}_c(k)\|^2}$$

$$=1-\rho\frac{b_1(m-1)\big(b_2-b_1(m-1)\big)}{\lambda+\|\hat{\varphi}_c(k)\|^2}<1-\rho\frac{2ab_1^2(m-1)^2}{\lambda+\|\hat{\varphi}_c(k)\|^2} \tag{2.112}$$

From resetting law (2.94)-(2.95) and Assumption 2.14, $\varphi_{ji}(k)\hat{\varphi}_{ji}(k)>0, i=1,\dots,m, j=1,\dots,m$. Therefore, there exists a constant $\lambda_{min}>0$ in which that the below equation holds for $\lambda>\lambda_{min}$.

$$\frac{\sum_{i=1}^{m}\varphi_{ji}(k)\hat{\varphi}_{ji}(k)}{\lambda+\|\hat{\varphi}_c(k)\|^2}=\frac{\sum_{i=1}^{m}\left|\varphi_{ji}(k)\right|\left|\hat{\varphi}_{ji}(k)\right|}{\lambda+\|\hat{\varphi}_c(k)\|^2}\leq\frac{ab_2^2+b_1^2(m-1)}{\lambda+\|\hat{\varphi}_c(k)\|^2}<\frac{a^2b_2^2+b_1^2(m-1)}{\lambda_{min}+\|\hat{\varphi}_c(k)\|^2}<1 \tag{2.113}$$

Precisely selecting $\rho\in(0,1]$ and $\lambda>\lambda_{min}$ such that

$$\left|1-\frac{\rho\sum_{i=1}^{m}\varphi_{ji}(k)\hat{\varphi}_{ji}(k)}{\lambda+\|\hat{\varphi}_c(k)\|^2}\right|=1-\frac{\rho\sum_{i=1}^{m}\left\|\hat{\varphi}_{ji}(k)\right\|}{\lambda+\|\hat{\varphi}_c(k)\|^2} \tag{2.114}$$

Clearly, following equation is valid for $\lambda>\lambda_{min}$:

$$0<M_1\leq\frac{2ab_1^2(m-1)^2}{\lambda+\|\hat{\varphi}_c(k)\|^2}<\frac{b_2^2}{\lambda+\|\hat{\varphi}_c(k)\|^2}\leq\frac{ab_2^2+b_1^2(m-1)}{\lambda+\|\hat{\varphi}_c(k)\|^2}<\frac{ab_2^2+b_1^2(m-1)}{\lambda_{min}+\|\hat{\varphi}_c(k)\|^2}<1 \tag{2.115}$$

From (2.112), (2.114) and (2.115) we have

$$\left|1-\frac{\rho\sum_{i=1}^{m}\varphi_{ji}(k)\hat{\varphi}_{ji}(k)}{\lambda+\|\hat{\varphi}_c(k)\|^2}\right|+\sum_{l=1,l\neq j}^{m}\left|\frac{\rho\sum_{i=1}^{m}\varphi_{ji}(k)\hat{\varphi}_{li}(k)}{\lambda+\|\hat{\varphi}_c(k)\|^2}\right|<1-\rho M_1<1 \tag{2.116}$$

According to (2.109) and (2.116) we reach to

$$s\left(I-\frac{\rho\varphi_c(k)\hat{\varphi}_c^T(k)}{\lambda+\|\hat{\varphi}_c(k)\|^2}\right)<1-\rho M_1 \tag{2.117}$$

where $s(A)=\underset{i\in\{1,2,\dots,m\}}{max}|z_i|$, is the spectral radius of matrix A. And the z_i stands as the eigenvalues for matrix A.

According to the deduction on spectral radius in [93], it is concluded that there exists an optional small positive constant ε_1 in which that

$$\left\|I-\frac{\rho\varphi_c(k)\hat{\varphi}_c^T(k)}{\lambda+\|\hat{\varphi}_c(k)\|^2}\right\|_v<s\left(I-\frac{\rho\varphi_c(k)\hat{\varphi}_c^T(k)}{\lambda+\|\hat{\varphi}_c(k)\|^2}\right)+\varepsilon_1\leq 1-\rho M_1+\varepsilon_1<1 \tag{2.118}$$

where $\|A\|_v$ is the consistent norm of the matrix A.

Take $d_2 = 1 - \rho M_1 + \varepsilon_1$. Taking norm on both sides of (2.107) brings

$$\|e(k+1)\|_v \le \left\| I - \frac{\rho \varphi_c(k) \hat{\varphi}_c^T(k)}{\lambda + \|\hat{\varphi}_c(k)\|^2} \right\|_v \|e(k)\|_v \le d_2 \|e(k)\|_v \le \cdots \le d_2^k \|e(1)\|_v \tag{2.119}$$

By this way, the conclusion (a) can be obtained directly from (2.119).

As y^* is bounded and $e(k)$ is also bounded, thus, the $y(k)$ is bounded too.

As $\hat{\varphi}_c(k)$ is bounded, there exists a constant $M_2 > 0$, such that

$$\left\| \frac{\rho \hat{\varphi}_c^T(k)}{\lambda + \|\hat{\varphi}_c(k)\|^2} \right\|_v \le M_2 \tag{2.120}$$

Using (2.91), (2.119) and (2.120) leads to

$$\begin{aligned} \|u(k)\|_v &\le \|u(k) - u(k-1)\|_v + \|u(k-1)\|_v \\ &\le \|u(k) - u(k-1)\|_v + \|u(k-1) - u(k-2)\|_v + \|u(k-2)\|_v \\ &\le \|\Delta u(k)\|_v + \|\Delta u(k-1)\|_v + \cdots + \|\Delta u(1)\|_v + \|u(0)\|_v \\ &\le M_2(\|e(k)\| + \|e(k-1)\| + \cdots + \|e(2)\| + \|e(1)\|) + \|u(0)\|_v \\ &\le M_2(d_2^{k-1}\|e(1)\| + d_2^{k-2}\|e(1)\| + \cdots + d_2\|e(1)\| + \|e(1)\|) + \|u(0)\|_v \\ &< M_2 \frac{1}{1-d_2}\|e(1)\| + \|u(0)\|_v \end{aligned} \tag{2.121}$$

Therefore, the conclusion (b) is proved.

2.2.2.1.4. Simulation Results

In order to verify the effectiveness of CFDL-based MFAC scheme, a numerical simulation study is carried out for a MIMO discrete-time nonlinear system. In this example, the model dynamics is not included in CFDL-based MFAC algorithm, and the controller have only used the I/O data of the controlled plant.

Example 2.4

Consider the following MIMO discrete-time nonlinear system:

$$\begin{cases} x_{11}(k+1) = \dfrac{x_{11}^2(k)}{1 + x_{11}^2(k)} + 0.3x_{12}(k) \\ x_{12}(k+1) = \dfrac{x_{11}^2(k)}{1 + x_{12}^2(k) + x_{21}^2(k) + x_{22}^2(k)} + a(k)u_1(k) \\ x_{21}(k+1) = \dfrac{x_{21}^2(k)}{1 + x_{21}^2(k)} + 0.2x_{22}(k) \\ x_{22}(k+1) = \dfrac{x_{21}^2(k)}{1 + x_{11}^2(k) + x_{12}^2(k) + x_{22}^2(k)} + b(k)u_2(k) \\ y_1(k+1) = x_{11}(k+1) \\ y_2(k+1) = x_{21}(k+1) \end{cases}$$

where

$$a(k) = 1 + 0.1\sin(2\pi k/1500)$$
$$b(k) = 1 + 0.1\cos(2\pi k/1500)$$

The initial condition of the system is

$$u_1(i) = u_2(i) = 0.5$$

$$x_{11}(i) = x_{21}(j) = 0.5,\ x_{12}(i) = x_{22}(j) = 0$$

and $y_{1,2}(k)$ and $u_{1,2}(k)$ are the system output and control input, respectively.

The desired output signal $y^*(k+1)$ is given as

$$\begin{cases} y_1^*(k) = 0.5 + 0.25\cos(0.25\pi k/100) + 0.25\sin(0.5\pi k/100) \\ y_2^*(k) = 0.5 + 0.25\sin(0.25\pi k/100) + 0.25\sin(0.5\pi k/100) \end{cases}$$

Using CFDL approach, the abovementioned nonlinear system is transformed into the following CFDL data model:

$$\begin{bmatrix} y_1(k+1) \\ y_2(k+1) \end{bmatrix} = \begin{bmatrix} \varphi_{11}(k) & \varphi_{12}(k) \\ \varphi_{21}(k) & \varphi_{22}(k) \end{bmatrix} \begin{bmatrix} \Delta u_1(k) \\ \Delta u_1(k) \end{bmatrix}$$

Where, only the variation of control input at the current time is included in this data model and previous variation of control input and system output are not considered.

The control algorithm, including the estimation of $\varphi_i(k)$ and controller design, is performed by selecting the proper controller parameters, as $\rho = 0.6$, $\mu = 1.5$, $\lambda = 2$ and $\eta = 1.2$. The initial condition for $\hat{\varphi}_{p,L}(k)$ is selected as $\hat{\varphi}_{p,L}(k) = \begin{bmatrix} 0.7 & 0 \\ 0 & 0.7 \end{bmatrix}$. The simulation results are shown in Figure 2.6. From the simulation results, the CFDL-based MFAC brings a satisfactory control performance for mentioned MIMO system.

2.2.2.2. PFDL Data Model Based MFAC

In section 2.1.2.2, it is proved that the MIMO nonlinear system (2.88), satisfying Assumptions 2.9 and 2.10, can be transformed into the PFDL data model as

$$\Delta y(k+1) = \varphi_{p,L}(k)\Delta U_L(k) \tag{2.122}$$

where $\varphi_{p,L}(k) = [\varphi_1(k)\ \dots\ \varphi_L(k)] \in R^{m\times mL}$ is the unknown bounded PPJM matrix and:

$$\varphi_i(k) = \begin{bmatrix} \varphi_{11i}(k) & \varphi_{12i}(k) & \varphi_{13i}(k) & \cdots & \varphi_{1mi}(k) \\ \varphi_{21i}(k) & \varphi_{22i}(k) & \varphi_{23i}(k) & \cdots & \varphi_{2mi}(k) \\ \varphi_{31i}(k) & \varphi_{32i}(k) & \varphi_{33i}(k) & \cdots & \varphi_{3mi}(k) \\ \vdots & \vdots & \vdots & \vdots & \vdots \\ \varphi_{m1i}(k) & \varphi_{m2i}(k) & \varphi_{m3i}(k) & \cdots & \varphi_{mmi}(k) \end{bmatrix}_{m\times m} \in R^{m\times m}, i = 1, \dots, L$$

and $\Delta U_L(k) = [\Delta u^T(k), \dots, \Delta u^T(k-L+1)\ ]^T$.

Assumption 2.15: The $\varphi_1(k)$ of the PPJM matrix $\varphi_{p,L}(k)$ is a diagonally dominant matrix in which that, $|\varphi_{ij1}(k)| \le b_1$, $b_2 \le |\varphi_{ij1}(k)| \le ab_2$, $a \ge 1$, and $b_2 > b_1(2a+1)(m-1), i = 1, \dots, m, j = 1, \dots, m, i \ne j$, and the sign of all the arrays of $\varphi_1(k)$ stay unchanged.

2.2.2.2.1. Controller Algorithm

Following cost function of the control input is used for controller design.

$$J(u(k)) = \|y^*(k+1) - y(k+1)\|^2 + \lambda\|u(k) - u(k-1)\|^2 \tag{2.123}$$

where the $\lambda > 0$ is a weight factor which is used to limit the changes of control input, and the $y^*(k+1)$ is the reference trajectory of system output.

Putting the PFDL data model (2.122) into cost function (2.123) and differentiating according to control input $u(k)$ and setting to be zero brings the controller algorithm as follows.

$$u(k) = u(k-1) + \frac{\varphi_1^T(k)\left(\rho_1\left(y^*(k+1) - y(k)\right) - \sum_{i=2}^{L}\varphi_i(k)\rho_i\Delta u(k-i+1)\right)}{\lambda + \|\varphi_1(k)\|^2} \tag{2.124}$$

where the $\rho \in (0, 1]$ is the step factor.

2.2.2.2.2. PPJM Estimation Algorithm

The following cost function of PPJM $\varphi_{p,L}(k)$estimation for MIMO systems is used for estimation of the PPJM matrix.

$$J\left(\varphi_{p,L}(k)\right) = \left\|y(k) - y(k-1) - \varphi_{p,L}(k)\Delta U_L(k-1)\right\|^2 + \mu\left\|\varphi_{p,L}(k) - \hat{\varphi}_{p,L}(k)\right\|^2 \tag{2.125}$$

where the $\mu > 0$ is a weight factor which is used to limit the changes of PPJM estimation.

Minimizing cost function (2.125) brings the following estimation algorithm.

$$\hat{\varphi}_{p,L}(k) = \hat{\varphi}_{p,L}(k-1) + \frac{\eta\left(\Delta y(k) - \hat{\varphi}_{p,L}(k-1)\Delta U_L(k-1)\right)\Delta {U_L}^T(k-1)}{\mu + \|\Delta U_L(k-1)\|^2} \tag{2.126}$$

where the $\eta \in (0, 2]$ is the step factor, and $\hat{\varphi}_{p,L}(k) = [\hat{\varphi}_1(k)\ \hat{\varphi}_2(k)\ \dots\ \hat{\varphi}_L(k)] \in R^{m\times mL}$ is the estimation of $\varphi_{p,L}(k)$, that

$$\hat{\varphi}_i(k) = \begin{bmatrix} \hat{\varphi}_{11i}(k) & \hat{\varphi}_{12i}(k) & \hat{\varphi}_{13i}(k) & \cdots & \hat{\varphi}_{1mi}(k) \\ \hat{\varphi}_{21i}(k) & \hat{\varphi}_{22i}(k) & \hat{\varphi}_{23i}(k) & \cdots & \hat{\varphi}_{2mi}(k) \\ \hat{\varphi}_{31i}(k) & \hat{\varphi}_{32i}(k) & \hat{\varphi}_{33i}(k) & \cdots & \hat{\varphi}_{3mi}(k) \\ \vdots & \vdots & \vdots & \vdots & \vdots \\ \hat{\varphi}_{m1i}(k) & \hat{\varphi}_{m2i}(k) & \hat{\varphi}_{m3i}(k) & \cdots & \hat{\varphi}_{mmi}(k) \end{bmatrix}_{m\times m} \in R^{m\times m}, i = 1, \dots, L.$$

In addition, a reset structure is used for estimation law (2.123) to empower this estimation algorithm with a powerful capability to track the time-varying parameter as below.

$$\hat{\varphi}_{ii1}(k) = \hat{\varphi}_{ii1}(1),\ if\ |\hat{\varphi}_{ii1}(k)| < b_2\ or\ |\hat{\varphi}_{ii1}(k)| > ab_2\ \ or\ sign\left(\hat{\varphi}_{ii1}(k)\right) \neq sign\left(\hat{\varphi}_{ii1}(1)\right), i = 1, \dots, m \tag{2.127}$$

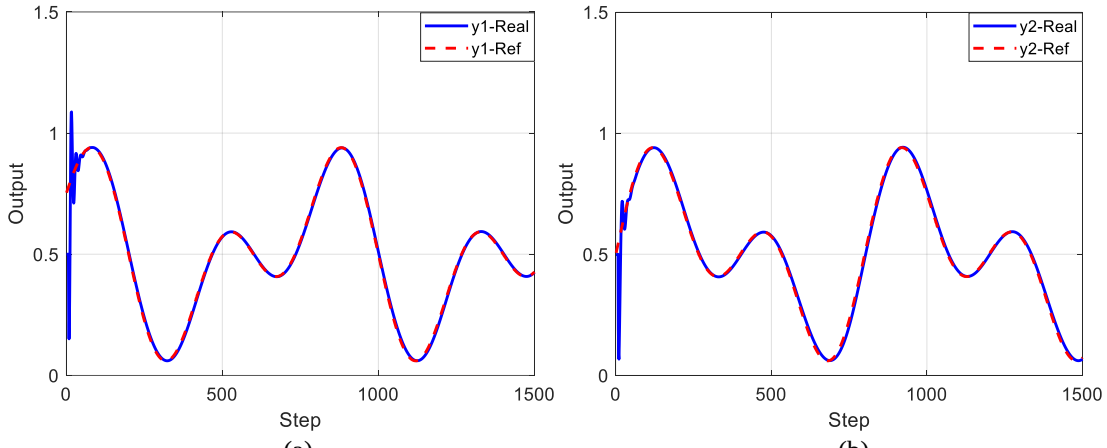

(a) (b)

Figure 2.6. Simulation results in Example 2.4 using CFDL-based MFAC for a) system output y_1, b) system output y_2.

$$\hat{\varphi}_{ij1}(k) = \hat{\varphi}_{ij1}(1), \qquad if\ |\hat{\varphi}_{ij1}(k)| < b_1\ \ or\ sign\left(\hat{\varphi}_{ij1}(k)\right) \neq sign\left(\hat{\varphi}_{ij1}(1)\right), i,j = 1,\dots,m, i \neq j \tag{2.128}$$

where the $\hat{\varphi}_{ij1}(1)$ denotes the initial value of $\hat{\varphi}_{ij1}(k)$, $i = 1,\dots,m, j = 1,\dots,m$, and the sign of parameter is supposed to stay unchanged for all k.

Remark 2.9

In the case of multi-input single-output (MISO) system, where $u(k) \in R^m$ and $y(k) \in R$, using PFDL data model of the general system $\Delta y(k+1) = \varphi_{p,L}^T(k)\Delta U_L(k)$, the PFDL-based MFAC algorithm is obtained as:

$$u(k) = u(k-1) + \frac{\varphi_1^T(k)\left(\rho_1\left(y^*(k+1) - y(k)\right) - \sum_{i=2}^{L}\varphi_i^T(k)\,\rho_i\Delta u(k-i+1)\right)}{\lambda + \|\varphi_1(k)\|^2} \tag{2.129}$$

$$\hat{\varphi}_{p,L}(k) = \hat{\varphi}_{p,L}(k-1) + \frac{\eta\left(\Delta y(k) - \hat{\varphi}_{p,L}^T(k-1)\Delta U_L(k-1)\right)\Delta U_L(k-1)}{\mu + \|\Delta U_L(k-1)\|^2} \tag{2.130}$$

$$\hat{\varphi}_{i1}(k) = \hat{\varphi}_{i1}(1), \qquad if\ |\hat{\varphi}_{i1}(k)| < b_2\ \ or\ sign\left(\hat{\varphi}_{i1}(k)\right) \neq sign\left(\hat{\varphi}_{i1}(1)\right), i = 1,\dots,m \tag{2.131}$$

where $\hat{\varphi}_{p,L}(k) = [\hat{\varphi}_1^T(k), \hat{\varphi}_2^T(k), \dots, \hat{\varphi}_L^T(k)]^T \in R^{mL}$ is the estimation of PPG in PFDL data model.

2.2.2.2.3. Stability Analysis

If the nonlinear system (2.88), satisfying Assumptions 2.9 and 2.10 is controlled by PFDL-based MFAC algorithm (2.124)-(2.128), for a regulation problem $y^*(k+1) = y^*$, then there exists a constant $\lambda_{min} > 0$, so that two characteristics keep for any $\lambda > \lambda_{min}$ as:

a. The tracking error sequence is convergent, such that, $\lim_{k\to\infty}\|y(k+1) - y^*\|_v = 0$.

b. The $\{y(k)\}$ and $\{u(k)\}$ are bounded and the closed-loop system is BIBO stable.

Proof

Similar to the previous section, take the tracking error as

$$e(k) = y^* - y(k) \tag{2.132}$$

Let

$$A_1(k) = \begin{bmatrix} -\frac{\rho_2\hat{\varphi}_1^T(k)\hat{\varphi}_2(k)}{\lambda + \|\hat{\varphi}_1(k)\|^2} & \cdots & \cdots & -\frac{\rho_L\hat{\varphi}_1^T(k)\hat{\varphi}_L(k)}{\lambda + \|\hat{\varphi}_1(k)\|^2} & 0 \\ I & \cdots & \cdots & 0 & 0 \\ \vdots & \vdots & \vdots & \cdots & \vdots \\ \vdots & \vdots & \vdots & \vdots & \vdots \\ 0 & \cdots & \cdots & I & 0 \end{bmatrix}_{mL\times mL}$$

$$C_1(k) = \begin{bmatrix} \frac{\hat{\varphi}_1(k)}{\lambda + \|\hat{\varphi}_1(k)\|^2} & 0 \\ 0 & 0 \end{bmatrix}, \qquad E(k) = \begin{bmatrix} e(k) \\ 0_{mL-m} \end{bmatrix} \in R^{mL}$$

Thus, the controller algorithm (2.124) is edited as

$$\Delta U_L(k) = A_1(k)\Delta U_L(k-1) + \rho_1 C_1(k)E(k) \tag{2.133}$$

Putting PFDL data model (2.122) and (2.133) into the (2.132) brings

$$e(k+1) = y^* - y(k) - \big(y(k+1) - y(k)\big) = e(k) - \varphi_{p,L}(k)\Delta U_L(k)$$
$$= \left(I - \frac{\rho_1 \varphi_1(k)\hat{\varphi}_1^T(k)}{\lambda + \|\hat{\varphi}_1(k)\|^2}\right) e(k) - \varphi_{p,L}(k)A_1(k)\Delta U_L(k-1) \tag{2.134}$$

Let

$A_2(k) = \begin{bmatrix} I - \frac{\rho_1 \varphi_1(k)\hat{\varphi}_1(k)}{\lambda + \|\hat{\varphi}_1(k)\|^2} & 0 \\ 0 & 0 \end{bmatrix}_{mL \times mL}$, and $C_2(k) = \begin{bmatrix} \varphi_{p,L}(k) \\ 0 \end{bmatrix}_{mL \times mL}$

Equation (2.134) can be transformed into

$$E(k+1) = E(k) - C_2(k)\Delta U_L(k) = A_2(k)E(k) - C_2(k)A_1(k)\Delta U_L(k-1) \tag{2.135}$$

As $\varphi_{p,L}(k)$ and $\hat{\varphi}_{p,L}(k)$ are bounded, there exists four positive constants M_1, M_2, M_3 and M_4 and $\lambda_{min} > 0$ in which the following six inequalities hold for any $\lambda > \lambda_{min}$:

$$0 < M_1 \leq \frac{2ab_1^2(m-1)^2}{\lambda + \|\hat{\varphi}_1(k)\|^2} < \frac{ab_2^2 + b_1^2(m-1)^2}{\lambda_{min} + \|\hat{\varphi}_1(k)\|^2} < 1 \tag{2.136}$$

$$s\big(A_1(k)\big) \leq 1 \tag{2.137}$$

$$\|C_1(k)\|_v \leq M_3 < 1 \tag{2.138}$$

$$\|C_2(k)\|_v \leq M_4 \tag{2.139}$$

$$M_1 + M_3 M_4 < 1 \tag{2.140}$$

$$s\big(A_2(k)\big) < 1 - \rho_1 M_1 < 1 \tag{2.141}$$

where $s(A)$ is the spectral radius of matrix A.

The specific equation of $A_1(k)$ is

$$z^m \det\left(z^{L-1}I + \sum_{i=2}^{L} z^{L-i} \frac{\rho_i \hat{\varphi}_1^T(k)\hat{\varphi}_i(k)}{\lambda + \|\hat{\varphi}_1(k)\|^2}\right) = 0 \tag{2.142}$$

As $\varphi_{p,L}(k)$ and $\hat{\varphi}_{p,L}(k)$ are bounded and $s\big(A_1(k)\big) \leq 1$, there exists a positive constant M_2, that

$$\frac{|c(z_i)|}{\lambda + \|\hat{\varphi}_1(k)\|^2} \leq M_2, \forall z_1, \dots, z_{mL} \tag{2.143}$$

where z_i is the eigenvalue of the $A_1(k)$ that $i = 1,2, \dots, mL$.

Select max ρ_i such that the following equation holds for any z_i, $i = 1,2, \dots, mL$,

$$|z_i|^{(L-1)m} \leq \max \rho_i \, M_2 < 1 \tag{2.144}$$

Thus, we have

$$s\big(A_1(k)\big) \leq (\max \rho_i \, M_2)^{\frac{1}{(L-1)m}} < 1 \tag{2.145}$$

The conclusion on spectral radius means that there exists an optional small positive constant ε that

$$\|A\|_v < s(A) + \varepsilon \tag{2.146}$$

From (2.141) and (2.145) we have

$$\|A_1(k)\|_v < s\big(A_1(k)\big) + \varepsilon \leq (\max \rho_i \, M_2)^{\frac{1}{(L-1)m}} + \varepsilon < 1 \tag{2.147}$$

and

$$\|A_2(k)\|_v < s\big(A_2(k)\big) + \varepsilon \leq 1 - \rho_1 M_1 + \varepsilon < 1 \tag{2.148}$$

Let

$$d_1 = (\max(\rho_i)\, M_2)^{\frac{1}{(L-1)m}} + \varepsilon \tag{2.149}$$

$$d_2 = 1 - \rho_1 M_1 + \varepsilon \tag{2.150}$$

Taking norm on both sides of (2.133) and using the $\|\Delta U_L(0)\|_v = 0$, brings

$$\begin{aligned}\|\Delta U_L(k)\|_v &= \|A_1(k)\|_v \|\Delta U_L(k-1)\|_v + \rho_1 \|C_1(k)\|_v \|E(k)\|_v \\ &< d_1 \|\Delta U_L(k-1)\|_v + \rho_1 \|M_3(k)\|_v \|E(k)\|_v < \cdots < \rho_1 M_3 \sum_{i=1}^{k} d_1^{k-i} \|E(i)\|_v\end{aligned} \tag{2.151}$$

Taking norm on both sides of (2.135) brings

$$\begin{aligned}\|E(k+1)\|_v &= \|A_2(k)\|_v \|E(k)\|_v + \|C_2(k)\|_v \|A_1(k)\|_v \|\Delta U_L(k-1)\|_v \\ &< d_2 \|E(k)\|_v + d_1 M_4(k) \|\Delta U_L(k-1)\|_v < \cdots \\ &< d_2^k \|E(1)\|_v + M_4 \sum_{j=1}^{k-1} d_2^{k-1-j} d_1 \|\Delta U_L(j)\|_v\end{aligned} \tag{2.152}$$

Let $d_3 = \rho_1 M_3 M_4$. Putting (2.151) into (2.152) brings

$$\begin{aligned}\|E(k+1)\|_v &< d_2^k \|E(1)\|_v + M_4 \sum_{j=1}^{k-1} d_2^{k-1-j} d_1 \|\Delta U_L(j)\|_v \\ &< d_2^k \|E(1)\|_v + M_4 \sum_{j=1}^{k-1} d_2^{k-1-j} d_1 \left(\rho_1 M_3 \sum_{i=1}^{J} d_1^{J-i} \|E(i)\|_v \right) = d_2^k \|E(1)\|_v \\ &+ d_1 d_3 \sum_{j=1}^{k-1} d_2^{k-1-j} \left(\sum_{i=1}^{j} d_1^{j-i} \|E(i)\|_v \right) = g(k+1)\end{aligned} \tag{2.153}$$

where $g(k+1) = d_2^k \|E(1)\|_v + d_1 d_3 \sum_{j=1}^{k-1} d_2^{k-1-j} \left(\sum_{i=1}^{j} d_1^{j-i} \|E(i)\|_v \right)$.

Clearly, $\|E(k+1)\|_v$ will converge to zero if $g(k+1)$ converges to zero.

Computing the $g(k+2)$ brings

$$\begin{aligned}g(k+2) &= d_2^{k+1} \|E(1)\|_v + d_1 d_3 \sum_{j=1}^{k} d_2^{k-j} \left(\sum_{i=1}^{j} d_1^{j-i} \|E(i)\|_v \right) = d_2 g(k+1) + d_3 d_1^k \|E(1)\|_v \\ &+ d_3 d_1^{k-1} \|E(2)\|_v + \cdots + d_1 d_3 \|E(k)\|_v \\ &< d_2 g(k+1) + d_3 d_1^k \|E(1)\|_v + d_3 d_1^{k-1} \|E(2)\|_v + \cdots + d_1 d_3 g(k) \\ &= d_2 g(k+1) + b(k)\end{aligned} \tag{2.154}$$

where $b(k) = d_3 d_1^k \|E(1)\|_v + d_3 d_1^{k-1} \|E(2)\|_v + \cdots + d_1 d_3 g(k)$.

Using (2.140), we have

$$d_2 = 1 - \rho_1 M_1 + \varepsilon > \rho_1 (M_1 + M_3 M_4) - \rho_1 M_1 + \varepsilon = \rho_1 M_3 M_4 + \varepsilon > d_3$$

Then by rewriting $b(k)$

$$
\begin{aligned}
b(k) &< d_3 d_1^k \|E(1)\|_v + d_3 d_1^{k-1} \|E(2)\|_v + \cdots + d_3 d_1^2 \|E(k-1)\|_v + d_2 d_1 g(k) \\
&< d_3 d_1^k \|E(1)\|_v + d_3 d_1^{k-1} \|E(2)\|_v + \cdots + d_3 d_1^2 \|E(k-1)\|_v \\
&+ d_2 d_1 \left(d_2^{k-1} \|E(1)\|_v + d_1 d_3 \sum_{j=1}^{k-1} d_2^{k-2-j} \left(\sum_{i=1}^{j} d_1^{j-i} \|E(i)\|_v \right) \right) \\
&< d_1 \left(d_2^k \|E(1)\|_v + d_1 d_3 \sum_{j=1}^{k-1} d_2^{k-1-j} \left(\sum_{i=1}^{j} d_1^{j-i} \|E(i)\|_v \right) \right) = d_1 g(k+1)
\end{aligned}
\tag{2.155}
$$

Putting (2.155) into (2.154)

$$
g(k+2) = d_2 g(k+1) + b(k) < (d_2 + d_1) g(k+1) \tag{2.156}
$$

Precisely selection for $\rho_i \in (0,1]$, holds the following equations.

$$
0 < (\max(\rho_i)\, M_2)^{\frac{1}{(L-1)m}} < \rho_1 M_1 < 1
$$

and

$$
0 < 1 - \rho_1 M_1 + (\max(\rho_i)\, M_2)^{\frac{1}{(L-1)m}} < 1 \tag{2.157}
$$

As ε is an optional small positive constant, we have,

$$
d_2 + d_1 = 1 - \rho_1 M_1 + \varepsilon + (\max(\rho_i)\, M_2)^{\frac{1}{(L-1)m}} + \varepsilon < 1 \tag{2.158}
$$

Putting (2.158) into (2.156) brings

$$
\lim_{k\to\infty} g(k+2) < \lim_{k\to\infty} (d_2 + d_1)\, g(k+1) < \cdots < \lim_{k\to\infty} (d_2 + d_1)^{k-1} g(2) = 0 \tag{2.159}
$$

where $g(2) = d_2 \|E(2)\|$.

Therefore, the conclusion (a) is directly obtained from (2.153) and (2.159).

As y^* is a known constant vector and $e(k)$ is a bounded vector, $y(k)$ is also bounded.

From (2.151), (2.153) and (2.159) we have

$$
\begin{aligned}
\|\Delta U_L(k)\|_v &\le \sum_{i=1}^{k} \|\Delta U_L(i)\|_v \le \rho_1 M_3 \sum_{i=1}^{k} \sum_{j=1}^{i} d_1^{i-j} \|E(j)\|_v < \frac{\rho_1 M_3}{1-d_1} (\|E(1)\|_v + \cdots + \|E(k)\|_v) \\
&< \frac{\rho_1 M_3}{1-d_1} \big(\|E(1)\|_v + g(2) + \cdots + g(k) \big) < \frac{\rho_1 M_3}{1-d_1} \left(\|E(1)\|_v + \frac{g(2)}{1-d_1-d_2} \right)
\end{aligned}
\tag{2.160}
$$

Therefore, conclusion (b) is also proved.

2.2.2.2.4. Simulation Results

In order to verify the effectiveness of PFDL-based MFAC scheme, a numerical simulation study is carried out for a MIMO discrete-time nonlinear system. In this example, the model dynamics is not included in PFDL-based MFAC algorithm, and the controller have only used the I/O data of the controlled plant.

Example 2.5

Consider the following MIMO discrete-time nonlinear system:

$$\begin{cases} y_1(k+1) = y1(k) + u_1^2(k) + round(k/50)u_2(k) - \sin(k/100)\,u_1(k-1) + u_2^2(k) \\ y_2(k+1) = 0.7\big(y1(k-1) + u_1^2(k) + round(k/50)u_2(k) - \sin(k/100)\,u_1(k-1) + u_2^2(k)\big) \end{cases}$$

where the initial condition of the system is

$$u_1(i) = u_2(i) = 0$$

$$y_1(i) = y_2(j) = 0,\ x_{12}(i) = x_{22}(j) = 0$$

and $y_{1,2}(k)$ and $u_{1,2}(k)$ are the system output and control input, respectively. In this system, variation of system output at next sampling time is dependent on previous variation of both control input and system outputs.

The desired output signal $y^*(k+1)$ is given as

$$\begin{cases} y_1^*(k) = 0.5(-1)^{round(k/100)} \\ y_2^*(k) = 0.35(-1)^{round(k/100)} \end{cases}$$

Selecting the linearization length constant (LLC) as $L = 3$, and using PFDL approach, the abovementioned nonlinear system is transformed into the following PFDL data model:

$$\begin{bmatrix} y_1(k+1) \\ y_2(k+1) \end{bmatrix} = \begin{bmatrix} \varphi_{11\_1}(k) & \varphi_{12\_1}(k) & \varphi_{11\_2}(k) & \varphi_{12\_2}(k) & \varphi_{11\_3}(k) & \varphi_{12\_3}(k) \\ \varphi_{21\_1}(k) & \varphi_{22\_1}(k) & \varphi_{21\_2}(k) & \varphi_{22\_2}(k) & \varphi_{21\_3}(k) & \varphi_{22\_3}(k) \end{bmatrix} \begin{bmatrix} \Delta u_1(k) \\ \Delta u_2(k) \\ \Delta u_1(k-1) \\ \Delta u_2(k-1) \\ \Delta u_1(k-2) \\ \Delta u_2(k-2) \end{bmatrix}$$

where, only the previous variations of control inputs are included in this linearized data model and variation of system outputs are not considered.

The controller parameters are selected as $\rho_1 = 0.65, \rho_2 = 0.5, \rho_3 = 0.7, \lambda = 15, \mu = 2, \eta = 0.9, b_2 = 4, b_1 = -0.5, a = 1.5$ and the initial condition of estimated $\hat{\varphi}_{p,L}(k)$ is also selected as $\hat{\varphi}_{p,L}(1)\begin{bmatrix} 4 & -0.5 & 0 & 0 & 0 & 0 \\ -0.5 & 4 & 0 & 0 & 0 & 0 \end{bmatrix}$. The tracking performance of PFDL-based MFAC for $y_1(k)$ and $y_2(k)$ is presented in Figure 2.7. These results show good tracking performance of PFDL-based MFAC for the mentioned MIMO system.

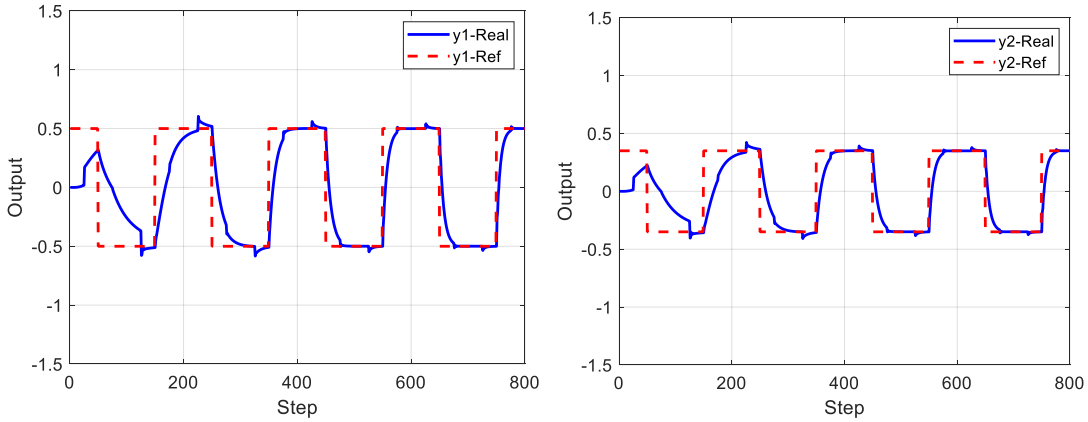

(a) (b)

Figure 2.7. Simulation results in Example 2.5 using PFDL-based MFAC for a) system output y_1, b) system output y_2.

2.2.2.3. FFDL Data Model Based MFAC

In section 2.1.2.3, it is proved that the MIMO nonlinear system (2.88), satisfying Assumptions 2.11 and 2.12, with $\left\|\Delta H_{L_u,L_y}\right\| \neq 0$, can be transformed into the FFDL data model as

$$\Delta y(k+1) = \varphi_{f,L_u,L_y}(k)\Delta H_{L_u,L_y}(k) \tag{2.161}$$

where $\varphi_{f,L_u,L_y}(k) = [\varphi_1(k) \dots \varphi_{L_u+L_y}(k)] \in R^{m\times(mL_u+mL_y)}$ is the unknown bounded PPJM matrix and:

$$\varphi_i(k) = \begin{bmatrix} \varphi_{11i}(k) & \varphi_{12i}(k) & \varphi_{13i}(k) & \cdots & \varphi_{1mi}(k) \\ \varphi_{21i}(k) & \varphi_{22i}(k) & \varphi_{23i}(k) & \cdots & \varphi_{2mi}(k) \\ \varphi_{31i}(k) & \varphi_{32i}(k) & \varphi_{33i}(k) & \cdots & \varphi_{3mi}(k) \\ \vdots & \vdots & \vdots & \vdots & \vdots \\ \varphi_{m1i}(k) & \varphi_{m2i}(k) & \varphi_{m3i}(k) & \cdots & \varphi_{mmi}(k) \end{bmatrix}_{m\times m} \in R^{m\times m}, i = 1, \dots, L$$

and $\Delta H_{L_u,L_y}(k) = [\Delta y^T(k), \dots, \Delta y^T(k-L_y+1), \Delta u^T(k), \dots, \Delta u^T(k-L_u+1)\ ]^T$.

Assumption 2.16: The $\varphi_1(k)$ of the PPJM matrix $\varphi_{f,L_u,L_y}(k)$ is a diagonally dominant matrix in which that, $|\varphi_{ij1}(k)| \leq b_1$, $b_2 \leq |\varphi_{ij1}(k)| \leq ab_2$, $a \geq 1$, and $b_2 > b_1(2a+1)(m-1), i = 1, \dots, m, j = 1, \dots, m, i \neq j$, and the sign of all the arrays of $\varphi_1(k)$ stay unchanged.

2.2.2.3.1. Controller Algorithm

Following cost function of the control input is used for controller design.

$$J(u(k)) = \|y^*(k+1) - y(k+1)\|^2 + \lambda\|u(k) - u(k-1)\|^2 \tag{2.162}$$

where the $\lambda > 0$ is a weight factor which is used to limit the changes of control input, and the $y^*(k+1)$ is the reference trajectory of system output.

Putting the FFDL data model (2.161) into cost function (2.162) and differentiating according to control input $u(k)$ and setting to be zero brings the controller algorithm as follows.

$$u(k) = u(k-1) + \frac{\varphi_{L_y+1}^T(k)\left(\rho_{L_y+1}(y^*(k+1) - y(k))\right)}{\lambda + \left\|\varphi_{L_y+1}(k)\right\|^2} - \frac{\varphi_{L_y+1}^T(k)\left(\sum_{i=1}^{L_y}\rho_i\,\varphi_i(k)\Delta y(k-i+1) + \sum_{i=L_y+2}^{L_y+L_u}\rho_i\,\varphi_i(k)\Delta u(k+L_y-i+1)\right)}{\lambda + \left\|\varphi_{L_y+1}(k)\right\|^2} \tag{2.163}$$

where the $\rho \in (0,1]$, $i = 1,2,\dots,L_y+L_u$ is the step factor.

2.2.2.3.2. PPJM Estimation Algorithm

The following cost function of PPJM φ_{f,L_u,L_y}estimation for MIMO systems is used for estimation of the PPJM matrix.

$$J\left(\varphi_{f,L_u,L_y}\right) = \left\|y(k) - y(k-1) - \varphi_{f,L_u,L_y}\Delta H_{L_u,L_y}(k-1)\right\|^2 + \mu\left\|\varphi_{f,L_u,L_y} - \hat{\varphi}_{f,L_u,L_y}(k)\right\|^2 \tag{2.164}$$

where the $\mu > 0$ is a weight factor which is used to limit the changes of PPJM estimation.

Minimizing cost function (2.164) brings the following estimation algorithm.

$$\hat{\varphi}_{f,L_u,L_y}(k) = \hat{\varphi}_{f,L_u,L_y}(k-1) + \frac{\eta\left(\Delta y(k) - \hat{\varphi}_{f,L_u,L_y}(k-1)\Delta H_{L_u,L_y}(k-1)\right)\Delta H_{L_u,L_y}{}^{T}(k-1)}{\mu + \left\|\Delta H_{L_u,L_y}(k-1)\right\|^2} \tag{2.165}$$

where the $\eta \in (0,2]$ is the step factor, and $\hat{\varphi}_{p,L_u,L_y}(k) = [\hat{\varphi}_1(k)\ \hat{\varphi}_2(k)\ \dots\ \hat{\varphi}_{L_u+L_y}(k)] \in R^{m\times m(L_u,L_y)}$ is the estimation of $\varphi_{p,L_u,L_y}(k)$, that

$$\hat{\varphi}_i(k) = \begin{bmatrix} \hat{\varphi}_{11i}(k) & \hat{\varphi}_{12i}(k) & \hat{\varphi}_{13i}(k) & \cdots & \hat{\varphi}_{1mi}(k) \\ \hat{\varphi}_{21i}(k) & \hat{\varphi}_{22i}(k) & \hat{\varphi}_{23i}(k) & \cdots & \hat{\varphi}_{2mi}(k) \\ \hat{\varphi}_{31i}(k) & \hat{\varphi}_{32i}(k) & \hat{\varphi}_{33i}(k) & \cdots & \hat{\varphi}_{3mi}(k) \\ \vdots & \vdots & \vdots & \vdots & \vdots \\ \hat{\varphi}_{m1i}(k) & \hat{\varphi}_{m2i}(k) & \hat{\varphi}_{m3i}(k) & \cdots & \hat{\varphi}_{mmi}(k) \end{bmatrix}_{m\times m} \in R^{m\times m}, i = 1, \dots, L.$$

In addition, a reset structure is used for estimation law (2.126) to empower this estimation algorithm with a powerful capability to track the time-varying parameter as below.

$$\hat{\varphi}_{ii(L_y+1)}(k) = \hat{\varphi}_{ii(L_y+1)}(1),\ if\ \left|\hat{\varphi}_{ii(L_y+1)}(k)\right| < b_2\ or\ \left|\hat{\varphi}_{ii(L_y+1)}(k)\right| > ab_2\ or\ sign\left(\hat{\varphi}_{ii(L_y+1)}(k)\right) \neq sign\left(\hat{\varphi}_{ii(L_y+1)}(1)\right), i = 1, \dots, m \tag{2.166}$$

$$\hat{\varphi}_{ij(L_y+1)}(k) = \hat{\varphi}_{ij(L_y+1)}(1),\ if\ \left|\hat{\varphi}_{ij(L_y+1)}(k)\right| < b_1\ or\ sign\left(\hat{\varphi}_{ij(L_y+1)}(k)\right) \neq sign\left(\hat{\varphi}_{ij(L_y+1)}(1)\right), i,j = 1, \dots, m, i \neq j \tag{2.167}$$

where the $\hat{\varphi}_{ij(L_y+1)}(1)$ denotes the initial value of $\hat{\varphi}_{ij(L_y+1)}(k)$, $i = 1, \dots, m, j = 1, \dots, m$, and the sign of parameter is supposed to stay unchanged for all k.

Remark 2.10

In the case of multi-input single-output (MISO) system, where $u(k) \in R^m$ and $y(k) \in R$, using FFDL data model of the general system $\Delta y(k+1) = \varphi_{f,L_u,L_y}^T(k)\Delta H_{L_u,L_y}(k)$, the FFDL-based MFAC algorithm is obtained as:

$$u(k) = u(k-1) + \frac{\varphi_{L_y+1}(k)\left(\rho_{L_y+1}\left(y^*(k+1) - y(k)\right)\right)}{\lambda + \left\|\varphi_{L_y+1}(k)\right\|^2} - \frac{\varphi_{L_y+1}(k)\left(\sum_{i=1}^{L_y}\rho_i\,\varphi_i(k)\Delta y(k-i+1) + \sum_{i=L_y+2}^{L_y+L_u}\rho_i\,\varphi_i(k)\Delta u\left(k+L_y-i+1\right)\right)}{\lambda + \left\|\varphi_{L_y+1}(k)\right\|^2} \tag{2.168}$$

$$\hat{\varphi}_{f,L_u,L_y}(k) = \hat{\varphi}_{f,L_u,L_y}(k-1) + \frac{\eta\left(\Delta y(k) - \hat{\varphi}_{f,L_u,L_y}^T(k-1)\Delta H_{L_u,L_y}(k-1)\right)\Delta H_{L_u,L_y}(k-1)}{\mu + \left\|\Delta H_{L_u,L_y}(k-1)\right\|^2} \tag{2.169}$$

$$\hat{\varphi}_{i(L_y+1)}(k) = \hat{\varphi}_{i(L_y+1)}(1),$$

$$if \ \left|\hat{\varphi}_{i(L_y+1)}(k)\right| < b_2 \ \ or \ sign\left(\hat{\varphi}_{i(L_y+1)}(k)\right) \neq sign\left(\hat{\varphi}_{i(L_y+1)}(1)\right), i = 1, \dots, m \tag{2.170}$$

where $\hat{\varphi}_{f,L_u,L_y}(k) = [\hat{\varphi}_1(k), \dots, \hat{\varphi}_{L_y}(k), \hat{\varphi}^T_{L_y+1}(k), \dots, \hat{\varphi}^T_{L_y+L_u}(k)]^T \in R^{L_y+mL_u}$ is the estimation of PPJM in FFDL data model, $\hat{\varphi}_i(k) = [\hat{\varphi}_{1i}(k), \hat{\varphi}_{2i}(k), \dots, \hat{\varphi}_{mi}(k)]^T$, $i = L_y + 1, \dots, L_y + L_u$.

2.2.2.3.3. Simulation Results

Example 2.6

The MIMO discrete-time nonlinear system, the desired trajectories and initial values are the same as example 2.5.

Selecting the input-related and output-related linearization length constant (LLC) as $L_u = L_y = 2$, and using FFDL approach, the abovementioned nonlinear system is transformed into the following PFDL data model:

$$\begin{bmatrix} y_1(k+1) \\ y_2(k+1) \end{bmatrix}$$

$$= \begin{bmatrix} \varphi_{11\_1}(k) & \varphi_{12\_1}(k) & \varphi_{11\_2}(k) & \varphi_{12\_2}(k) & \varphi_{11\_3}(k) & \varphi_{12\_3}(k) & \varphi_{11\_4}(k) & \varphi_{12\_4}(k) \\ \varphi_{21\_1}(k) & \varphi_{22\_1}(k) & \varphi_{21\_2}(k) & \varphi_{22\_2}(k) & \varphi_{21\_3}(k) & \varphi_{22\_3}(k) & \varphi_{21\_4}(k) & \varphi_{22\_4}(k) \end{bmatrix} \begin{bmatrix} \Delta y_1(k) \\ \Delta y_2(k) \\ \Delta y_1(k-1) \\ \Delta y_2(k-1) \\ \Delta u_1(k) \\ \Delta u_2(k) \\ \Delta u_1(k-1) \\ \Delta u_2(k-1) \end{bmatrix}$$

where the previous variation of both control inputs and system outputs are included in this linearized data model.

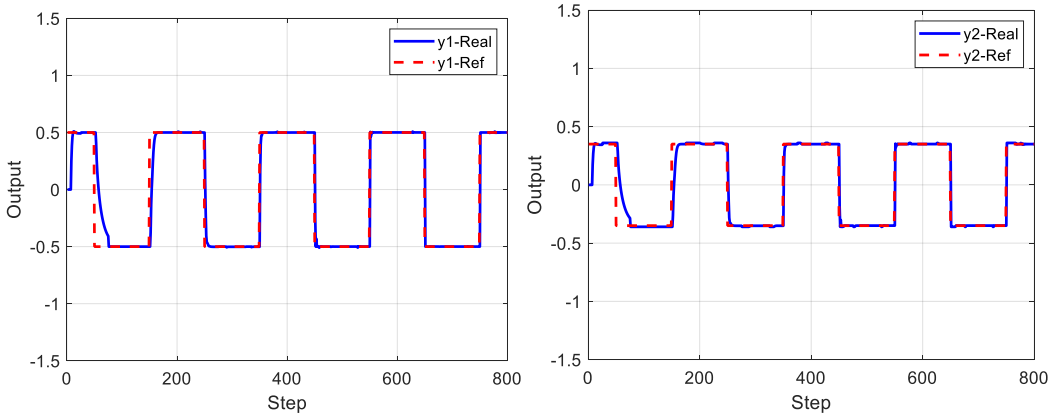

(a) (b)

Figure 2.8. Simulation results in Example 2.6 using FFDL-based MFAC for a) system output y_1, b) system output y_2.

The controller parameters are selected as $\rho_1 = \rho_3 = 0.65, \rho_2 = \rho_4 = 0.5, \rho_5 = \rho_6 = 0.7$, $\lambda = 15$, $\mu = 2$, $\eta = 0.9$, $b_2 = 4, b_1 = -0.5, a = 1.5$ and the initial condition of estimated $\hat{\varphi}_{p,L}(k)$ is also selected as $\hat{\varphi}_{p,L}(1)\begin{bmatrix} 0 & 0 & 0 & 0 & 4 & -0.5 & 0 & 0 \\ 0 & 0 & 0 & 0 & -0.5 & 4 & 0 & 0 \end{bmatrix}$. The tracking performance of FFDL-based MFAC for $y_1(k)$ and $y_2(k)$ is presented in Figure 2.8. These results show good tracking performance of FFDL-based MFAC for the mentioned MIMO system. The simulation results show that the tracking performance of FFDL-based MFAC scheme is quite better than PFDL-based MFAC.

Conclusion

In this chapter, a description of data driven control theories, particularly MFAC, has been given with details. MFAC is a data-driven control method that uses only the I/O data measured from the system output and input to design the controller, and is independent of the system model. The MFAC algorithm includes three main steps. First, using a novel dynamic linearization method, the model of the studied system is transformed into a linearized data model, which is a matrix (called PG) with unknown parameters. Then, the elements of the PG matrix are estimated at each sampling time using the measured I/O data from the controlled system. The third step involves designing a weighted step-ahead controller by using the estimated PG matrix and the measured I/O data.

In order to explain the theory of MFAC, a novel dynamic linearization approach for discrete-time nonlinear systems is presented in detail. In this case, three kinds of dynamic linearization data models, including compact form (CF) partial form (PF) and full form dynamic linearization (FFDL), are presented for single-input single-output (SISO), multi-input single-output (MISO) and multi-input multi-output (MIMO) nonlinear systems, respectively. Afterward, on the basis of these dynamic linearization approaches, three kinds of MFAC algorithms, CFDL-MFAC, PFDL-MFAC and FFDL-MFAC, are investigated for the unknown SISO and MIMO discrete-time nonlinear systems, respectively. The controller design, convergence analysis and simulation study related to each category of the MFAC have been given in detail.

Comparing the three kinds of MFAC schemes, the CFDL-MFAC is the simplest one which is usually used for simple systems. On the other hand, the last two methods are the special cases which can be used for more complex systems due to their more adjustable degree of freedom and more design flexibility by introducing more parameters during dynamic linearization data model.

Summing up, The MFAC approaches only use the online I/O data of the controlled plant to design the controller directly, and thus it is independent of the mathematical model of the controlled plant. The MFAC controllers have a few parameters to update online, which can be designed more easily than that of traditional adaptive control systems.

Chapter-3 TWO CONTROL ALGORITHMS FOR WRSM DRIVE SYSTEM USING MFAC

Contents

Introduction

Over the last few years, the synchronous machines are widely used in industrial and automotive applications due to their considerable energy density, high torque ratio and efficiency. Using this kind of machines brings some challenges related to improvement of system reliability, manufacturing and maintenance cost reduction, and reducing the errors created by the sensors. Motivated by these challenges, the main objective of the work realized within this study is to control the i-StARS electric powertrain designed by Valeo with and without using the current sensors on the stator of the machine.

However, the traditional model-based control (MBC) methods in current control of the machine require an accurate model of the studied powertrain to design the controller. In addition, relying on the exist current sensorless control methods, if the stator currents are not measured by sensors, they must be estimated using an accurate model of studied powertrain. However, it is difficult or at least time consuming to reach to a very precise model, especially in transient. Furthermore, the wear of the different components of the system due to electrical (current peaks and large voltage gradient) and mechanical conditions (temperature, humidity or dust) change their expected values. On the other hand, the temperature variation and saturation of the machine are other candidates which may cause to variation in value of resistor (in rotor and stator of the machine and other resistors used in powertrain) and inductances.

All the abovementioned considerations led to find a solution to fix the limitations related to the model-based and estimation-based controllers that are highly dependent on a precise dynamics model of studied system. Relying on the advantages and characteristics of the DDC theories described in Chapter 2, the MFAC as a DDC method is presented here to be used as an alternative for the MBC and estimation-based control algorithms.

As a first step, the studied powertrain and the related state space mathematical model is presented in this chapter. In the second part of this chapter, the Model-Free-Adaptive-Control MFAC is developed to be used for current control of a wound-rotor-synchronous-machine (WRSM) drive system, in which the phase currents are measured and controlled directly. A PI controller as a well-known MBC method, is also developed to compare with the MFAC. The third part of this chapter provides a current sensorless control algorithm of a WRSM using MFAC. In this control method, the rotor speed is the only controlled variable and there is no control or estimation on phase currents. The presented controller is also compared with a current sensorless control method which uses a Lyapunov-based observer to estimate the unmeasured phase currents. All the developed control algorithms are firstly tested in simulation under several operating conditions such as starting, tracking, parameter variation and load step. Then, several experimental tests have been done to validate the simulation performance of the developed control algorithms. According to these results, an effective performance of MFAC is obtained to control the phase currents with and without using current sensors in stator side.

3.1. Modelling of The Studied WRSM

As mentioned in the Introduction of this chapter, this chapter study will focus on the control of the WRSM drive, with and without current sensors, to improve the performance of existing control algorithms. Before starting to control work, having some information about the different elements, modelling and functioning of the i-StARS machine will be helpful to better understanding of the control procedure. The theoretical study of the functioning, electromagnetic modeling and electric modelling of the i-StARS machine have been already conducted in PhD study of Geoffrey Devornique [94] and Adrien Corne [32] in the GREEN laboratory. According to some parts of these two studies, a brief description of the components and modelling of the studied i-StARS machine is presented here to give the important details related to this system. Once again, it is notable that this study has no new added value on design or modelling of the studied system and only focus on control side to improve its performance.

3.1.1. Description of the Different Elements of the Studied Electric Powertrain

3.1.1.1. Valeo's i-StARS starter-alternator [32]

In this application, Valeo has used an electric powertrain supplied by a 12V battery for hybridization of vehicles. In order to protect the inverter from voltage peaks from the battery, an input filter with a small inductance and a big capacitor is implemented between the battery and inverter. This configuration is presented in Figure 3.8. As shown in Figure 3.1, in the real powertrain, the inverter is mounted directly on the WRSM chassis and the two parts are interlocked with each other. In this figure, the DC positive terminal is shown on the bottom right and the negative terminal is connected to the chassis of the machine. The control unit is located in the center. The black device contains the system inverter. The inverter consists of six legs of power MOSFETs. Using the HDTMOS power technology [95] for these MOSFETs, led to a very compact inverter of this application.

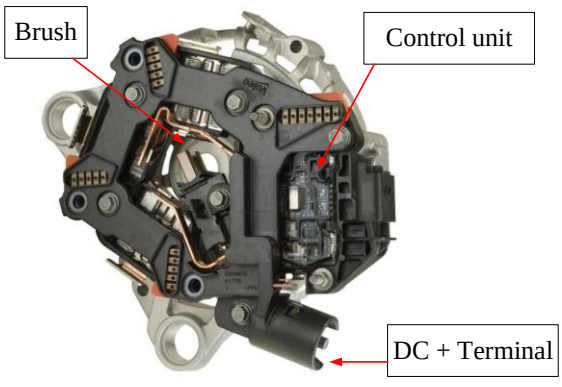

Figure 3.1 Schematic of the WRSM chassis with the interlocked inverter.

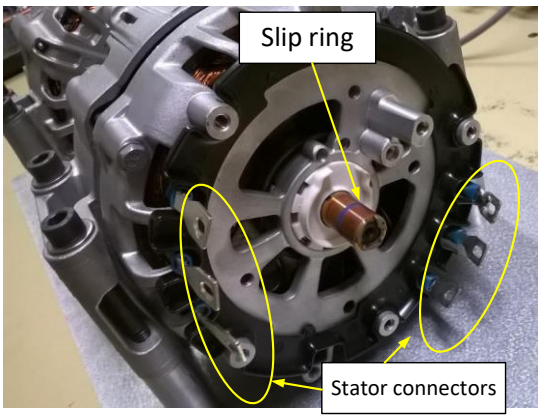

Figure 3.2. The i-StARS machine without the inverter and the brush.

The MOSFETs used in this application are special ones, in which the length and width of each MOSFET is less than 8mm and its thickness is less than 0.3mm. the drain source ON resistance $R_{DS(ON)}$ is between 0.8 and 1.3$m\Omega$. Furthermore, the nominal drain current is $I_D = 500A$with a maximum peak current of 700A. These special types of power MOSFETs are designed for harsh automotive environment with a low drain source ON resistance and a rugged avalanche performance.

The i-StARS system is a wound rotor synchronous machine with two three-phase delta stators. While the supply voltage is small, the obtained torque density in delta connection is higher than star connection, for this, the delta connection is usually used for automotive applications. According to the design specifications, the nominal speed of i-StARS is 1500 rpm for a current of $130A_{rms}$, with peaks up to $300A_{rms}$. Its rotor is a claw-pole wired rotor. A pair of poles is formed by two teeth from each claw. The i-StARS machine has 6pairs of poles and small magnets are placed between each teeth of a claw. Their task is to desaturate the machine iron parts and restrict the magnetic leakage. Some other motivations to choose a wired rotor instead of a permanent magnet synchronous machine is listed as follows. 1) using the wired rotor reduces the manufacturing costs, because the magnets are quite costly compared to copper. 2) using the wired rotor brings this freedom to increase or decrease the excitation flux with controlling the excitation current.

The rotor excitation current is separately controlled by a simple boost converter which is supplied by the 12V battery. As shown in Figure 3.1, the connection between the converter and the wired rotor is built by a and the brush. In addition, the slip ring on the rotor is shown in Figure 3.2.

3.1.1.2. Developed Experimental Test Bench for This Study

The prepared system in the GREEN laboratory to be used in current control and sensorless control of wound rotor synchronous machine (WRSM), is a little different from the electric powertrain commercialized by Valeo. Indeed, there was no combustion engine available to connect to the electric powertrain. In addition, since the control unit made by Valeo was not easily applicable, another alternative is used for control unit. The following paragraph will present the test bench prepared in the laboratory and will clear the differences with Valeo system.

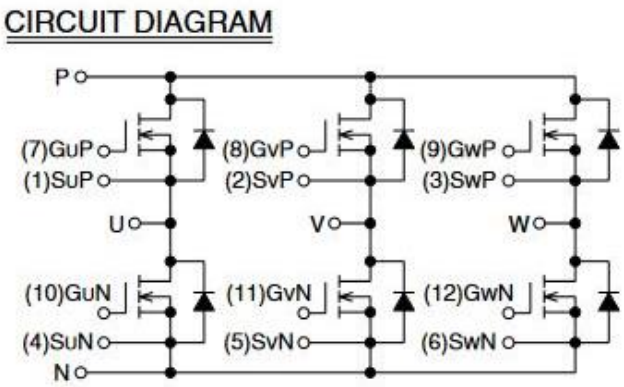

Figure 3.3. Diagram of the MOSFET's connection in the FM600TU-07A module [96].

In this study, instead of using a battery, a controllable power supply is used to feed the powertrain. The reason of this replacement can be explained by the fact that a battery needs to be charged frequently and its voltage varies due to the charge level. On the other hand, using the power supply gives the possibility to apply the saturation condition on the output current which provides a general protection during testing different scenarios.

The developed WRSM by Valeo is an i-StARS machine that its inverter is interlinked on the stator. However, since the inverter and control unit in this configuration was not easy to be used, we removed this part and kept only the machine. Alternatively, a new inverter, using MOSFETs module, has been designed to be used in this work. The Mitsubishi Electric's FM600TU-07A MOSFETs module [96] was adopted in this work. As shown in Figure 3.3, this module is in a three-legs inverter configuration that includes 6 MOSFETs. this module also has a maximum drain source voltage of $V_{DSS} = 75V$ and a maximum drain current of $I_D = 300A$. The drain-source ON resistance $R_{DS(ON)}$ is between 0.5 and 0.75 $m\Omega$. Two of the mentioned modules are have been installed on a big radiator. The radiator is decided to be big enough since the compactness and thermal issues are not a part of our study. Using six SKHI22BH4R drivers, 3 for each module, provided the

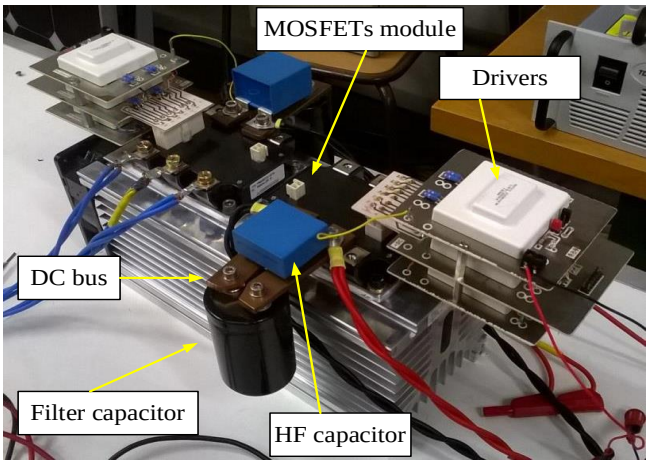

Figure 3.4. Diagram of the electronic device assembled together.

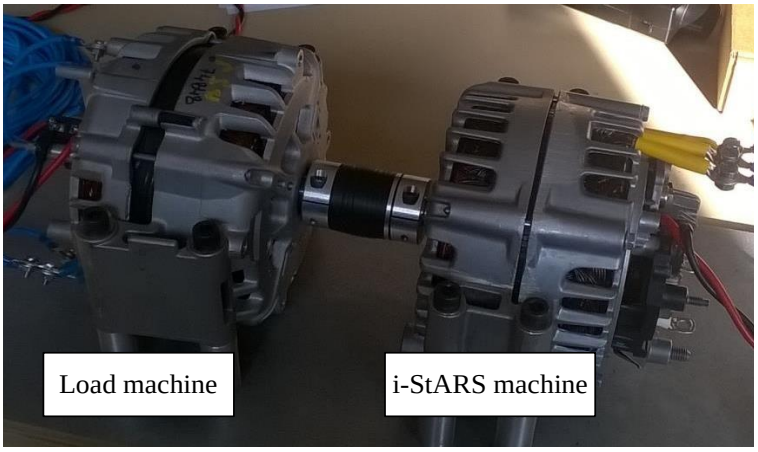

Figure 3.5. The i-StARS machine and the coupled load machine.

control of the MOSFETs. this driver is a dual driver that drives interlinked top and bottom MOSFETs of a leg in which one can control the two MOSFETs of one leg.

In the prepared inverter, the input filter has also been included. For this, a big aluminum electrolytic capacitor 6.8 mF is connected to the DC bus of the inverter with a bus bar. In parallel with this big capacitor, a decoupling capacitor is added to filter the high frequency noises from the inverter. The whole prepared device, including the MOSFETs, radiator, driver and input filter is shown in Figure 3.4.

In this study, the control of a WRSM is considered. This controlled motor is also connected to a load to have opportunity to do several tests under different loads. Here, in order to load the controlled machine, another electric machine is connected to the controlled one to play the role of a load. This load machine is also supplying a resistor through a rectifier. This configuration is shown in Figure 3.5.

To control the rotor excitation current, another boost converter is designed and built to be used in this study. It is notable that both the inverter and Boost converter control signals are created from a dSpace MicroLabBox. The switching frequency is also set on 10KHz for all the tests of this study.

Several sensors are added on the test bench to test the sensorless control and for the security of the system. Valeo has supplied the mechanical sensor, a voltage supplied Hall effect sensor that gives sin and cosine voltage in output that gives an image of the rotor position and speed after signal processing with a Phase-

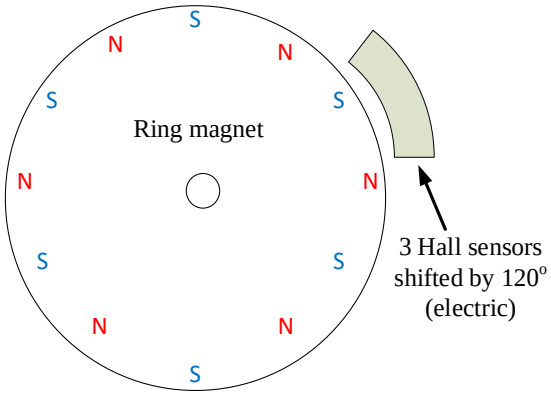

Figure 3.6. Diagram of the Hall effect based position sensor.

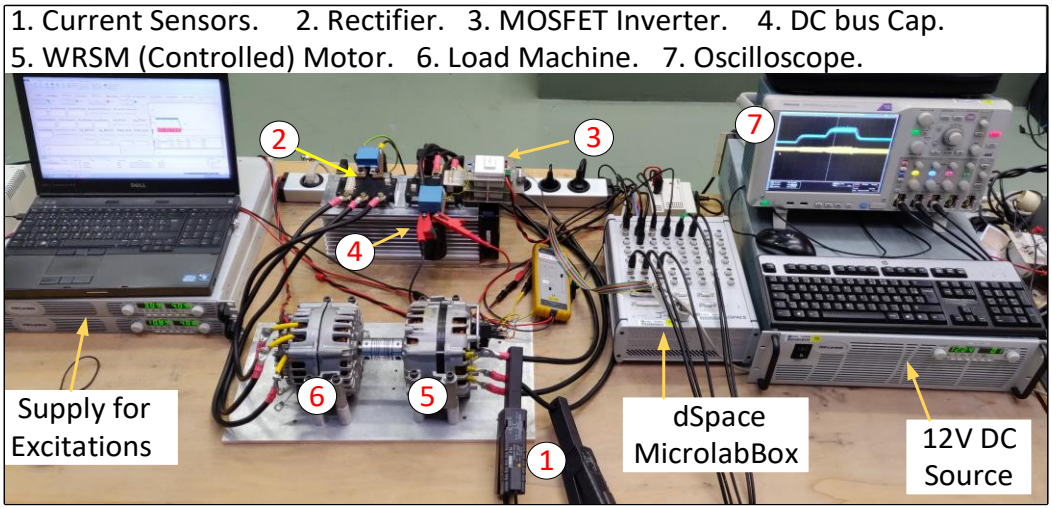

Figure 3.7. Practical test bench prepared in the laboratory.

Locked Loop (PLL). The principle of the Hall effect speed sensor is described in [97]. As shown in Figure 3.6, it consists in a ring magnet mounted on the rotor shaft of the machine with Hall sensors placed around and shifted by 120° electric which corresponds to 120° divided by the number of pair of poles. The ring magnet is a homogeneous piece of permanent magnet material into which a chosen number of poles have been magnetized. In the Hall effect sensors used in Valeo's system, 6 pair of poles have been magnetized so that voltage output of the Hall effect sensors directly give the electric speed and position of the rotor.

According to the abovementioned considerations, the whole test bench is made as shown in Figure 3.7. In this configuration, two WRSMs, dSpace MicroLabBox, PC, sensors, inverter, input filter, rectifier and power supplies can be seen in the final version of the prepared powertrain. Related to this powertrain, the electric diagram is also presented in Figure 3.8.

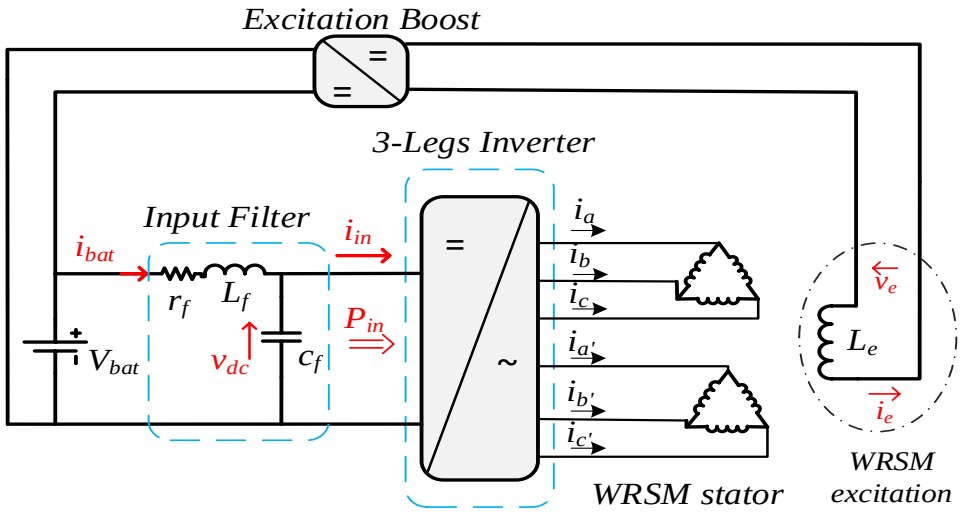

Figure 3.8. Electric diagram of the prepared powertrain.

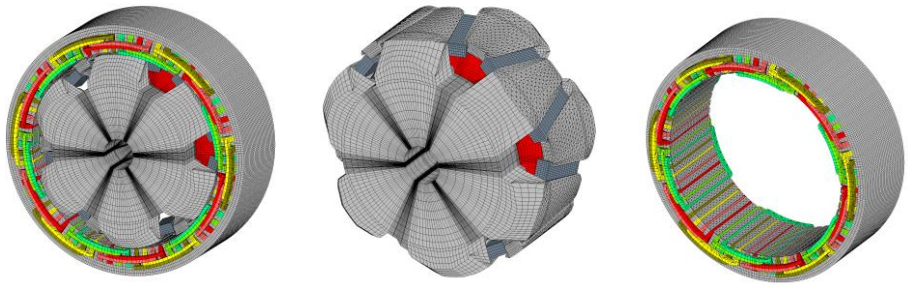

Figure 3.9. Meshing of the full i-StARS machine with Gmsh-GetDP [94].

3.1.2. Electromagnetic Modeling [94]

As mentioned before, the electromagnetic modeling of the studied WRSM is already done by Dr. Devornique during his PhD study [94]. He proposed an electromagnetic model of the WRSM that combines robustness of the electromagnetic fields while dividing the computational time by at least 4. The main purpose of developing this electromagnetic modeling was to be able to introduce an optimization of the geometry of the i-StARS machine to increase the performance of the WRSM. This optimization generally focuses on the geometry of the claw-poles of the rotor, with and without magnets between the poles. The modeling is carried out based on the finite element method and using the Gmsh-GetDP software. To obtain a mesh geometry as close as possible to the real machine, a 3D model of the i-StARS machine has been meshed on CAD files by Valeo. The results related to meshing of i-StARS is given in Figure 3.9 [94].

According to this work, the stator can be divided in 6 similar parts in which that each part serves an angle of 60° of the full stator. Actually, stator represents a rotational 6-fold symmetry. The rotor has also the same symmetric features. Then, it is proven that only $1/6^{th}$ of the full machine is enough to be meshed for calculation of the whole machine. This feature avoids doing unnecessary calculations and save a big amount of time. The related meshing results are given in Figure 3.10, the tables of calculation time are also presented in [94].

Figure 3.11 shows the calculation of the flux on a double pole pitch for a specific operating point in the full meshed machine of Figure 3.9 (in dashed line style) and the single pole meshed of Figure 3.10 (in solid line style). The calculation method of the flux on the three phases of each stator is explained in [94]. According

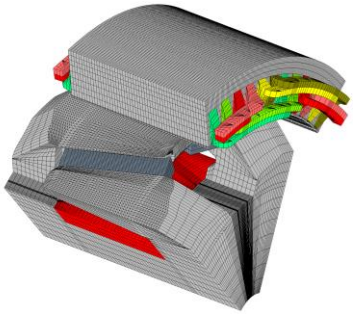

Figure 3.10. Meshing of 1 pole of the i-StARS rotor and stator with Gmsh-GetDP [94].

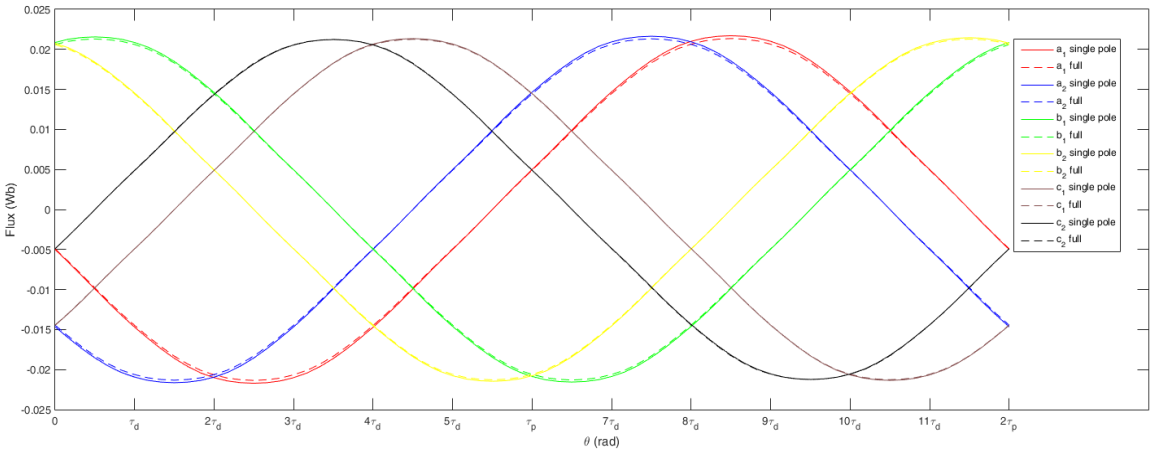

Figure 3.11. Comparison of the flux calculations in the complete meshed mashine and in the periodic meshed mashine.

to this figure, two different types of meshing lead to a very close results, which tend to validate the single pole meshing use.

All the presented results were based on a finite element analysis (FEA) model of the machine and requires to be validated by some experimental tests on the practical test bench. Indeed, with finite element method, the obtained results are highly dependent on the calculation method and on the meshing of the machine. Comparison between several methods of the flux calculation and between several meshing methods are presented in Dr. Devornique's work.

In [32], to validate the model of the machine, presented in 3.10, the back-EMF induced in the stator at no-load condition, while it is driven by another machine (see Figure 3.5) at 520 rpm, is compared with the results obtained from Dr. Devornique's FEA model. To do so, the second machine (left one) has been controlled to reach to the speed reference. The stator of the i-StARS machine was in open circuit and only the voltage sensors were connected to the stator. The back-EMF measurements of i-StARS were done for a rotor excitation current starting from 0 to 8A with a step of 0.5A between each measurement. The same test is performed in the finite element model of the machine. The obtained results are shown in Figure 3.12.

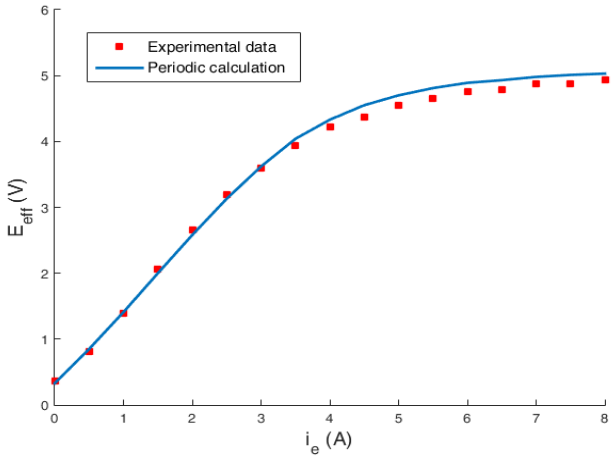

Figure 3.12. Back-EMF in the i-StARS driven at 520 rpm as a function of the excitation

According to the Figure 3.12, it is notable that the obtained results from simulation and test bench measurements are very close. These results can also give valuable knowledge about the electric model of the machine. According to the blue curve in Figure 3.12, it can be concluded that the machine operates in a linear operational range for an excitation current between 0 and 4A. The saturation occurs between 4A and 5A. It is notable that while the excitation current is zero, there is still a small back-EMF of $0.4V_{rms}$ generated in the machine. This is because of the magnet's effects between the claw-poles of the rotor. Their task is to limit the flux leakage in the rotor, but they also have a weak contribution to the back-EMF.

3.1.3. Circuit-based Electric model [32]

According to the obtained information from electromagnetic modeling and relation between the back-EMF and the excitation current, we will try to create a dq-model constructed by state equations representing the functioning of a WRSM running by an inverter. For simplicity and better understanding, the model will be developed for a single stator.

A typical 3-phase stator of a synchronous machine can be described by an inductance with an internal resistance on 3 phases a, b and c located by a phase shift of $\frac{2\pi}{3}$ radians. The rotor can be described by an inductance with an internal resistance aligned with an axis "dr" and in quadrature with the axis "qr" shifted by an angle θ from the a-axis. This configuration is presented in Figure 3.13.

According to this configuration of WRSM, the following equations can be obtained:

$$[V_s] = r_s.[i_s] + [\frac{d\varphi_s}{dt}]$$
$$V_r = r_r.i_r + \frac{d\varphi_r}{dt} \quad (3.1)$$

where $[X_s] = \begin{bmatrix} X_a \\ X_b \\ X_c \end{bmatrix}$, and V_s is the stator voltages vector, i_s is the stator currents vector, φ_s is the magnet flux in the stator and r_s is the matrix of stator resistances. The V_r, i_r, r_r and φ_r are the rotor voltage, rotor current, rotor resistance and rotor magnet flux, respectively. The machine is supposed to be balanced as $r_a = r_b = r_c = R_s$.

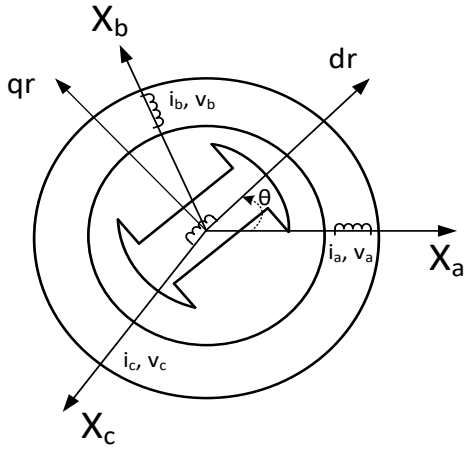

Figure 3.13. Simplified representation of the WRSM.

Since the sum of the stator current is zero, we are able to presents the related 3-phase equations of the stator into the two-phase frame of $\alpha\beta$ reference. Using the Concordia matrix, the abc frame can be transformed into the $\alpha\beta$ frame as follows:

$$\begin{bmatrix} V_\alpha \\ V_\beta \end{bmatrix} = R_s . \begin{bmatrix} i_\alpha \\ i_\beta \end{bmatrix} + \frac{d}{dt} \begin{bmatrix} \varphi_\alpha \\ \varphi_\beta \end{bmatrix} \tag{3.2}$$

where $\begin{bmatrix} X_\alpha \\ X_\beta \end{bmatrix} = T_{32}^t . \begin{bmatrix} X_a \\ X_b \\ X_c \end{bmatrix}$ with $T_{32} = \sqrt{\frac{2}{3}} \begin{bmatrix} 1 & 0 \\ -\frac{1}{2} & \frac{\sqrt{3}}{2} \\ -\frac{1}{2} & -\frac{\sqrt{3}}{2} \end{bmatrix}$.

By this way, we can describe the variables linked to the stator in the two-phase frame, but in this situation, the system is still dependent on the position of the rotor where the voltages, currents and fluxes depends on the angle θ. To prevent this dependence, the stator variables are presented in a rotating frame dq, linked to the rotor frame. In this frame, the d-axis is the same with the dr-axis shown in Figure 3.13, and the q-axis is the same with the qr-axis. According to the Park transformation, the $\alpha\beta$ frame can be transformed to the dq frame as follows:

$$\begin{bmatrix} V_d \\ V_q \end{bmatrix} = R_s . \begin{bmatrix} i_d \\ i_q \end{bmatrix} + \frac{d}{dt} \begin{bmatrix} \varphi_d \\ \varphi_q \end{bmatrix} + \dot{\theta} . P\left(\frac{\pi}{2}\right) . \begin{bmatrix} \varphi_d \\ \varphi_q \end{bmatrix} \tag{3.3}$$

where $\begin{bmatrix} X_d \\ X_q \end{bmatrix} = P(-\theta) . \begin{bmatrix} X_\alpha \\ X_\beta \end{bmatrix}$ is the Park transformation and $P(\theta) = \begin{bmatrix} \cos(\theta) & -\sin(\theta) \\ \sin(\theta) & \cos(\theta) \end{bmatrix}$ is the rotational matrix.

In the new dq frame, the Figure 3.13 can be shown in two-phase dq axis as shown in Fig. 3.14.

The related dq axis fluxes can be written as:

$$\begin{aligned} \varphi_d &= L_d . i_d + \varphi_{ed} \\ \varphi_q &= L_q . i_q \\ \varphi_r &= L_e . i_e + \varphi_{de} \end{aligned} \tag{3.4}$$

where φ_{ed} is generated by the excitation current in the stator d-axis which can be presented as:

$$\varphi_{ed} = M . i_e + \Psi_f \tag{3.5}$$

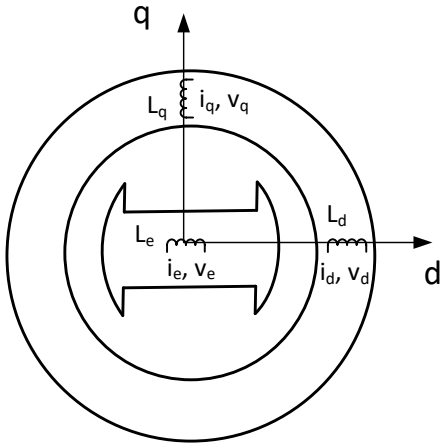

Figure 3.14. Representation of the WRSM in the dq fram.

where M is the mutual inductance between the stator and rotor and Ψ_f is the flux created by the inter-pole magnets through the stator windings. Since its amount is small compared to $M.i_e$, its impact on the machine torque can be neglectable. For the rest of this study we will neglect the Ψ_f and will use the following equation:

$$\varphi_{ed} = M.i_e \tag{3.6}$$

In the same manner, φ_{de} is the flux created by the d-axis current of the stator in the rotor as follows:

$$\varphi_{de} = M.i_d - \Psi_r \tag{3.7}$$

where Ψ_r is the flux created by the rotor magnets through the rotor winding. This flux is effective to decrease the saturation of the rotor magnetic circuit. It is considered to be constant. It is noteworthy that if the stator inductances are dependent on the position of the rotor in the 3-phase reference frame, the dq axis inductances are constant.

According to the equations 3.3 to 3.7, the following electric state equations can be obtained for the system.

$$\begin{aligned} V_d &= R_s.i_d + \frac{d\varphi_d}{dt} - \omega.\varphi_q \\ V_q &= R_s.i_q + \frac{d\varphi_q}{dt} + \omega.\varphi_d \\ V_e &= R_e.i_e + \frac{d\varphi_r}{dt} \end{aligned} \tag{3.8}$$

Then by substituting the equations 3.4-3.7 into the 3.8, we have

$$\begin{aligned} V_d &= R_s.i_d + L_d\frac{di_d}{dt} + M\frac{di_e}{dt} - \omega L_q i_q \\ V_q &= R_s.i_q + L_q\frac{di_q}{dt} + \omega(L_d i_d + M i_e) \\ V_e &= R_e.i_e + L_e\frac{di_e}{dt} + M\frac{di_d}{dt} \end{aligned} \tag{3.9}$$

where $\omega = \dot{\theta}$ is the electric angular speed of the rotor. This electric speed can be linked to the mechanical speed of the rotor Ω with $\omega = p.\Omega$, where p is the number of pole pairs of the machine.

the equation 3.9 can be edited as follows to be in a general form of the state equations for the studied system:

$$\begin{aligned} &\frac{di_d}{dt} + \frac{M}{L_d}\frac{di_e}{dt} = \frac{1}{L_d}\left(V_d - R_s.i_d + \omega L_q i_q\right) \\ &\frac{di_q}{dt} = \frac{1}{L_q}\left(V_q - R_s.i_q - \omega.(L_d i_d + M i_e)\right) \\ &\frac{di_e}{dt} + \frac{M}{L_e}\frac{di_d}{dt} = \frac{1}{L_e}(V_e - R_e.i_e) \end{aligned} \tag{3.10}$$

Then by replacing the $\frac{di_e}{dt}$ and $\frac{di_d}{dt}$ term in the equation of i_d and i_e, respectively, the following state equations can be obtained.

$$\begin{cases} \frac{di_e}{dt} = \frac{L_d}{L_d L_e - M^2}\left(v_e - R_e i_e - \frac{M}{L_d}(v_d - R_s i_d + p.\omega.L_q.i_q)\right) \\ \frac{di_d}{dt} = \frac{L_e}{L_d L_e - M^2}\left(v_d - R_s.i_d + p.\omega.L_q.i_q - \frac{M}{L_e}(v_e - R_e.i_e)\right) \\ \frac{di_q}{dt} = \frac{1}{L_q}\left(v_q - R_s.i_q - p.\omega(L_d.i_d + M.i_e)\right) \\ \frac{d\omega}{dt} = \frac{1}{J}\left(p.i_q i_d\left(\left(L_d - L_q\right) + M.i_e\right) - \Gamma_{load}\right) \end{cases} \tag{3.11}$$

TABLE 3.1: SYMBOLES USED IN (3.13)

Parameter	Symbol & Range	Nominal values
Stator Resistance	$0.03 \leq R_s \leq 0.2\ \Omega$	$R_s = 0.1\ \Omega$
dq-axis inductance	$0.1 \leq L_{dq} \leq 0.9$ mH	$L_{dq} = 0.5$ mH
Excitation inductance	$0.4 \leq L_e \leq 0.6$ H	$L_e = 0.45$ H
Mutual inductance	$1.5 \leq M \leq 3$ mH	M = 2.1 mH
Excitation resistance	$0.5 \leq R_e \leq 1\ \Omega$	$R_e = 0.7\ \Omega$
Pole pair number	p=6	p = 6
Moment of inertia	$0.007 \leq J \leq 0.02$	J = 0.01
Friction coefficient	$0.002 \leq f \leq 0.004$	f = 0.003
Battery voltage	V_{bat} =12V	V_{bat} =12V
dc bus capacitor	C_f =33 mF	C_f = 33 mF

where J is the moment of inertia and $\Gamma_{load} = f.\omega + \Gamma_0$ is the load torque equation in which the f stands as a friction coefficient. The state equation of the DC bus voltage v_{dc}, according to the input filter shown in Figure 3.7, also comes as:

$$\frac{dv_{dc}}{dt} = \frac{1}{c_f}\left(i_{bat} - \frac{P_{in}}{v_{dc}}\right) \tag{3.12}$$

where P_{in} is the injected power into inverter and can be written as $P_{in} = v_d i_d + v_q i_q$.

As stated in previous chapter, the MFAC is supposed to be developed in this study to control the mentioned WRSM system. However, since MFAC consider the discrete-time system to design the controller. For this, the state equations (3.11) can be easily transformed into the following discrete-time model:

$$\begin{cases} i_e(k+1) = \frac{dt.L_d}{L_d L_e - M^2}\left(v_e(k) - R_e i_e(k) - \frac{M}{L_d}\left(v_d(k) - R_s i_d(k) + p.\omega(k).L_q.i_q(k)\right)\right) + i_e(k) \\ i_d(k+1) = \frac{dt.L_e}{L_d L_e - M^2}\left(v_d(k) - R_s.i_d(k) + p.\omega(k).L_q.i_q(k) - \frac{M}{L_e}\left(v_e(k) - R_e.i_e(k)\right)\right) + i_d(k) \\ i_q(k+1) = \frac{dt}{L_q}\left(v_q(k) - R_s.i_q(k) - p.\omega(k)\left(L_d.i_d(k) + M.i_e(k)\right)\right) + i_q(k) \\ \omega(k+1) = \frac{dt}{J}\left(p.i_q(k).i_d(k)\left(\left(L_d - L_q\right) + M.i_e(k)\right) - \Gamma_{load}(k)\right) + \omega(k) \end{cases} \tag{3.13}$$

where k and dt are the current time instant and time step size, respectively.

According to the WRSM system presented in this section and theory of MFAC explained in chapter 2, two different control schemes will be developed for this system in the following sections of this chapter. It is notable that the MFAC is a data-driven control which does not require any mathematical model of studied system to design the controller. By this way, the presented model of studied WRSM system (3.13) will be used only in simulation work and the controller will be designed merely using the I/O data related to system output and control inputs. In addition, the saturation, damping and parasitic effects in machine are not included in the presented mathematical model (3.13). Consequently, these effects will not be included in the simulation work. However, all these effects are existing in real system and will be tested by experimental works.

Since the parameter values of the studied system were changing according to the temperature, magnetic saturation and aging, the exact value for each parameter are not available. For this, in simulation we used the nominal parameter values given in Table 3.1. It should be noted that in practice ambient temperature varies in

a wide range from nearly $-40℃$ to $+60℃$. In addition, in this machine, magnetic saturation effect is significant which is generally the case of claw-pole rotor machines.

3.2. Current Control for WRSM Using MFAC

In current control of a WRSM drive system, the crucial objective is to guarantee that the stator currents track the reference values with minimum errors in both transient and steady-state conditions [98]. Looking at the literature, a couple of current control approaches have been applied for better current tracking performance. For example, hysteresis current control [99], internal model control [100], pulse width modulation control method [101], sliding mode control [102][103], fuzzy control [104] and widely developed proportional-integral (PI) control method [105][106]. To design a robust controller with acceptable tracking performance, all the mentioned model-based control (MBC) methods require good knowledge about the dynamics and the model of the studied system. However, in industrial applications and especially in complex nonlinear systems, it is quite difficult and time consuming to find a correct dynamic model of the studied system. Since the unexpected dynamic variation of system and parametric errors are very common in industrial applications, the MBC performance can be affected under such conditions. In addition, since the MBC methods require an accurate model of the controlled system to design the controller, these methods may not be applicable for the systems whose model is not available. Thus, to get rid of the limitations of MBC, the industry demands the controllers with less dependence on the model of the plant. Thus, the model predictive control (MPC) technique has been proposed as an appropriate current control scheme for electric machines which guarantees a fast dynamic and a remarkable safety factor [107], [108]. This method's principle is based on making a prediction of controlled variables in the next calculation step by using the measured variables and a mathematical model of the controlled system. Then, analyzing the predicted results using a cost function related to the difference between the desired trajectories and real outputs of the system. Compared to the previously mentioned control techniques, safety and fast dynamics are two remarkable features of the MPC method. Despite these advantages, since the MPC uses a mathematical model in the prediction section, its performance highly depends on the correctness of the model [109]. In addition, using the prediction at each sampling time of the MPC algorithms, import some additional mathematical calculations into the control algorithm.

Facing those limitations of abovementioned MPC and MBC techniques clarifies the crucial role of the development of the data-driven control (DDC) theory which is already investigated in Chapter 2. Motivated by abovementioned considerations, a data-driven model-free adaptive control based on full form dynamic linearization (FFDL) technique is developed for current control of a wound rotor synchronous machine (WRSM) drive system, manufactured by Valeo as a mild-hybrid system called i-StARS. A well-known model-based PI controller is also developed to compare with the MFAC method. As concluded before, the MBC techniques are however sensitive against electrical parameter variation and parameter error, while MFAC method is completely robust towards these phenomena. Thus, developing an effective attitude control for the AC machine drive applications by using the MFAC, which is rarely used before, is of a high importance to get ride of limitations of commonly used MBC schemes. This work may also be useful to demonstrate the capability of data-driven control methods in some other industrial applications.

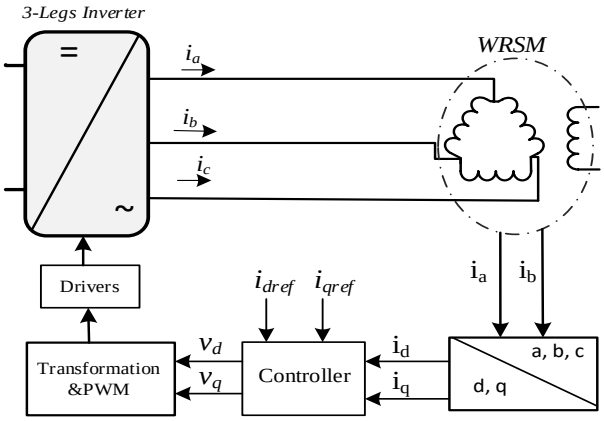

Figure 3.15. Control diagram of the studied WRSM drive system.

3.2.1. MFAC Design for Current Control of Studied WRSM System

According to the theory of MFAC presented in Chapter 2, a FFDL-based MFAC is developed for the studied WRSM system (3.13). In this system, the rotor excitation current i_e is assumed to be precisely controlled at $i_e = 4A$. As shown in Figure 3.15, the dq-frame phase currents $[i_d, i_q]$ are the measured system outputs and the dq-frame phase voltages $[v_d, v_q]$ are the control input signals which should be created by the controller. Indeed, this system is considered as a MIMO system including two system outputs and two control inputs which satisfies the Assumption 1.11 and the inputs and outputs of the system are observable and controllable. Also, this system meets the generalized Lipschitz condition, in which for any k

$$\left\|\Delta\begin{bmatrix} i_d(k+1) \\ i_q(k+1) \end{bmatrix}\right\| \le b \left\| \Delta\left[\begin{bmatrix} i_d(k) \\ i_q(k) \end{bmatrix}^T, \dots, \begin{bmatrix} i_d(k-L_y+1) \\ i_q(k-L_y+1) \end{bmatrix}^T, \begin{bmatrix} v_d(k) \\ v_q(k) \end{bmatrix}^T, \dots, \begin{bmatrix} v_d(k-L_y+1) \\ v_q(k-L_y+1) \end{bmatrix}^T\right]^T \right\| \tag{3.14}$$

Where b is a constant and $\Delta\begin{bmatrix} i_d(k+1) \\ i_q(k+1) \end{bmatrix} = \begin{bmatrix} i_d(k+1) \\ i_q(k+1) \end{bmatrix} - \begin{bmatrix} i_d(k) \\ i_q(k) \end{bmatrix}$. It means that the changes of system outputs are totally bounded by changes of all system variables including control input. Furthermore, this condition clarifies that the limited changes of control input signals $\begin{bmatrix} v_d \\ v_q \end{bmatrix}$ will not cause to the infinite variation of the system output $\begin{bmatrix} i_d \\ i_q \end{bmatrix}$.

Therefore, selecting the output-related and input-related linearization orders as $L_y = L_u = 5$, the nonlinear system (3.13) is transformed into the following full-form dynamic linearization data model

$$\begin{bmatrix} i_d(k+1) \\ i_q(k+1) \end{bmatrix} = \varphi_{p,L_u,L_y}(k)\, \Delta\left[\begin{bmatrix} i_d(k) \\ i_q(k) \end{bmatrix}^T, \dots, \begin{bmatrix} i_d(k-4) \\ i_q(k-4) \end{bmatrix}^T, \begin{bmatrix} v_d(k) \\ v_q(k) \end{bmatrix}^T, \dots, \begin{bmatrix} v_d(k-4) \\ v_q(k-4) \end{bmatrix}^T\right]^T + \begin{bmatrix} i_d(k) \\ i_q(k) \end{bmatrix} \tag{3.15}$$

where

$$\varphi_{p,L_u,L_y}(k) = \left[\begin{bmatrix} \varphi_{11(1)}(k) & \varphi_{12(1)}(k) \\ \varphi_{21(1)}(k) & \varphi_{22(1)}(k) \end{bmatrix} \begin{bmatrix} \varphi_{11(2)}(k) & \varphi_{12(2)}(k) \\ \varphi_{21(2)}(k) & \varphi_{22(2)}(k) \end{bmatrix} \dots \begin{bmatrix} \varphi_{11(10)}(k) & \varphi_{12(10)}(k) \\ \varphi_{21(10)}(k) & \varphi_{22(10)}(k) \end{bmatrix}\right] \in R^{2\times 20},$$

is an unknown time-varying matrix that includes all the possible complicated behaviors of the system (3.13). Since this matrix is unknown, its arrays should be estimated at each sampling time. For this, following cost function of the $\varphi_{p,L_u,L_y}(k)$ estimation is used:

$$J\left(\varphi_{p,L_u,L_y}(k)\right) = \left\|\Delta\begin{bmatrix} i_d(k) \\ i_q(k) \end{bmatrix} - \varphi_{p,L_u,L_y}(k)\Delta H_{L_y,L_u}(k-1)\right\|^2 + \mu\left\|\varphi_{p,L_u,L_y}(k) - \hat{\varphi}_{p,L_u,L_y}(k-1)\right\|^2 \tag{3.16}$$

Where $\Delta H_{L_y,L_u}(k) = \Delta\left[\begin{bmatrix} i_d(k) \\ i_q(k) \end{bmatrix}^T, \dots, \begin{bmatrix} i_d(k-4) \\ i_q(k-4) \end{bmatrix}^T, \begin{bmatrix} v_d(k) \\ v_q(k) \end{bmatrix}^T, \dots, \begin{bmatrix} v_d(k-4) \\ v_q(k-4) \end{bmatrix}^T\right]^T$ and $\hat{\varphi}_{p,L_u,L_y}(k)$ is the estimated value of the $\varphi_{p,L_u,L_y}(k)$.

Minimizing cost function (3.16) according to the $\varphi_{p,L_u,L_y}(k)$ brings the following estimation algorithm of $\varphi_{p,L_u,L_y}(k)$.

$$\hat{\varphi}_{p,L_u,L_y}(k) = \hat{\varphi}_{p,L_u,L_y}(k-1) + \frac{\eta\left(\Delta\begin{bmatrix} i_d(k) \\ i_q(k) \end{bmatrix} - \hat{\varphi}_{f,L_u,L_y}(k-1)\Delta H_{L_u,L_y}(k-1)\right)\Delta H_{L_u,L_y}{}^T(k-1)}{\mu + \left\|\Delta H_{L_u,L_y}(k-1)\right\|^2} \tag{3.17}$$

In addition, a reset structure is used for estimation law (3.17) to empower this estimation algorithm with a powerful capability to track the time-varying parameter as below.

$$\hat{\varphi}_{ii(6)}(k) = \hat{\varphi}_{ii(6)}(1),$$
$$if\ \left|\hat{\varphi}_{ii(6)}(k)\right| < b_2\ or\ \left|\hat{\varphi}_{ii(6)}(k)\right| > ab_2\ \ or\ sign\left(\hat{\varphi}_{ii(L_y+1)}(k)\right) \neq sign\left(\hat{\varphi}_{ii(6)}(1)\right), i = 1, \dots, m \tag{3.18}$$

$$\hat{\varphi}_{ij(6)}(k) = \hat{\varphi}_{ij(6)}(1), \qquad if\ \left|\hat{\varphi}_{ij(6)}(k)\right| < b_1\ \ or\ sign\left(\hat{\varphi}_{ij(6)}(k)\right) \neq sign\left(\hat{\varphi}_{ij(6)}(1)\right), i, j = 1, \dots, m, i \neq j \tag{3.19}$$

where the $\hat{\varphi}_{ij(L_y+1)}(1)$ denotes the initial value of $\hat{\varphi}_{ij(L_y+1)}(k)$, $i = 1, \dots, m, j = 1, \dots, m$, and the sign of parameter is supposed to stay unchanged for all k.

By estimation of the $\varphi_{p,L_u,L_y}(k)$, controller can be designed properly. To do so, following cost function of the control input is used.

$$J\left(\left[v_d(k), v_q(k)\right]\right) = \left\|\begin{bmatrix} i_d^*(k+1) \\ i_q^*(k+1) \end{bmatrix} - \begin{bmatrix} i_d(k+1) \\ i_q(k+1) \end{bmatrix}\right\|^2 + \lambda\left\|\begin{bmatrix} v_d(k) \\ v_q(k) \end{bmatrix} - \begin{bmatrix} v_d(k-1) \\ v_q(k-1) \end{bmatrix}\right\|^2 \tag{3.20}$$

where the $\lambda > 0$ is a weight factor which is used to limit the changes of control input, and the $y^*(k+1)$ is the reference trajectory of system output.

Putting the FFDL data model (3.15) into cost function (3.20) and differentiating according to control input $\begin{bmatrix} v_d(k) \\ v_q(k) \end{bmatrix}$ and setting to be zero brings the controller algorithm as follows.

$$\begin{bmatrix} v_d(k) \\ v_q(k) \end{bmatrix} = \begin{bmatrix} v_d(k-1) \\ v_q(k-1) \end{bmatrix} + \frac{\varphi_6^T(k)\left(\rho_6\left(\begin{bmatrix} i_d^*(k+1) \\ i_q^*(k)+1 \end{bmatrix} - \begin{bmatrix} i_d(k+1) \\ i_q(k+1) \end{bmatrix}\right)\right)}{\lambda + \|\varphi_6(k)\|^2}$$
$$- \frac{\varphi_6^T(k)\left(\sum_{i=1}^{5}\rho_i\,\varphi_i(k)\Delta\begin{bmatrix} i_d(k-i+1) \\ i_q(k-i+1) \end{bmatrix} + \sum_{i=7}^{10}\rho_i\,\varphi_i(k)\Delta\begin{bmatrix} v_d(k+6-i) \\ v_q(k+6-i) \end{bmatrix}\right)}{\lambda + \|\varphi_6(k)\|^2} \quad (3.21)$$

Thus, using the control law (3.21), the control signals $\begin{bmatrix} v_d(k) \\ v_q(k) \end{bmatrix}$ will be obtained at each sampling time. As shown in Figure 3.16, all the application of the MFAC, including estimation of matrix $\varphi_{p,L_u,L_y}(k)$ and creating the control signals $\begin{bmatrix} v_d(k) \\ v_q(k) \end{bmatrix}$, are performed merely using the I/O data obtained from system output and control input. As stated before, several parameters are used in controller design $i.e.\ \lambda, \mu, \eta, \rho_i, a, b_1$ and b_2. Selection of optimal parameters for controller is challenging and they are normally chosen by trial and error. In this paper, the selection of these parameters is performed by using a genetic algorithm optimization method. The cost function to be minimized is the mean square error of the *dq*-currents tracking a given profile. This error is calculated in simulation using the nominal model. Once these parameters are set, they are used in both simulation and experimental tests, while in the latter the parameters are rather uncertain and different from their nominal values. The selected controller parameters are presented in Table 3.2.

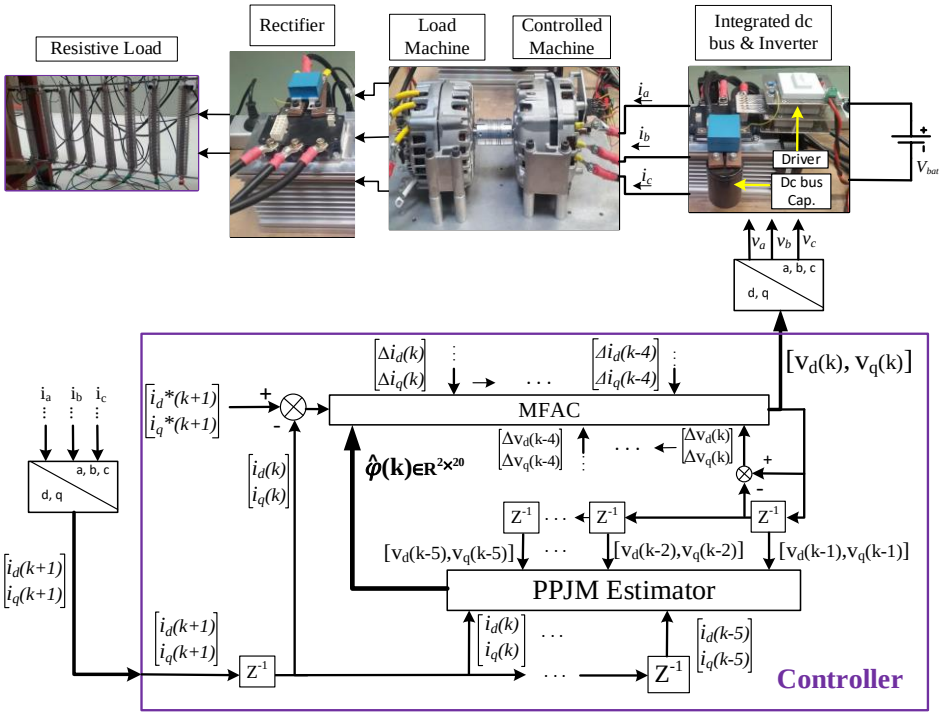

Figure 3.16. General control diagram of the studied system.

TABLE 3.2: PARAMETERS USED IN MFAC

Parameter	Value
b_1	1
b_2	20
a	2
ε	1e-6
λ	5
μ	2
η	0.72
ρ_1	0.71
ρ_2	0.87
ρ_3	0.19
ρ_4	0.55
ρ_5	0.13
ρ_6	0.31
ρ_7	0.67
ρ_8	0.53
ρ_9	0.17
ρ_{10}	0.52

3.2.2. Simulation Results

In this section the numerical simulation study, using MATLAB Simulink, is performed to observe the effectiveness of the MFAC in current control of a WRSM system. Figure 3.16 shows the control diagram of the studied system. The rotor excitation current i_e, is supposed to be precisely controlled at $i_e = 4A$ and the switching frequency is set on 10kHz for all tests.

Since the parameter values of the studied system were changing according to the temperature, magnetic saturation and aging, the exact value for each parameter is not available. For this reason, the simulation was done using the nominal parameter as given in Table 3.1. It should be noted that in practice ambient temperature varies in a wide range from nearly $-40℃$ to $+60℃$. In addition, in this machine, magnetic saturation effect is significant which is generally the case of claw-pole rotor machines.

3.2.2.1. Simulation Results with MFAC

In order to verify the robustness of developed MFAC, the simulation study is carried out under starting performance, operating point variation, parameter variation and in presence of load torque disturbance. Since any parameter is used to design the controller, the parametric error is also added automatically in simulation conditions.

A. Starting Performance and Operating Point Variation

At the first step of simulation ($t = 0.5s$), the operating point corresponds to a $q - axis$ stator current of 20A, then it rises to 40A and 60A at the $t = 5s$ and $t = 11s$ respectively. Finally, the $q - axis$ stator current drops to 35A at fourth simulation step ($t = 15s$). During all simulation steps, the desired d-axis stator current is supposed to be zero ($i_{dref} = 0A$). The simulation results for measured variables (i_d, i_q), unmeasured variable (ω) and control input signals (v_d, v_d) are shown in Figure 3.17. As shown in these results, there is no

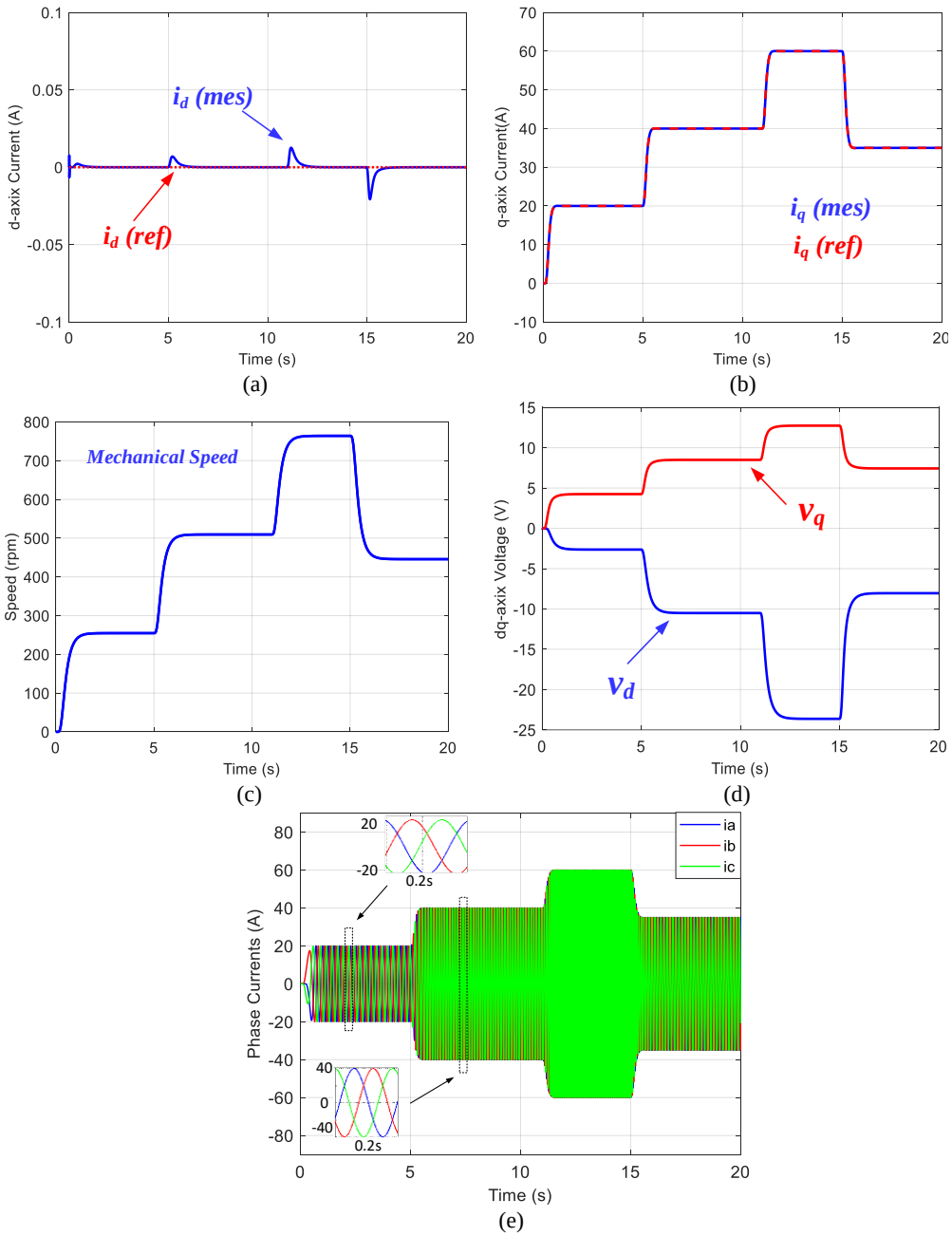

Figure 3.17. Simulation results of MFAC for, a) current, b) i_q current, c) Mechanical speed of rotor, d) Control input signals, e) Phase currents i_a, i_b, i_c in different operating points.

control error in the steady state of stator currents and just a very small error occurs during transient because of the variation of the operating point.

B. Parameter Variation and Load Torque Disturbance

In the practical works, the capacitors, resistances, inductances, and other parameters of the system can change due to temperature or other factors. Besides, the load torque equation, Γ_{load}, is generally unknown and an approximate equation, like $\Gamma_{load} = f.\Omega - \Gamma_0$ in (3.13), is usually used in calculations. This characteristic may lead to suddenly and unexpected variation of Γ_{load} and affect control performance as well. To see the

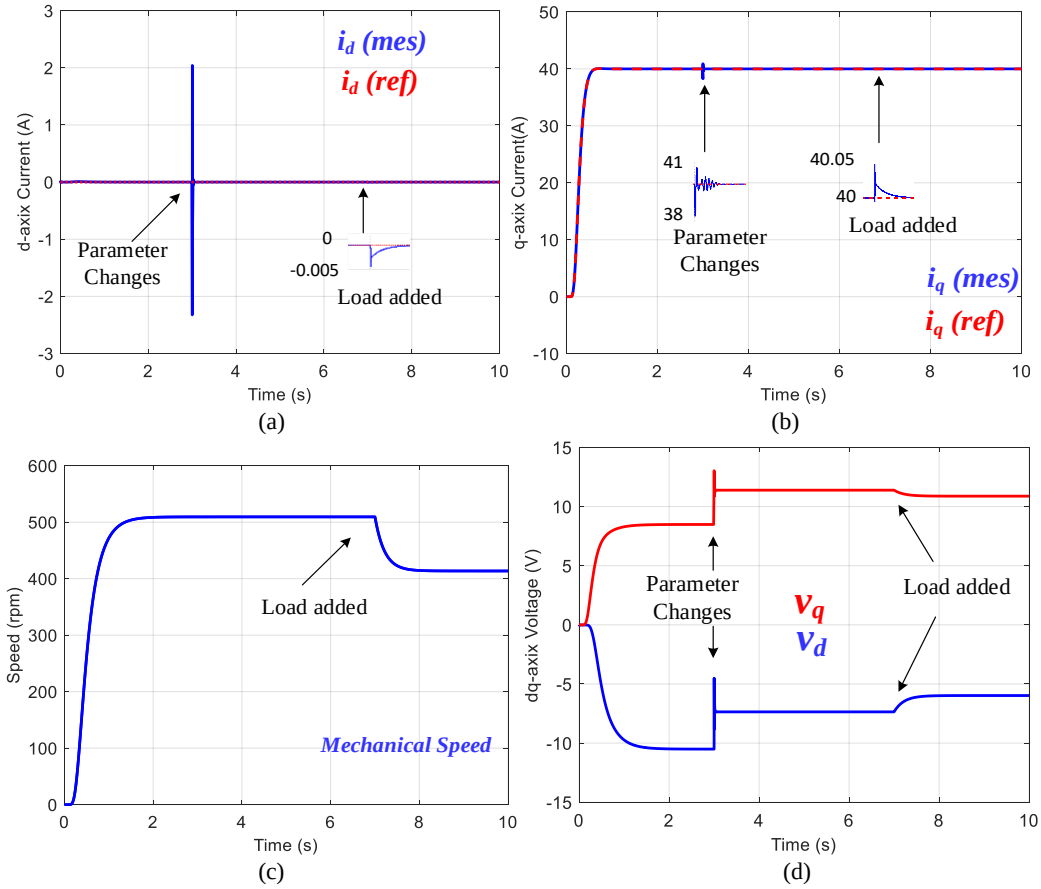

Figure 3.18. Simulation results of MFAC for, a) i_d current, b) i_q current, c) Mechanical speed of rotor, d) Control input signals, under +50% parameter variation and load torque disturbances.

effects of these two phenomena, the simulation is carried out in operating point with $i_d = 0A, i_q = 40A$. Firstly, the system parameters, R_s, L_d, L_q, are increased 50% at $t = 3s$, then an unexpected load is added to the system at $t = 7s$. While this manner of parameter variation cannot practically happen, but the worst case is considered to be tested in this work. The results related to this study is shown in Figure 3.18. According to these results, there is no error in steady state and transient of the measured and unmeasured variables that indicates a strong performance of MFAC under parameter variation and load torque disturbance.

3.2.2.2. Simulation Results with PI Controller

Relying on the fact that the PI controller is commonly used in industry, as a reliable controller, this controller is developed to compare with MFAC strategy. Since the PI controller is a model- based method, it requires some knowledge about the model and parameters of the studied system to design the controller gains (K_p and K_i). Thus, the mathematical model (3.13) and the nominal parameter values, shown in Table 3.1, are used to design the PI controller. Considering the rated parameters as $R_s = 0.1\ \Omega$ and $L_d = L_q = 0.5\ mH$, and using the pole-zero compensation technique, the controller parameters was designed as $K_p = 0.4, K_i = 80$. The simulation performance of the designed PI controller with these gains is presented in Figure 3.19 and 3.20 for

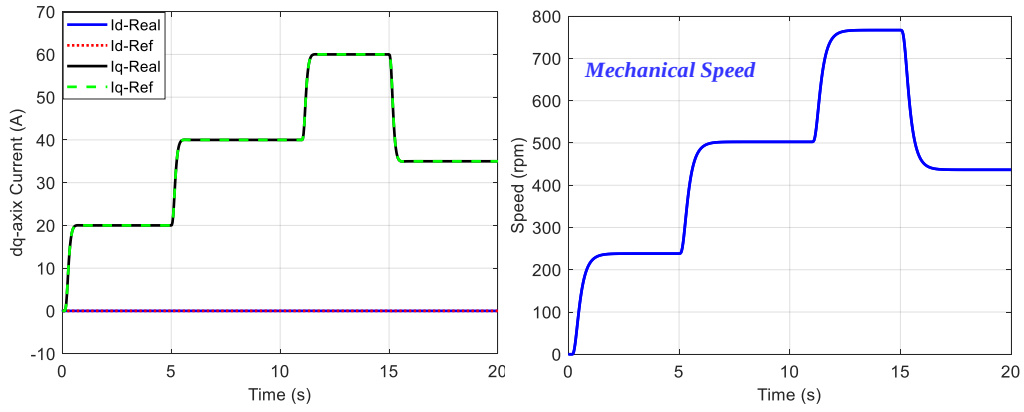

(a) (b)

Figure 3.19. Simulation results of PI controller for, a) i_d and i_q currents, b) Mechanical speed of rotor, in different operating points.

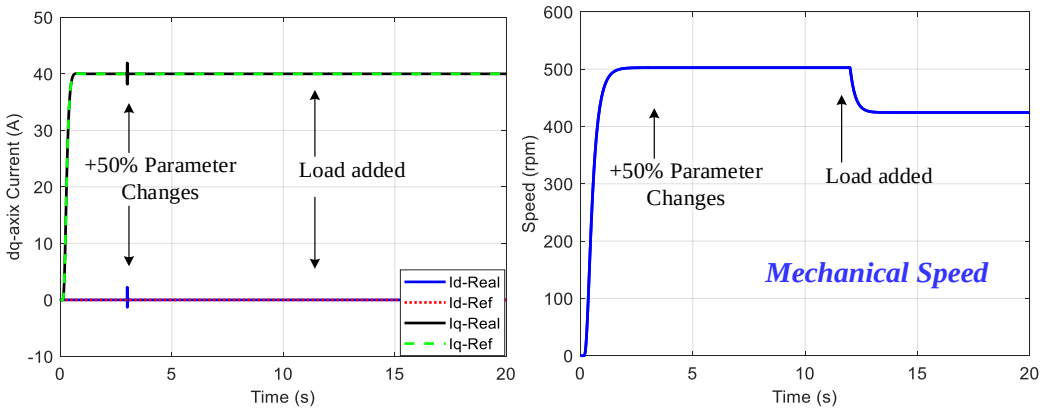

(a) (b)

Figure 3.20. Simulation results of PI controller for, a) i_d and i_q currents, b) Mechanical speed of rotor, under +50% parameter variation and load torque disturbances.

different operating points, parameter variations and load disturbances, respectively. As shown in these results, the obtained simulation performance of PI controller is very close to MFAC.

3.2.3. Experimental Results

As shown by simulation results, the developed MFAC method sounds to be a robust and effective control method under different operation conditions. In this step, in order to validate the simulation results, the performance of MFAC is tested on a real experimental test bench of the WRSM system. Moreover, a PI controller is also developed to compare with MFAC's performance.

Looking at the experimental test bench illustrated in Figure 3.7, the studied test bench consists of two WRSM, the one of the right stands as the controlled machine while the other is used as load. In this work, the load is presented by a machine supplying a resistor through a rectifier. A fixed 12V DC voltage source, instead of the battery, is connected to the DC bus capacitor. A dSPACE MicroLabBox is used to control the three-leg MOSFET inverter. The sampling and switching frequencies are also set on 10kHz. Besides, the general diagram of the studied system, including the electrical machines, representation of the control approach, the

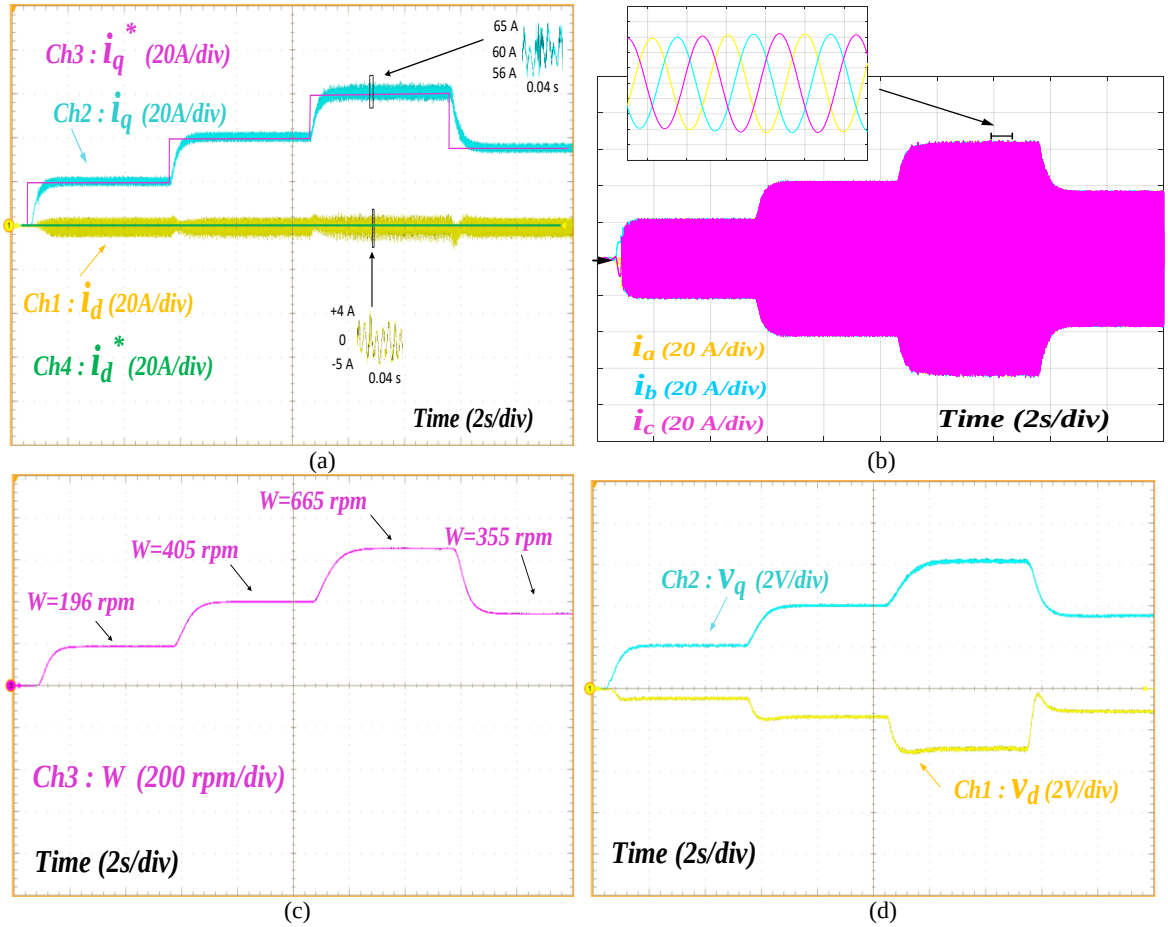

Figure 3.21. Experimental results of MFAC for, a) dq frame phase currents, b) abc frame phase currents, c) Mechanical speed of rotor, d) Control input signals, during different operating points.

power electronic interface and the resistive load, is presented in Figure 3.16 to show the connection and application of the test bench.

Similarly to the simulation work, different series of tests have been done in this section too. The first series includes the MFAC performance under different operating points and load torque disturbances. The second series of tests are done with a PI controller to compare with the MFAC performance.

3.2.3.1. Experimental Results with MFAC

In this section, the developed MFAC is applied to the experimental test bench. The same MFAC which is used in simulation work, is also used in practical work with no change in controller parameters and design approach. In the first step of experimental tests, the performance of MFAC is tested during different operating points. Similarly to the simulation work, the corresponding operating points for i_q are $20A, 40A, 60A, 35A$. The reference value of i_d is also supposed to be controlled at $i_d = 0A$. The obtained results are shown in Figure 3.21. The illustrated figures are a screenshot extracted directly from the oscilloscope. In the second step of this section, the MFAC performance has been tested under load torque disturbance effects: during a fixed operating

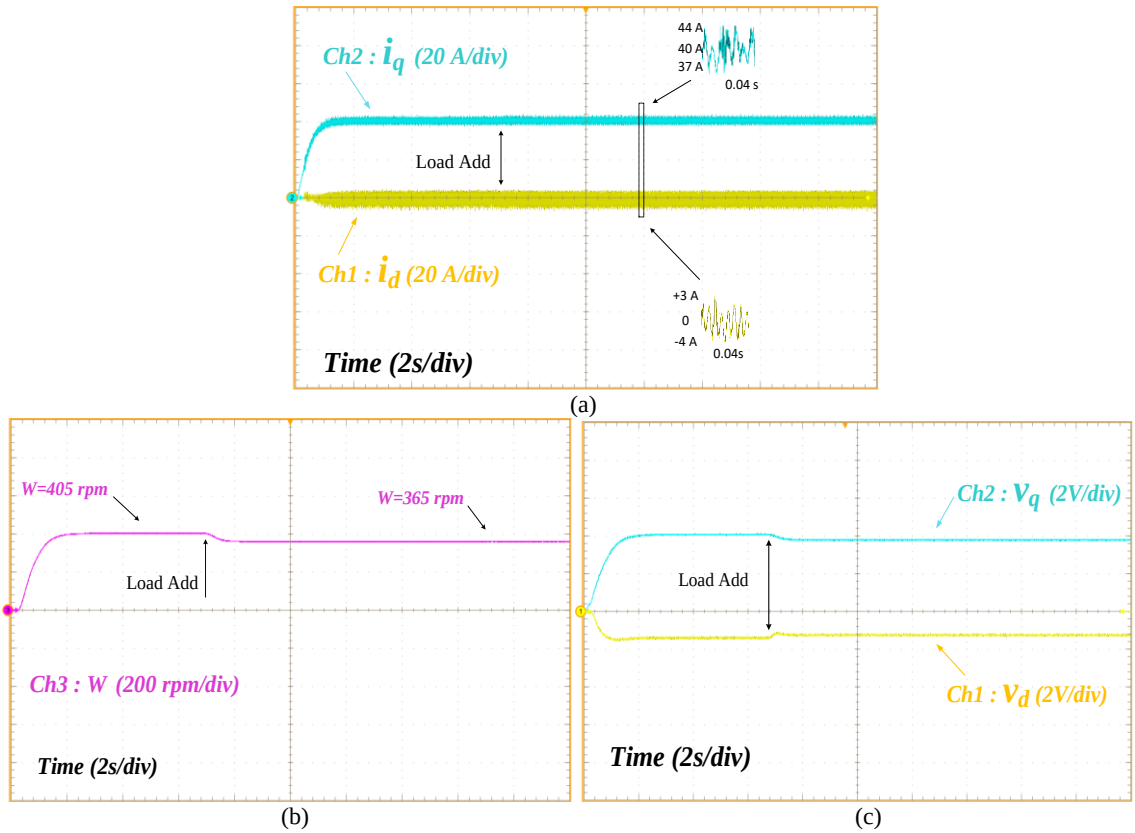

Figure 3.22. Experimental results of MFAC for, a) i_d and i_q currents, b) Mechanical speed of rotor, d) Control input signals, under load torque disturbance.

point of $i_q = 40A, i_d = 0A$, some load is added to the system. The effects of this added load on control performance are illustrated in Figure 3.22.

Comparing the experimental performance of MFAC, shown in Figure 3.21 and 3.22, with its performance in the simulation study, given in Figure 3.17 and 3.18, two main differences can be noticed. First, the convergence value of mechanical speed ω and control input signals v_d, v_q for the same i_{dq} references in simulation and experimental works are different. Second, the i_{dq} currents are converging with some oscillations around the operating point in experimental work, whereas in simulation study they have a smooth convergence. As mentioned before, since the precise model of the system was not available, an approximated model was used in simulation work. The parameters used in this approximate model also included some errors which are different from real values. This difference between real and approximated parameter values led to different steady state values of system variables. By this way, the good tracking performance of MFAC in both experimental and simulation works, practically confirms that the MFAC is an appropriate control method for the system with an unknown or badly known model. The oscillation of i_{dq} around the operating point can also be investigated from two aspects. First, the studied WRSM machine is designed for automotive applications and has low stator inductances. These low stator inductances may lead the stator currents to oscillate around the operating points. The weakness of the controller to create the proper signals can be the second reason for

i_{dq} oscillations. To check this hypothesis and validate the previously provided results, a PI controller is developed to compare with the MFAC.

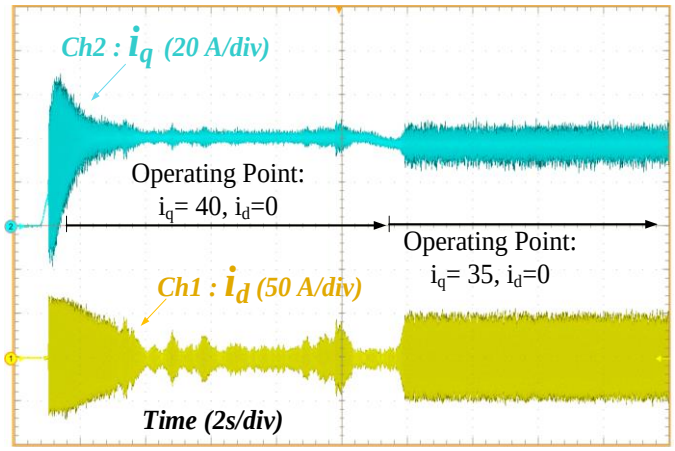

Figure 3.23. Experimental performance of PI controller with inappropriate gains ($K_p = 0.4, K_i = 80$).

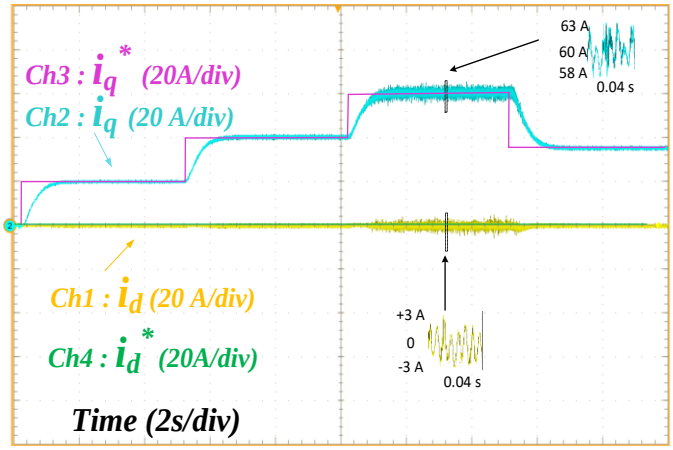

(a)

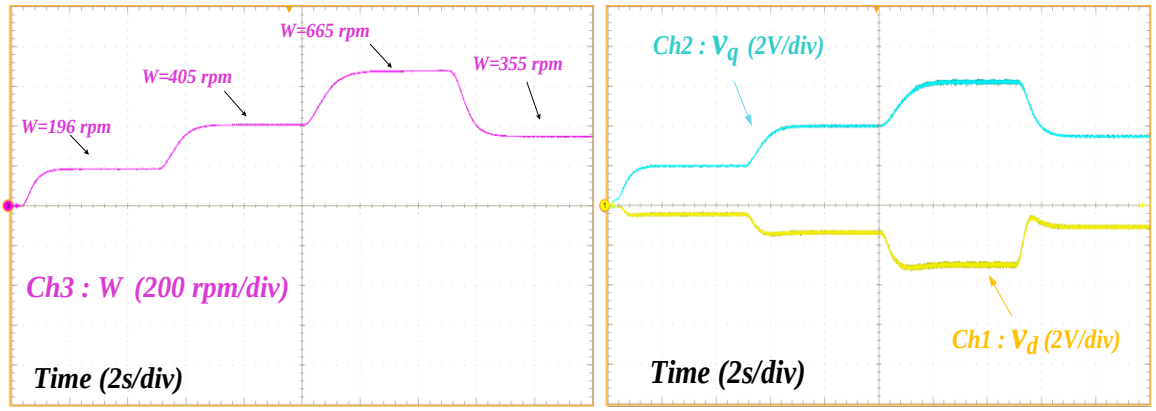

(b) (c)

Figure 3.24. Experimental results of PI controller for, a) i_d and i_q currents, b) Mechanical speed of rotor, in different operating poins.

3.2.3.2. Experimental Results with PI Controller

To study the experimental performance of PI controller, the first step is to use the controller gains ($K_p = 0.4, K_i = 80$) which were already tested successfully in simulation work. Contrarily with the simulation work, these gains reflected unsuitable control performance during the experimental tests, resulting to large oscillations of i_{dq} around their operating points and losing the control of the system by changing the operating point. This can be explained by the fact that the average model of system is used in simulation and the controller gains are also designed according to this averaged model, but in experimental work the system model is affected by several factors such as saturation and parameter variations which may lead to different controller performance. The performance of the PI controller, using $K_p = 0.4, K_i = 80$, is given in Figure 3.23 for two operating points of $i_q = 40A$ and $i_q = 35A$. Facing this problem led to do more analysis on the dynamic and model of the system to adjust the proper controller gains. Finally, by trial and error, the proper controller gains were fixed as $K_p = 0.1, K_i = 5$. Using these proper gains of PI controller, the experimental were carried out in the same platform used in MFAC. Figure 3.24 and Figure 3.25 show the experimental performance of proper PI controller under operating point variation and load torque disturbances, respectively.

Comparing the obtained results by PI and MFAC approaches, the obtained performance from both controllers are very close in terms of common figures of merit. Both controllers truly track the desired trajectories, i_{dq-ref}, during different operating points and both caused to the same operating point of mechanical rotor speed. Load torque disturbance doesn't affect the tracking performance of two mentioned controllers, and it can be concluded that they are totally robust against this phenomenon. Under PI controller also, i_{dq} are converged with some oscillations which are smaller than that of MFAC. It means that the small stator inductance of studied machine, as the main reason, intrinsically adds some oscillations on stator currents. Plus, the MFAC also adds a negligible additional oscillation on i_{dq} currents during convergence. Since the precise parameter values were not available, the designed PI controller using approximate values reflected considerable control error. While the MFAC design did not depend on the model of the system and had similar performance in both simulation and practical application.

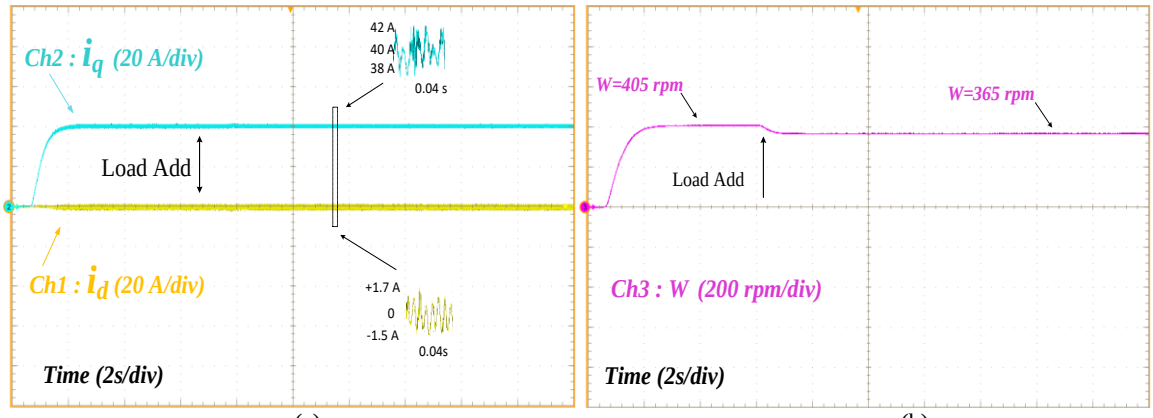

(a) (b)

Figure 3.25. Experimental results of PI controller for, a) i_d and i_q currents, b) Mechanical speed of rotor, under load torque disturbance.

Summing up, the experimental results validate the tracking performance of MFAC obtained in simulation work. Comparing the experimental performance of PI and MFAC, they lead almost to the same results. The only difference is that MFAC adds negligible additional steady state oscillation on the stator currents. Considering all the provided results, the effectiveness of MFAC can be concluded under different operating conditions. Since it is a model-free method, the controller design will face fewer restrictions and could be easily adaptable for practical applications. All these features clarify that the MFAC strategy can be a strong alternative to control of any unknown complex non-linear systems.

Relying on the effective performance obtained from simulation and experimental test for MFAC, this work will continue in the next section to develop another control algorithm for the WRSM system using the MFAC. In this control algorithm, the MFAC will be used for current sensorless control of the WRSM.

3.3. Current Sensorless Control of WRSM Using MFAC

Controlling the machine by removing the mechanical sensors is a sensorless control approach that is already widely developed in the literature. In this case, several sensorless control candidates are presented for synchronous machine. The back EMF estimation method [110]–[113] is one of the most widely developed methods that performs efficiently in mid and high speed, but there are some limitations related to its performance in low speed condition. Some of the other examples of sensorless methods can be listed as follows. The sliding mode observer [114], [115], Flatness based controller [116], high-frequency signal injection, classic PID and model-based adaptive methods. While removing the mechanical sensor reduces the costs and brings efficient control performance, each stator winding of a multi-phase machine still uses at least two current sensors which may considerably increase the cost due to increase of the number of sensors. Furthermore, in the hybrid vehicle applications, the electric machines are mostly operating in low voltage and high current conditions with multiple three phase stator windings which indicate the necessity of using multiple expensive current sensors. Considering these aspects, removing the several stator phase current sensors, instead of removing mechanical sensor, may be a superior approach for cost optimization and saving more space to increase the power density of the whole drive system.

In current sensorless control approach, since no current feedback is used, this is difficult to directly use the abovementioned controllers which all require a current feedback. That is the reason why the current sensorless control is rarely developed in industrial applications. According to the literature, some solutions are already proposed to validate the current sensorless approach. In [117], [118] instead of using the phase current sensors, the authors proposed to reconstruct the unmeasured phase currents using a good knowledge of the switching state and the DC current injecting to the inverter. This scheme requires a precise current sensor in DC bus which can be more expensive and bulkier. The phase currents also can be reconstructed by a numerical and step-by-step manner. However, this solution also needs a precise model of the system and correct information of the component used in the studied system. In [119], the Extended Kalman Filter (EKF) technique is used to estimate the stator currents. The paper [120] proves that the effectiveness of the EKF is highly dependent of the correctness of the model and parameters used in the studied system. Furthermore, the EKF intrinsically is a complex observer method due to using much numerical calculations during the estimation

procedure which can increase the complexity and response time of the controller. Considering these features of EKF, a new Lyapunov based observer is proposed in [120] for estimation of phase currents. Comparing to the EKF, the Lyapunov based estimator has a faster response and more reliable performance under parametric error. In all given examples, since an observer is used to estimate the phase currents, using the state model of the system is inevitable and the effectiveness of the controller is also highly dependent on the correctness of this model. However, reaching a very precise model is usually impossible or at least time-consuming. On the other hand, the system components can be changed due to the temperature or aging phenomena [121], [122] which can affect the control performance.

Summing up, sensorless control of AC drives have been studied in GREEN laboratory for over two decades, first as mechanical sensorless control of PMSM [1], then as current sensorless control in PhD study of Dr. Corne [32] [123]. Indeed, according to abovementioned considerations, a new project started on the current sensorless control of an AC drive for automotive applications. The aim was to reduce the cost without degrading the drive performances provided by an already implemented vector control. This project led to some new estimation approaches to estimate the phase currents. As a result, an observer-based current sensoless control for a WRSM was developed in [120]. However, the nonlinear estimators require a good knowledge of the dynamic model of the controlled system. Hence, they are sensitive to the model accuracy. This conclusion has been verified by employing several observers. To overcome this drawback, the model-free adaptive control (MFAC) in particular, and the data-driven control (DDC) in general, appear as appropriate alternatives due to their intrinsic independence from the model of the studied system. In this paper, the focus is on the MFAC as a solution to fix the previously mentioned limitations of the model-based approaches.

Looking at the literature, different kinds of model-free control algorithms have been applied in electrical machine field. Some of the important examples are listed as follows. A model-free predictive current control for interior PMSM drive based on current difference detection technique is presented in [98]. In [124] and [125], an improved model-free predictive current control is proposed for synchronous reluctance motor. The authors in [126] propose a continuous voltage vector model-free predictive current control of surface mounted PMSM to reduce the current ripples of finite control set model predictive control. A model-free non-singular terminal sliding mode control approach is also developed for PMSM demagnetization fault in [127]. A modulated model-free predictive control algorithm with minimum switching losses have been applied for PMSM drive system in [128].

According to the abovementioned control approaches, two current measurements are required at each sampling period to provide an effective model-free control performance. Besides, an ultra local model of the controlled system, instead of state-space model, is used in these approaches to realize the model-free control algorithm. The parameters of the ultra local models are also considered to be estimated using some algebraic parameter identification methods [128]. Since the ultra local models have only a finite number of parameters to estimate the behavior of the controlled system, some complicated behavior of the controlled system may not be evaluated properly. For this, the controller performance can be affected under several operating conditions such as load torque disturbances and parameter variation. Meanwhile, the MFAC is a data-driven control method that designs a weighted step ahead controller with creating an equivalent dynamic linearization data

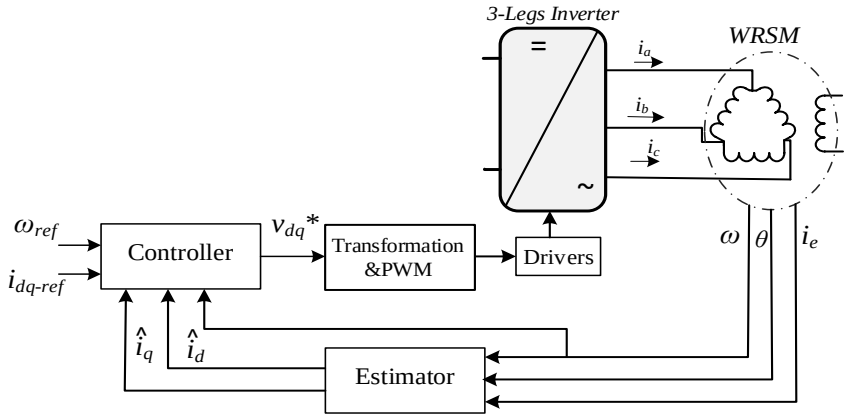

Figure 3.26. Control diagram using Lyapunov based estimator [32].

model of the controlled system at each sampling time and estimating system PJM, PG or PPD only using the I/O data of the controlled system and with no need of the identification process. In addition, since the DL data model of the system can include more parameters, the complicated behavior of the controlled system can be evaluated correctly and bring a robust controller under different operating conditions.

Relying on the MFAC's characteristics explained in chapter 2, the FFDL-based MFAC, as a data-driven controller, is proposed in this paper to be used in current sensorless control algorithm for i-StARS wound rotor synchronous machine (WRSM) drive system, designed by Valeo for mild-hybrid applications. The performance of proposed MFAC-based current sensorless control scheme is compared with the estimation-based current sensorless control scheme which is already developed by Dr. Corne in his PhD study [32]. The architecture of the estimation-based control algorithm is shown in Figure 3.26. In the developed current sensorless control scheme by Dr. Corne, instead of measuring the phase currents, an estimated value of these currents is used to be controlled. Whereas, this work will continue in this section to reach to a current sensorless controller with no estimation of the phase currents, which is commonly used in sensorless schemes, and without using the knowledge of the dynamics model of the system to design the controller. In this manner, the main limitations of previously used sensorless control techniques, the need for a precise model and parameter information, can be considerably fixed. In addition, since there is no additional estimation section, the complexity of the controller can be also reduced, which can lead to a faster controller.

3.3.1. Implementation of MFAC for current sensorless control of WRSM system

According to the control theory presented in Chapter 2, a FFDL-based MFAC is implemented for current sensorless control of the WRSM system (3.13). As shown in Figure 3.27.a, the system (3.13) is considered as a MISO system with one output and two control inputs, in which, the mechanical rotor speed ω, is the only system output and the stator dq voltages $[v_d, v_q]$ are considered as control inputs. It is noteworthy that the phase currents are not measured here because the objective of this work is to develop a current sensorless vector control for WRSM. This MISO system satisfies the Assumption 2.11 where the control inputs and

system output are controllable and observable. Besides, this system meets Assumption 2.12 condition which means that is a generalized Lipschitz for any k as follows:

$$\|\Delta\omega(k+1)\| \le b \left\| \Delta\left[\omega(k),\dots,\omega\left(k-L_y+1\right),\begin{bmatrix}v_d(k)\\ v_q(k)\end{bmatrix}^T,\dots,\begin{bmatrix}v_d\left(k-L_y+1\right)\\ v_q\left(k-L_y+1\right)\end{bmatrix}^T\right]^T \right\| \tag{3.22}$$

where b is a constant and $\Delta\omega(k+1)=\omega(k+1)-\omega(k)$.

Indeed, this condition represents that the variation of the system output is completely bounded by variation of all variables of the system.

Thus, choosing the input-related and output-related pseudo orders as $L_u = \mathrm{y} = 5$, the nonlinear MISO system (3.13) can be transformed into the following full-form dynamic linearization data model,

$$\omega(k+1)=\varphi_{p,L_u,L_y}(k)\,\Delta\left[\omega(k),\dots,\omega(k-4),\begin{bmatrix}v_d(k)\\ v_q(k)\end{bmatrix}^T,\dots,\begin{bmatrix}v_d(k-4)\\ v_q(k-4)\end{bmatrix}^T\right]^T+\omega(k) \tag{3.23}$$

where$\varphi_{p,L_u,L_y}(k)=\left[\varphi_1(k)\quad\cdots\quad\varphi_5(k),\begin{bmatrix}\varphi_{1(6)}(k)\\ \varphi_{2(6)}(k)\end{bmatrix}^T,\dots,\begin{bmatrix}\varphi_{1(10)}(k)\\ \varphi_{2(10)}(k)\end{bmatrix}^T\right]\in R^{1\times 15}$ is a matrix that stands for the full-form dynamic linearization data model of the studied system. The elements of this matrix are unknown and should be estimated during each sampling time. According to the estimation algorithm presented in Chapter 2, the following cost function of the $\varphi_{p,L_u,L_y}(k)$ is taken in account:

$$J\left(\varphi_{p,L_u,L_y}(k)\right)=\left\|\Delta\omega(k)-\varphi_{p,L_u,L_y}(k)\Delta H(k-1)\right\|^2+\mu\left\|\varphi_{p,L_u,L_y}(k)-\hat{\varphi}_{p,L_u,L_y}(k-1)\right\|^2 \tag{3.24}$$

where $\Delta H(k-1)=\Delta\left[\omega(k-1),\dots,\omega(k-5),\begin{bmatrix}v_d(k-1)\\ v_q(k-1)\end{bmatrix}^T,\dots,\begin{bmatrix}v_d(k-5)\\ v_q(k-5)\end{bmatrix}^T\right]^T$, $\hat{\varphi}_{p,L_u,L_y}$ is the estimated value of φ_{p,L_u,L_y} and μ is a weight factor.

Minimizing the cost function (3.24) according to $\varphi_{f,L_y,L_u}(k)$ brings the estimation algorithm as:

$$\hat{\varphi}_{f,L_y,L_u}(k)=\hat{\varphi}_{f,L_y,L_u}(k-1)+\frac{\eta\left(\Delta\omega(k)-\hat{\varphi}_{f,L_y,L_u}(k-1)\Delta H(k-1)\right)\Delta H^T(k-1)}{\mu+\|\Delta H(k-1)\|^2} \tag{3.25}$$

With resetting condition as:

$$\hat{\varphi}_{i(6)}(k)=\hat{\varphi}_{i(6)}(1),\ \text{if}\ \left|\hat{\varphi}_{i(6)}(k)\right|<b_2\ \text{or}\ \ sign\left(\hat{\varphi}_{i(6)}(k)\right)\neq sign\left(\hat{\varphi}_{i(6)}(1)\right),i=1,2 \tag{3.26}$$

To design the controller, the following cost function of the control inputs is considered:

$$J\left(\begin{bmatrix}v_d(k)\\ v_q(k)\end{bmatrix}\right)=\|\omega^*(k+1)-\omega(k+1)\|^2+\lambda\left\|\begin{bmatrix}v_d(k)\\ v_q(k)\end{bmatrix}-\begin{bmatrix}v_d(k-1)\\ v_q(k-1)\end{bmatrix}\right\|^2 \tag{3.27}$$

Then, minimizing the cost function (3.27) with respect to the $\begin{bmatrix}v_d(k)\\ v_q(k)\end{bmatrix}$, brings the control algorithms as follows:

$$\begin{bmatrix}v_d(k)\\ v_q(k)\end{bmatrix}=\begin{bmatrix}v_d(k-1)\\ v_q(k-1)\end{bmatrix}+\frac{\hat{\varphi}_6(k)\left(\rho_6\left(\omega^*(k+1)-\omega(k)\right)\right)}{\lambda+\|\hat{\varphi}_6(k)\|^2}$$
$$-\frac{\hat{\varphi}_6(k)\left(\sum_{i=1}^{5}\rho_i\hat{\varphi}_i(k)\Delta\omega(k-i+1)\ +\ \sum_{i=7}^{10}\rho_i\hat{\varphi}_i(k)\Delta\begin{bmatrix}v_d(k+6-i)\\ v_q(k+6-i)\end{bmatrix}\right)}{\lambda+\|\varphi_6(k)\|^2}$$

(3.28)

As stated before, no mathematical model of the controlled system is used in this control algorithm and the controller is designed merely using the I/O data related to system output and control inputs.

As mentioned before, several parameters are used in the controller $i.e.\ \lambda, \mu, \eta, \rho_i, a, b_1$ and b_2. Optimal selection of these parameters is always challenging. To fix this issue, some parameter tuning tools, such as hyper-optimization tools [129] and other automatic parameter tuning method presented in [130] have been already proposed in the literature to avoid using trial and error. However, in this paper, a Genetic Algorithm (GA) optimization method is used for selection of MFAC parameters. In this algorithm, the mean square error of the *dq*-currents tracking a given profile is considered as the cost function to be minimized. This error is calculated in simulation using the nominal model. Once the controller parameters are set, they are used in both simulation and experimental tests, while in the latter the parameters are rather uncertain and different from their nominal values due to variable operating point. It should be

noted that during the tests, different profiles than those used in GA have been realized. The selected controller parameters are presented in Table 3.3. The structure of the designed FFDL-based MFAC is illustrated in Figure 3.27.b.

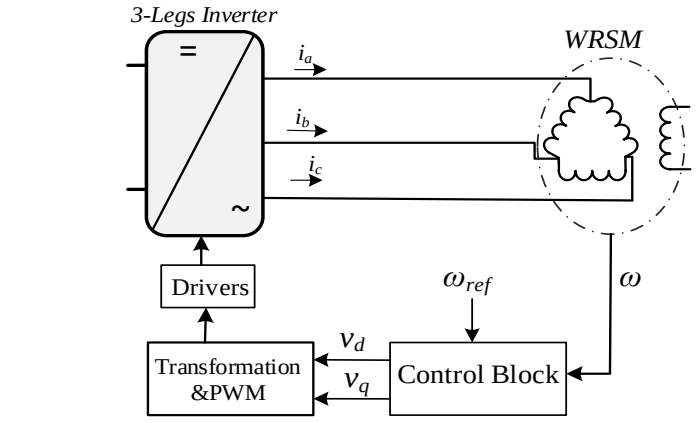

(a)

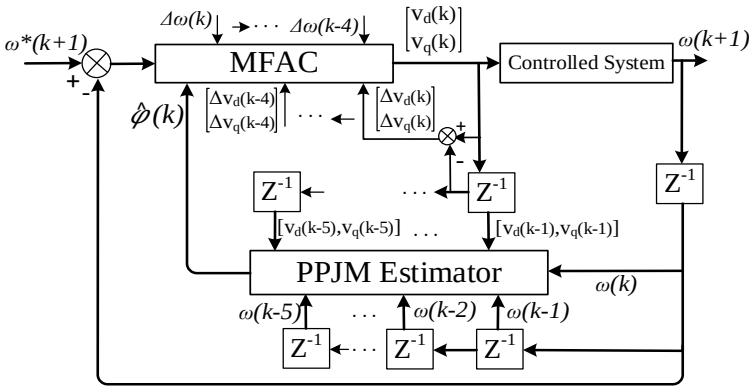

(b)

Figure 3.27. a) Current sensorless control diagram of the studied WRSM drive system, b) Structure of FFDL-based MFAC with $L_u = L_y = 5$.

TABLE 3.3: PARAMETERS USED IN MFAC

Parameter	Value
b_1	1
b_2	300
a	2
ε	1e-6
λ	25
μ	5
η	0.92
ρ_1	0.61
ρ_2	0.57
ρ_3	0.29
ρ_4	0.55
ρ_5	0.13
ρ_6	0.05
ρ_7	0.71
ρ_8	0.035
ρ_9	0.27
ρ_{10}	0.92

3.3.2. Simulation Results

In this section the simulation work, using MATLAB Simulink, is performed to test the effectiveness of the MFAC in current sensorless control algorithm. Figure 3.27 shows the control diagram which is used in this paper. The rotor excitation current i_e, is separately controlled at $i_e = 4A$ and the switching frequency is set on 10kHz for all tests of this work.

In this simulation work, several tests were performed on the proposed controller in order to evaluate its performance. Startup, operating point variation, parameter changes and load torque disturbances are considered. Indeed, as no system parameter is used in control algorithm, the parameter error is also considered automatically for this work. Since the exact value of the system components was not available, the simulation was done using specification presented on Table 3.1.

According to the platform used in this work, the system starts at the standstill of the WRSM then at 0.1s the operating point corresponds to a rotor speed of 500 rpm, then at 3.5s there is a second speed variation from 500 rpm to 800 rpm finally at 6.5s there is the third step from 800 rpm to 600 rpm. According to the parameter values and the full load condition used in simulation, the expected $q-axis$ stator current related to the rotor speed of 500 rpm, 800 rpm and 600 rpm are 218 A, 312 A and 250 A, respectively. In this work, the $i_d = 0$ control strategy is also used for $d-axis$ stator current. The results shown in Figure 3.28 represent the robustness of MFAC in which there is no error in the steady state of rotor speed (measured and controlled variable) and the phase currents (unmeasured and uncontrolled variables), which they all converged to the expected values of their operating points. Comparing the tracking performance of MFAC with observation-based control scheme, shown in Figure 3.29, the obtained simulation performance from both control methodologies are very close in which the unmeasured dq-currents converge truly toward the desired values.

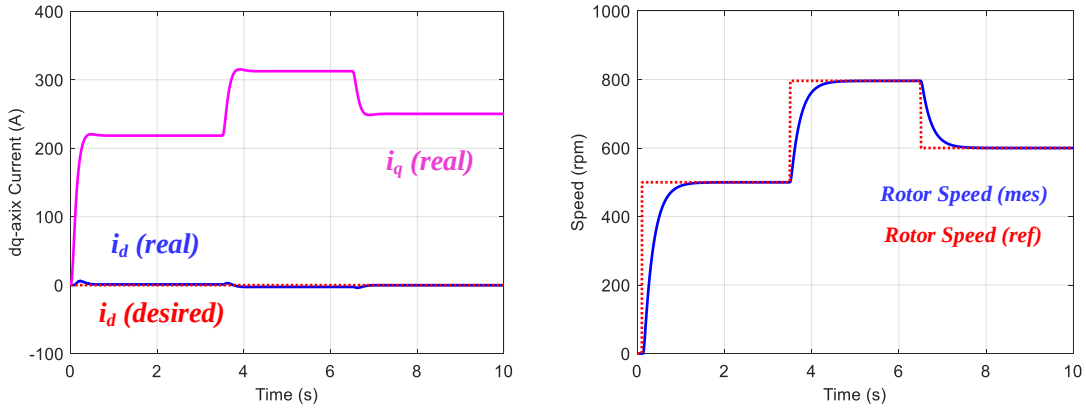

(a) (b)

Figure 3.28. Simulation results of MFAC for, a) i_{dq} current, b) Mechanical speed of rotor, in different operating points.

In practical applications, some system components, such as resistances, inductances, and capacitors, may vary due to aging, temperature or other factors. To test the MFAC performance under this phenomenon, parameter variation of +50% on R_s, L_d and L_q are included during an operating point of 500 rpm for rotor speed under a full load condition. While this amount of parameter changes cannot occur suddenly, the worst case is tested in this section. As presented in Figure 3.30, parameter variation adds nearly no error in steady state of rotor speed and $q-axis$ phase current. There is only a small static error in the convergence of $d-axis$ phase current in steady state. This error can be explained by the fact that the parameters of MFAC was firstly selected for the parameters of machine which are used in simulation, but by highly variation of parameters of machine, the previously selected controller parameters may not be fitted for the new situation. To better understanding the effectiveness of MFAC performance against parametric error and parameter variation, its performance can be compared with the simulation results of dq-currents, which is obtained under +50% error of R_s, L_d and L_q, using observation-based control method, that is shown in Figure 3.31. According

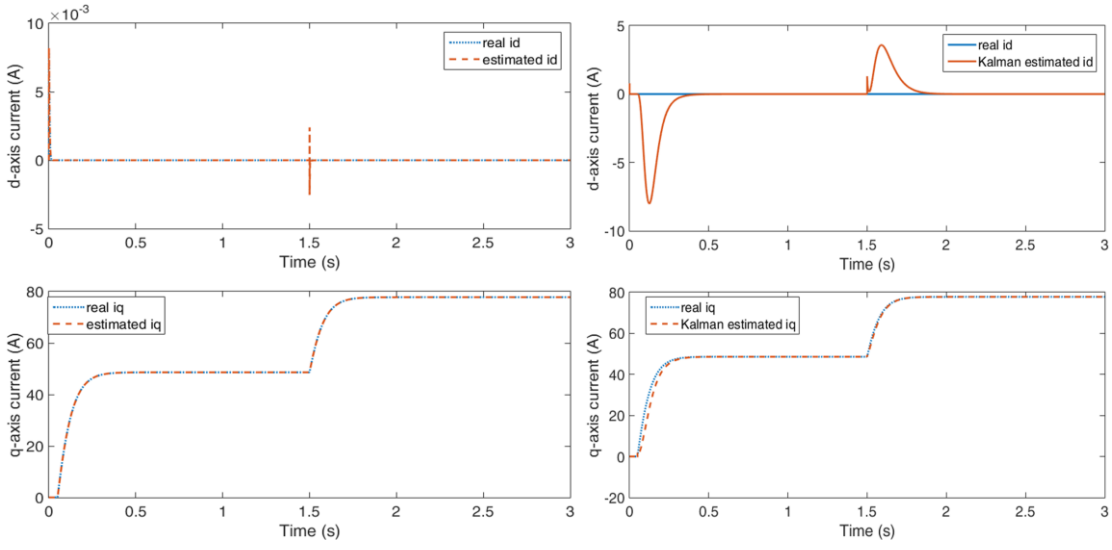

(a) (b)

Figure 3.29. Simulation results of i_{dq} estimation compared to the actual current with a) nonlinear observer, b) EKF proposed in [32].

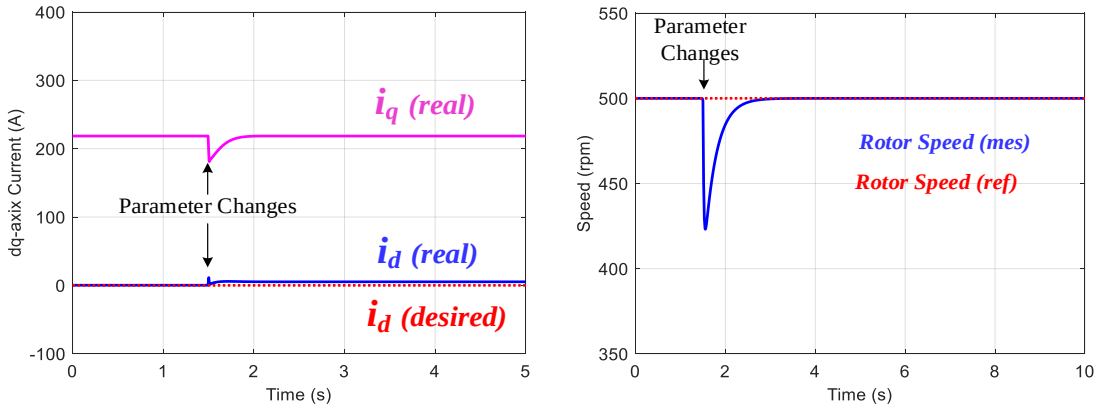

(a) (b)

Figure 3.30. Simulation results of MFAC for, a) i_{dq} current, b) Mechanical speed of rotor, under +50% parameter variation.

to these results, performance of observation-based control method is highly sensitive to parametric error where, estimation of dq-currents contain a considerable amount of error and they converge to the wrong values. Whereas, using the MFAC, a small static error is added only on d-axis current while the q-axis current converged precisely to the desired value. This difference can be cleared once again by relying on the fact that all the observation-based control methods use a dynamics model of the studied system and its performance is highly dependent on correctness of this model, while the MFAC does not require any model and works with only utilizing the I/O data measured from controlled system.

An additional test is carried out by simulation to test the robustness of MFAC to load torque disturbances. In this case, a load step is applied while system is operating at 500 rpm of rotor speed. According to this step, the load is decreased from full load to half load condition. Similarly to parameter variation, this phenomenon also doesn't causes any steady state error of rotor speed and $q-axis$ phase current and just adds some static error on convergence value of $d-axis$ phase current. In this case, since the rotor speed is controlled, by

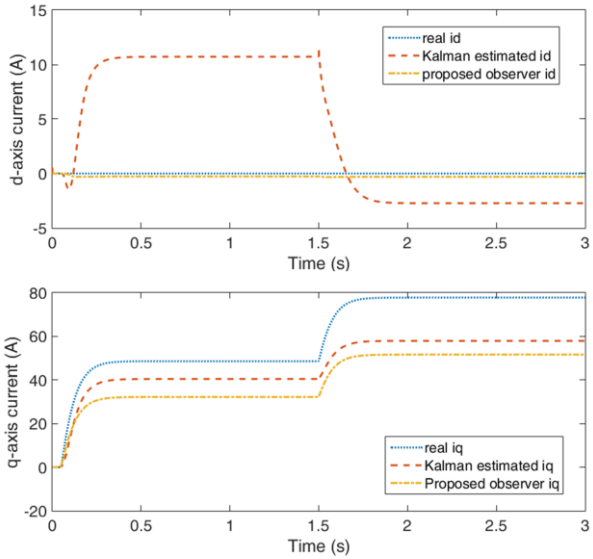

Figure 3.31. Simulation results of MFAC for, a) i_{dq} current, b) Mechanical rotor speed, under +50% parameter variation [32].

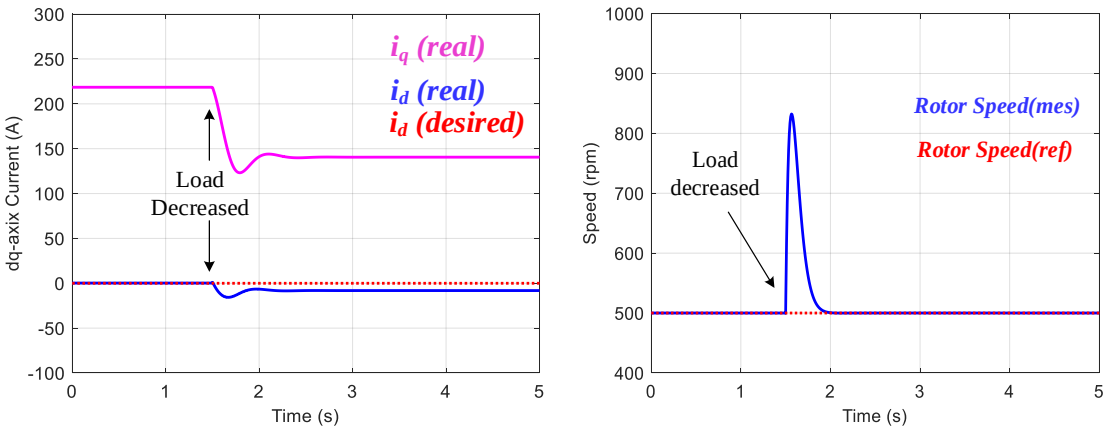

Figure 3.32. Simulation results of MFAC for, a) i_{dq} current, b) Mechanical speed of rotor, by load variation from full-load to half-load.

reducing the load, the $q-axis$ phase current is expected to be decreased to keep the same speed under new load condition. The related results are shown in Figure 3.32.

3.3.3. Experimental Results

The current sensorless control for WRSM based on MFAC was verified at the prototype platform as shown in Figure 3.7. In this section, several series of practical tests, such as start performance, different operating points and sudden load variation, have been performed to analyze the effectiveness of MFAC in sensorless control algorithm. As mentioned before, another current sensorless control method, which is already developed by Dr. Corne in his PhD study, is also used to compare with MFAC. During the experimental tests, for safety reasons, the operating condition of the studied test bench were limited, in fact the tests were carried with a smaller load and phase currents compared to the variables used in the numerical simulation tests.

First, the experimental tests have been performed at different operating points of rotor speed under a given load. Figure 3.33 – Figure 3.35 shows the tracking performance of MFAC compared to the estimation-based current sensorless control at a rotor speed of 200 rpm, 600 rpm and 950 rpm, respectively. These results show a good tracking performance for MFAC at all different operating points which the uncontrolled phase currents, i_{dq}, are almost converged to the expected values. But, according to the Figure 3.34, variation of the operating point affects the performance of the observation-based control method and adds some considerable estimation error of phase currents compared to the real ones. This case can be explained by the fact that the observation-based controller uses the parameters and mathematical model of the system for estimation of phase currents. Since the parameters used in estimation are measured in a rotor speed of 600 rpm, changing the operating point generates a parametric error between the actual system parameters and the parameters used in observer and causes to the estimation errors [32] [120]. However, since the MFAC does not use any parametric information, its performance is not remarkably affected by variation of operating point and leads to a desired convergence of all measured (ω) and unmeasured variables (i_{dq}). It is noteworthy that the considerable current ripples, seen

in the results, are inevitable in this setup because of a very small stator inductance used in the WRSM and are not related to the control performance.

In the second series of experimental tests, the transient behavior and starting performance of MFAC is tested. To do so, an operation of the machine from standstill to 600 rpm has been accomplished. As shown in Figure 3.36, applying a step on the speed reference causes to current variation from zero to almost 30A on the

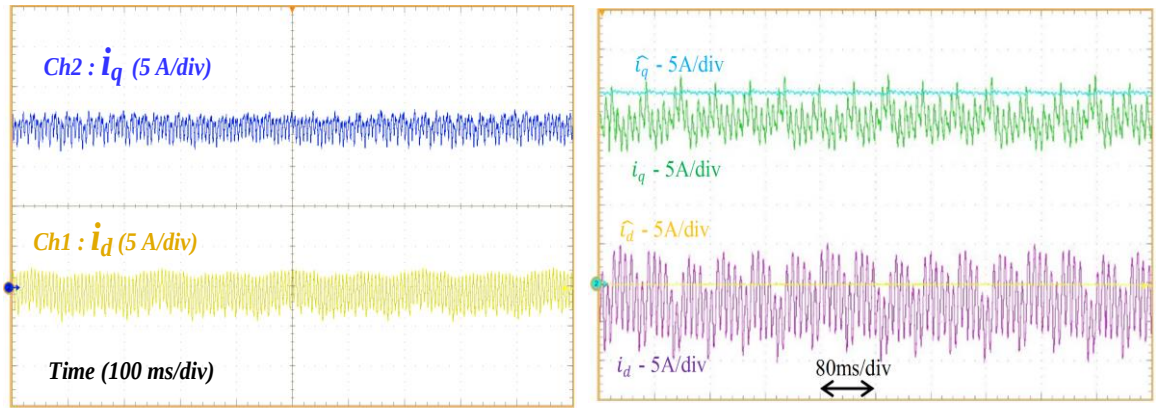

(a) (b)

Figure 3.33. a) MFAC tracking performance, b) online current estimation [120], at $\omega = 200$ rpm.

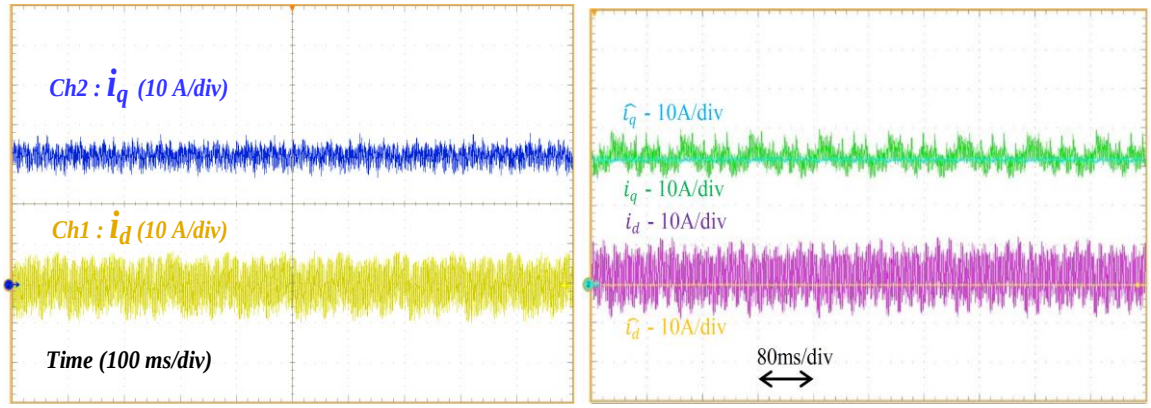

(a) (b)

Figure 3.34. a) MFAC tracking performance, b) online current estimation [120], at $\omega = 600$ rpm.

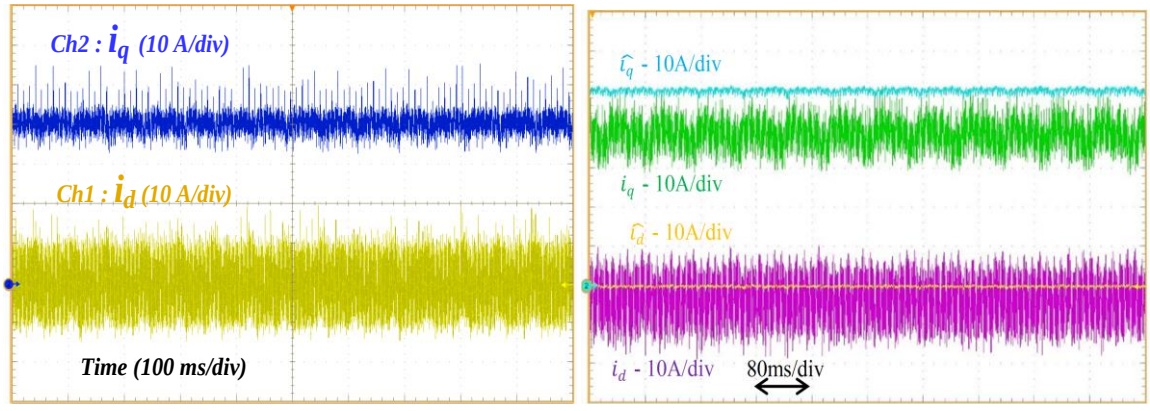

(a) (b)

Figure 3.35. a) MFAC tracking performance, b) online current estimation [32], at $\omega = 950$ rpm.

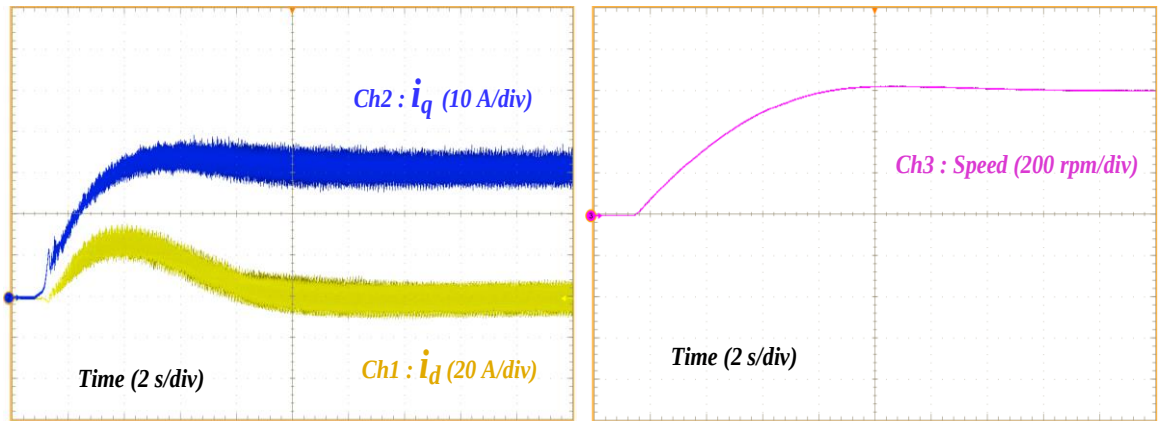

(a) (b)

Figure 3.36. Starting performance of MFAC for, a) i_d and i_q currents, and b) Mechanical speed of rotor at ω=600 rpm.

$q-axis$ current. Comparing the MFAC performance with observation-based control method, shown in Figure 3.37, both have nearly same performance and leads to the convergence of all variable with almost no steady state error. But, the dynamic of MFAC is considerably slow and it needs longer time for convergence toward the observation-based control method. Reason for this is that in MFAC method there is no control on the phase currents and all the control task is being done by only controlling the rotor speed. Whereas, the observation-based control method, not only controls the rotor speed but also controls the estimated phase currents which may lead to faster dynamic.

The last series of experimental tests in this study are allocated to check the robustness of MFAC to a sudden load variation. For this purpose, the output resistor of the load machine was changed suddenly while the rotor speed was controlled and its reference unchanged. Applying a load step down during observation-based control, please see the Figure 3.39, both of the real and estimated $d-axis$ phase currents converge to the desired value of 0, but for the $q-axis$ phase current there is a remarkable error between the real and estimated one which is due to a machine saturation and inductance variation. According to the MFAC performance presented in Figure 3.38, the $q-axis$ current decreases and converges to the expected value, $\bar{\imath}_q = 22A$, and the $d-axis$ current is also converge to 0 with a small static error, $\bar{\imath}_d = -5A$, which leads to a

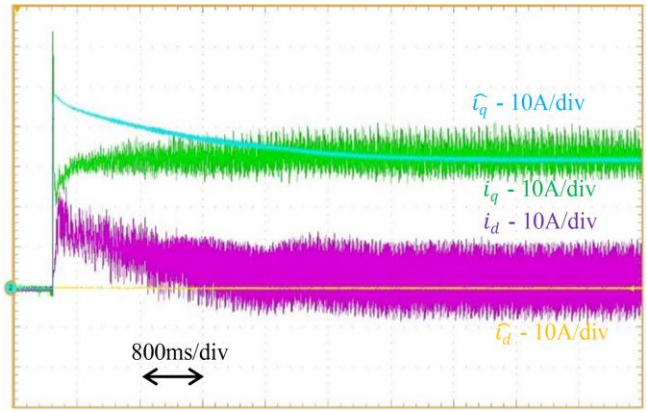

Figure 3.37. Online i_{dq} current estimation in starting condition [32].

stator current of $I_s = \sqrt{{i_d}^2 + {i_q}^2} = 22.5A$, while the desired stator current is supposed to be $I_s = 22A$. However, since the difference between the desired current value and real one is not big, this does not much affect cupper losses (less than 5%) and is also quit smaller than the losses created from the error of $q - axis$ current in observation-based control. Figure 3.40 also represents the effective performance of MFAC with a load step up. By this way, a robust performance of MFAC can be seen during these tests which guarantees the control with acceptable steady state error.

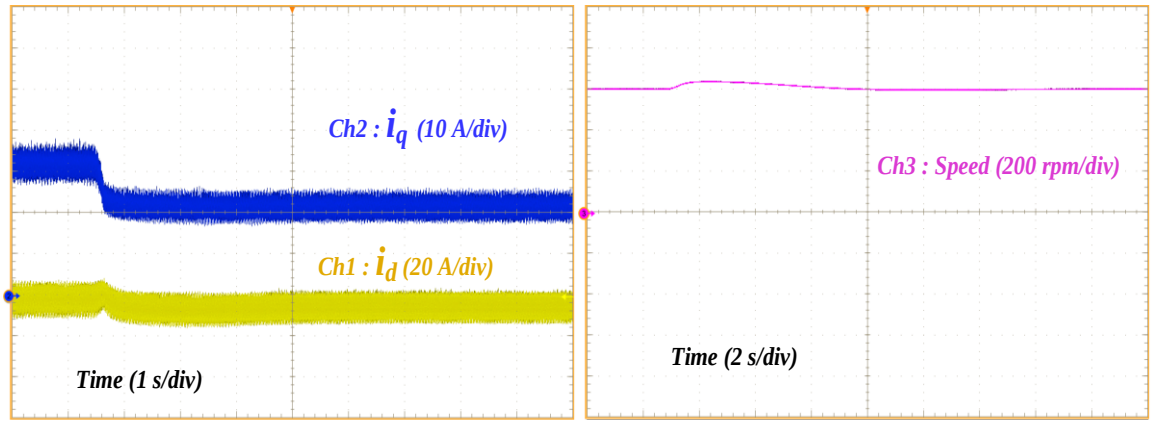

(a) (b)

Figure 3.38. MFAC performance with a load step down at 600 rpm for, a) i_d and i_q currents, and b) Mechanical speed of rotor.

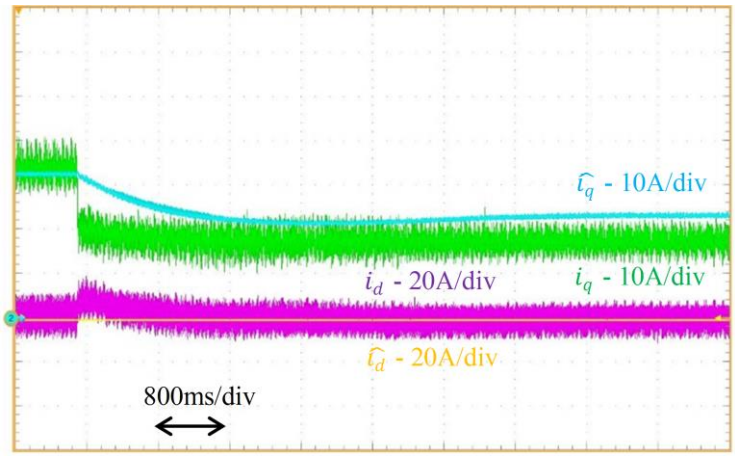

Figure 3.39. Online i_{dq} current estimation at 600 rpm with a load step down [32].

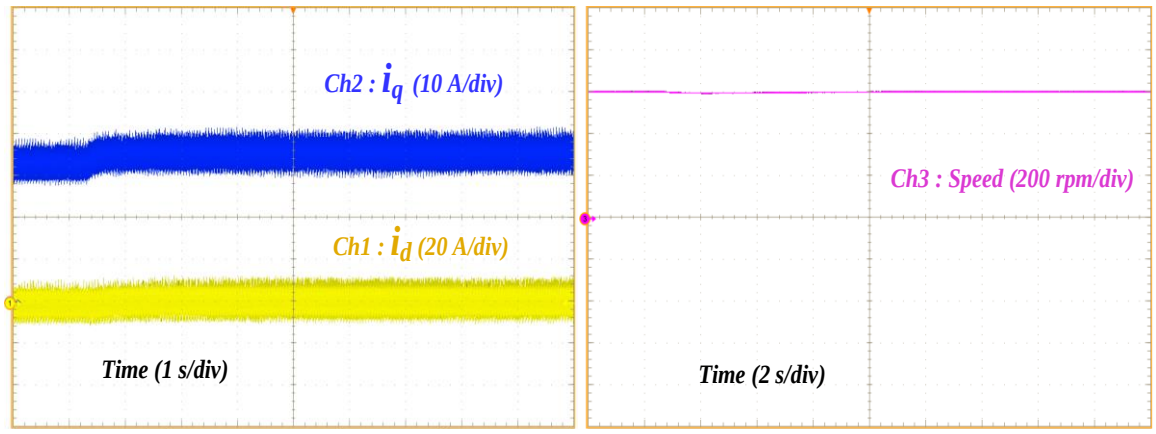

(a) (b)

Figure 3.40. MFAC performance with a load step up at 600 rpm for, a) i_d and i_q currents, and b) Mechanical speed of rotor.

Conclusion

In this chapter, the model-free-adaptive controller is developed to control a Wound-Rotor Synchronous Machine. This MFAC is a data-driven control method which merely uses the online I/O data measured from the controlled system and does not use any knowledge of the system model to be designed. Since the PI controller is a well-known tool commonly used for the current control, it has been also developed to compare with MFAC.

The first section of this chapter is allocated for introducing the studied WRSM system. In this section, the different components of the studied system are firstly explained, then the electromagnetic model of the powertrain is presented briefly. Afterward, the electric model of the system is presented by mathematical state equations.

In the second part of this chapter, the MFAC is used to control the phase currents of the studied machine. In this method, the phase currents are directly measured and controlled by MFAC. Since the PI controller is a well-known tool commonly used for the current control, it has been also developed to compare with MFAC. The simulation work is carried out to test the performance of the MFAC. The obtained simulation results represent a strong performance of MFAC under different operating conditions such as operating point variation, parameter variation and load torque disturbance. The experimental results validate the tracking performance of MFAC obtained in simulation work. Comparing the experimental performance of PI and MFAC, they lead almost to the same results. Considering all the provided results, the effectiveness of MFAC in current control algorithm can be concluded under different operating conditions.

According to the third part of this chapter, the Model-Free-Adaptive-Control (MFAC) is developed for current sensorless control of a Wound Rotor Synchronous Machine (WRSM) with only measuring the rotor speed. Another observation-based current sensorless control theory, proposed by Dr. Corne in his PhD study [32], is also used to compare with MFAC. In this method, the estimated phase currents are used in control task while the MFAC does not uses any measured or estimated phase currents and uses only the rotor speed measurements. The proposed control algorithm is firstly tested in simulation under several operating conditions.

Startup, tracking, parameter variation and load step are considered. The obtained simulation results represent an effective performance of developed control algorithm. The only small error is reported on $d-axis$ current due to a remarkable variation of system parameters and load torque. Several experimental tests are performed to analyze the effectiveness of developed controller in which the obtained results highly validated the simulation performance of MFAC. Compare to the observation-based control method, since the MFAC does not depend on parameter of system, its tracking performance is more acceptable during variation of load or operating point. Since MFAC has no action on phase currents and controls only the rotor speed, its dynamic is relatively slow, and the currents need more time to converge to the desired references.

Chapter-4 MFAC FOR SWITCHING POWER CONVERTERS

Contents

4.1. DC/DC Boost Converter

In recent decades, DC-DC converters have been increasingly used in a variety of applications such as automotive power systems, DC microgrids, and transportation systems [131]–[137]. A switching DC-DC converter is one of the most important components of an electrical energy conversion system, where it is used as a connector to deliver energy from the source to the load. With the electrification of transportation systems, there has been a significant increase in the demand for DC-DC converters. The step-up (boost) converter is a type of DC-DC converter used to increase the output voltage level to a desired level. This converter is a piecewise-switched circuit, which can contain several kinds of nonlinear phenomena. The use of power electronic circuits, especially DC-DC converters, usually involves having to deal with several issues due to the complex nature of these circuits. The chaotic operation, quasi-periodic behavior, parameter variations, saturation, and variations in performance due to temperature or other factors, are some of the undesirable properties of these circuits [138]. Hence, the reliability and stability of DC-DC converters are crucial concerns due to the complex behavior and nonlinear characteristics of these converters, which can generate unstable oscillations in the system. To overcome these problems, different approaches, including active and passive methods, have been presented in the literature to stabilize power electronic systems [139]. While stabilization using passive components is the easiest approach, it may increase the losses, volume, and weight of the system, which is not suitable for industrial applications. Contrarily, the active stabilization method does not add any new passive element to the system and focuses only on the control algorithm. It is considered that all the aforementioned complex behaviors can be solved simply by designing a powerful controller without using any additional passive component. The following paragraph lists some of the active stabilization methods described in the literature to control DC-DC converters.

Thus far, several approaches have been developed for the active stabilization of DC-DC converters. In [140], [141], stabilization was achieved by injecting the instability information into the current loop. In this approach, the dynamics of the stabilizer are limited by its current controller. In the approach proposed in [142], information about the output voltage ripples is applied to an output voltage loop, and the dynamics of the stabilizer are limited by the bandwidth of the voltage controller. In another method, all the state variables are controlled using the state-space method to prevent instability of the controlled plant [143]. Several approaches have been proposed to control a boost converter. The commonly used classic proportional integral (PI) controller [144], flatness-based controller [145], sliding mode controller [146], [147], fuzzy logic controller [148], and passivity-based controller [149], [150] are some of the important approaches that have been used so far. A cascade control approach, using PI and sliding mode controllers, has also been proposed in [151]. Among these control methods, the PI controller represents a well-known approach; it has a simple control design algorithm and is widely used to control DC-DC converters. The control diagram of a boost converter using PI controller is presented in Figure. 4.1 [152]. As shown in the figure, the control block includes an outer loop and an inner loop. The outer loop controls the output voltage to provide a current reference. The inner loop controls the inductor current using the current reference generated by the outer control loop. Finally, the control signal generated by the inner loop is used to generate the switching command signal u, based on a PWM

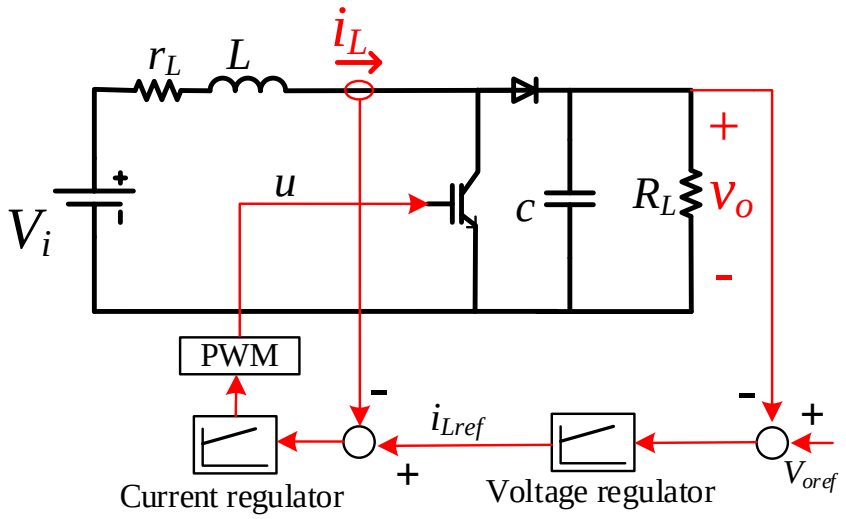

Figure 4.1. Two-loop control for a boost converter [152].

approach. The Lyapunov-based control algorithm is another approach proposed in the literature to control DC-DC converters using a continuous average model of the controlled system. In [153], [154], a Lyapunov-based control algorithm is proposed to control DC-DC converters. All the control approaches mentioned above are called model-based control (MBC) approaches, which require precise information about the dynamics model of the system being controlled in order to design a robust controller. Therefore, the lack of an accurate model of the controlled system will significantly affect the performance of the designed controller.Thus far, several approaches have been developed for the active stabilization of DC-DC converters. In [140], [141], stabilization was achieved by injecting the instability information into the current loop. In this approach, the dynamics of the stabilizer are limited by its current controller. In the approach proposed in [142], information about the output voltage ripples is applied to an output voltage loop, and the dynamics of the stabilizer are limited by the bandwidth of the voltage controller. In another method, all the state variables are controlled using the state-space method to prevent instability of the controlled plant [143]. Several approaches have been proposed to control a boost converter. The commonly used classic proportional integral (PI) controller [144], flatness-based controller [145], sliding mode controller [146], [147], fuzzy logic controller [148], and passivity-based controller [149], [150] are some of the important approaches that have been used so far. A cascade control approach, using PI and sliding mode controllers, has also been proposed in [151]. Among these control methods, the PI controller represents a well-known approach; it has a simple control design algorithm and is widely used to control DC-DC converters. The control diagram of a boost converter using PI controller is presented in Fig. 1 [152]. As shown in the figure, the control block includes an outer loop and an inner loop. The outer loop controls the output voltage to provide a current reference. The inner loop controls the inductor current using the current reference generated by the outer control loop. Finally, the control signal generated by the inner loop is used to generate the switching command signal u, based on a PWM approach. The Lyapunov-based control algorithm is another approach proposed in the literature to control DC-DC converters using a continuous average model of the controlled system. In [153], [154], a Lyapunov-based control algorithm is proposed to control DC-DC converters. All the control approaches mentioned above are called model-based control (MBC)

approaches, which require precise information about the dynamics model of the system being controlled in order to design a robust controller. Therefore, the lack of an accurate model of the controlled system will significantly affect the performance of the designed controller.

In most studies, control systems for converters have been implemented using several sensors to measure the input and output voltages as well as the inductor current. However, increasing the number of sensors may result in a bulkier system with greater amounts of sensor noise and a higher manufacturing cost, which are not suitable for industrial applications. To overcome this problem, observers have been proposed to reduce the number of sensors. Observers are used to estimate the unmeasured variable, and the estimated variable is used in the control algorithm. For example, in [155], an observer is used to estimate the inductor current by using the information obtained by measuring the input and output voltages as well as the switching commands. In [156], an adaptive observer is used to estimate the input and output currents of a boost converter; this represents a current sensorless control approach. In [139], the authors proposed a Lyapunov-based control algorithm for a boost converter, in which the input current is estimated using the data obtained from the measured variables. In all these examples, an observer is used to estimate the unmeasured variables; therefore, it is inevitable to use an average model of the system for designing the dynamics of the observer. However, the effectiveness of the designed observer and controller is highly dependent on the accuracy of the average model used in the observer structure. In addition, using an additional observer may increase the complexity of the control system.

According to the literature review presented earlier, almost all control algorithms require information about the dynamic model of the system. More specifically, the observation-based control methods, which are used to reduce the number of sensors, require a precise dynamic model of the system to ensure the effectiveness of both the observer and controller. However, it is almost impossible to obtain a very precise model or is at least time-consuming. In this study, the data-driven control (DDC) theory is considered as a solution to address the lack of a precise model for nonlinear systems.

In this study, MFAC is used to control a boost converter by only measuring the output voltage. A proportional-integral (PI) controller is also developed for comparison with MFAC. As shown in Figure. 4.1, the PI controller uses two sensors to measure and control the output voltage and current of the inductor. On the other hand, MFAC uses only a voltage sensor to measure the output voltage and does not consider the inductor current. The main contributions of this study are as follows.

1) This work presents a control method that does not require information about the dynamic model of the system to design the controller.
2) The presented control method can reduce the number of sensors without using any observer. This method can be used to control a boost converter by just measuring the output voltage, and does not require any additional observation of the unmeasured inductor current.

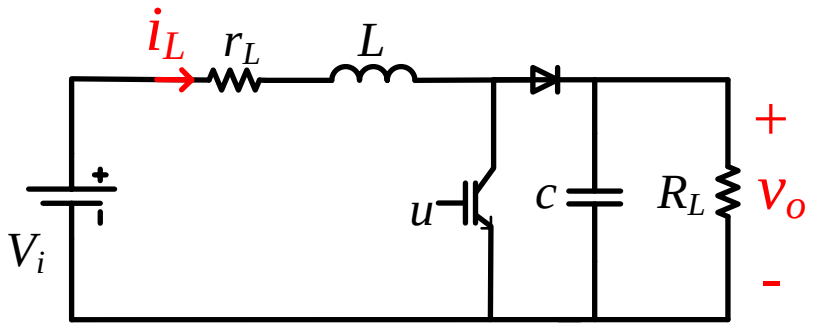

Figure 4.2. Studied boost converter.

4.1.1. Description of the Studied System

A. Modelling of the Boost Converter

A DC-DC converter can operate either in the continuous conduction mode (CCM) or discontinuous conduction mode (DCM) of the inductor current. In CCM, the inductor current flows continuously during all the switching cycles under steady-state operation. In DCM, the inductor current is zero during a part of the switching cycle. It starts at zero, goes to the peak value, and returns to zero during each switching cycle. These operation modes have already been investigated in previous studies [157], [158]. The system studied in this work (shown in Figure. 4.2) is a boost converter operating in CCM with a switching period of T and and a duty cycle of D. The command of the converter switch is considered as $u \in \{0, 1\}$.

Based on the different elements used in this converter, the related differential equations can be obtained as follows:

$$\begin{cases} \frac{di_L}{dt} = \frac{1}{L}(V_i - r_L i_L - (1-u)v_o) \\ \frac{dv_o}{dt} = \frac{1}{c}\left((1-u)\, i_L - \frac{v_o}{R_L}\right) \end{cases} \tag{4.1}$$

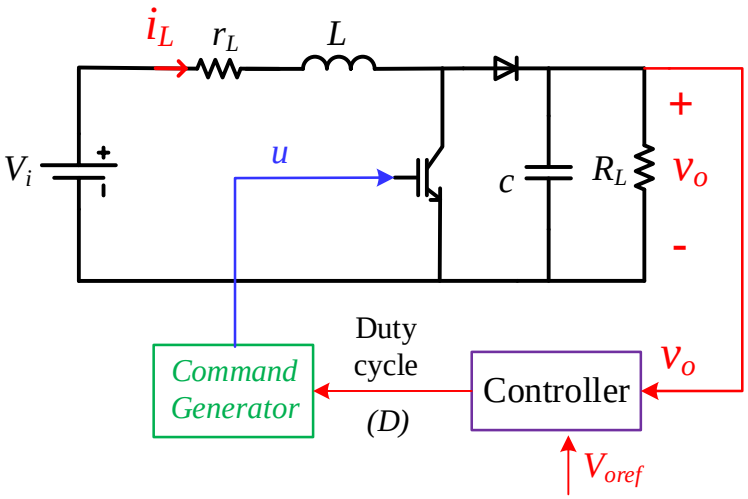

Figure 4.3. Control block diagram of the studied boost converter.

where R_L is the load resistance, r is the parasitic resistance of the inductor, $u \in \{0, 1\}$ is the switch command, V_i is the input voltage, and v_o is the output voltage.

As stated in the previous section, the MFAC is developed to control the boost converter. As MFAC requires a discrete-time system to design the controller, the following discrete-time model of the state equations (4.1) is presented to show that the boost system satisfies this requirement:

$$\begin{cases} i_L(k+1) = \frac{\Delta t}{L}\Big(V_i(k) - r.\, i_L(k) - \big(1 - u(k)\big)v_o(k)\Big) + i_L(k) \\ v_o(k+1) = \frac{\Delta t}{c}\left(\big(1 - u(k)\big)\, i_L(k) - \frac{v_o(k)}{R_L}\right) + \ v_o(k) \end{cases} \tag{4.2}$$

where Δt is the time step size and k is the time instant.

B. Control Scheme

Figure 4.3 shows the control diagram of the boost converter considered in this study. In this figure, the controller block includes an FFDL-based MFAC. The output voltage v_o is the only system output that is measured, and the duty cycle D is the only control input signal that needs to be generated by the controller. This system is considered to be a SISO system with one system output and one control input signal, which satisfies Assumption 2.5, and the inputs and outputs of the system are observable and controllable. Moreover, this system meets the generalized Lipschitz condition, which is as follows. For any k,

$$\|\Delta v_o(k+1)\| \le b \,\|\, \Delta\big[v_o(k), \dots, v_o(k - L_y + 1), D(k), \dots, D(k - L_u + 1)\big] \,\|$$

where b is a constant and $\Delta v_o(k+1) = v_o(k+1) - v_o(k)$. This means that the changes in the system outputs are completely bounded by the changes in all the system variables including the control input. Furthermore, this condition shows that limited changes in the control input signal D will not cause infinite variations in the system output v_o.

Therefore, by selecting the output-related and input-related linearization orders as $L_y = L_u = 3$, the nonlinear system (4.2) is transformed into the following full-form dynamic linearization data model:

$$v_o(k+1) = \varphi_{p,L_u,L_y}(k)\ \Delta[v_o(k), v_o(k-1), v_o(k-2), D(k), D(k-1), D(k-2)]^T + v_o(k) \tag{4.3}$$

where $\varphi_{p,L_u,L_y}(k) = [\varphi_1(k), \varphi_2(k), \dots, \varphi_6(k)] \in R^{1\times 6}$, is an unknown time-varying matrix that includes all the possible complicated behaviors of the system given by (4.2). As this matrix is not available, its arrays should be estimated at each sampling time using only the I/O data obtained from system output and control input.

Based on the theories presented in Chapter 2, the following cost function is used to estimate of the matrix $\varphi_{p,L_u,L_y}(k)$

$$J\left(\varphi_{p,L_u,L_y}(k)\right) = \left\|\Delta v_o(k) - \varphi_{p,L_u,L_y}(k)\Delta H(k-1)\right\|^2 + \mu \left\|\varphi_{p,L_u,L_y}(k) - \hat{\varphi}_{p,L_u,L_y}(k-1)\right\|^2 \tag{4.4}$$

where $\Delta H(k-1) = \Delta[v_o(k-1), v_o(k-2), v_o(k-3), D(k-1), D(k-2), D(k-3)]^T$, $\hat{\varphi}_{p,L_u,L_y}$ is the estimated value of φ_{p,L_u,L_y} and μ is a weight factor.

According to the optimum condition, the estimation algorithm is obtained as follows:

$$\hat{\varphi}_{p,L_u,L_y}(k) = \hat{\varphi}_{p,L_u,L_y}(k-1) + \frac{\eta\left(\Delta v_o(k) - \hat{\varphi}_{p,L_u,L_y}(k-1)\Delta H(k-1)\right)\Delta H^T(k-1)}{\mu + \|\Delta H(k-1)\|^2} \tag{4.5}$$

In order to satisfy the condition $\|\Delta H(k)\| \neq 0$, for equation (4.3), the resetting algorithm is added to the estimation algorithm (4.5) as follows:

$$\hat{\varphi}_{p,L_u,L_y}(k) = \hat{\varphi}_{p,L_u,L_y}(1), \text{ if } \left\|\hat{\varphi}_{p,L_u,L_y}(k)\right\| < \varepsilon \text{ or } \|\Delta H(k-1)\| < \varepsilon \text{ or } sign\left(\hat{\varphi}_4(k)\right) \neq sign\left(\hat{\varphi}_4(1)\right) \tag{4.6}$$

where $\hat{\varphi}_{p,L_u,L_y}(1)$ is the initial value of $\hat{\varphi}_{p,L_u,L_y}(k)$.

For the output voltage controller, the goal is to find a suitable duty cycle (D), so that the output voltage error $\left(e(k) = v_{oref}(k) - v_o(k)\right)$ converges to zero. Thus, the cost function of the control input $\left(D(k)\right)$ is used to design the controller.

$$J\left(D(k)\right) = \left|v_{oref}(k+1) - v_o(k+1)\right|^2 + \lambda|D(k) - D(k-1)|^2 \tag{4.7}$$

By minimizing the cost function (4.7) according to the control input $D(k)$, the control algorithm is designed as follows:

$$\begin{aligned} D(k) = D(k-1) &+ \frac{\rho_4\varphi_4(k)\left(v_{oref}(k+1) - v_o(k)\right)}{\lambda + \|\varphi_4(k)\|^2} \\ &- \frac{\varphi_4(k)\left(\rho_1\varphi_1(k)\Delta v_o(k) + \rho_2\varphi_2(k)\Delta v_o(k-1) + \rho_3\varphi_3(k)\Delta v_o(k-2)\right)}{\lambda + \|\varphi_4(k)\|^2} \\ &- \frac{\varphi_4(k)\left(\rho_4\varphi_4(k)\Delta D(k) + \rho_5\varphi_5(k)\Delta D(k-1) + \rho_6\varphi_6(k)\Delta D(k-2)\right)}{\lambda + \|\varphi_4(k)\|^2} \end{aligned} \tag{4.8}$$

where $\rho_i \in (0, 1], i = 1, \ldots, 6$ are the step factor.

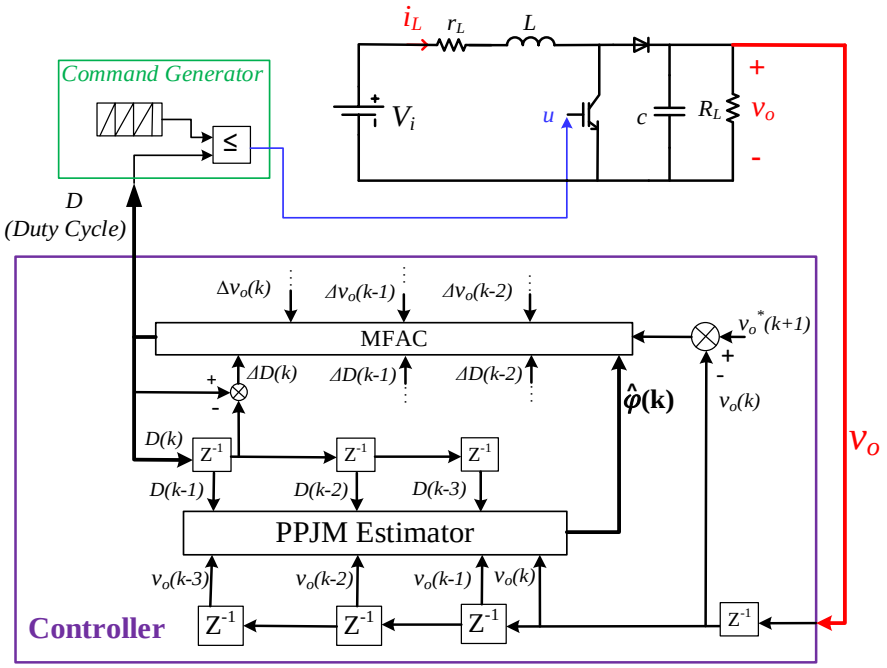

Figure 4.4. General control block diagram of the studied boost converter.

TABLE 4.1: SYSTEM PARAMETERS

Parameter	Quantity	Value
V_{in}	Input voltage	24 V
L	Inductance	1 mH
c	Output capacitor	1000 µF
r_L	Resistance of inductor	0.76 Ω
f_s	Sampling frequency	40 KHz

TABLE 4.2: CONTROL PARAMETERS FOR PI

Parameter	Value
Current controller K_{pi}	0.0852
Current controller K_{ii}	192
Voltage controller K_{pv}	0.011
Voltage controller K_{iv}	6.1466

Finally, the FFDL-based MFAC scheme is obtained by synthesizing the estimation algorithm (4.5) and (4.6) and the control algorithm (4.8). From these equations, it can be concluded that this control scheme does not utilize any information about the components or a dynamic model of the system under consideration. The application of the MFAC, including the estimation of matrix $\varphi_{p,L_u,L_y}(k)$ and the design of the control signal $D(k)$, is performed merely using the I/O data obtained from the system output and the control input. The general control diagram of the studied system is shown in Figure. 4.4 to illustrate the application of MFAC.

As stated earlier, several parameters are used in the controller design, namely $\lambda, \mu, \eta, \rho_i, a, b_1$, and b_2. The selection of optimal parameters for the controller is challenging, and they are usually chosen by trial and error. In this study, the parameters are selected using a genetic algorithm optimization method. The cost function to be minimized is the mean square error of the output voltage tracking a given profile. In the simulation, this error is calculated using a nominal model. Once these parameters are set, they are used in both the simulation and experiment; however, in the latter, the parameters are rather uncertain and different from their nominal values. The selected controller parameters are presented inTable 4.3.

4.1.2. Simulation Results

To verify the effectiveness of the MFAC approach in controlling the boost converter, a series of numerical simulations are performed using MATLAB/Simulink. A PI controller is also developed for comparison with the MFAC. Since the PI controller is a model-based method, it requires some information about the model and the parameters of the controlled system for designing the controller gains (K_p and K_i). Thus, considering an average model (4.2) and its rated parameter values, which are shown in Table 4.1, the PI controller parameters were designed as shown in Table 4.2. The switching frequency is also set on 40 KHz for all tests of this work.

The control diagrams shown in Figure 4.4 and Figure 4.1, were used to evaluate the simulation performance of MFAC and the PI controller, respectively. Several tests were performed using the proposed controller to evaluate its performance. The startup and steady-state responses, tracking response, regulation, and parameter variations were considered.

A. Startup and steady-state responses

The startup performance of the MFAC was evaluated to ensure that the startup current is not very high. In this test, the output voltage reference was set as $v_{oref} = 40\ V$ and the input voltage was fixed at $V_i = 24V$. In addition, the converter was loaded with a resistance $R_L = 17.8\ \Omega$ while being started up. The obtained simulation results are presented in Figure 4.5.

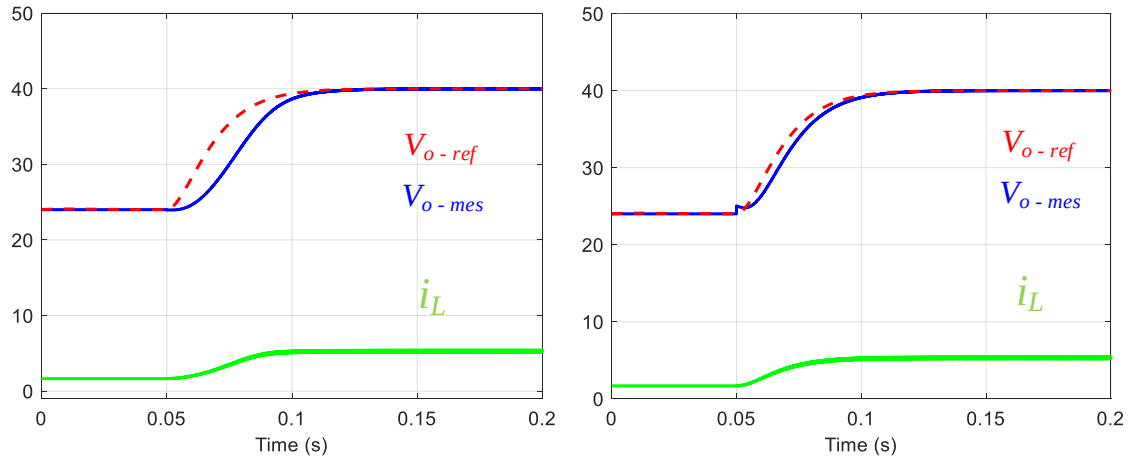

Figure 4.6. Startup and steady-state responses of inductor current and output voltage with a) MFAC, and b) PI controller.

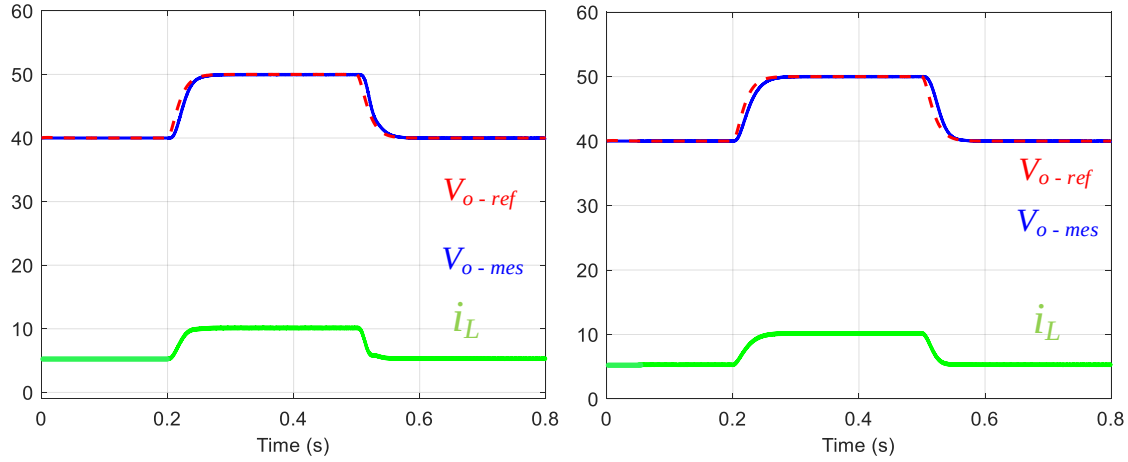

Figure 4.5. Tracking responses of inductor current and output voltage with a) MFAC, and b) PI controller.

As shown in these results, the performance of both controllers are almost similar; the inductor current and output voltage converge to the expected trajectories with no steady state error. The only difference is during the transient, where the PI controller has a slightly faster dynamic compared to that of the MFAC.

B. Tracking responses

In these simulation tests, the tracking performance of the MFAC was tested using the condition that the output voltage reference changes when the system is operating under a resistive load of $R_L = 17.8\Omega$. The system starts with an output voltage of $v_{oref} = 40V$. Then, at $t = 0.2s$ the operating point corresponds to an output voltage of $v_{oref} = 50V$. The second variation of output voltage reference occurs at $t = 0.5s$, where it

TABLE 4.3: MFAC PARAMETERS

Parameter	λ	η	μ	ρ_1	ρ_2	ρ_3	ρ_4	ρ_5	ρ_6
Value	23	0.12	2	0.35	0.53	0.4	0.6	0.5	0.54

drops back to $v_{oref} = 40V$. The related simulation results are shown in Figure 4.6. These results indicate similar performance for both the MFAC and PI controller; the inductor current and the output voltage converge toward the expected trajectories with almost zero steady-state error and an acceptable transient performance.

C. Regulation

In this section, the variation of the resistance load and the input voltage are considered for validating the regulation tests. For this, a resistance load step (from $R_L = 17.8\Omega$ to $R_L = 8.9\Omega$) was applied to the system. In the next step, the input voltage is also varied (+10%). Figure 4.7 and 4.8 show the results obtained by varying the resistance load and input voltage, respectively.

From these results, it can be seen that neither the resistance load step nor the variation of input voltage affects the control performance of the MFAC, and the output voltage and inductor current converge to the expected values with no steady-state or transient errors. This statement can be proved by comparing these results with the results obtained using a PI controller whose control performance is similar to that of MFAC.

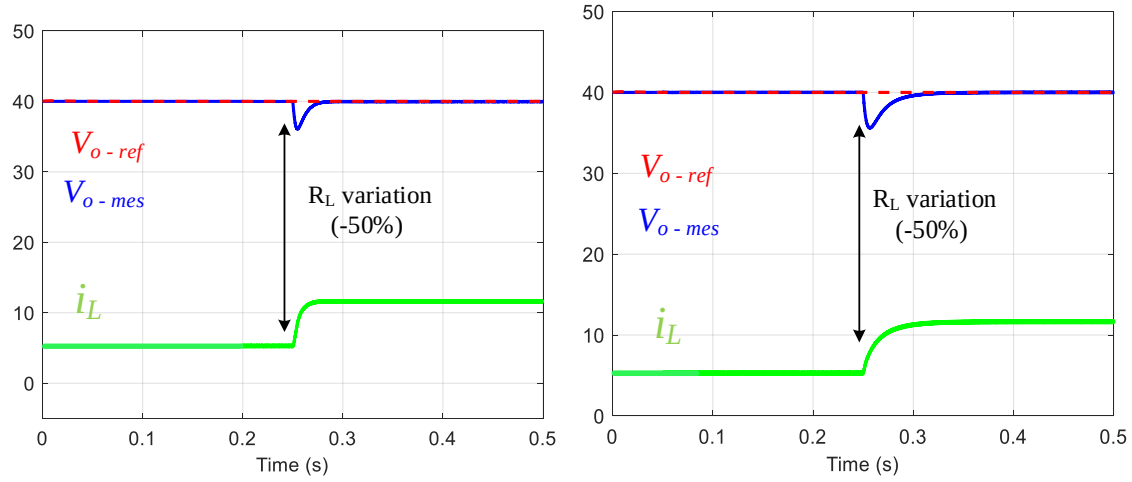

Figure 4.7. Responses of inductor current and output voltage with a resistance load step using a) MFAC, and b) PI controller.

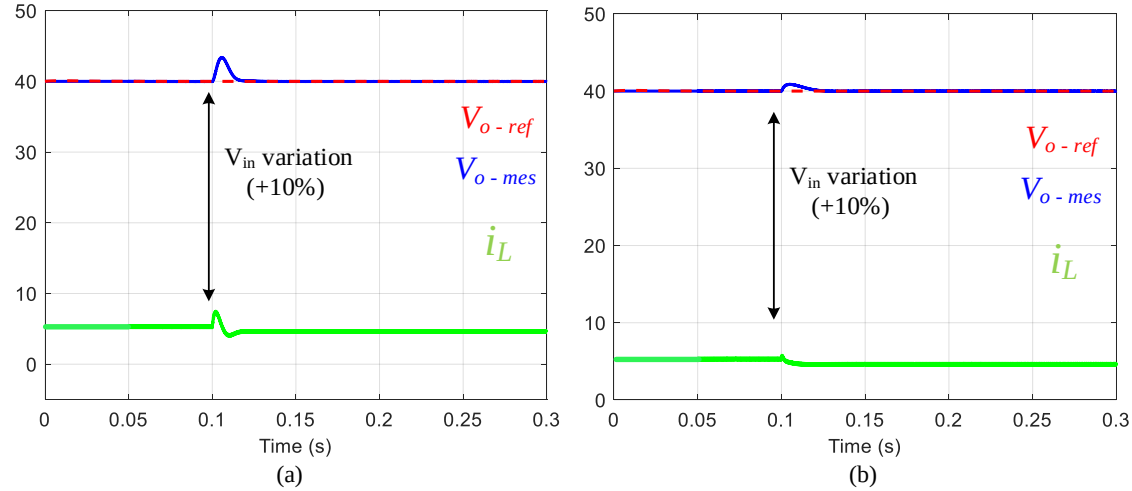

Figure 4.8. Responses of inductor current and output voltage with a variation of input voltage using a) MFAC, and b) PI controller.

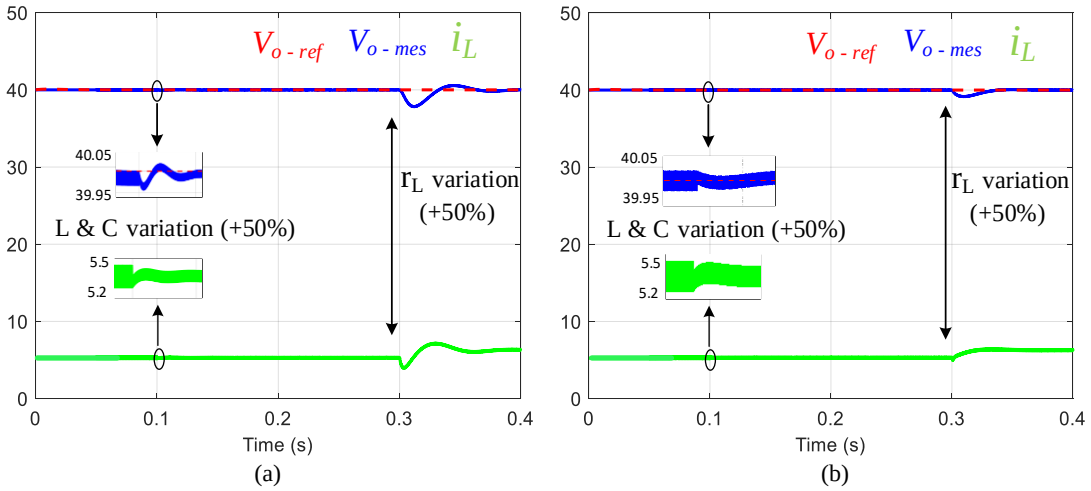

Figure 4.9. Responses of inductor current and output voltage under parameter variation using a) MFAC, and b) PI controller.

D. Parameter variation

In practical applications, the parameters of the system components may vary due to several factors such as aging and temperature. In this section, this phenomenon will be considered while testing the performance of MFAC. Here, a parameter variation of +50% is considered for r_L, L, and c at an operating point of 40 V for the output voltage with a resistance load of $R_L = 17.8\ \Omega$. While a sudden change in these parameters is unlikely, the worst-case scenario is tested. As shown in Figure. 4.9, the parameter variation causes almost no error in the responses of the output voltage and inductor current. It can be concluded that the MFAC is robust against parametric error and parameter variations, which are common in industrial applications.

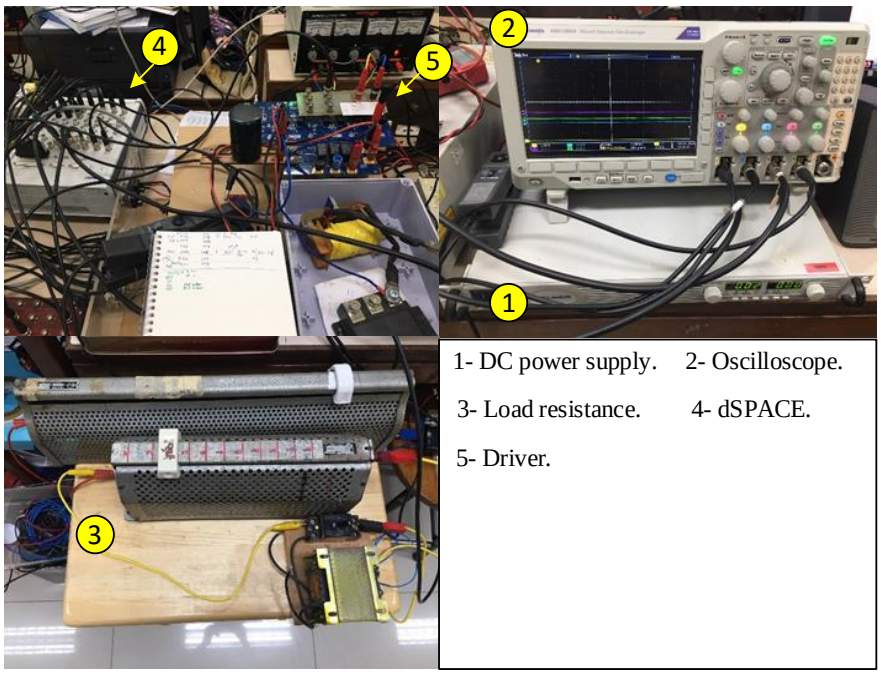

Figure 4.10. Experimental setup.

4.1.3. Experimental Results

The simulation results show that MFAC is very efficient in controlling DC-DC converters. However, the operating conditions of a simulation study are always different from that of a real system, which may include many uncertainties. Therefore, further experiments were conducted using a real test bench to validate the simulation performance of the MFAC. In addition, a PI controller was used for comparison with MFAC.

As shown in Figure 4.10the experimental setup consists of a controllable DC power supply (used as the input voltage source of the converter), a load resistance, a PC, an oscilloscope, and the control unit. The control program was developed in MATLAB/Simulink and then transferred to the system using a dSPACE real-time control card.

Experiments were conducted for several scenarios in order to demonstrate the effectiveness of the proposed controller. Similar to that in the case of the simulation, the startup, tracking, regulation, and robustness were investigated.

A. Startup and Steady-State Responses

In this section, the experimental waveforms related to the startup response of the output voltage (measured and controlled variable) and inductor current (unmeasured and uncontrolled variable) are presented. In this test, the output voltage reference was first set as $v_{oref} = 50\,V$. Then, the second series of startup tests was

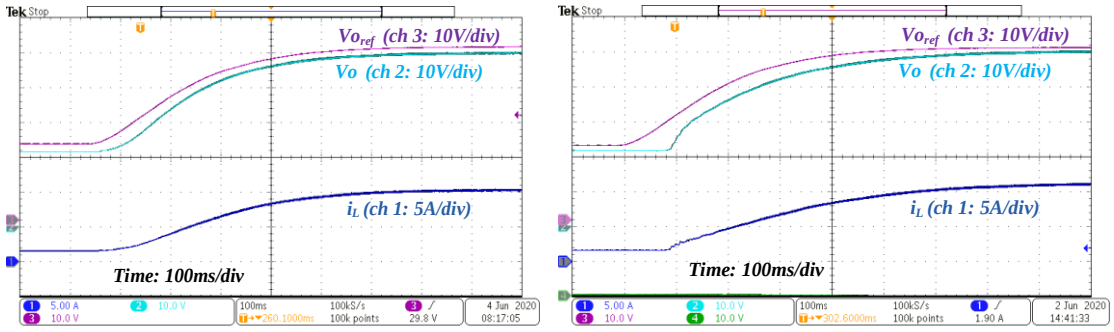

(a) (b)

Figure 4.11. Startup and steady-state responses of inductor current and output voltage while $v_{oref} = 50V$ using a) MFAC, and b) PI controller.

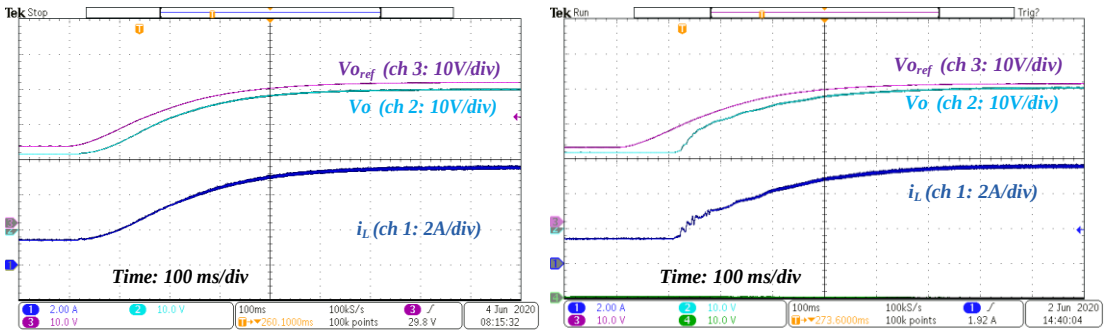

(a) (b)

Figure 4.12. Startup and steady-state responses of inductor current and output voltage while $v_{oref} = 40V$ using a) MFAC, and b) PI controller.

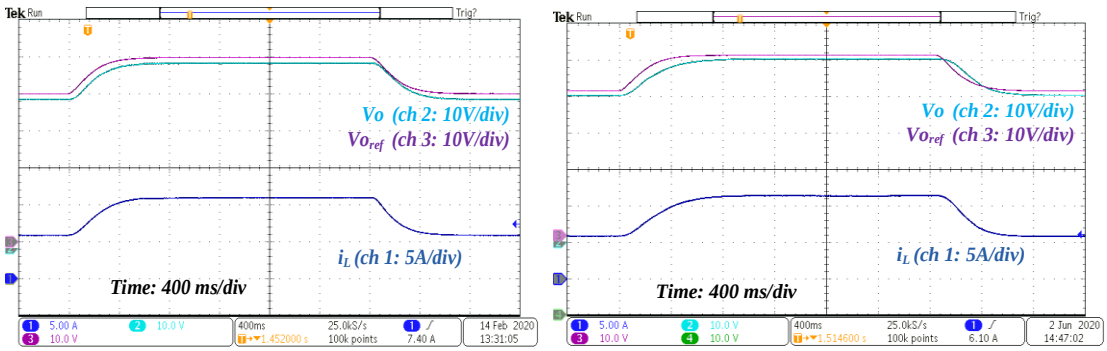

(a) (b)

Figure 4.13. Tracking responses of inductor current and output voltage using a) MFAC, and b) PI controller, while output voltage vary as $v_{oref} = 40V \rightarrow 50V \rightarrow 40V$.

conducted with $v_{oref} = 40\ V$. For both output voltage references, the input voltage was fixed at $V_i = 24\ V$, and the converter was loaded with a resistance $R_L = 24\ \Omega$ while being started up. The experimental results obtained with $v_{oref} = 40\ V$ and $v_{oref} = 50\ V$ are presented in Figure. 4.11 and Figure. 4.12, respectively.

It can be seen that the application of a step on the output voltage reference causes the inductor current to vary from 0.7 A to almost 2.8 A. On comparing the performance of MFAC with that of the PI controller, it can be seen that both have similar starting performances and lead to the convergence of all variables with almost zero steady state error, thus ensuring the stability of the system.

B. Tracking Responses

The tracking performance of MFAC was evaluated under the condition that the output voltage reference changes when the system is operating under a resistive load of $R_L = 24\ \Omega$. The output voltage reference was varied in two ways. In the first case, the system starts with an output voltage of $v_{oref} = 40\ V$, and at $t = 40\ ms$, the operating point corresponds to an output voltage of $v_{oref} = 50\ V$. Then, the second variation of the output voltage reference occurs at $t = 260\ ms$, where it drops back to $v_{oref} = 40\ V$. In the second case, the output voltage reference was changed as follows: $v_{oref} = 30V \rightarrow 50V \rightarrow 30V$. The experimental results of the performance of MFAC and its comparison with the PI controller for the first and second cases are shown in Figure 4.13 and Figure 4.14, respectively. The obtained results show that the performance of MFAC and the PI controller is very similar, as the inductor current and output voltage converge toward the expected

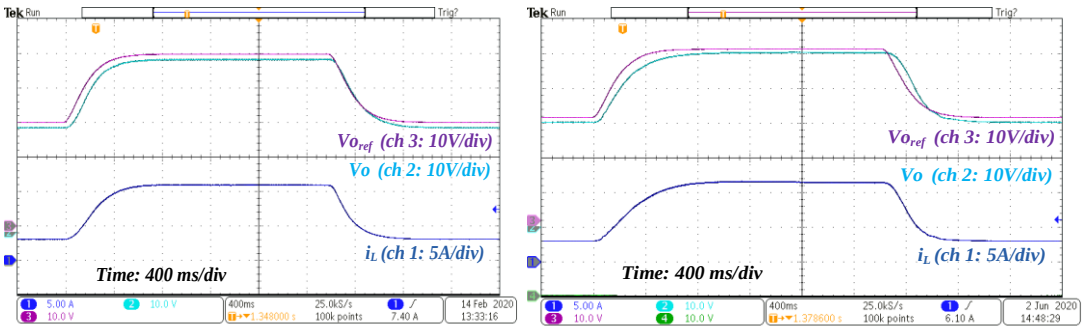

(a) (b)

Figure 4.14. Tracking responses of inductor current and output voltage using a) MFAC, and b) PI controller, while output voltage vars as $v_{oref} = 30V \rightarrow 50V \rightarrow 30V$.

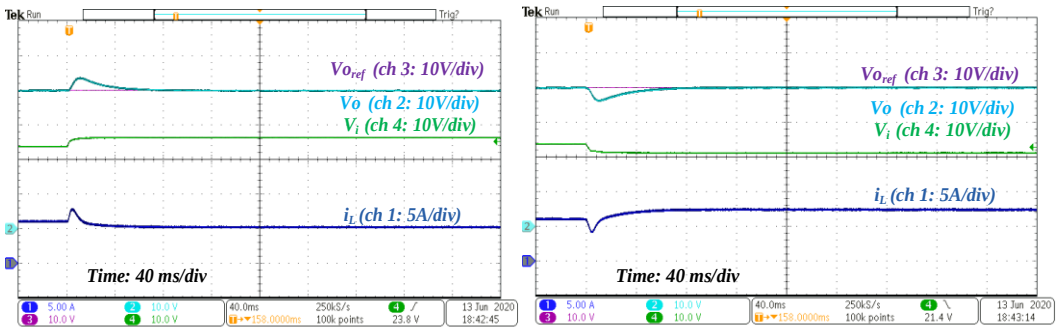

(a) (b)

Figure 4.15. Experimental results using MFAC with a) +10%, and b) -10%, changes of input voltage V_{in}.

trajectories; in addition, nearly no steady-state error was observed, and the transient performance was acceptable.

C. Regulation Performance (Changing of R_L and V_{in})

In the following tests, the variations in resistance load and input voltage that occur during practical applications were considered. The input voltage V_{in} was varied by $\pm 10\%$ when the system was operating with an output voltage of 40 V and a resistance load of $R_L = 45\ \Omega$. Figures 4.15.a and 4.15.b show the control performance of MFAC under incremental and decremental variations in input voltage, respectively. It can be seen that when the input voltage is changed, the output voltage v_o remains constant and the inductor current i_L convergence to a new reference value. All these scenarios are desired cases, which means that the system has a stable operation.

To verify the robustness of the MFAC against variations in input voltage, the experiments were repeated under the same conditions using with the PI controller, and the results are shown in Figure. 16.a and Figure. 16.b. On comparing the MFAC with the PI controller, it can be seen that the performances of both controllers are almost similar in terms of the common figures of merit (steady-state error, response time, and overshoot).

Another series of regulation tests was performed by varying the resistance load R_L. In this case, the resistance load was changed suddenly from $R_L = 45\ \Omega$ to $R_L = 17.8\ \Omega$, while the input voltage was fixed at $V_i = 24$ V and the output voltage was $v_o = 40$ V. Based on the MFAC performance results shown in Figure. 17.a, after the resistance load is stepped down, the output voltage v_o rapidly responds to its reference. Although

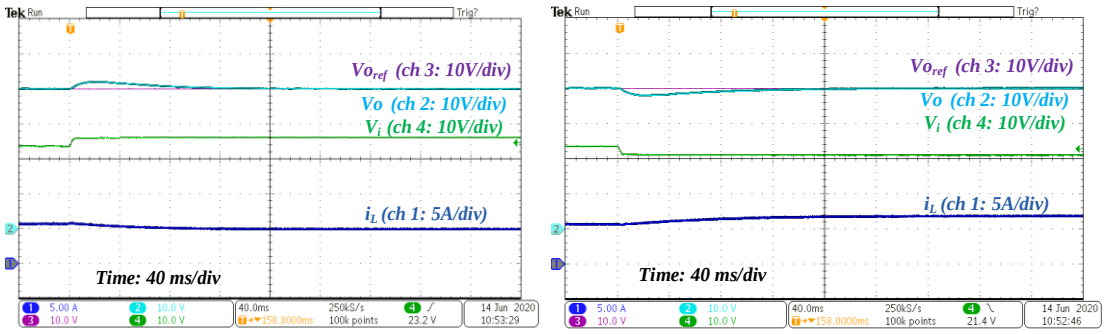

(a) (b)

Figure 4.16. Experimental results using PI controller with a) +10%, and b) -10%, changes of input voltage V_i.

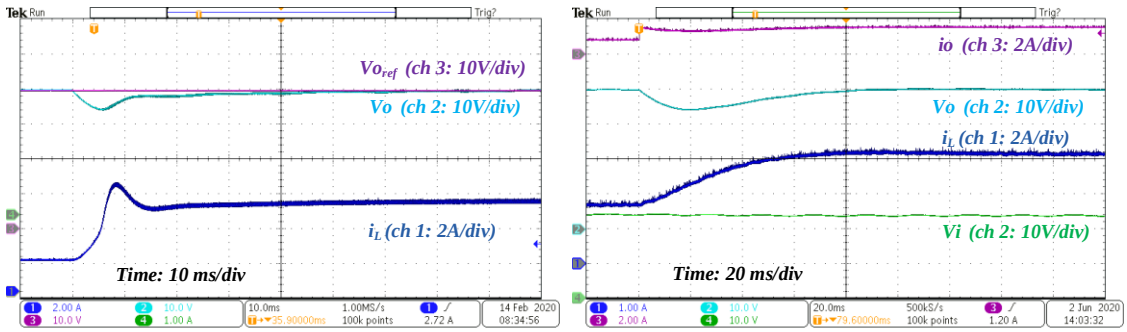

(a) (b)

Figure 4.17. Experimental results under -50% variation of resistance load R_L using a) MFAC, and b) PI controller.

there is no control on the inductor current, it also converges to the expected value with an acceptable transient behavior. As in the previous tests, the performance of the PI controller in practical conditions is also shown (Fig. 17.b) for comparison with MFAC. The similar behaviors of both controllers confirms that the MFAC has a reliable performance under resistance load variation and can ensure stable operation of the system.

To sum up, from the analysis of the experimental results generated by the MFAC and PI controllers, it can be seen that both controllers have almost similar performance in terms of the common figures of merit. In addition, the experimental results validate the simulation performance of the controllers, where both controllers accurately tracked the expected trajectories under various operation scenarios. Since the PI controller is considered to be a reliable control method and has already been developed for similar industrial applications, the similarity between the performances of PI and MFAC show that the MFAC can be considered as an effective control approach for DC-DC boost converters. In addition, MFAC has several other advantages as follows.

1- Since MFAC operates with only measuring the output voltage, and with no action on inductor current, this may be a superior approach for cost optimization of the DC-DC converters by reducing the number of sensors.

2- This control approach is a model-free method, any information about the model of the controlled system is required to design the controller. This characteristic helps MFAC method to be applicable for any system with unknown or complicated structure.

4.2. Three-Phase Dual Active Bridge Converter

4.2.1. Background

With the current trend towards greener energy sources, the integration of Energy Storage Systems (ESS) is the key to sustain the grid against fluctuations of energy generation. This raises a major concern for the inclusion of an efficient, fully controllable power conversion stage to allow an intermediate processing of energy flow.

The dc/dc isolated high frequency conversion is a crucial algorithm in some applications such as electric (EV) and hybrid electric vehicles (HEV), photovoltaic (PV) power generation systems, fuel cell power generation systems and so on.

The dual active bridge (DAB) converters are one of the most important soft switching dc/dc converter topologies for high power application which is capable for tens to hundreds of kilowatts. The DAB converters offer several advantages which can be listed as follows:

a. Natural soft switching, zero voltage switching (ZVS)
b. Buck-boost capability
c. Fixed frequency operation
d. Bidirectional operation
e. Galvanic isolation

The DAB topology was first proposed by *De Doncker* in 1991 for high power applications [159]. So far, this converter has been developed for several application as listed below [160]–[162].

A. *Automotive Applications*: The EV, HEV and fuel cell vehicles (FCV) are the most interesting vehicle technologies to reduce the emissions and fuel consumption. The powertrain of the EVs and HEVs includes a high-power dc battery. Besides, a low voltage (LV) dc bus and a high voltage (HV) dc bus is required in order to supply the low power and high power automotive loads, respectively. Thus, the dc/dc converters are needed to provide the different voltage levels. In addition, a bidirectional power transfer is also needed in order to allow for charging the battery during the regenerative breaking. According to these considerations, the DAB has been studied for this kind of vehicles in [163], [164]. The operation and design approach of a novel three phase DAB converter with six inverter legs for EV applications is also investigated in [165].

B. *Renewable Power Systems*: Increasing integration of the renewable power systems bring more attention in battery energy storage systems (BESSs) which causes to design a reliable isolated battery-driven grid interface (IBDGI). However, DAB converters introduce a solid-state transformer (SST) structure which lead to an isolated interface between an ac power system and a renewable power source. Some examples are given in [166]–[169].

C. Smart-Grid Systems: These applications require an efficient energy storage/recovery system to provide a reliable electric power flow. In this basis, the design procedure of a DAB converter in terms of energy storage/recovery system for smart grids is described in [170].

D. Uninterruptable Power Supplies (UPS): A UPS is a reliable topology that provides electric power to the loads. A UPS is normally powered by a rectifier, a battery buffered HV dc bus, and an inverter. In the case of using a low voltage battery, a bidirectional isolated dc/dc converter is normally used due to the large ratio of the HV and LV dc bus voltages. In [171] the design of an UPS is investigated based on DAB topology.

The DAB converter can be implemented with a single-phase or a three-phase structure. The general description of these topologies is given in following sections.

4.2.1.1. Single-Phase DAB Converter

Figure 4.18 shows the topology of a single-phase DAB. In this configuration, $S_1 - S_4$ and $Q_1 - Q_4$ are the active bridges (controllable switches) on primary and secondary sides of the converter. Besides, L is the leakage inductance of the transformer. Normally, the single phase-shift (SPS) modulation strategy is used in DAB converters. In this case, a phase shift φ is applied between the primary and secondary side switches which lead to a voltage difference v_L across the leakage inductance. The created voltage v_L also cause to the inductor current i_L that goes through the transformer. Then, the power p_{pri} can be transferred from primary to the secondary side or the other side around. The related operation waveforms of single-phase DAB converter are given in Figure 4.19. In this figure, the grey area stands as the backflow power created by negative leakage inductance current.

Looking at the literature, several studies have been done to investigate the single-phase DAB converter. A comprehensive analysis of a single-phase DAB converter is presented in [172] and [173]. The reactive power elimination and efficiency increasing approaches of an isolated bidirectional DAB converter is investigated in [174]. Stability analysis of an isolated DAB converter with triple phase shift is given in [175]. Some advanced control strategies such as dual phase shift (DPS) and hybrid phase shift control methods are illustrated in [176]–[178].

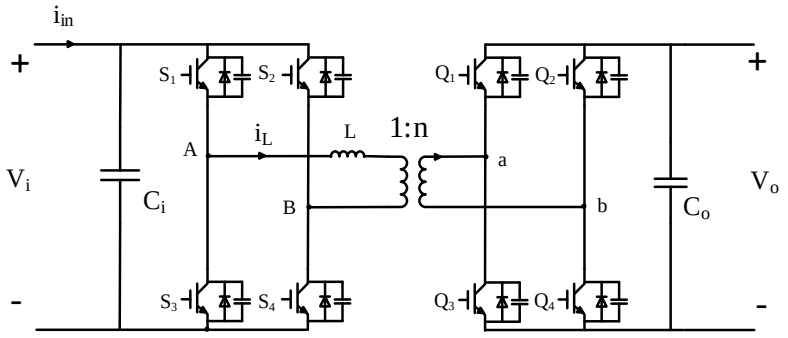

Figure 4.18. Topology of single-phase DAB converter.

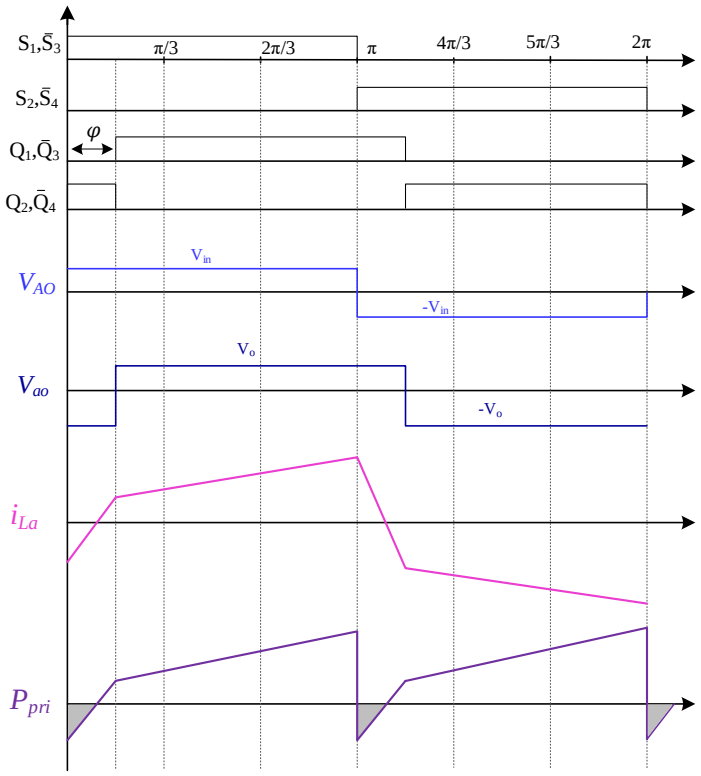

Figure 4.19. Operation waveforms of single-phase DAB converter.

By investigating all aspects of the single-phase DAB converter, its biggest advantage is simply achieving the ZVS for both primary and secondary side switches. On the other hand, it requires large capacitors on both input and output sides which is considered as a drawback for this topology.

4.2.1.2. Three-Phase DAB Converter

Compared with single-phase DAB converter, the three-phase DAB has the advantages of higher power density, lower rms current rating and smaller capacitor for both input side and output side of the converter [159]. The topology of a three-phase DAB converter is presented in Figure 4.20 which is composed by three-phase active bridges and a three-phase high frequency transformer in Y-Y connection with turn ratio n. The design and functional principles of a three-phase DAB converter is provided in [159], [179] and [161], [180]. The performance evaluation of a three-phase DAB converter with different transformer windings is presented in [181].

The conventional modulation strategy for three-phase DAB converters is the single-phase-shift (SPS) control [159], [182]–[184]. In this case, a phase shift φ is applied between the primary and secondary side switches which lead to a voltage difference v_L across the leakage inductance. The created voltage v_L also cause to the inductor current i_L that goes through the transformer. Then, the power p_{pri} can be transferred from primary to the secondary side or the other side around. In this control scheme, each bridge is usually driven by a 50% duty-cycle square voltage waveform. The power flow is controlled by switching both active bridge by applying a phase shift φ between the voltages imposed by the bridges on both sides of the transformers.

According to the phase-shift range, there are two operation modes where the phase-shift φ changes as $0 \leq \varphi \leq {}^{\pi}/_{3}$ and ${}^{\pi}/_{3} < \varphi \leq {}^{2\pi}/_{3}$. The related operation waveforms of the three-phase DAB converter are shown in Figure 4.21.

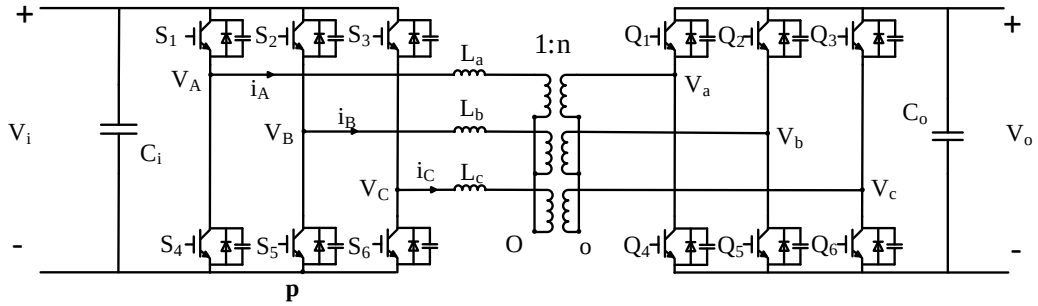

Figure 4.20. Topology of three-phase DAB converter.

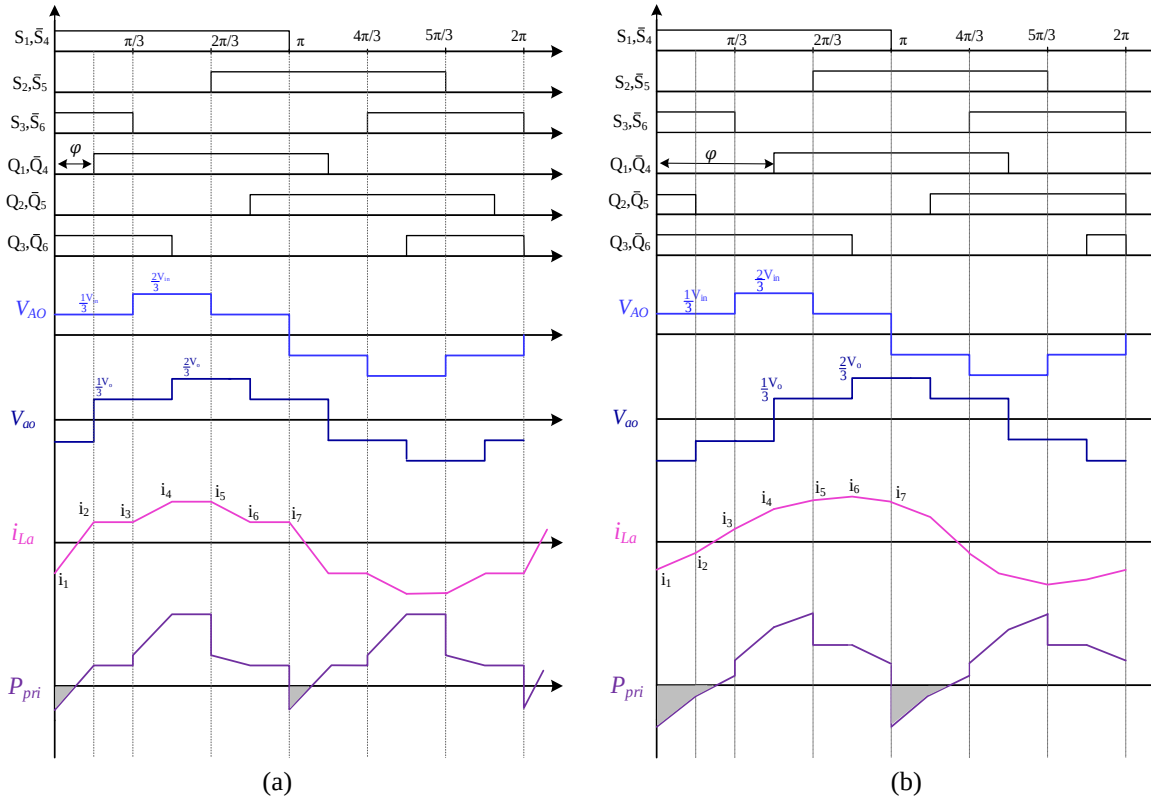

Figure 4.21. Operation waveforms of three-phase DAB converter: a) $0 < \varphi \leq \frac{\pi}{3}$, b) $\frac{\pi}{3} < \varphi \leq \frac{2\pi}{3}$.

The single-phase shift (SPS) control strategy has also some limitations due to its poor partial load efficiency. In order to increase efficiency in a wide operating range, several modulation techniques have been proposed for three-phase DAB converters to keep soft switching conditions and decrease the reactive power loss. A dual-phase-shift (DPS) control is presented in [185] to decrease the reactive power and increase the system efficiency while the input and output voltages are not match. Another modulation approach as phase shift plus one side modulation (PSPM) is proposed in [186] to keep ZVS conditions. This method consists of driving the bridge with the largest dc voltage to generate a three-level pulse-width-modulation (PWM) voltage waveform while the other bridge generates a constant-frequency 50% duty-cycle square voltage waveform. A novel PWM control method, ruled by phase shift between primary and secondary side and modulation index, is explained in [187]. However, using the DSP and PSPM methods lead to a very complex control algorithm of the converter. The reason behind is the output power is related to two phase-shift variables and the circulating current is still exist in this mode [188]. For this reason, these advanced modulation methods are not widely used in practical applications. Whereas the SPS method is an interesting approach for practical application because of its simplicity.

Regardless of what kind of the phase-shift method (SPS or advance methods) is used, in most studies control systems for DAB converters have been implemented using several sensors to measure the primary and secondary side voltages as well as the currents. The transferred power from primary to secondary, is an important variable which is usualy used in control of DAB converters. According to the equations provided in [187]–[189], the calculation of the transferred power need a good information about the system components and input voltage measurement. On the other hand, these control algorithms usually use a conventional model-based controller (MBC), such as PI, to create the desired control signals [190], [191]. Since these controllers are model-based, they need a precise model of the controlled system to design the controller.

Based on the discussion above, the available control algorithms for DAB converters has some limitations according to 1) using several sensors to measure the system variables, and 2) need for a precise information of the model and components of the controlled system.

In this section, the MFAC is used to control of a three-phase DAB converter by only measuring the output voltage. Since this control method is model-free, no information of the controlled system will be required to design the controller and all the control application will be done only using the I/O data measured from the system output. In order to avoid from a complicated control approach, the MFAC will operate in SPS mode to keep the ZVS and reliability of the system by creating the phase-shift angle φ between the primary and secondary sides of the transformers.

This section is organized as follows. A description of the three-phase DAB topology and its operating modes are firstly given in Section 4.2.2. MFAC design approach for the DAB converter is explained in Section 4.2.3. The simulation results are given in Section 4.2.4.

4.2.2. Basic Configuration and Operation Principles of the Three-Phase DAB Converter

The equivalent circuit of a three-phase DAB converter is given in Figure 4.20. In this diagram, V_i is the input voltage on the primary side while V_o is the output voltage on the secondary side, n is the turn ratio of the transformer from primary to secondary side and L_a, L_b, L_c are the leakage inductance. Resistances of the magnetic components are also neglected. Three-phase voltages on primary side are shown as V_{AO}, V_{BO}, V_{CO} and the secondary side voltages are shown as V_{ao}, V_{bo}, V_{co}. Due to the symmetry, only the analysis of the primary phase A and secondary phase B are given as an example. The same analysis is also valid for other phases.

As it mentioned earlier, the three-phase DAB converter has the possibility for bidirectional operation. Indeed, the power can be transferred from primary side to secondary side and vise versa. To facilitate the analysis flow, we suppose that the power transfer is from primary side (V_i) to secondary side (V_o), then the opposite condition can be investigated similarly. The primary side and secondary side switches are defined as S_i and Q_i ($i = 1, \dots, 6$) respectively. Each switch has two different states where $S_i = Q_i = 1$ means that the switch is conducting (On state) and the $S_i = Q_i = 0$ means that the switch is not conducting (Off state). According to these switching operation conditions and dc voltage of the primary side V_i, the three-phase voltages of the primary side legs can be obtained as:

$$\begin{cases} V_{Ap} = S_1 V_i \\ V_{Bp} = S_2 V_i \\ V_{Cp} = S_3 V_i \end{cases} \tag{4.9}$$

From the diagram shown in Figure 4.20, the following equation can be obtained to show the connection between the voltages of three-phase legs and the primary phase voltages of the transformer $V_{Ox} (x = A, B, C)$.

$$\begin{cases} V_{AO} = V_{AP} - V_{OP} \\ V_{BO} = V_{BP} - V_{OP} \\ V_{CO} = V_{CP} - V_{OP} \end{cases} \tag{4.10}$$

Where V_{OP} is the primary side neutral point voltage of the transformer that is referenced to the point p. Besides, the sum of the transformer phase voltages should be zero as:

$$V_{AO} + V_{BO} + V_{CO} = 0 \tag{4.11}$$

Finally, merging the equations (4.9)-(4.11), we can derive the expressions of the primary phase voltages of the transformer as follows.

$$\begin{cases} V_{AO} = \frac{1}{3}(2S_1 - S_2 - S_3)V_i \\ V_{BO} = \frac{1}{3}(2S_2 - S_1 - S_3)V_i \\ V_{CO} = \frac{1}{3}(2S_3 - S_1 - S_2)V_i \end{cases} \tag{4.12}$$

Similarly, using the switching states and dc voltage of the secondary side V_o, the secondary phase voltages of the transformer $V_{ox} (x = a, b, c)$ can be obtained as follows.

$$\begin{cases} V_{ao} = \frac{1}{3}(2Q_1 - Q_2 - Q_3)V_o \\ V_{bo} = \frac{1}{3}(2Q_2 - Q_1 - Q_3)V_o \\ V_{co} = \frac{1}{3}(2Q_3 - Q_1 - Q_2)V_o \end{cases} \tag{4.13}$$

According to the SPS control algorithm, the DAB converter operates only by applying a phase shift φ between the ac voltages of the primary and secondary sides. Each switch operates in one half period. From switching states shown in Table 4.4, a six-stage voltage waveform must be generated in both sides of the transformer. All the switching states and the generated waveforms for phase voltages of the transformer are presented in Figure 4.21.

Using the primary and secondary phase voltages of the transformer, the induced voltage across the leakage inductance can be calculated simply as:

$$V_{L_a} = V_{AO} - \frac{1}{n} V_{ao} \tag{4.14}$$

Thus, the inductor current in phase A can be obtained as:

$$L_a \frac{di_{L_a}}{dt} = V_{AO} - \frac{1}{n} V_{ao} \tag{4.15}$$

Using the current equation (4.15), the current on the primary side of the transformer is calculated as (4.16).

$$\begin{cases} i_1 = \dfrac{dV_o(2\pi d - 2\pi - 3d\varphi)}{18\pi n f L_a} \\ i_2 = \dfrac{dV_o(3\varphi - 2\pi + 2\pi d)}{18\pi n f L_a} \\ i_3 = \dfrac{dV_o(3d\varphi - \pi + \pi d)}{18\pi n f L_a} \\ i_4 = \dfrac{dV_o(6\varphi - \pi + \pi d)}{18\pi n f L_a} \\ i_5 = \dfrac{dV_o(\pi + 6d\varphi - \pi d)}{18\pi n f L_a} \\ i_6 = \dfrac{dV_o(3\varphi + \pi - \pi d)}{18\pi n f L_a} \end{cases} \quad 0 \le \varphi \le \frac{\pi}{3} \tag{4.16.a}$$

$$\begin{cases} i_1 = \dfrac{dV_o(3\pi d - 2\pi - 6d\varphi)}{18\pi n f L_a} \\ i_2 = \dfrac{dV_o(3\varphi - 3\pi + \pi d)}{18\pi n f L_a} \\ i_3 = \dfrac{dV_o(3\pi d - 3d\varphi - \pi)}{18\pi n f L_a} \\ i_4 = \dfrac{dV_o(6\varphi - 3\pi + 2\pi d)}{18\pi n f L_a} \\ i_5 = \dfrac{dV_o(\pi + 6d\varphi)}{18\pi n f L_a} \\ i_6 = \dfrac{dV_o(3\varphi + \pi d)}{18\pi n f L_a} \end{cases} \quad \frac{\pi}{3} \le \varphi \le \frac{2\pi}{3} \tag{4.16.b}$$

TABLE 4.4: SWITCHING STATES OF THREE-PHASE DAB CONVERTER

	state 1	*state 2*	*state 3*	*state 4*	*state 5*	*state 6*
S_1	1	1	1	0	0	0
S_2	0	0	1	1	1	0
S_3	1	0	0	0	1	1

Where $d = \frac{V_o}{nV_i}$ is the conversion ratio, f is the switching frequency, L_a is the leakage inductance, φ is the applied phase shift, V_i and V_o are the input and output voltages, respectively.

Average transferred power from primary side to secondary side of the transformer can be obtained as:

$$P = \frac{3}{\pi}\int_0^{\pi} V_{AO}(\theta) i_{L_a}(\theta) d\theta \tag{4.17}$$

Then the simplified equation is obtained as:

$$P = \begin{cases} \frac{V_o^2 d^3 \varphi}{2\pi n^2 f L_a}\left(\frac{2}{3} - \frac{\varphi}{2\pi}\right) & 0 \le \varphi \le \frac{\pi}{3} \\ \frac{V_o^2 d^3}{2\pi n^2 f L_a}\left(\varphi - \frac{\varphi^2}{\pi} - \frac{\pi}{18}\right) & \frac{\pi}{3} < \varphi \le \frac{2\pi}{3} \end{cases} \tag{4.18}$$

It is notable that the losses effects are not included in power calculation (4.18).

4.2.3. Description of the Studied System

4.2.3.1. Specifications of the Studied Three-Phase DAB Converter

The step-by-step controller design of the three-phase DAB converter with single-phase-shift (SPS) modulation is given in this section. Based on the discussion above, the SPS is used due to its simplicity and naturally achieved ZVS for all switches. The diagram of the studied three-phase DAB converter is given in Figure 4.22. Three single transformers with Y-Y connection is used in ac side. A typical 48V battery is used in primary side of the converter while the output dc bus voltage is 400V. The other specification of the studied three-phase DAB converter is given in Table 4.5. The secondary side of the converter is connected to resistive load as R_L. It is remarkable that this converter have been already designed by Dr Wang Deqiang during his PhD thesis [180] to achieve high efficiency for the half load to full load operation in whole input voltage range, while we will only work to design a controller for this three-phase DAB converter.

4.2.3.2. Controller Design for Studied Three-Phase DAB Converter

In this section, the MFAC algorithm is supposed to be used for control of the studied three-phase DAB converter. Since the MFAC is a data-driven control method, it does not require any information about the model of the controlled system to design the controller. This method uses only the I/O data measured from the system outputs and control inputs. From Figure 4.22, the output voltage V_o in secondary side of the converter is the only system output and the phase shift ratio φ is the only control input signal that supposed to be generated by the controller. Indeed, this system is considered as a SISO system with one system output and

TABLE 4.5: THREE-PHASE DAB PARAMETERS

Parameter	Quantity	Value
V_i	Input voltage	48 V
V_O	Output voltage	400 V
P	Power rating	3 kW
L_a, L_b, L_c	Leakage inductance	33 uH
f_s	Switching frequency	100 KHz
n	Transformer turn ratio	8
c_i	Input capacitor	80 uF
c_i	Output capacitor	10 uF

one control input signal. Thus, according to the MFAC theory of the SISO systems based on the FFDL data model, explained in Chapter 2, a controller will be designed for the studied three-phase DAB converter.

First, the system output V_o and control input φ satisfy the following inequality for any time instant k as:

$$\|\Delta V_o(k+1)\| \le b \left\| \Delta\left[V_o(k), \dots, V_o(k-L_y+1), \varphi(k), \dots, \varphi(k-L_u+1)\right] \right\|$$

where b is a constant and $\Delta V_o(k+1) = V(k+1) - V_o(k)$. This inequality indicates that the changes of the system output $\Delta V_o(k)$ is completely bounded by the changes of control input $\Delta\varphi(k)$. Indeed, this system meets the generalized Lipschitz condition and is eligible for MFAC.

In second step, by selecting the output-related and input-related linearization orders as $L_y = L_u = 4$, all the characteristics of the studied three-phase DAB converter is transformed into the full-form dynamic linearization data model (4.19) that does not include any information about the parameters or mathematical model of the system.

$$V_o(k+1) = \Psi_{p,L_u,L_y}(k)\, \Delta[V_o(k), \dots, V_o(k-3), \varphi(k), \dots, \varphi(k-3)]^T + V_o(k) \qquad (4.19)$$

where $\Psi_{p,L_u,L_y}(k) = [\Psi_1(k), \Psi_2(k), \dots, \Psi_8(k)] \in R^{1\times 8}$ is an unknown time-varying matrix that includes all the

possible complicated behaviors of the system given by (9). As this matrix is not available, its arrays should be estimated at each sampling time using only the I/O data obtained from the system output and control input.

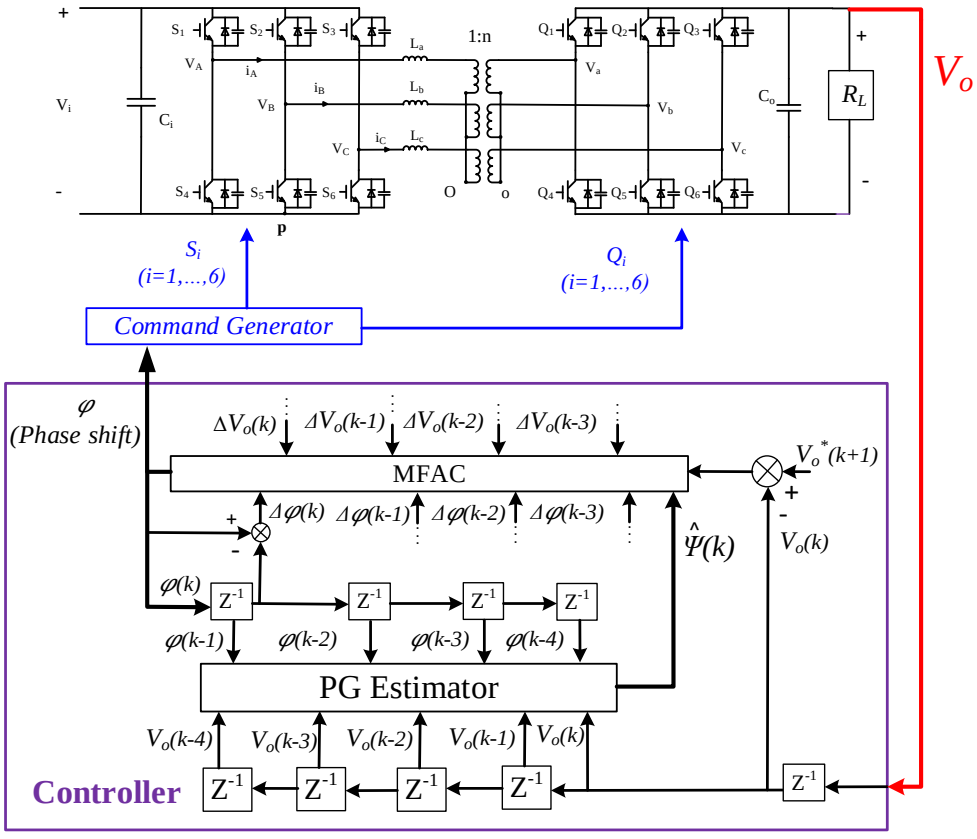

Figure 4.22. Control diagram of the studied three-phase DAB converter..

Based on the theories presented in Chapter 2, the following cost function is used to estimate the matrix $\Psi_{p,L_u,L_y}(k)$.

$$J\left(\Psi_{p,L_u,L_y}(k)\right) = \left\|\Delta v_o(k) - \Psi_{p,L_u,L_y}(k)\Delta H(k-1)\right\|^2 + \mu\left\|\Psi_{p,L_u,L_y}(k) - \widehat{\Psi}_{p,L_u,L_y}(k-1)\right\|^2 \quad (4.20)$$

where $\Delta H(k-1) = \Delta[V_o(k-1), \dots, V_o(k-4), \varphi(k-1), \dots, \varphi(k-4)]^T$, $\widehat{\Psi}_{p,L_u,L_y}$ is the estimated value of Ψ_{p,L_u,L_y}, and μ is a weight factor.

According to the optimum condition, the estimation algorithm is obtained as follows:

$$\widehat{\Psi}_{p,L_u,L_y}(k) = \widehat{\Psi}_{p,L_u,L_y}(k-1) + \frac{\eta\left(\Delta v_o(k) - \widehat{\Psi}_{p,L_u,L_y}(k-1)\Delta H(k-1)\right)\Delta H^T(k-1)}{\mu + \|\Delta H(k-1)\|^2} \quad (4.21)$$

In order to avoid from $\|\Delta H(k)\| = 0$ condition, the following resetting algorithm is also added to the estimation algorithm (4.21),

$$\widehat{\Psi}_{p,L_u,L_y}(k) = \widehat{\Psi}_{p,L_u,L_y}(1), \text{ if } \left\|\widehat{\Psi}_{p,L_u,L_y}(k)\right\| < \varepsilon \text{ or } \|\Delta H(k-1)\| < \varepsilon \text{ or } sign\left(\widehat{\Psi}_4(k)\right) \neq sign\left(\widehat{\Psi}_4(1)\right) \quad (4.22)$$

where $\widehat{\Psi}_{p,L_u,L_y}(1)$ is the initial value of $\widehat{\Psi}_{p,L_u,L_y}(k)$.

For the output voltage controller, the goal is to find a suitable phase shift ratio (φ), so that the output voltage error $\left(e(k) = V_{oref}(k) - V_o(k)\right)$ converges to zero. Thus, the cost function of the control input $\left(\varphi(k)\right)$ is used to design the controller.

$$J\left(\varphi(k)\right) = \left|V_{oref}(k+1) - V_o(k+1)\right|^2 + \lambda|\varphi(k) - \varphi(k-1)|^2 \quad (4.23)$$

By minimizing the cost function (4.23) according to the control input $\varphi(k)$, the control algorithm is designed as follows:

$$\begin{aligned}
&\varphi(k)\\
&= \varphi(k-1) + \frac{\rho_5\Psi_5(k)\left(V_{oref}(k+1) - V_o(k)\right)}{\lambda + \|\Psi_5(k)\|^2}\\
&- \frac{\Psi_5(k)\left(\rho_1\varphi_1(k)\Delta V_o(k) + \rho_2\Psi_2(k)\Delta V_o(k-1) + \rho_3\Psi_3(k)\Delta V_o(k-2) + \rho_4\Psi_4(k)\Delta V_o(k-3)\right)}{\lambda + \|\Psi_5(k)\|^2}\\
&- \frac{\Psi_6(k)\left(\rho_5\Psi_5(k)\Delta\varphi(k) + \rho_6\Psi_6(k)\Delta\varphi(k-1) + \rho_7\Psi_7(k)\Delta\varphi(k-2) + \rho_8\Psi_8(k)\Delta\varphi(k-3)\right)}{\lambda + \|\Psi_5(k)\|^2}
\end{aligned} \quad (4.24)$$

where $\rho_i \in (0, 1], i = 1, \dots, 8$ are the step factors.

TABLE 4.6: MFAC PARAMETERS FOR THREE-PHASE DAB CONVERTER

Parameter	λ	η	μ	ρ_1	ρ_2	ρ_3	ρ_4	ρ_5	ρ_6	ρ_7	ρ_8
Value	2	0.05	0.1	0.05	0.03	0.1	0.06	0.02	0.04	0.08	0.04

Finally, the FFDL-based MFAC scheme is obtained by synthesizing the estimation algorithms (4.21) and (4.22) and the control algorithm (4.24). From these equations, it can be concluded that this control scheme does not utilize any information about the components or a dynamic model of the system under consideration. The application of the MFAC, including the estimation of matrix $\Psi_{p,L_u,L_y}(k)$ and the design of the control signal $\varphi(k)$, is performed merely using the I/O data obtained from the system output and the control input. The general control diagram of the studied system is shown in Figure. 4.22 to illustrate the application of MFAC.

As stated earlier, several parameters are used in the controller design, namely $\lambda, \mu, \eta, \rho_i, a, b_1$, and b_2. The selection of optimal parameters for the controller is challenging, and they are usually chosen by trial and error. In this study, the parameters are selected using a genetic algorithm optimization method. The cost function to be minimized is the mean square error of the output voltage tracking a given profile. In the simulation, this error is calculated using a nominal model. The selected controller parameters are presented in Table 4.6.

4.2.4. Simulation Results

To verify the effectiveness of the MFAC approach in controlling the three-phase DAB converter, a series of numerical simulations are performed using MATLAB/Simulink. The simulation work has been done using an average model (4.12)-(4.18) and the rated parameter values, which are shown in Table 4.5. Besides, a dq-frame model of the primary side voltages and currents of the transformer were used to calculate the active and reactive power transferred to the secondary side. Applying synchronous frame transformation (abc-dq frame transformation) to equations (4.12) and (4.15), the three phase voltages and currents of the primary side were converted to dq-frame. Then, the transferred active and reactive powers were calculated as follows:

$$P = v_d i_d + v_q i_q \tag{4.25}$$

$$Q = v_d i_q - v_q i_d \tag{4.26}$$

where P and Q are the active and reactive powers, respectively.

The control diagrams shown in Figure 4.22, were used to evaluate the simulation performance of MFAC. Several tests were performed using the proposed controller to evaluate its performance. The startup and steady-state responses, setpoint tracking response, load variation, and parameter variations were considered.

A. Startup and steady-state responses

In this test, the output voltage reference was set as $v_{oref} = 400\ V$ and the input voltage was fixed at $V_i = 48V$. In addition, the startup performance of the MFAC was investigated for two different loads. In this case, the converter was loaded firstly as $P = 1500\ W$ (half load), then the next tests were performed for full-load condition where converter was loaded as $P = 3000\ W$, while being started up. The obtained simulation results according to the half load and full load conditions are presented in Figure. 4.23, and Figure 4.24, respectively.

As shown in these results, the performance of the controller for both controllers are almost similar; the output voltage converges to the expected trajectories with no steady state error. The only difference is about the transferred reactive power, where under nominal power operation ($P = 3000W$) the average reactive power transferred to the secondary side is about $Q = -4VA$, but during half-load operation its value increases to the $Q = -142VA$.

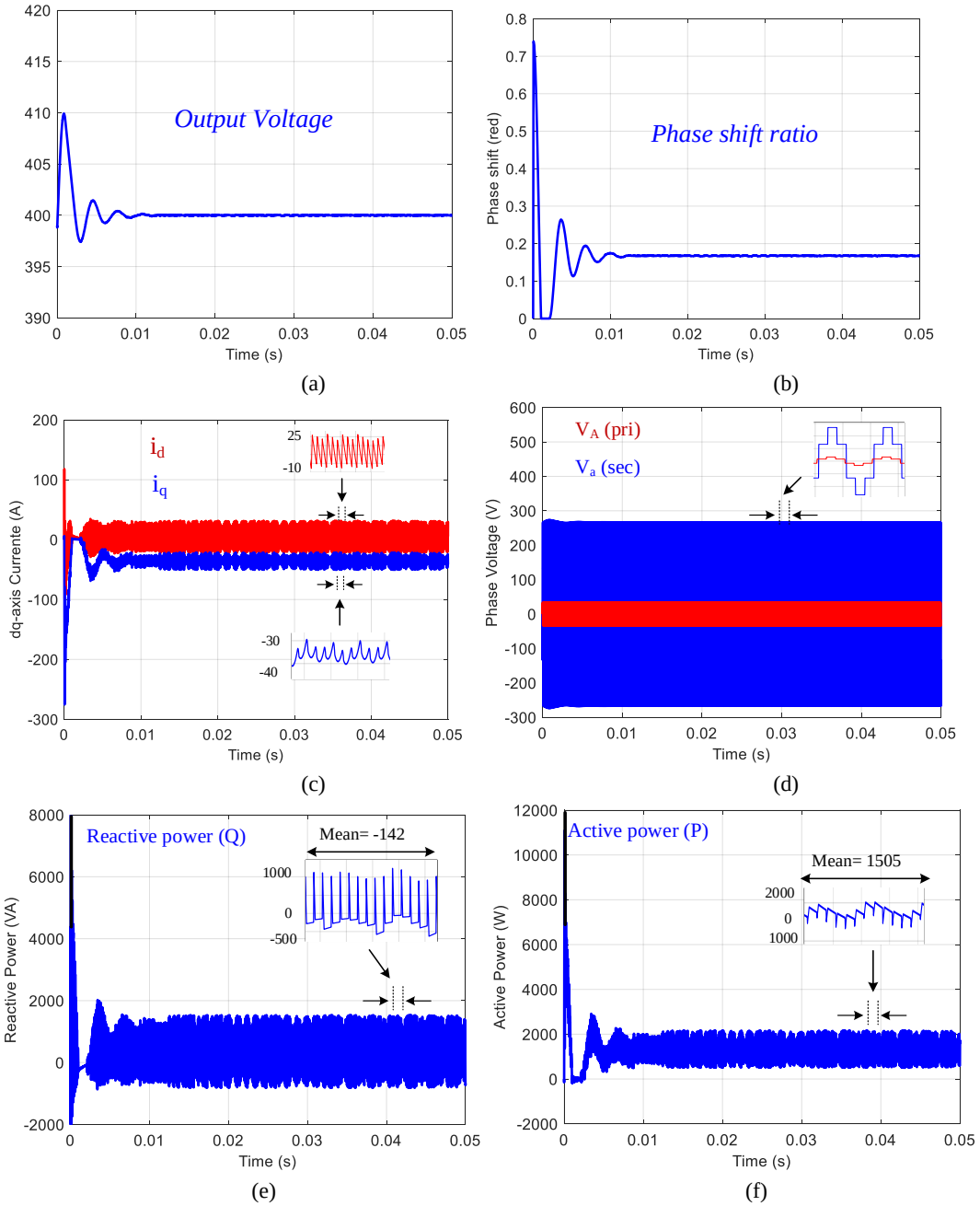

Figure 4.23. Startup and steady-state responses while converter is loaded by $P = 1500W$, a)output voltage, b)created phase shift, c)dq frame primary side currents, d) primary and secondary side phase voltages, e) reactive power and f) active power..

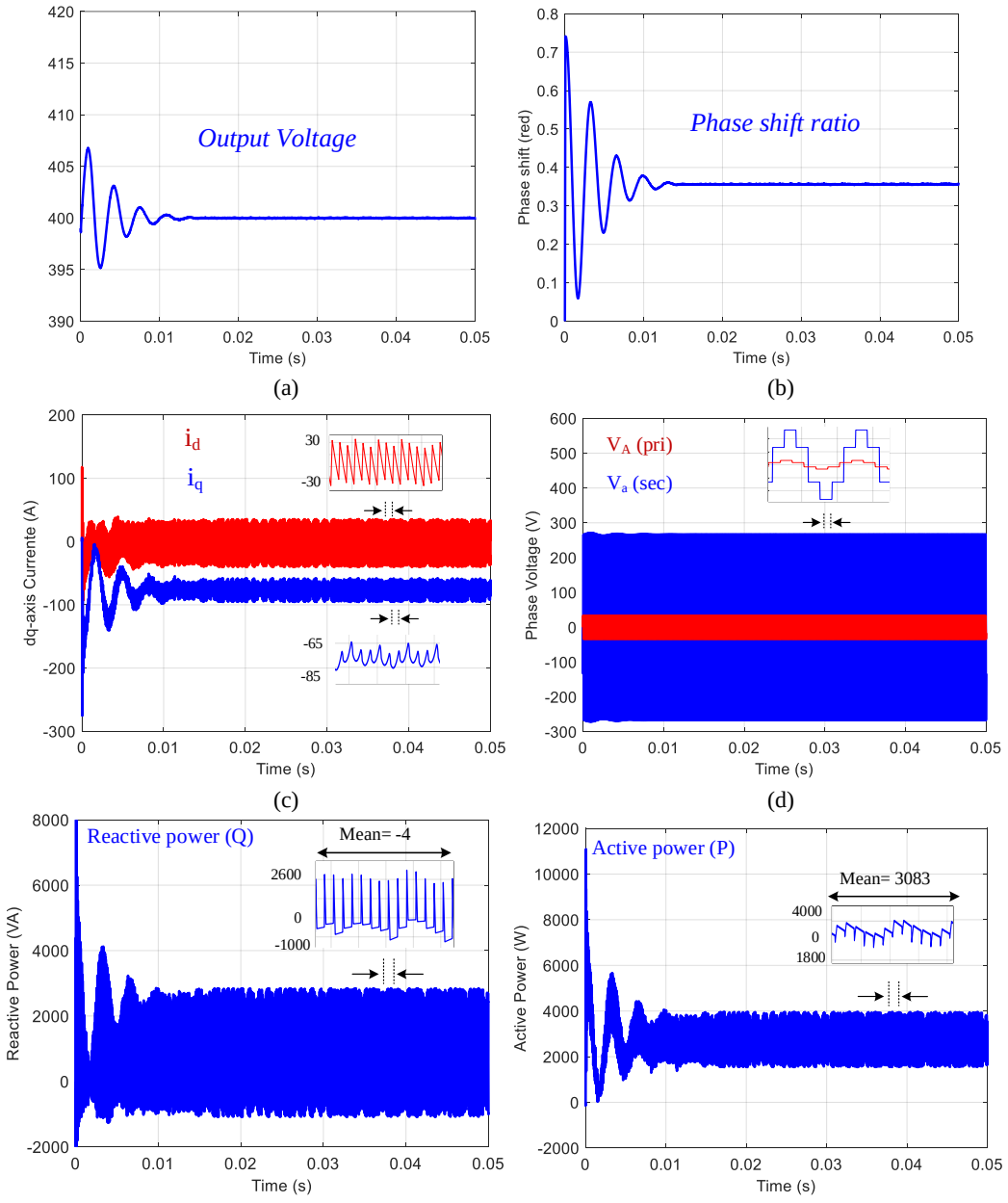

Figure 4.24. Startup and steady-state responses while converter is loaded by $P = 3000W$, a)output voltage, b)created phase shift, c)dq frame primary side currents, d) primary and secondary side phase voltages, e) reactive power and f) active power..

B. Parameter and Load variations

In this section, the effectiveness of the developed controller was tested under variation of the system parameters and the output load. Here, firstly (at $t = 0.04$) a parameter variation of +30% was considered for L, c_i and c_o at an operating point of $V_o = 400V$ with a load of $3000W$. Then, (at $t = 0.07$) a load step (from 3000W to 1500W) was applied to the system. Figure 4.25 shows the results obtained by varying the system parameters and load.

These results indicate a robust performance for the MFAC controller under load and parameter variations; the output voltage converges toward the expected trajectories with almost zero steady-state error and an acceptable transient performance.

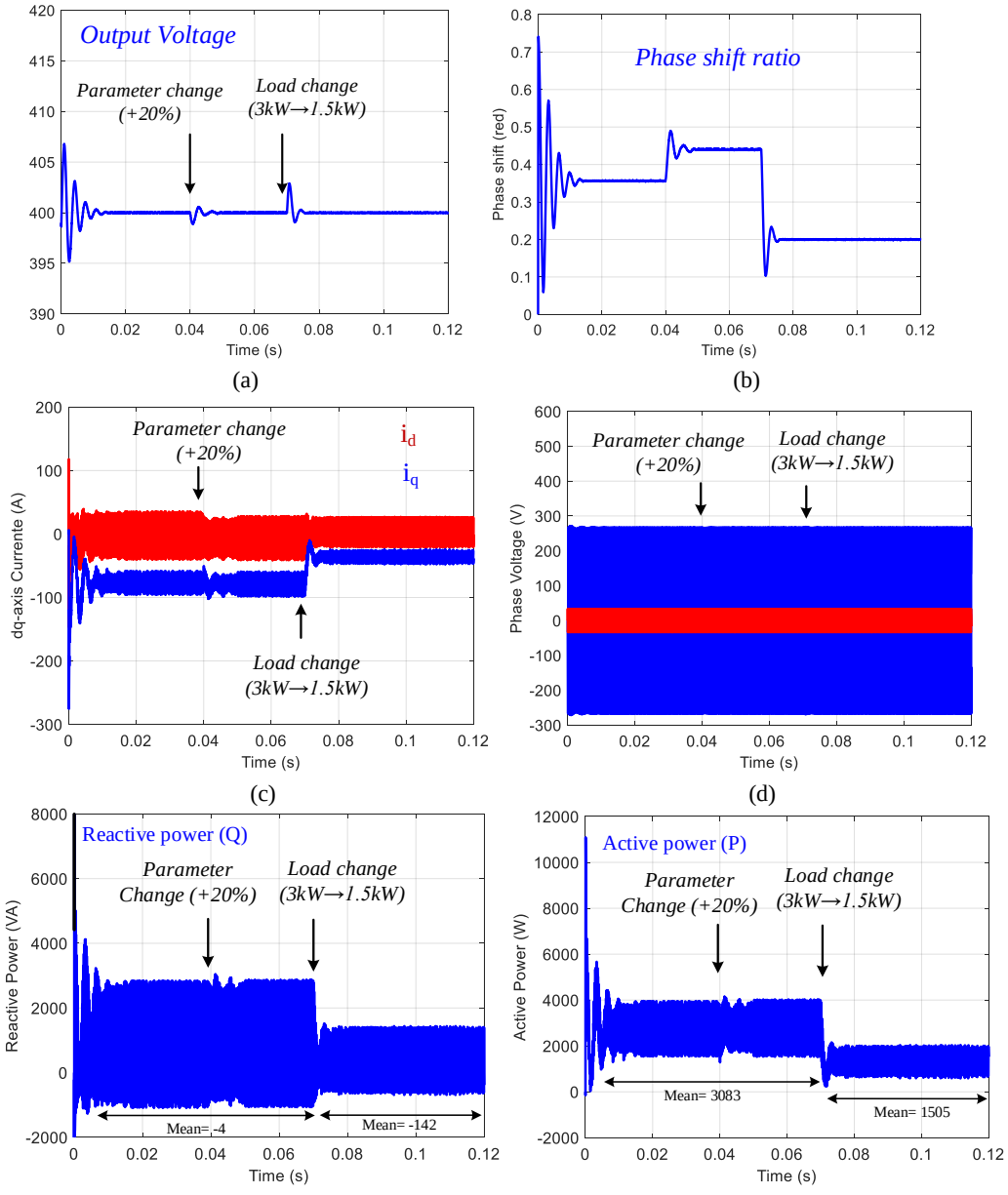

Figure 4.25. Obtained results by parameters and load variations for a) output voltage, b) created phase shift, c) *dq* frame primary side currents, d) primary and secondary side phase voltages, e) reactive power and f) active power.

C. Setpoint tracking

In these simulation tests, the tracking performance of the MFAC was tested using the condition that the output voltage reference changes when the system is operating under a load of 3000W. The system starts with an output voltage of $v_{oref} = 400\,V$. Then, at $t = 0.05\,s$, the operating point corresponds to an output voltage of $v_{oref} = 370V$. The related simulation results are shown in Figure 4.26. According to these results, the output voltage converges toward the expected trajectories with almost zero steady-state error and an acceptable transient performance. But, the reactive power (transferred to the secondary side) is increased by changing the output voltage. The reason behind is that the converter is designed with specific turn ratio n to be operated under certain input voltage V_i and output voltage V_o. Thus, operation of the converter may be affected by

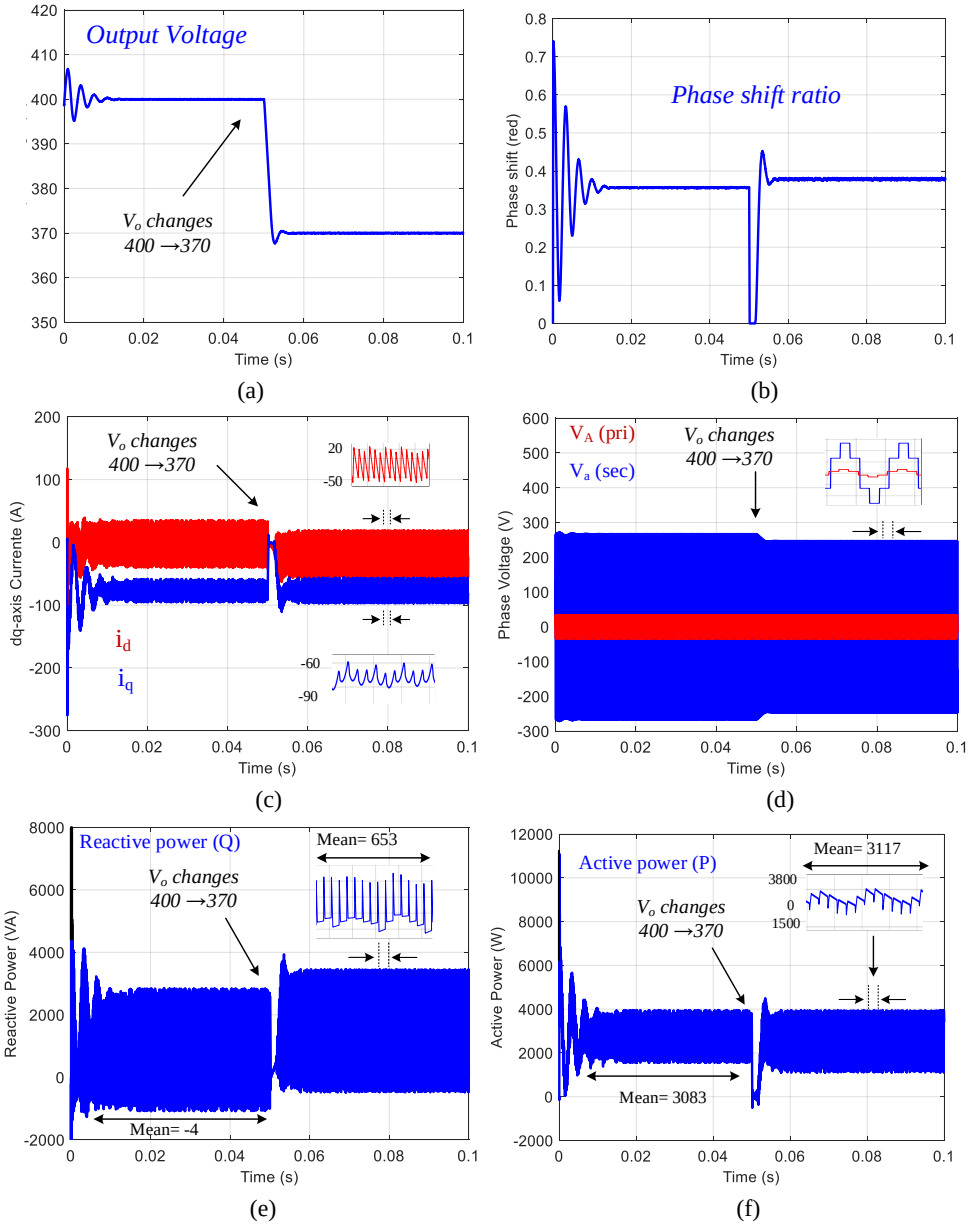

Figure 4.26. Obtained results under output voltage variation for a) output voltage, b) created phase shift, c) dq frame primary side currents, d) primary and secondary side phase voltages, e) reactive power and f) active

changing the output voltage, while the input voltage and turn ratio stay unchanged. Furthermore, since the output voltage is the only controlled variable and there is no control on the currents and system power, the impact of this variation is emitted on the transferred power.

Conclusion

A method for improving the performance of the control system of the power converters, used in electric drives, was proposed in this Chapter. Conventional control techniques are generally limited by the lack of a precise model of the controlled system and require several sensors and measured variables to design the controller. This study presents MFAC as a suitable alternative for the conventional MBC methods by overcoming their limitations.

MFAC is a data-driven control method that uses only the I/O data measured from the system output and input to design the controller, and is independent of the system model. The MFAC algorithm includes three main steps. First, using a novel dynamic linearization method, the model of the studied system is transformed into a linearized data model, which is a matrix (called PG) with unknown parameters. Then, the elements of the PG matrix are estimated at each sampling time using the measured I/O data from the controlled system. The third step involves designing a weighted step-ahead controller by using the estimated PG matrix and the measured I/O data.

In first section of this chapter, a MFAC was developed and used to control a DC-DC boost converter. In addition, a PI controller, which is a well-known control method, was developed to compare with the MFAC. The simulation and experimental results show that the MFAC is an efficient method to control DC-DC boost converters, as it requires only the measurement of the output voltage.

In second part of this chapter a three-phase DAB converter has been investigated. The basic configuration and operation principles are reviewed. Then the MFAC has been developed for control of the studied three-phase DAB converter with only measuring the output voltage. Performance of the developed MFAC has been tested in simulation under different operating conditions. The obtained simulation results represent a good performance for MFAC in control of the three-phase DAB converter.

CONCLUSION

The main goal of this thesis work was to develop a reliable and robust controller for AC drive systems, used in electric and hybrid electric vehicles, in such a way that the controller be operated with a minimum number of sensors and independent from the state model of the controlled system. Since an AC drive system consists of an AC machine and some power converters, the control of each part had to be considered separately. The reason behind the reduction of number of sensors can be explained as follows: in these last decades, the automotive industry have become more and more competitive where the companies needs to propose a cost optimization way to stay competitive. Reducing the number of electronic sensors, specially phase current sensors of the AC machine, is a solution to reduce the manufacturing and maintenance costs. Looking at the literature, the mechanical sensorless control strategy is widely studied and developed for these applications. On the other hand, as mentioned in chapter 1, the vehicle electrification goes toward using the low voltage and high current machines that however require some expensive current sensors. The i-StARS system is an example that is designed by Valeo to be used in mild-hybrid applications. By this way, the current sensorless control can also be considered as a good solution to reduce the costs due to removing several current sensors from drivetrain. Despite of mechanical sensorless control strategy, the current sensorless control approach is not broadly studied in the literature. The observation-based current sensorless control method is an approach that recently proposed by Dr. Corne in his PhD thesis. According to this approach, a nonlinear state observer is used to estimate the unmeasured current sensors. Then, the estimated variables are injected into a control loop. This control approach, and the related challenges are investigated in the chapter 1. Finally, in the last section of chapter 1, the data-driven control technologies, particularly model-free adaptive control, are proposed as a solution to fix the limitations of observation-based sensorless control methods.

In chapter 2, a description of data driven control theories, particularly MFAC, has been given with details. In order to explain the theory of MFAC, a novel dynamic linearization approach for discrete-time nonlinear systems is firstly presented in detail. In this case, three kinds of dynamic linearization data models, including compact form (CF) partial form (PF) and full form dynamic linearization (FFDL), are presented for single-input single-output (SISO), multi-input single-output (MISO) and multi-input multi-output (MIMO) nonlinear systems, respectively. Afterward, on the basis of these dynamic linearization approaches, three kinds of MFAC algorithms, CFDL-MFAC, PFDL-MFAC and FFDL-MFAC, are investigated for the unknown SISO and MIMO discrete-time nonlinear systems, respectively. Comparing the three kinds of MFAC schemes, the CFDL-MFAC is the simplest one which is usually used for simple systems. On the other hand, the last two methods are the special cases which can be used for more complex systems due to their more adjustable degree of freedom and more design flexibility by introducing more parameters during dynamic linearization data model.

In chapter 3, the studied WRSM system is firstly described by introducing the relate electromagnetic and electric model of the studied system. In second section of this chapter, the MFAC is developed for current control of the studied WRSM machine. Another PI controller is also developed to compare with MFAC. Several simulation and experimental tests have been carried out to check the effectiveness of the MFAC in

current control of the WRSM system. Comparing the experimental performance of PI and MFAC, an effective performance is concluded for MFAC. In third part of this chapter, a current sensorless control algorithm, using MFAC, is developed for WRSM system with only measuring the rotor speed. According to this control approach, neither measurement nor observations of the phase currents are used in control system. Another observation-based current sensorless control theory, proposed by Dr. Corne in his PhD thesis, is also used to compare with MFAC. The proposed control algorithm is firstly tested in simulation under several operating conditions. Startup, tracking, parameter variation and load step are considered. The obtained simulation results represent an effective performance of MFAC-based control algorithm. The only small error is reported on $d-axis$ current due to a remarkable variation of system parameters and load torque. Several experimental tests are performed to analyze the effectiveness of developed controller in which the obtained results highly validated the simulation performance of MFAC. Compare to the observation-based control method, since the MFAC does not depend on parameter of system, its tracking performance is more acceptable during variation of load or operating point. Since MFAC has no action on phase currents and controls only the rotor speed, its dynamic is relatively slow, and the currents need more time to converge to the desired references.

In chapter 4, the control study of the power converters, used in electric drive systems, is provided. Conventional control techniques are generally limited by the lack of a precise model of the controlled system and require several sensors and measured variables to design the controller. This study presents MFAC as a suitable alternative for the conventional MBC methods by overcoming their limitations. In first section of this chapter, the MFAC was developed and used to control a DC-DC boost converter. In addition, a PI controller, which is a well-known control method, was developed to compare with the MFAC. The simulation and experimental results show that the MFAC is an efficient method to control DC-DC boost converters, as it requires only the measurement of the output voltage. In second part of this chapter a three-phase DAB converter has been investigated. The basic configuration and operation principles are reviewed. Then, the MFAC has been developed for control of the studied three-phase DAB converter with only measuring the output voltage. Performance of the developed MFAC has been tested in simulation under different operating conditions. The obtained simulation results represent a good performance for MFAC in control of the three-phase DAB converter.

FUTURE WORKS

For further investigations into the control of the electric vehicles drive system several aspects can be discussed. The temperature of the conversion chain can be considered in the control of the electric drive system. Indeed, there are already temperature sensors in the traction chains. However, these generate significant additional costs because of their frequent failures and the need for a very expensive replacement of manpower. In this context, the thermal modeling of all the elements constituting the traction chain will be necessary to estimate the temperature of the critical points of the chain.

It could be interesting to test the solution proposed in this thesis to other electric machines than the WRSM for the sake of generality. Indeed, similar solution could be tested for a PMSM, an induction machine or a reluctance motor which are all potentially suitable for HEV application.

Regarding the intrinsic independence of MFAC from any information about the model of the studied system, the presented MFAC method could be used for different applications to improve the reliability of on electric powertrain. Indeed, the possibility to switch from a classic model-based controller to a model-free controller in case of a complex non-linear system could benefit the reliability of the whole electric system.

REFERENCES

[1] B. Sarlioglu, C. T. Morris, D. Han, and S. Li, "Driving Toward Accessibility," *IEEE Ind. Appl. Mag.*, vol. 23, no. 1, pp. 14–25, 2017, doi: 10.1109/MIAS.2016.2600739.

[2] M. Ehsani, Y. Gao, S. E.Gay, and A. Emadi, *Modern Electric, Hybrid Electric, and Fuel Cell Vehicles Fundamentals, Theory, and Design*. New York: Boca Raton, 2005.

[3] "Global ev outlook 2018 - international energy agency.," 2018.

[4] F. Badin, J. Scordia, R. Trigui, E. Vinot, and B. Jeanneret, "Hybrid electric vehicles energy consumption decrease according to drive train architecture, energy management and vehicle use," in *IET Hybrid Vehicle Conference*, 2006.

[5] C. C. Chan, "The state of the art of electric, hybrid, and fuel cell vehicles," *Proc. IEEE*, vol. 95, no. 4, pp. 704–718, 2007, doi: 10.1109/JPROC.2007.892489.

[6] K. Rajashekara, "Present status and future trends in electric vehicle propulsion technologies," *IEEE J. Emerg. Sel. Top. Power Electron.*, vol. 1, no. 1, pp. 3–10, 2013, doi: 10.1109/JESTPE.2013.2259614.

[7] I. Moutafidis, "Architecture and impacts of electric vehicles Architecture and impacts of electric vehicles," Hellenic University, 2011.

[8] Samuel E. de Lucena, *Electric Vehicles - The Benefits and Barriers*. Rijeka- Croatia, 2011.

[9] S. N. Jha, *A Text of Automobile Technology: For Class 9*. Goyal Brothers Prakashan, 2013.

[10] M. Boxwell, *The Electric Car Guide - 2015 Edition*. Coventry, UK: Greenstream Publishing Limited, 2014.

[11] M. Palinski, "A Comparison of Electric Vehicles and Conventional Automobiles : Costs and Quality Perspective," 2017.

[12] J. Erjavec, *Hybrid, Electric, and Fuel-Cell Vehicles*. New York, USA: Cengage Learning, 2012.

[13] E. WESOFF, "How Soon Can Tesla Get Battery Cell Costs Below $100 per Kilowatt-Hour?," 2015. [Online]. Available: https://www.greentechmedia.com/articles/read/How-Soon-Can-Tesla-Get-Battery-Cell-Cost-Below-100-per-Kilowatt-Hour.

[14] S. Edelstein, "Electric car price guide: every 2017 all-electric car, with specs," 2017. [Online]. Available: http://www.greencarreports.com/news/1080871_electric-car-price-guide-every-2015-2016-%0Aplug-in-car-with-specs-updated.

[15] A. Emadi, K. Rajashekara, S. S. Williamson, and S. M. Lukic, "Topological overview of hybrid electric and fuel cell vehicular power system architectures and configurations," *IEEE Trans. Veh. Technol.*, vol. 54, no. 3, pp. 763–770, 2005, doi: 10.1109/TVT.2005.847445.

[16] A. Emadi, M. Ehsani, and J. M. Miller, *Vehicular Electric Power Sys- tems: Land, Sea, Air, and Space Vehicles*. New York, USA: Marcel Dekker, 2013.

[17] B. Sarlioglu, C. T. Morris, D. Han, and S. Li, "Driving Toward Accessibility: A Review of Technological Improvements for Electric Machines, Power Electronics, and Batteries for Electric and Hybrid Vehicles," *IEEE Ind. Appl. Mag.*, vol. 23, no. 1, pp. 14–25, 2017, doi:

10.1109/MIAS.2016.2600739.

[18] S. A. Odhano, “Power Electronics, Electrical Machines and Drives,” Politecnico di Torino, 2014.

[19] F. Blaschke, “The principle of Field Orientation as Applied to the New TRANSVEKTOR Closed-Loop Control System for Rotating-Field Machines,” *Siemens Rev.*, vol. 34, no. 1972, pp. 217–220.

[20] L. Zhou, W. Gruber, and D. L. Trumper, “Position Control for Hysteresis Motors: Transient-Time Model and Field-Oriented Control,” *IEEE Trans. Ind. Appl.*, vol. 54, no. 4, pp. 3197–3207, 2018, doi: 10.1109/TIA.2018.2812143.

[21] B. J. Seibel, “Field-oriented control of an induction machine in the field-weakening region with dc-link and load disturbance rejection,” *IEEE Trans. Ind. Appl.*, vol. 33, no. 6, pp. 1578–1584, 1997, doi: 10.1109/28.649971.

[22] R. M. Prasad and M. A. Mulla, “Mathematical Modeling and Position-Sensorless Algorithm for Stator-Side Field-Oriented Control of Rotor-Tied DFIG in Rotor Flux Reference Frame,” *IEEE Trans. Energy Convers.*, vol. 35, no. 2, pp. 631–639, 2020, doi: 10.1109/TEC.2019.2956255.

[23] M. S. Naït Saïd and M. E. H. Benbouzid, “Induction motors Direct Field Oriented Control with robust on-line tuning of rotor resistance,” *IEEE Trans. Energy Convers.*, vol. 14, no. 4, pp. 1038–1042, 1999, doi: 10.1109/60.815025.

[24] Y. Inoue, S. Morimoto, and M. Sanada, “Comparative study of PMSM drive systems based on current control and direct torque control in flux-weakening control region,” *IEEE Trans. Ind. Appl.*, vol. 48, no. 6, pp. 2382–2389, 2012, doi: 10.1109/TIA.2012.2227134.

[25] Z. Zhang, S. Member, Y. Zhao, and S. Member, “A Space-Vector-Modulated Sensorless Direct-Torque Control for Direct-Drive PMSGWind Turbines,” *IEEE Trans. Ind. Appl.*, vol. 50, no. 4, pp. 2331–2341, 2014.

[26] Z. Zhang, Y. Zhao, W. Qiao, and L. Qu, “A Discrete-Time Direct Torque Control for Direct-Drive PMSG-Based Wind Energy Conversion Systems,” *IEEE Trans. Ind. Appl.*, vol. 51, no. 4, pp. 3504–3514, 2015, doi: 10.1109/TIA.2015.2413760.

[27] Y. S. Choi, H. H. Choi, and J. W. Jung, “Feedback Linearization Direct Torque Control with Reduced Torque and Flux Ripples for IPMSM Drives,” *IEEE Trans. Power Electron.*, vol. 31, no. 5, pp. 3728–3737, 2016, doi: 10.1109/TPEL.2015.2460249.

[28] G. H. B. Foo and X. Zhang, “Constant Switching Frequency Based Direct Torque Control of Interior Permanent Magnet Synchronous Motors with Reduced Ripples and Fast Torque Dynamics,” *IEEE Trans. Power Electron.*, vol. 31, no. 9, pp. 6485–6493, 2016, doi: 10.1109/TPEL.2015.2503292.

[29] G. Pellegrino, R. I. Bojoi, and P. Guglielmi, “Unified direct-flux vector control for AC motor drives,” *IEEE Trans. Ind. Appl.*, vol. 47, no. 5, pp. 2093–2102, 2011, doi: 10.1109/TIA.2011.2161532.

[30] S. A. Odhano, A. Boglietti, R. Bojoi, and E. Armando, “Unified direct-flux vector control of induction motor self-commissioning drive with analysis of parameter detuning effects,” *2013 IEEE Energy Convers. Congr. Expo. ECCE 2013*, pp. 2071–2078, 2013, doi: 10.1109/ECCE.2013.6646962.

[31] R. Bojoi, Z. Li, S. A. Odhano, G. Griva, and A. Tenconi, “Unified direct-flux vector control of induction motor drives with maximum torque per ampere operation,” *2013 IEEE Energy Convers.*

Congr. Expo. ECCE 2013, pp. 3888–3895, 2013, doi: 10.1109/ECCE.2013.6647216.

[32] A. Corne, "Current Sensorless Control Strategies for an Automotive Electric Powertrain," PhD thesis, IAEM - GREEN Université de Lorraine, 2019.

[33] X. Zhang, L. Sun, K. Zhao, And, and L. Sun, "Nonlinear speed control for PMSM system using sliding-mode control and disturbance compensation techniques," *IEEE Trans. Power Electron.*, vol. 28, no. 3, pp. 1358–1365, 2013.

[34] R. S. Munoz-Aguilar, E. F. Arnau Doria-Cerezo, and R. Cardoner, "Sliding mode control of a stand-alone wound rotor synchronous generator," *IEEE Trans. Ind. Electron.*, vol. 58, no. 10, pp. 4888–4897, 2011.

[35] Z. Hou and S. Jin, *Model Free Adaptive Control: Theory and Application*. Boca Raton: CRC Press, 2014.

[36] R. E. Kalman, "A new approach to linear filtering and prediction problems," *J. Basic Eng. Trans. ASME, Ser. D*, vol. 82, pp. 34–45, 1960.

[37] R. E. Kalman, "Contributions to the theory of optimal control," *Bol. la Soc. Mat. Mex.*, vol. 5, pp. 102–119, 1960.

[38] R. E. Skelton, "Model error concepts in control design," *Int. J. Control*, vol. 49, no. 5, pp. 1725–1753, 1989.

[39] H. Hjalmarsson, S. Gunnarsson, and M. Gevers, "A convergent iterative restricted com- plexity control design scheme," in *33rd IEEE Conference on Decision and Control, Orlando, USA*, 1994, pp. 1735–1740.

[40] H. Hjalmarsson, "Control of nonlinear systems using iterative feedback tuning," in *in Proc. 1998 American Control Conference, Philadephia, USA*, 1998, pp. 2083–2087.

[41] J. Sjöbergm and M. Agarwal, "Nonlinear controller tuning based on linearized time- variant model, in Albuquerque," in *Proc. 1997 American Control Conference,New Mexico*, 1997, pp. 3336–3340.

[42] J. Sjöberg, F. De Bruyne, M. Agarwal, B. D. O. Anderson, F. J. K. M. Gevers, and N. Linard, "Iterative controller optimization for nonlinear systems," *Control Eng. Pract.*, vol. 11, no. 9, pp. 1079–1086, 2003.

[43] J. Sjöberg, P. O. Gutman, M. Agarwal, and M. Bax, "Nonlinear controller tuning based on a sequence of identifications of linearized time-varying models," *Control Eng. Pract.*, vol. 17, no. 2, pp. 311–321, 2009.

[44] H. Hjalmarsson, M. Gevers, and S. Gunnarson, "Iterative feedback tuning-theory and applications," *IEEE Control Syst.*, vol. 18, no. 4, pp. 26–41, 1998.

[45] H. Hjalmarsson, "Iterative feedback tuning: An overview," *Int. J. Adapt. Control Signal Process.*, vol. 16, no. 5, pp. 373–395, 2002.

[46] R. Chi, Z. Hou, S. Jin, D. Wang, and J. Hao, "A data-driven iterative feedback tuning approach of ALINEA for freeway traffic ramp metering with PARAMICS simulations," *IEEE Trans. Ind. Informatics*, vol. 9, no. 4, pp. 2310–2317, 2013, doi: 10.1109/TII.2013.2238548.

[47] G. O. Guardabassi and S. M. Savaresi, "Virtual reference direct design method: an off-line approach

to data-based control system design," *IEEE Trans. Automat. Contr.*, vol. 45, no. 5, pp. 954–959, 2000.

[48] M. C. Campi, A. Lecchini, and S. M. Savaresi, "Virtual reference feedback tuning: A direct method for the design of feedback controllers," *Automatica*, vol. 38, no. 8, pp. 1337–1346, 2002.

[49] M. C. Campi and S. M. Savaresi, "Direct nonlinear control design: The virtual reference feedback tuning (VRFT) approach," *IEEE Trans. Automat. Contr.*, vol. 51, no. 1, pp. 14–27, 2006.

[50] M. Nakamoto, "An application of the virtual reference feedback tuning for an MIMO process," in *in Proc. 2004 SICE Annual Conference, Sapporo, Japan*, 2004, pp. 2208–2213.

[51] S. Yabui, K. Yubai, and H. J, "Direct design of switching control system by VRFT- application to vertical-type one-link arm," in *in Proc. 2007 SICE Annual Conference, Kagawa, Japan*, 2007, pp. 120–123.

[52] M. C. Campi, A. Lecchini, and S. M. Savaresi, "An application of the virtual reference feedback tuning method to a benchmark problem," *Eur. J. Control.*, vol. 9, pp. 66–76, 2003.

[53] Y. Jiang, Y. Zhu, K. Yang, C. Hu, and D. Yu, "A data-driven iterative decoupling feedforward control strategy with application to an ultraprecision motion stage," *IEEE Trans. Ind. Electron.*, vol. 62, no. 1, pp. 620–627, 2015, doi: 10.1109/TIE.2014.2327559.

[54] L. Duan, Z. Hou, X. Yu, S. Jin, and K. Lu, "Data-Driven Model-Free Adaptive Attitude Control Approach for Launch Vehicle with Virtual Reference Feedback Parameters Tuning Method," *IEEE Access*, vol. 7, pp. 54106–54116, 2019, doi: 10.1109/ACCESS.2019.2912902.

[55] H. S. Ahn, Y. Q. Chen, and K. L. Moore, "Iterative learning control: Brief survey and categorization," *IEEE Trans. Syst. Man, Cybern. Part C Appl. Rev.*, vol. 37, no. 6, pp. 1099–1121, 2007.

[56] Z. S. Hou, J. X. Xu, and J. W. Yan, "An iterative learning approach for density control of freeway traffic flow via ramp metering," *Transp. Res. Part C*, vol. 16, no. 1, pp. 71–79, 2008.

[57] J. C. Spall, "Multivariate stochastic approximation using a simultaneous perturba- tion gradient approximation," *IEEE Trans. Automat. Contr.*, vol. 37, no. 3, pp. 332–341, 1992.

[58] F. Rezayat, "On the use of an SPSA-based model-free controller in quality improve- ment," *Automatica*, vol. 31, no. 6, pp. 913–915, 1995.

[59] J. C. S. Chin and D. C., "Traffic-responsive signal timing for system-wide traffic control," *Transp. Res. Part C*, vol. 5, no. 3–4, pp. 153–163, 1997.

[60] Z. S. Hou, "The Parameter Identification, Adaptive Control and Model Free Learning Adaptive Control for Nonlinear Systems," Northeastern University, Shenyang, China, 1994.

[61] Z. S. Hou, *Nonparametric Models and Its Adaptive Control Theory*. Beijing: Science Press, 1999.

[62] Z. S. Hou and S. T. Jin, "A novel data-driven control approach for a class of discrete- time nonlinear systems," *IEEE Trans. Control Syst. Technol.*, vol. 19, no. 6, pp. 1549–1558, 2011.

[63] Z. S. Hou and S. T. Jin, "Data driven model-free adaptive control for a class of MIMO nonlinear discrete-time systems," *IEEE Trans. Neural Networks*, vol. 22, no. 12, pp. 2173–2188, 2011.

[64] S. A. Hashjin and B. Nahid-Mobarakeh, "Active stabilization of a microgrid using model free adaptive control," in *2017 IEEE Industry Applications Society Annual Meeting, IAS 2017*, 2017, vol. 2017-Janua, doi: 10.1109/IAS.2017.8101797.

[65] H. Zhang, J. Zhou, Q. Sun, J. M. Guerrero, and D. Ma, "Data-Driven Control for Interlinked AC/DC Microgrids Via Model-Free Adaptive Control and Dual-Droop Control," *IEEE Trans. Smart Grid*, vol. 8, no. 2, pp. 557–571, 2017, doi: 10.1109/TSG.2015.2500269.

[66] Y. Zhu, Z. Hou, F. Qian, and W. Du, "Dual RBFNNs-Based Model-Free Adaptive Control with Aspen HYSYS Simulation," *IEEE Trans. Neural Networks Learn. Syst.*, vol. 28, no. 3, pp. 759–765, 2017, doi: 10.1109/TNNLS.2016.2522098.

[67] Y. Zhao, Z. Yuan, C. Lu, G. Zhang, X. Li, and Y. Chen, "Improved model-free adaptive wide-area coordination damping controller for multiple-input-multiple-output power systems," *IET Gener. Transm. Distrib.*, vol. 10, no. 13, pp. 3264–3275, 2016, doi: 10.1049/iet-gtd.2016.0069.

[68] R. C. Roman, M. B. Radac, and R. E. Precup, "Multi-input-multi-output system experimental validation of model-free control and virtual reference feedback tuning techniques," *IET Control Theory Appl.*, vol. 10, no. 12, pp. 1395–1403, 2016, doi: 10.1049/iet-cta.2016.0028.

[69] S. A. Hashjin, E.-H. Miliani, K. Ait-Abderrahirrr, and B. Nahid-Mobarakeh, "Current Sensorless Model Free Control Applied on PMSM Drive System," *2019 IEEE Transp. Electrif. Conf. Expo*, pp. 1–5, Jun. 2019, doi: 10.1109/ITEC.2019.8790572.

[70] Z. S. Hou and W. H. Huang, "The model-free learning adaptive control of a class of SISO nonlinear systems," in *in Proc. 1997 American Control Conference, Albuquerque, New Mexico*, 1997, pp. 343–344.

[71] Z. S. Hou, "On model-free adaptive control: The state of the art and perspective," *Control Theory Appl.*, vol. 23, no. 4, pp. 586–592, 2006.

[72] Z. S. Hou and X. H. Bu, "Model free adaptive control with data dropouts," *Expert Syst. Appl.*, vol. 38, no. 8, pp. 10709–10717, 2011.

[73] W. Rudin, *Principles of mathematical analysis*. New York: McGraw-Hill, 1976.

[74] F. C. C. and H. K. Khalil, "Adaptive control of a class of nonlinear discrete-time systems," *IEEE Trans. Automat. Contr.*, vol. 40, no. 5, pp. 791–801, 1995.

[75] Y. Zhang, C. Y. Wen, and Y. C. Soh, "Robust adaptive control of uncertain discrete- time systems," *Automatica*, vol. 35, no. 5, pp. 321–329, 1999.

[76] R. 1Findeisen, L. Imsland, F. Allgöwer, and B. A. Foss, "State and output feedback nonlinear model predictive control: An overview," *Eur. J. Control.*, vol. 9, no. 2–3, pp. 190–206, 2003.

[77] M. A. Henson, "Nonlinear model predictive control: current status and future direc- tions," *Comput. Chem. Eng.*, vol. 23, no. 2, pp. 187–202, 1998.

[78] B. Kouvaritakis and M. Cannon, *Nonlinear Predictive Control: Theory and Practice*. London: The Institution of Engineering and Technology, 2001.

[79] L. Magni, D. M. Raimondo, and F. Allögwer, *Nonlinear Model Predictive Control: Towards New Challenging Applications*. Berlin Heidelberg: Springer-Verlag, 2009.

[80] M. Krstic and A. Smyshlyaev, "Adaptive boundary control for unstable parabolic PDEs-Part I: Lyapunov design," *IEEE Trans. Automat. Contr.*, vol. 53, no. 7, pp. 1575–1591, 2008.

[81] Y. Zhang, W. H. Chen, and Y. C. Soh, "Improved robust backstepping adaptive control for nonlinear

discrete-time systems without overparameterization," *Automatica*, vol. 44, no. 3, pp. 864–867, 2008.

[82] J. Zhou and C. Y. Wen, "Decentralized backstepping adaptive output tracking of inter- connected nonlinear systems," *IEEE Trans. Automat. Contr.*, vol. 53, no. 10, pp. 2378–2384, 2008.

[83] J. Zhou, C. Y. Wen, and Y. Zhang, "Adaptive backstepping control of a class of uncer- tain nonlinear systems with unknown backlash-like hysteresis," *IEEE Trans. Automat. Contr.*, vol. 49, no. 10, pp. 1751–1759, 2004.

[84] X. K. Chen, T. Fukuda, and K. D. Young, "Adaptive quasi-sliding-mode tracking control for discrete uncertain input output systems," *IEEE Trans. Ind. Electron.*, vol. 48, no. 1, pp. 216–224, 2001.

[85] X. K. Chen, "Adaptive sliding mode control for discrete-time multi-input multi-output systems," *Automatica*, vol. 42, no. 3, pp. 427–435, 2006.

[86] K. S. Narendra and C. Xiang, "Adaptive control of discrete-time systems using mul- tiple models," *IEEE Trans. Automat. Contr.*, vol. 45, no. 9, pp. 1669–1686, 2000.

[87] K. S. Narendra, M. F. O. A. Driollet, and K. George, "Adaptive control using mul- tiple models, switching and tuning," *Int. J. Adapt. Control Signal Process.*, vol. 17, no. 2, pp. 87–102, 2003.

[88] Z. Hou, "The parameter identification, adaptive control and model free learning adaptive control for nonlinear systems," Northeastern Univ. Shenyang, China, 1994.

[89] Z. Hou and S. Xiong, "On Model-Free Adaptive Control and Its Stability Analysis," *IEEE Trans. Automat. Contr.*, vol. 64, no. 11, pp. 4555–4569, 2019, doi: 10.1109/TAC.2019.2894586.

[90] K. J. Åström and B. Wittenmark, *Adaptive Control*. Boston, MA: Addison-Wesley Longman Publishing Co., Inc, 1994.

[91] E. I. Jury, *Theory and Application of the z-Transform Method*. New York: Wiley, 1964.

[92] S. Gerschgorin, "Uber die abgrenzung der eigenwerte einer matrix," *Akad. Nauk. USSR Otd. Fiz. -Mat. Nauk 7, Izv*, pp. 749–754, 1931.

[93] L. Huang, *Linear Algebra in System and Control Theory*. Beijing: Science Press, 1984.

[94] G. Devornique, "Modélisation et optimisation d'un alterno-démarreur synchrone à griffes pour l'application mild-hybrid," PhD thesis, IAEM - GREEN Université de Lorraine, 2017.

[95] B. Beatrice, "Caractérisation de MOSFETs de puissance cyclés en avalanche pour des applications automobile micro-hybrides," PhD thesis, INSA Toulouse, 2010.

[96] Mitsubishi Electric, "FM600TU-07A," Technical report, 2006.

[97] E. Ramsden, "Hall-Effect Sensors: Theory and Application," Newnes, 2006.

[98] C. K. Lin, T. H. Liu, J. Te Yu, L. C. Fu, and C. F. Hsiao, "Model-free predictive current control for interior permanent-magnet synchronous motor drives based on current difference detection technique," *IEEE Trans. Ind. Electron.*, vol. 61, no. 2, pp. 667–681, 2014, doi: 10.1109/TIE.2013.2253065.

[99] J. A. Suul, K. Ljøkelsøy, T. Midtsund, and T. Undeland, "Synchronous reference frame hysteresis current control for grid converter applications," *IEEE Trans. Ind. Appl.*, vol. 47, no. 5, pp. 2183–2194, 2011, doi: 10.1109/TIA.2011.2161738.

[100] X. Sun, Z. Shi, L. Chen, and Z. Yang, "Internal model control for a bearingless permanent magnet synchronous motor based on inverse system method," *IEEE Trans. Energy Convers.*, vol. 31, no. 4,

pp. 1539–1548, 2016, doi: 10.1109/TEC.2016.2591925.

[101] K. M. Cho, W. S. Oh, Y. T. Kim, and H. J. Kim, “A new switching strategy for pulse width modulation (PWM) power converters,” *IEEE Trans. Ind. Electron.*, vol. 54, no. 1, pp. 330–337, 2007, doi: 10.1109/TIE.2006.888793.

[102] L. Sun, X. Zhang, L. Sun, and K. Zhao, “Nonlinear speed control for PMSM system using sliding-mode control and disturbance compensation techniques,” *IEEE Trans. Power Electron.*, vol. 28, no. 3, pp. 1358–1365, 2013, doi: 10.1109/TPEL.2012.2206610.

[103] A. Dòria-Cerezo, V. I. Utkin, R. S. Muñoz-Aguilar, and E. Fossas, “Two sliding mode control approaches for the stator voltage amplitude regulation of a stand-alone WRSM,” *Proc. 2010 11th Int. Work. Var. Struct. Syst. VSS 2010*, pp. 440–445, 2010, doi: 10.1109/VSS.2010.5544707.

[104] S. Barkat, A. Tlemçani, and H. Nouri, “Noninteracting adaptive control of PMSM using interval type-2 fuzzy logic systems,” *IEEE Trans. Fuzzy Syst.*, vol. 19, no. 5, pp. 925–936, 2011, doi: 10.1109/TFUZZ.2011.2152815.

[105] C. S. Lim, E. Levi, M. Jones, N. A. Rahim, and W. P. Hew, “A comparative study of synchronous current control schemes based on FCS-MPC and PI-PWM for a two-motor three-phase drive,” *IEEE Trans. Ind. Electron.*, vol. 61, no. 8, pp. 3867–3878, 2014, doi: 10.1109/TIE.2013.2286573.

[106] B. Bahrani, S. Kenzelmann, and A. Rufer, “Multivariable-PI-based dq current control of voltage source converters with superior axis decoupling capability,” *IEEE Trans. Ind. Electron.*, vol. 58, no. 7, pp. 3016–3026, 2011, doi: 10.1109/TIE.2010.2070776.

[107] S. Mariethoz, A. Domahidi, and M. Morari, “High-bandwidth explicit model predictive control of electrical drives,” *IEEE Trans. Ind. Appl.*, vol. 48, no. 6, pp. 1980–1992, 2012, doi: 10.1109/TIA.2012.2226198.

[108] Z. Mynar, L. Vesely, and P. Vaclavek, “PMSM Model Predictive Control with Field-Weakening Implementation,” *IEEE Trans. Ind. Electron.*, vol. 63, no. 8, pp. 5156–5166, 2016, doi: 10.1109/TIE.2016.2558165.

[109] C. Jia, X. Wang, Y. Liang, and K. Zhou, “Robust Current Controller for IPMSM Drives Based on Explicit Model Predictive Control with Online Disturbance Observer,” *IEEE Access*, vol. 7, pp. 45898–45910, 2019, doi: 10.1109/ACCESS.2019.2908383.

[110] B. Nahid-Mobarakeh, F. Meibody-Tabar, and F. M. Sargos, “Mechanical sensorless control of PMSM with online estimation of stator resistance,” *IEEE Trans. Ind. Appl.*, vol. 40, no. 2, pp. 457–471, 2004, doi: 10.1109/TIA.2004.824490.

[111] F. Genduso, R. Miceli, C. Rando, and G. R. Galluzzo, “Back EMF sensorless-control algorithm for high-dynamic performance PMSM,” *IEEE Trans. Ind. Electron.*, vol. 57, no. 6, pp. 2092–2100, 2010, doi: 10.1109/TIE.2009.2034182.

[112] G. Liu, C. Cui, K. Wang, B. Han, and S. Zheng, “Sensorless Control for High-Speed Brushless DC Motor Based on the Line-to-Line Back EMF,” *IEEE Trans. Power Electron.*, vol. 31, no. 7, pp. 4669–4683, 2016, doi: 10.1109/TPEL.2014.2328655.

[113] X. Song, B. Han, S. Zheng, and J. Fang, “High-Precision Sensorless Drive for High-Speed BLDC

Motors Based on the Virtual Third Harmonic Back-EMF," *IEEE Trans. Power Electron.*, vol. 33, no. 2, pp. 1528–1540, 2018, doi: 10.1109/TPEL.2017.2688478.

[114] A. T. Woldegiorgis, X. Ge, S. Li, and M. Hassan, "Extended Sliding Mode Disturbance Observer-Based Sensorless Control of IPMSM for Medium and High-Speed Range Considering Railway Application," *IEEE Access*, vol. 7, pp. 175302–175312, 2019, doi: 10.1109/ACCESS.2019.2957274.

[115] Y. S. Han, J. S. Choi, and Y. S. Kim, "Sensorless PMSM drive with a sliding mode control based adaptive speed and stator resistance estimator," *IEEE Trans. Magn.*, vol. 36, no. 5 I, pp. 3588–3591, 2000, doi: 10.1109/20.908910.

[116] S. Ebersberger, M. Seilmeier, and B. Piepenbreier, "Flatness based sensorless control of PMSM using test current signal injection and compensation for differential cross-coupling inductances at standstill and low speed range," *SLED/PRECEDE 2013 - 2013 IEEE Int. Symp. Sensorless Control Electr. Drives Predict. Control Electr. Drives Power Electron.*, 2013, doi: 10.1109/SLED-PRECEDE.2013.6684510.

[117] N. Ansari, N. Khan, and S. B. Rewatkar, "Reconstruction of Phase Current of Induction Motor Drive based on DC Link Measurement," *IOSR J. Electr. Electron. Eng.*, vol. 2014, pp. 58–65, 2014.

[118] L. Ying and N. Ertugrul, "An observer-based three-phase current reconstruction using DC link measurement in PMAC motors," *Conf. Proc. - IPEMC 2006 CES/IEEE 5th Int. Power Electron. Motion Control Conf.*, vol. 1, pp. 147–151, 2007, doi: 10.1109/IPEMC.2006.297062.

[119] Y. Li, M. Yang, J. Long, Z. Liu, and D. Xu, "Current sensorless predictive control based on extended kalman filter for pmsm drives," *2017 IEEE Transp. Electrif. Conf. Expo, Asia-Pacific, ITEC Asia-Pacific 2017*, no. 3, 2017, doi: 10.1109/ITEC-AP.2017.8080902.

[120] A. Corne, N. Yang, J. P. Martin, B. Nahid-Mobarakeh, and S. Pierfederici, "Nonlinear Estimation of Stator Currents in a Wound Rotor Synchronous Machine," *IEEE Trans. Ind. Appl.*, vol. 54, no. 4, pp. 3858–3867, 2018, doi: 10.1109/TIA.2018.2824765.

[121] B. Vaseghi, N. Takorabet, and F. Meibody-Tabar, "Fault analysis and parameter identification of permanent-magnet motors by the finite-element method," *IEEE Trans. Magn.*, vol. 45, no. 9, pp. 3290–3295, 2009, doi: 10.1109/TMAG.2009.2022156.

[122] J. J. Guedes, M. F. Castoldi, and A. Goedtel, "Temperature influence analysis on parameter estimation of induction motors using differential evolution," *IEEE Lat. Am. Trans.*, vol. 14, no. 9, pp. 4097–4105, 2016, doi: 10.1109/TLA.2016.7785939.

[123] A. Corne, J. P. Martin, B. Nahid-Mobarakeh, and S. Pierfederici, "Current sensorless control using a nonlinear observer applied to a wound rotor synchronous machine," *2017 IEEE Transp. Electrif. Conf. Expo, ITEC 2017*, pp. 436–441, 2017, doi: 10.1109/ITEC.2017.7993310.

[124] C. K. Lin, J. Te Yu, Y. S. Lai, and H. C. Yu, "Improved Model-Free Predictive Current Control for Synchronous Reluctance Motor Drives," *IEEE Trans. Ind. Electron.*, vol. 63, no. 6, pp. 3942–3953, 2016, doi: 10.1109/TIE.2016.2527629.

[125] P. G. Carlet, F. Tinazzi, S. Bolognani, and M. Zigliotto, "An Effective Model-Free Predictive Current Control for Synchronous Reluctance Motor Drives," *IEEE Trans. Ind. Appl.*, vol. 55, no. 4, pp. 3781–

3790, 2019, doi: 10.1109/TIA.2019.2910494.

[126] Y. Zhou, H. Li, R. Liu, and J. Mao, “Continuous Voltage Vector Model-Free Predictive Current Control of Surface Mounted Permanent Magnet Synchronous Motor,” *IEEE Trans. Energy Convers.*, vol. 34, no. 2, pp. 899–908, 2019, doi: 10.1109/TEC.2018.2867218.

[127] K. Zhao *et al.*, “Robust Model-Free Nonsingular Terminal Sliding Mode Control for PMSM Demagnetization Fault,” *IEEE Access*, vol. 7, pp. 15737–15748, 2019, doi: 10.1109/ACCESS.2019.2895512.

[128] Y. Wang, H. Li, R. Liu, L. Yang, and X. Wang, “Modulated model-free predictive control with minimum switching losses for PMSM drive system,” *IEEE Access*, vol. 8, pp. 20942–20953, 2020, doi: 10.1109/ACCESS.2020.2968379.

[129] C. Maurice, J. Francisco, M. Diaz, and F. Lerasle, “Hyper-optimization tools comparison for parameter tuning applications,” in *2017 14th IEEE International Conference on Advanced Video and Signal Based Surveillance (AVSS)*, 2017, pp. 1–6.

[130] C. Huang, Y. Li, and X. Yao, “A Survey of Automatic Parameter Tuning Methods for Metaheuristics,” *IEEE Trans. Evol. Comput.*, vol. 24, no. 2, pp. 201–216, 2019, doi: 10.1109/tevc.2019.2921598.

[131] M. Gleissner and M. M. Bakran, “Design and control of fault-tolerant nonisolated multiphase multilevel DC–DC converters for automotive power systems,” *IEEE Trans. Ind. Appl.*, vol. 52, no. 2, pp. 1785–1795, 2016.

[132] J. J. More, P. F. Puleston, C. Kunusch, and M. A. Fantova, “Development and implementation of a supervisor strategy and sliding mode control setup for fuel-cell-based hybrid generation systems,” *IEEE Trans. Energy Convers.*, vol. 30, no. 1, pp. 218–225, 2015.

[133] M. Kumar, S. C. Srivastava, and S. N. Singh, “Control strategies of a dc microgrid for grid connected and islanded operations,” vol. 6, no. 4, pp. 1588–1601, 2015.

[134] A. Khorsandi, M. Ashourloo, and H. Mokhtari, “A decentralized control method for a low-voltage dc microgrid,” *IEEE Trans. Energy Convers.*, vol. 29, no. 4, pp. 793–801, 2014.

[135] M. Phattanasak, R. Gavagsaz-Ghoachani, J.-P. Martin, B. N.- Mobarakeh, S. Pierfederici, and B. Davat, “Control of a hybrid energy source comprising a fuel cell and two storage devices using isolated three-port bidirectional dc–dc converters,” *IEEE Trans. Ind. Appl.*, vol. 51, no. 1, pp. 491–497, 2015.

[136] R. Gavagsaz-Ghoachani, M. Phattanasak, J.-P. Martin, S. Pierfederici, and B. Davat, “Predicting the onset of bifurcation an stability study of a hybrid current controller for a boost converter,” *Math. Comput. Simul.*, vol. 91, pp. 262–273, 2013.

[137] R. Gavagsaz-Ghoachani, M. Phattanasak, J. P. Martin, S. Pierfederici, B. Nahid-Mobarakeh, and B. Davat, “Generalisation of an averagedmodel approach to estimate the period-doubling bifurcation onset in power con- verters,” *IET Power Electron.*, vol. 9, no. 5, pp. 977–988, 2016.

[138] C. K. Tse and M. Di Bernardo, “Complex behavior in switching power converters,” *Proc. IEEE*, vol. 90, no. 5, pp. 768–781, 2002.

[139] R. Gavagsaz-Ghoachani, M. Phattanasak, J. P. Martin, B. Nahid-Mobarakeh, S. Pierfederici, and P. Riedinger, “Observer and Lyapunov-Based Control for Switching Power Converters with LC Input

Filter," *IEEE Trans. Power Electron.*, vol. 34, no. 7, pp. 7053–7066, 2019, doi: 10.1109/TPEL.2018.2877180.

[140] A. B. Awan, S. Pierfederici, B. Nahid-Mobarakeh, and F. Meibody-Tabar, "Active stabilization of a poorly damped input filter supplying a constant power load," in *IEEE Energy Convers. Congr. Expo.*, 2009, pp. 2991–2997.

[141] L.-M. Saublet, R. Gavagsaz-Ghoachani, N.-M. B., J. P. Martin, and S. Pierfederici, "Stability analysis, discrete time modeling and active stabilization of dc-dc converter, taking into account the load dynamics," in *IEEE Transp. El.*, 2015, pp. 1–6.

[142] M. Wu and D. D.-C. Lu, "A novel stabilization method of LC input filter with constant power loads without load performance compromise in dc microgrids," *IEEE Trans. Ind. Electron.*, vol. 62, no. 7, pp. 4552–4562, 2015.

[143] R. Gavagsaz-Ghoachani, M. Phattanasak, J. P. Martin, S. Pierfederici, B. Nahid-Mobarakeh, and P. Riedinger, "A Lyapunov function for switching command of a DC–DC power converter with an LC input filter," *IEEE Trans. Ind. Appl.*, vol. 53, no. 5, pp. 5041–5050, 2017.

[144] J. Alvarez-Ramirez, I. Cervantes, G. Espinosa-Perez, P. Maya, and A. Morales, "A stable design of PI control for DC-DC converters with an RHS zero," *IEEE Trans. Circuits Syst. I, Fundam. Theory Appl.*, vol. 48, no. 1, pp. 103–106, 2001.

[145] M. Phattanasak, R. Gavagsaz-Ghoachani, J. P. Martin, S. Pierfederici, and B. Davat, "Flatness based control of an isolated three-port bidi- rectional DC-DC converter for a fuel cell hybrid source," in *IEEE Energy Convers. Congr. Expo.*

[146] S. Oucheriah and L. Guo, "PWM-based adaptive sliding-mode control for boost DC-DC converters," *IEEE Trans. Ind. Electron.*, vol. 60, no. 8, pp. 3291–3294, 2018.

[147] A. Ghasemian and A. Taheri, "Constrained near-time-optimal sliding- mode control of boost converters based on switched affine model analysis," *IEEE Trans. Ind. Electron.*, vol. 65, no. 1, pp. 887–897, 2018.

[148] S. E. Beid and S. Doubabi, "DSP-based implementation of fuzzy output tracking control for a boost converter," *IEEE Trans. Ind. Electron.*, vol. 61, no. 1, pp. 196–209, 2014.

[149] G. Cimini, G. Ippoliti, G. Orlando, and M. Pirro, "Sensorless power fac- tor control for mixed conduction mode boost converter using passivity- based control," *IET Power Electron.*, vol. 7, no. 12, pp. 2988–2995, 2014.

[150] J. Linares-Flores, J. Reger, and H. Sira-Ramírez, "Load torque esti- mation and passivity-based control of a boost-converter/DC-motor combination," *IEEE Trans. Control Syst. Technol.*, vol. 18, no. 6, pp. 1398–1405, 2010.

[151] Z. Chen, W. Gao, J. Hu, and X. Ye, "Closed-loop analysis and cascade control of a nonminimum phase boost converter," *IEEE Trans. Power Electron.*, vol. 26, no. 4, pp. 1237–1252, 2011.

[152] R. Gavagsaz-Ghoachani, M. Phattanasak, J. P. Martin, B. Nahid-Mobarakeh, and S. Pierfederici, "A Fixed-Frequency Optimization of PWM Current Controller-Modeling and Design of Control Parameters," *IEEE Trans. Transp. Electrif.*, vol. 4, no. 3, pp. 671–683, 2018, doi:

10.1109/TTE.2018.2841801.

[153] C. Yfoulis, D. Giaouris, C. Ziogou, F. Stergiopoulos, S. Voutetakis, and S. Papadopoulou, “Optimal switching Lyapunov-based control of power electronic converters,” *Int. J. Circuit Theory Appl.*, vol. 45, pp. 354–375, 2016.

[154] S. R. Sanders and G. C. Verghese, “Lyapunov-based control for switched power converters,” *IEEE Trans. Power Electron.*, vol. 7, no. 1, pp. 17–24, 1992.

[155] H. Cho, S. J. Yoo, and S. Kwak, “State observer based sensorless control using Lyapunov’s method for boost converters,” *IET Power Electron.*, vol. 8, no. 1, pp. 11–19, 2015.

[156] M. Pahlevani, S. Pan, S. Eren, A. Bakhshai, and P. Jain, “An adaptive nonlinear current observer for boost PFCAC/DC converters,” *IEEETrans. Ind. Electron.*, vol. 61, no. 12, pp. 6720–6729, 2014.

[157] B. Abdessamad, K. Salah-ddine, and C. E. Mohamed, “Design and Modeling of DC / DC Boost Converter for Mobile Device Applications,” *Int. J. Sci. Technol.*, vol. 2, no. 5, pp. 394–401, 2013.

[158] B. M. Hasaneen and A. A. E. Mohammed, “Design and simulation of DC/DC boost converter,” *2008 12th Int. Middle East Power Syst. Conf. MEPCON 2008*, pp. 335–340, 2008, doi: 10.1109/MEPCON.2008.4562340.

[159] R. W. A. A. De Doncker, D. M. Divan, and M. H. Kheraluwala, “A Three-Phase Soft-Switched High-Power-Density DC/DC Converter for High-Power Applications,” *IEEE Trans. Ind. Appl.*, vol. 27, no. 1, pp. 63–73, 1991, doi: 10.1109/28.67533.

[160] Sarah Saeed Hazkial Gerges, “Design and Construction of an Isolated DC to DC Switching Converter for Integration of Energy Storage Systems in Power Electronic Applications,” UNIVERSIDAD DE OVIEDO, 2015.

[161] Cui Ying, “Three-Phase dual active bridge converter: design considerations and planar transformer design,” McMASTER UNIVERSITY, 2017.

[162] F. KRISMER, “Modeling and Optimization of Bidirectional Dual Active Bridge DC – DC Converter Topologies,” Universität Wien, 2010.

[163] J. H. Jung, C. K. Kwon, J. P. Hong, E. C. Nho, H. G. Kim, and T. W.CHun, “Power control and transformer design method of bidirectional dc-dc converter for a hybrid generation system,” in *IEEE VehiclePower Propulsion Conf*, 2012, pp. 1512–1515.

[164] G. J. Su and L. Tang, “A three-phase bidirectional dc-dc converter for automotive applications,” in *IEEE Ind. Appl. Soc. Annu. Meet*, 2008, pp. 1–7.

[165] G. Waltrich, M. A. M. Hendrix, and J. L. Duarte, “Three-Phase Bidirectional DC/DC Converter with Six Inverter Legs in Parallel for EV Applications,” *IEEE Trans. Ind. Electron.*, vol. 63, no. 3, pp. 1372–1384, 2016, doi: 10.1109/TIE.2015.2494001.

[166] N. Tan, N. Tan, S. Inoue, S. Inoue, A. Kobayashi, and H. Akagi, “Voltage balancing of a 320-V, 12-F electric double-layer capacitor bank combined with a 10-kW bidirectional isolated dc-dc converter,” *IEEE Trans. Power Electron.*, vol. 23, pp. 2755–2765, 2008.

[167] S. Inoue and H. Akagi, “A bidirectional dc-dc converter for an energy storage system with galvanic isolation,” *Trans. Power Electron.*, vol. 22, pp. 2299–2306, 2007.

[168] S. Inoue and H. Akagi, “A bidirectional isolated dc-dc converter as a core circuit of the next-generation medium-voltage power conversion system,” *IEEE Trans. Power Electron.*, vol. 22, pp. 535–542, 2007.

[169] H. Krishnaswami and N. Mohan, “Three-port series-resonant dc-dc converter to interface renewable energy sources with bidirectional load and energy storage ports,” *IEEE Trans. Power Electron*, vol. 24, no. 10, pp. 2289–2297, 2009.

[170] M. Rico-Secades, D. Garcia-Llera, E. Lopez Corominas, and A. Calleja, “Designing Dual-Active Bridge (DAB) Converter for Energy Storage/Recovery Systems in a Lighting Smart Grid context,” *Work. J.*, vol. 1, 2014, doi: 10.15592/workrooms.2014.0003.

[171] R. Morrison and M. Egan, “A new power-factor-corrected single-transformer UPS design,” *IEEE Trans. Ind. Appl.*, vol. 36, pp. 171–179, 2000.

[172] D. Segaran, D. G. Holmes, and B. P. McGrath, “Comparative analysis of single- And three-phase dual active bridge bidirectional DC-DC converters,” *Aust. J. Electr. Electron. Eng.*, vol. 6, no. 3, pp. 329–337, 2009, doi: 10.1080/1448837X.2009.11464251.

[173] A. R. Alonso, J. Sebastian, D. G. Lamar, M. M. Hernando, and A. Vazquez, “An overall study of a dual active bridge for bidirectional DC/DC conversion,” in *Proc. ECCE*, 2010, pp. 1129–1135.

[174] H. Bai and C. Mi, “Eliminate reactive power and increase system efficiency of isolated bidirectional dual-active-bridge dc-dc converters using novel dual-phase-shift control,” *IEEE Trans. Power Electron.*, vol. 23, no. 6, pp. 2905–2914, 2008, doi: 10.1109/TPEL.2008.2005103.

[175] K. Wu, C. W. De Silva, and W. G. Dunford, “Stability analysis of isolated bidirectional dual active full-bridge DC-DC converter with triple phase-shift control,” *IEEE Trans. Power Electron.*, vol. 27, no. 4, pp. 2007–2017, 2012, doi: 10.1109/TPEL.2011.2167243.

[176] M. Kim, M. Rosekeit, S. K. Sul, and R. W. A. A. De Doncker, “A dual-phase-shift control strategy for dual-active-bridge DC-DC converter in wide voltage range,” *8th Int. Conf. Power Electron. - ECCE Asia "Green World with Power Electron. ICPE 2011-ECCE Asia*, pp. 364–371, 2011, doi: 10.1109/ICPE.2011.5944548.

[177] H. Bai, C. Mi, C. Wang, and S. Gargies, “The dynamic model and hybrid phase-shift control of a dual-active-bridge converter,” *IECON Proc. (Industrial Electron. Conf.*, no. 1, pp. 2840–2845, 2008, doi: 10.1109/IECON.2008.4758409.

[178] A. K. Jain and R. Ayyanar, “PWM control of dual active bridge: Comprehensive analysis and experimental verification,” *IEEE Trans. Power Electron.*, vol. 26, no. 4, pp. 1215–1227, 2011, doi: 10.1109/TPEL.2010.2070519.

[179] L. Jin, B. Liu, and S. Duan, “ZVS operation range analysis of three-level dual active bridge DC-DC converter with phase-shift control,” *Conf. Proc. - IEEE Appl. Power Electron. Conf. Expo. - APEC*, pp. 362–366, 2017, doi: 10.1109/APEC.2017.7930718.

[180] D. Wang, “Design and Control of an Isolated Battery-Driven Grid Interface With Converter Design and Control of an Isolated Battery-Driven,” McMaster, 2018.

[181] N. H. Baars, J. Everts, C. G. E. Wijnands, and E. A. Lomonova, “Performance Evaluation of a Three-Phase Dual Active Bridge DC-DC Converter with Different Transformer Winding Configurations,”

IEEE Trans. Power Electron., vol. 31, no. 10, pp. 6814–6823, 2016, doi: 10.1109/TPEL.2015.2506703.

[182] H. Fan and H. Li, "High-frequency transformer isolated bidirectional DC-DC converter modules with high efficiency over wide load range for 20 kVA solid-state transformer," *IEEE Trans. Power Electron.*, vol. 26, no. 12, pp. 3599–3608, 2011, doi: 10.1109/TPEL.2011.2160652.

[183] R. W. De Doncker, D. M. Divan, and M. H. Kheraluwala, "Three-phase soft-switched high power density dc/dc converter for high power applications," *Conf. Rec. - IAS Annu. Meet. (IEEE Ind. Appl. Soc.*, vol. 35 n 6, pp. 796–805, 1988, doi: 10.1109/ias.1988.25153.

[184] Z. Li, Y. Wang, Y. Cui, L. Shi, J. Huang, and W. Lei, "Fast transient current control for three-phase dual-active-bridge DC-DC converters with variable duty cycles," *Conf. Proc. - IEEE Appl. Power Electron. Conf. Expo. - APEC*, pp. 1209–1215, 2017, doi: 10.1109/APEC.2017.7930849.

[185] H. Bai and C. Mi, "Eliminate reactive power and increase system efficiency of isolated bidirectional dual-active-bridge DC-DC converters using novel dual-phase-shift control," *IEEE Trans. Power Electron*, vol. 23, no. 6, pp. 2905–2914, 2008.

[186] H. Tao, J. L. Duarte, and M. A. M. Hendrix, "Three-port triple-half-bridge bidirectional converter with zero-voltage switching," *IEEE Trans. Power Electron*, vol. 23, no. 2, pp. 782–792, 2008.

[187] A. R. Oliva, "Switching Control Strategy to Minimize Dual Active Bridge Converter Losses," *IEEE Trans. Power Electron.*, vol. 24, no. 7, pp. 1826–1838, 2009, doi: 10.1109/TPEL.2009.2020902.

[188] Z. Wang and H. Li, "A soft switching three-phase current-fed bidirectional DC-DC converter with high efficiency over a wide input voltage range," *IEEE Trans. Power Electron.*, vol. 27, no. 2, pp. 669–684, 2012, doi: 10.1109/TPEL.2011.2160284.

[189] J. Huang, Y. Wang, Z. Li, Y. Jiang, and W. Lei, "Simultaneous PWM control to operate the three-phase dual active bridge converter under soft switching in the whole load range," *Conf. Proc. - IEEE Appl. Power Electron. Conf. Expo. - APEC*, vol. 2015-May, no. May, pp. 2885–2891, 2015, doi: 10.1109/APEC.2015.7104760.

[190] E. De Din, H. A. B. Siddique, M. Cupelli, A. Monti, and R. W. De Doncker, "Voltage Control of Parallel-Connected Dual-Active Bridge Converters for Shipboard Applications," *IEEE J. Emerg. Sel. Top. Power Electron.*, vol. 6, no. 2, pp. 664–673, 2018, doi: 10.1109/JESTPE.2017.2786350.

[191] J. Venkat, A. Shukla, and S. V. Kulkarni, "A novel dq-vector based control for the three phase active rectifier in a power electronic transformer," *2013 Annu. IEEE India Conf. INDICON 2013*, pp. 8–13, 2013, doi: 10.1109/INDCON.2013.6725915.

[192] B. K. Bose, *Power Electronics and Motor Drives - Advances and Trends*. 2006.

PUBLICATIONS

International journal

S. A. Hashjin, S. Pang, E. Miliani, K. Ait-Abderrahim and B. Nahid-Mobarakeh, "Data-Driven Model Free Adaptive Current Control of a Wound Rotor Synchronous Machine Drive System," in *IEEE Transactions on Transportation Electrification*, doi: 10.1109/TTE.2020.3006722 (June 2020).

Saeid Aghaei Hashjin, Adrien Corne, Shengzhao Pang, El-hadj Miliani, Karim Ait-Abderrahim, BabakNahid-Mobarakeh**,** "Current Sensorless Control for WRSM Using Model Free Adaptive Control", *in IEEE Transactions on Transportation Electrification,* doi: 10.1109/TTE.2020.3030111.

Saeid Aghaei Hashjin, Roghayeh Gavagsaz-Goachani, Mtheepot Phattanasak, El-hadj Miliani, Serge Pierfederici, BabakNahid-Mobarakeh**,** "Active Stabilization of a Boost Converter Using MFAC", *IEEE Journal of Emerging and Selected Topics in Power Electronics, (under Review).*

S. Pang, S. A. Hashjin, B. Nahid-Mobarakeh, S. Pierfederici, Y. Huangfu, G. Luo, and F. Gao, "Large-Signal Stabilization of Power Converters Cascaded Input Filter Using Adaptive Energy Shaping Control," in *IEEE Transactions on Transportation Electrification*, doi: 10.1109/TTE.2020.3021954 (Sep. 2020).

International conferences

S. A. Hashjin and B. Nahid-Mobarakeh, "Active stabilization of a microgrid using model free adaptive control," *2017 IEEE Industry Applications Society Annual Meeting*, Cincinnati, OH, 2017, pp. 1-8, doi: 10.1109/IAS.2017.8101797.

S. A. Hashjin, E. Miliani, K. Ait-Abderrahirrr and B. Nahid-Mobarakeh, "Current Sensorless Model Free Control Applied on PMSM Drive System," *2019 IEEE Transportation Electrification Conference and Expo (ITEC)*, Detroit, MI, USA, 2019, pp. 1-5, doi: 10.1109/ITEC.2019.8790572.

P. Haghgooei, S. Aghaei-Hashjin, N. Takorabet, D. Arab-Khaburi and B. Nahid-Mobarakeh, "Comprehensive Online Parameters Identification of Wound Rotor Synchronous Machine (WRSM) by Proposing Two New Parameters and Using Kalman Observer," *2020 IEEE Transportation Electrification Conference & Expo (ITEC)*, Chicago, IL, USA, 2020, pp. 192-197, doi: 10.1109/ITEC48692.2020.9161552.